Tropospheric Greenhouse Gases: Emission Characteristics and Dynamical Effects

A thesis submitted in partial fulfillment of

the requirements for the degree of

Doctor of Philosophy

by

Naveen Chandra

(Roll No. 11330007)

Under the guidance of

Prof. Shyam Lal

Space and Atmospheric Sciences Division

Physical Research Laboratory, Ahmedabad, India.

DISCIPLINE OF PHYSICS

INDIAN INSTITUTE OF TECHNOLOGY GANDHINAGAR

2015

to

my parents and grand parents

Declaration

I declare that this written submission represents my ideas in my own words and where others' ideas or words have been included, I have adequately cited and referenced the original sources. I also declare that I have adhered to all principles of academic honesty and integrity and have not misrepresented or fabricated or falsified any idea/data/fact/source in my submission. I understand that any violation of the above will be cause for disciplinary action by the Institute and can also evoke penal action from the sources which have thus not been properly cited or from whom proper permission has not been taken when needed.

(Signature)

(Name: Naveen Chandra)

(Roll No: 11330007)

Date: December 30, 2015

CERTIFICATE

It is certified that the work contained in this thesis titled **"Tropospheric Greenhouse Gases: Emission Characteristics and Dynamical Effects"** by **Mr. Naveen Chandra** (Roll No. 11330007), has been carried out under my supervision and that this work has not been submitted elsewhere for a degree.

Prof. Shyam Lal
(Thesis Supervisor)
Space and Atmospheric Sciences Division
Physical Research Laboratory,
Ahmedabad, India.

Date: December 30, 2015

Acknowledgements

Ph.D diary, witness of five and half wonderful years of my journey, has reached in its closing phase with the pages of bittersweet experiences and nostalgic memories. A happy ending note is that, in spite of being alone on the first page of this journey, now I find myself in the company of many wonderful people on the last page of this journey. Some of them I admire and respect and some of them became my friends. It is not possible to list here all the people who influenced my life and worked to achieved this milestone. However, even if they are not mentioned here, I am grateful to all of them nonetheless.

I feel esteemed pleasure and privilege to express my profound sense of gratitude and thankfulness to my mentor, philosopher and Ph.D supervisor Prof. Shyam Lal for his invaluable and meticulous guidance, constant supervision, and continuous encouragement on every advancement that I have made in this journey. In addition, his recognition of my weaknesses and pushing me to overcome them has been the most gratifying part of this experience. Not only academically, but personally also he has always been very supportive and helpful in all aspects during my entire stay in Ahmedabad and I will forever remember his kindness and support.

I am grateful to Prof. Varun Sheel and Prof. Sunil Singh for their continuous support, encouragement, constructive feedbacks, suggestions from time to time and critical evaluation of this thesis before its submission. I would also like to thank Prof. S. Ramachandran for his helping hand and support throughout the tenure of this work. I am deeply indebted to Mr. S. Venkataramani for his valuable help in learning the fundamentals of measurements, his wholehearted support and many useful interactions. I am also grateful to Mr. T. A. Rajesh for his unselfish support, helpful discussions in science and encouragement at every step of my scientific journey. I gratefully acknowledge Mr. T. K. Sunil Kumar for his continuous support in the operation and maintenance of various instruments. I am highly obliged to Dr. M. Naja (ARIES, Nainital), Dr. S. K. Sharma and

Dr. L. K. Sahu for various scientific discussions and motivations. I also cherish my interactions with Dr. Y. B. Acharya, Prof. R. Sekar, Prof. D. Pallamraju, Prof. H. Chandra, Prof. S.A. Haider, Dr. D. Chakrabarty, Prof J. Bhatt, Prof. S. Mohanty, Dr. Navin Juyal, Dr. Namit Mahajan, Dr. R. D. Deshpande, Prof. R. Sridharan, Dr. A. Guharay, Prof. H. S. Sinha, Mr. R.P. Singh, Mr. Atul Manke and Mr. Mitesh Bhavsar. I will be forever indebted to Prof. R. Ramesh and Prof. R. Rangarajan for their inspiring lectures during our course work.

I would like to express my sincere thanks to the Director and the Dean of PRL, for providing me the necessary facilities, academic, non-academic support and help to complete my research work. The moments, which I spent in PRL during my research tenure, will always remind me the golden moments of my life. I thank all the PRL "academic committee members" during $2010 - 2015$*, whose critical review and guidance at various stages of my thesis tenure helped me to improve in my research pursuits. I would like to thank Dr. Bhushit Vaishnav, Head Academic Services, PRL, for his support during this period. My warm thanks extend to Director, Dean and all staffs member of IIT Gandhinagar, specially Piyush Bhai for their kind help and co-operation.*

During this work I have collaborated with many colleagues for whom I have great regard, and I wish to extend my warmest gratefulness to all of them. I owe my most sincere gratitude to Dr. Prabir Patra from JAMSTEC, Japan and consider myself lucky to get an opportunity to work with him. I have been greatly benefited and learned very much from his exemplary scientific and personal integrity, generosity, never ending enthusiasm, and positive approach to understand research problems. He always showed deep interest in my work and provided time from his busy schedule for many useful and insightful discussions. I extend my sincere thanks to to Prof. Michel Ramonet (LSCE, France) for providing me an opportunity to visit his laboratory LSCE, Paris, for scientific discussions as well as visiting their atmospheric measurement lab. I am truly thankful to Xin Lin for her wholehearted support and various fruitful discussions regarding the methane

modeling during my stay in Paris.

I have been blessed with intellectual guidance, inspiration and moral support from my school teachers, specially from Shri O.P. Semwal. I am extremely grateful to all of them. I wish to express my warm and sincere thanks to Dr. Ishan Purohit, who persuaded me for this journey as well as gave me moral support during my struggling days. The critical supports of CONTRAIL, MOPITT, TRMM and NCEP science team members for providing the in-situ and satellite data products, are greatly acknowledged.

Many PRL staff members have also been extremely helpful in advancing my research. I thank all the staff members of PRL computer center especially to Jigar ji, Hitendra ji, Alok ji, Samual ji and Tejas ji, for providing excellent computational and Internet facilities. I express my appreciation for the cooperation and help extended by the library and its staff members in general and Mrs. Nistha Anilkumar and Pragya Pandey in particular. In addition, I would like to express my deepest appreciation to workshop people (Ubale ji and his team members; Vipul bhai, Vishnu bhai, Rajesh Kaila and others), administrative and technical staff (Hemal ji, Gandhi ji, Parul ben, Preeti ben, Nandini ben, Richa ben, Jaishree ben Yadav ji, Gupta ji, Senthil ji, Sashi Ji, Shivadasan ji, Hota ji, Ranganathan ji, Pradeep ji, Bankim bhai and Sneha Nair), for their helpful hands and noble cooperation throughout the tenure of my thesis.

Completing a thesis is an intensive learning process on many different levels and one of the most important lessons I have learned during this work is the value of support from the friends, I deeply respect their encouragement, love and care. I would remain ever grateful to my lab seniors Chinmay Mallik and Shuchita Srivastava for their selfless help, consistent encouragement and interest in the progress of my work. The most amazing officemates Ashim and Jagat are especially acknowledged, since without their corporation and joyful company, it was not be so easy to accomplish this work. I feel blessed to have seniors like Arvind,

Pankaj, Vineet and Vimal, with whom I have interacted and spent maximum time during my beginning PRL days and due to have such seniors this memorable journey started very smoothly. The company and innumerable late night gatherings with Girish Kumar, Arko, Monojit, Tanmoy (Chattopadhyay), and Chandan (Hati) have kept me sane and focused on the other fun things in life, I sincerely thank them for adding such pleasant memories in my life. I feel fortunate to have wonderful company of my batchmates Avdhesh, Aadhi, Anjali, Bhavya, Damu, Dillip, Dinesh, Gaurav (Tomar), Gaurav (Sharma), Gangi, Girish, Gulab, Lekshmy, Midhun, Priyanka, Upendra, Uma, Wageesh and Yashpal, who fills different colours in my life and provided me huge moral supports during my struggling days of my research. My dearest junior friends Shraddha, Ikshu, Arun, Manu, Mondal, Anirban, and Abhaya deserve special mention for their enormous love, care, support and deep respect for me. In addition, I also express my sincere thanks to Guru, Kuldeep, Sanjay, Tiwari, Chithra, Ujjal, Sushanta, Sunil, Arun (Awasthi), Abhishek (Basak), Sashi, Fazlul, Sneha (Yadav), Shweta, Ila, Amrendra, Deepti, Deepak, Bivin, Chandana, Upasana, Sneha (Shawant), Lalit, Rahul, Jinia, Apurv, Venky, Newton, Pankaj, Jabir, Ali, Navpreet, Rukmani, Rupa, Satish, Kumar, Chandan (Gupta), Devendra, Manish, Wriju, Niharika, Shubha, Ravi, Debrup, Sudip, Kaustav, Varun, Subir and several others who made my stay at PRL cozy and made the hostel a happening place. I greatly acknowledge to Narendra (ARIES, Nainital), Tapaswini (ARIES, Nainital) and Srabanti Ballav (JU, Kolkata) for giving me a hand on experience on atmospheric model (WRF). I am also thankful to all those who were around me directly or indirectly during this work, specially, Piyush, Santosh, Naresh and my long time friends Alok, Tinku, Pari, Deepak, Ajay, Gaurav and Himanshu for their constant support and encouragements. Their constant push and motivational chats have always helped me to recover from odd times.

Above all, I owe my deepest respect and gratitude to my parents and grandparents for their love, encouragement and unending support. Beyond giving me life itself, my parents made countless sacrifices as they cared for and nurtured

me through my infancy and childhood, provided me with the necessities of life, nursed me through physical illnesses and the emotional stresses of growing up. They are an unfailing inspiration and source of strength and joy for me. Special thanks to my younger sister Nutan and younger brother Praveen, who made my periodic visits to home a delight every time. Last but not the least, I express my gratefulness towards my entire family members who always encouraged me during my thesis period. I personally believe that my thesis is purely an outcome of my parents and grandparents blessings and prayers, and that is why I dedicate this dissertation to them.

(Naveen Chandra)

Preface

The urban areas consist of more than half of the world's population and contribute about 70% of the fossil fuel CO_2 emissions (in 2010) as well as significant amount of anthropogenic emissions of CH_4 into the atmosphere. India is a fast developing country, where fossil fuel emissions have increased dramatically in last three decade and further predicted to continue to grow at least 6% per year through to 2025. In order to provide independent verification of future mitigation activities and predicting future climate, there is an urgent need of the measurements of greenhouse gases over representative urban regions.

Realising the importance of the study of greenhouse gases over urban locations, measurements of CO_2 and CH_4 along with an anthropogenic emission tracer CO have been initiated at a major urban site Ahmedabad in India, using a state of the art laser based cavity ring down spectrometer. The observed year-long data are analysed using suitable global chemistry transport models (JAMSTECs ACTM for CO_2 and CH_4, LMDz−OR−INCA for CH_4), and correlations among them. The effects of land ecosystem on CO_2 variation as well as anthropogenic emissions and atmospheric transport on CO_2 and CH_4 variations have been identified. The inventory (EDGAR) emissions of CH_4 and CO are tested using the observed data for the study location and found that the inventory emissions are underestimated. The CO_2 observations and model comparison brings out the need for improvement in the terrestrial flux simulated by the Carnegie-Anes-Stanford Approach (CASA) ecosystem model. Furthermore, comparison of the seasonal cycle of CH_4 with both models revel that the afternoon mixing ratios have the potential to represent the footprint of its emission of larger area and hence this data can be used in regional and global CH_4 inversion study with some caution.

Analyses of vertical profiles of CO_2 and CO in the troposphere using aircraft measurements of CO_2 over Delhi and satellite data of CO over five selected regions in India are also conducted. The amplitude of seasonal variability in CO_2

shows direct, but a delayed link with the strength of the Indian summer monsoon rainfall in Delhi. The model simulations are more close to the observations in the upper troposphere (3-8 km) as compared to lower troposphere (below 3 km). Average seasonal distributions of CO in the troposphere over all the study regions show very large spatial and vertical variability. Significant contribution at $300 - 200$ hPa, due to strong convection during the monsoon season as well as long range transport from the biomass burning regions of Central Africa and East Asia during other seasons particularly over south of Ahmedabad, have been observed. The annual variations in the CO concentrations at 900 and 300 hPa are found to be in opposite phase with lower values during monsoon at 900 hPa and higher values at 300 hPa. Simulations from two photochemical-transport models (MOZART and EMAC) are able to capture these variations broadly.

Measurements of CO_2 and CH_4 coupled with the atmospheric transport models could be used to assess the sources and sinks of CO_2 and CH_4 at regional level by inverse modeling studies. This is, however an objective for the future, since it can only be achieved using data records covering multiple years and at a network of stations. In summary, this thesis contributes in providing precise atmospheric measurements of important GHGs - CO_2 and CH_4 along with the anthropogenic tracer CO over an urban location in India which is not done so far to the best of our knowledge. This dataset is very helpful for understanding processes and phenomena related to the land-atmosphere exchange of CO_2, constraining the CH_4 and CO emission inventories as well as understanding the contributions of anthropogenic sources in a mega-city to observed variations.

Keywords: Greenhouse gases, CRDS technique, India, Urban region, Anthropogenic emissions, Biospheric emissions, Long range transport, Photochemical-transport models.

Acronyms and Abbreviations

ACTM	AGCM-based chemistry- transport model
AGCM	Atmospheric general circulation model
AK	Averaging Kernel
AMSL	Above Mean Sea Level
CARIBIC	Civil Aircraft for the regular Investigation of the atmosphere Based on an Instrument Container
CASA	Carnegie-Ames-Stanford Approach
CFC	Chlorofluorocarbon
CH_4	Methane
CO_2	Carbon dioxide
CO	Carbon monoxide
CME	Continuous CO_2 Measuring Equipment
CNG	Compressed Natural Gas
CRDS	Cavity Ring Down Spectroscopy
CRI	Cape Rama
CSIRO	Commonwealth Scientific and Industrial Research Organization
CTM	Chemistry Transport Model
DOF	Degrees Of Freedom
ECHAM	European Centre Hamburg general circulation model
ECMWF	European Centre for Medium-range Weather Forecasting
EDGAR	Emissions Database for Global Atmospheric Research
GCM	General Circulation Model
GHGs	Greenhouse gases
GMT	Greenwich Mean Time
GPP	Gross Primary production
HLE	Hanle
HYSPLIT	Hybrid Single Particle Lagrangian Integrated Trajectory Model
IGP	Indo Gangetic Plain
INCA	Interactions between Chemistry and Aerosols
IPCC	Intergovernmental Panel on Climate Change
IR	Infrared radiation
ITCZ	Inter-Tropical Convergence Zone
JAL	Japan Airline
LT	Lower troposphere
MB	Mean Bias
MEERA	Modern-Era Retrospective Analysis for Research and Applications

MESSy	Modular Earth Submodel System
MLO	Mauna Loa
MNMB	Modified and Normalized Mean Bias
MODIS	Moderate Resolution Imaging Spectroradiometer
MOPITT	Measurements Of Pollution In The Troposphere
MOZART	Model of Ozone and Related Tracers
MT	Middle troposphere
N_2O	Nitrous oxide
NCEP	National Centers for Environmental Prediction
NDIR	Non Dispersive Infrared
NIO	National Institute of Oceanography
ORCHIDEE	Organizing Carbon and Hydrology in Dynamic Ecosystems
PBL	Planetary Boundary Layer
POET	Precursors of Ozone and their Effects in the Troposphere
POB	Port Blair
PON	Pondicherry
PPB	Parts per Billion
PPM	Parts per Million
PRL	Physical Research Laboratory (Ahmedabad, India)
PTFE	Polytetrafluoroethylene
REAS	Regional Emission inventory in Asia
RMSE	Root Mean Square Error
SEY	Seychelles
SNG	Sinhagad
TRMM	Tropical Rainfall Measuring Mission
UT	Upper troposphere
VC	Ventilation Coefficient
WMO	World Meteorological Organization

Contents

List of Figures

List of Tables

Chapter 1

Introduction

1.1 Background

The Earth's atmosphere is being perturbed since the time humans started using agriculture for food, and energy for transport and industry. The demand for these has been growing at an exponential rate, which has led to a substantial increase in the levels of greenhouse gases (GHGs) and several pollutants in the atmosphere. The GHGs are important constituents of the Earth's climate, since they control the global surface temperature by trapping the heat radiation, emitted from the Earth's surface. GHGs include carbon dioxide (CO_2), methane (CH_4), nitrous oxide (N_2O), water vapour (H_2O), ozone (O_3) and chlorofluorocarbons (CFCs) [1]. Out of these gases, CO_2 and CH_4 are most important GHGs due to their higher atmospheric mixing ratios as compared to other gases and longer lifetimes in the atmosphere. The Intergovernmental Panel on Climate Change (IPCC) in its latest Assessment Report-5 stated that the increasing levels of GHGs have increased the global surface temperature by 0.85°C from 1880 to 2012 [1]. The temperature increased in the past also, but the time frame for the increase was very high as compared to the present increase. The Vostock ice core records show the close correlations between CO_2, CH_4, and temperature during the past 420,000 years, which infer that the past climate change was in a part forced by changes in atmospheric mixing ratios of these gases (Figure 1.1; [2]). During this period, the time frame of the oscillations of atmospheric CO_2 and CH_4 is observed

roughly 100,000 year cycle between 180 and 280 ppm, and between 0.2 and 0.7 ppm, respectively, as the climate system pulsed between glacial and interglacial states (Figure 1.1). However, the Earth's system has dramatically left this glacial-interglacial regular cycle in the short time interval of last 250 years, as mixing ratios of atmospheric CO_2 have increased by 100 ppm than that of the interglacial maximum and also the rate of increase has been at least 10 times faster than at any other time in the past 420,000 years. Concentrations of other GHGs such as CH_4 and nitrous oxide (N_2O) have been increased significantly also in same time interval [1].

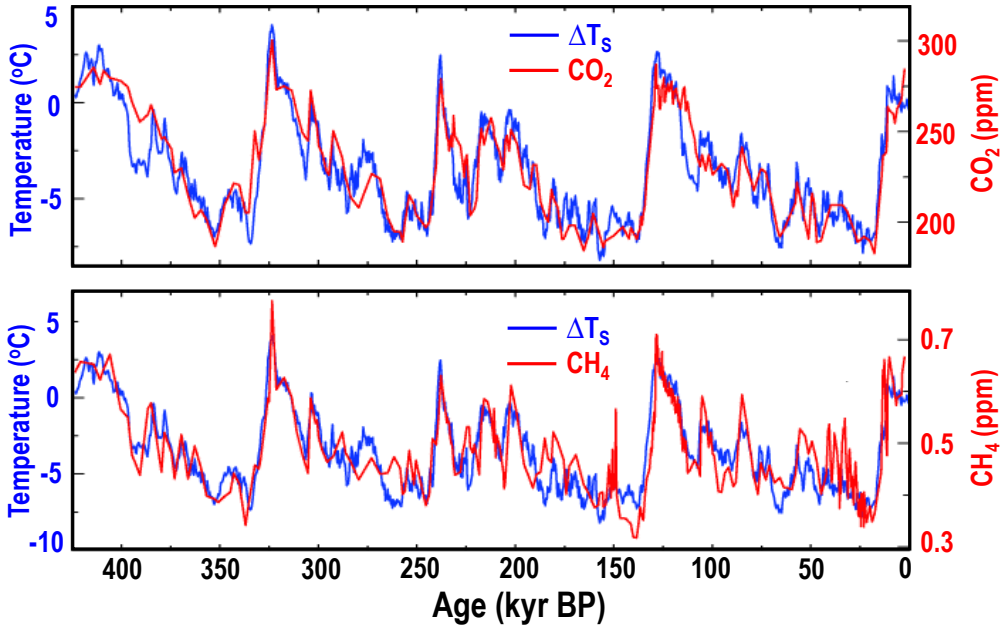

Figure 1.1: Variations in atmospheric temperature, CO_2 and CH_4 mixing ratios in past 420,000 years, recorded by the air trapped in the Vostok ice core from the Antarctica [2]. The temperature is calculated by using the ratio of deuterium to hydrogen in the trapped air and the time series shows the difference with respect to the mean of recent time temperature value (∼15°C).

The increasing level of GHGs is one of the major cause for the recent global warming induced climate change. Global scale warming, aggravation of sea-ice and glacier melting, rise in global mean sea level and increase in the frequency and intensity of extreme weather events such as the floods, droughts, wildfires

and cyclonic storms are the fingerprints of climate change. These changes in the levels of GHGs are unquestionably due to human activities which are known to produce CO_2 from fossil fuel combustion, deforestation, and CH_4 from agriculture, livestock, energy production and waste management. It indicates that the anthropogenic activities have drove the Earth's system well outside the range in which the carbon cycle operated over the past half million years [1].

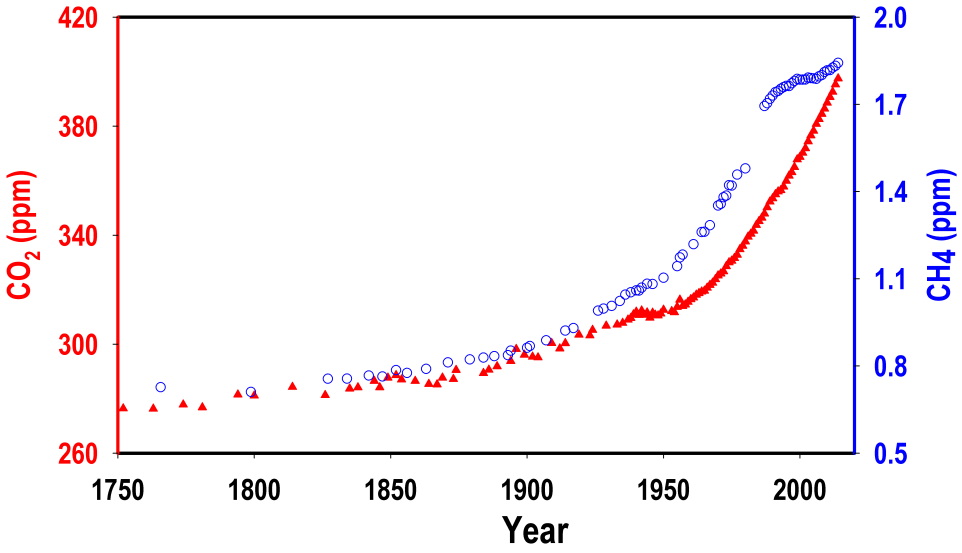

Figure 1.2: Variations in CO_2 (red triangles) and CH_4 (blue circles) mixing ratios from 1750 to 2014, based on ice core data before 1958 for CO_2 as well as before 1981 for CH_4, and yearly averages of direct observations from Mauna Loa and South Pole (Source: "http://scrippsco2.ucsd.edu").

CO_2 and CH_4 are the two most radiatively important GHGs attributable to human activity. The atmospheric measurements indicate that the total burdens of atmospheric CO_2 and CH_4 have increased by about 40% (Figure 1.2; based on merged ice-core and atmospheric CO_2 data; http://scrippsco2.ucsd.edu) and 150% (Figure 1.2; [3]; NOAA/AGAGE websites for recent data), respectively within very short time period (from 1750 to 2014) and hence it drew the attention of climate scientists [1]. Together, they contribute about 80% of the global warming and hence lead to significant impact on the climate system [4]. CH_4 has 75 times more potential to trap heat than CO_2 on per molecule basis over a

20-year timescale [5]. Also, it has a shorter lifetime (about 9 years) than CO_2, and many other GHGs, thus a reduction in its anthropogenic emission would be an effective way of abating global warming in the near future. Although most of the emission processes of CO_2 and CH_4 have been identified, but significant uncertainties exist in their magnitude and variability. Both the CO_2 and CH_4 cycles have significant natural components, which complicate the quantification of their total budgets due to limited understanding. Better understanding of their budgets are important for predicting their future levels and subsequently the future climate. Mitigation strategies that seek to reduce atmospheric mixing ratios of CO_2 and CH_4 also require better estimates of their sources and sinks. Therefore, atmospheric measurements of GHGs combined with model simulations are necessary to understand the present state and predict future behavior of GHGs emissions. Rapidly expanding economie of East Asia are showing a swift increase in GHGs emission. From 1993 to 2002, CO_2 emissions from India have increased by 57%, and such trend will likely continue since per capita emissions are still far behind those of Europe and the United States. The development of the Indian sub-continent with a population about $\sim$1.4 billion, may lead to significant changes in the regional distribution of GHGs in the atmosphere. Such developments emphasize the need for the atmospheric measurement of the levels of GHGs, to understand the present state of their levels and for the purpose of mitigation policies over the Indian subcontinent and also for prediction of future levels of GHGs emissions.

1.2 Greenhouse gases and their role in Earth's atmosphere

GHGs are those gaseous compounds in the atmosphere, which are generally transparent to incoming solar radiation and opaque to Earth's radiation (they absorb and transfer the Earth's infrared radiation (IR) by a variety of means). GHGs do not really "trap Earth's heat" permanently, but could be fairly described as delaying the energy transfer from Earth to space. This process is the fundamental

cause for Greenhouse Effect. The primary GHGs in the Earth's atmosphere are water vapor, CO_2, CH_4, N_2O, and O_3. The prime requirement for considering molecules as GHGs (or being IR active) is that the molecule must change its dipole moment (μ) after absorbing the IR radiation. The electric dipole formed when the adjacent atoms inside the molecules have different charges, separated by a distance "r" and dipole moment (μ) is defined by the product of charge and the separation vector. The change in dipole moment occurs when the distance between two atoms forming the dipole gets disturbed by the vibration and rotation in the molecule. If the frequency of electromagnetic radiation matches with the vibrational frequency of the molecule, then the radiation will be absorbed. It results in the change in the energy level and increases the vibrational or rotational quantum number. The molecular vibrations give rise to the absorption bands mostly in the near IR (wavelength (λ) in the region of 0.75 - 2.5 μm) and mid IR (λ in the region of 2.5 - 10 μm) region of electromagnetic radiation. The far IR (λ from 10 μm to 1 mm), lying adjacent to the microwave region has low energy and responsible for the molecular rotation only. The molecular vibrations consist of two modes, i.e., stretching (also two type symmetric and asymmetric stretching) and bending.

CO_2 is a triatomic linear molecule, which has 4 fundamental vibrations mode (according to 3N-5 rule; N: numbers of atom); one symmetric stretch, two antisymmetric stretch and one bending mode. It does not have a permanent dipole moment, since the change in electric dipole of the C=O bond is the same but in the opposite direction. So symmetric stretching does not allow for the absorption of IR radiation and termed as IR inactive. Asymmetric bond stretching and bond bending result fluctuating dipole moments in CO_2 molecule and hence produces absorption bands at 4 μm and 15 μm, respectively. Bending mode is the most likely to absorb infrared radiation strongly at 15 μm from the Earth before it can escape to space. There are many more combinations and overtone of vibrations producing 11 additional bands from 0.87 to 15 μm [6–8], but they are weakly absorbing by CO_2 molecule. For example, the 10 μm absorption band is 10^6 times

weaker than the peak of 15 μm band [6]. CH_4 is a tetrahedral molecule, which is highly symmetric in shape and has four vibrational modes. But only two of the vibrational modes depict direct interaction with infrared light (At 3.2 μm and 7.3 μm: the ones where the carbon and hydrogen both move), and these modes are the most likely to absorb or scatter infrared heat radiation emitted from the Earth's surface.

1.2.1 Radiation budget

Solar radiation is the major source of energy in the atmosphere and Earth's surface. Its spectrum is roughly represented by a black body radiation characteristic of about 6000 K [6–8]. A black body is a conceptual mass of matter that vibrate at all possible frequencies and would be able to absorb or emit all the different frequencies of light. According to Wien's displacement law, at 6000 K solar radiation peaks in the visible range of wavelengths ($\lambda = 0.4 - 0.7$ μm) and is maximum in the green ($\lambda = 0.5$ μm). The sunlight at Earth's surface consists about 52 -55% of infrared radiations (IR; $\lambda > 0.7$ μm), about 42-43% of visible radiations ($\lambda < 0.7$ μm) and small fraction about 3-5% of ultraviolet radiation (UV; $\lambda < 0.4$ μm) [9].

The total power (E_s) emitted by the Sun is [6–8]

$$E_s = \text{surface area of Sun} \times \text{radiation flux of Sun per unit area}, \tag{1.1}$$

$$= 4\pi R_s^2 \times \sigma T_S^4, \tag{1.2}$$

where $R_s = 7 \times 10^5$ km is the Sun's radius. The distance between Earth and Sun is about $d = 1.5 \times 10^8$ km. Assuming a hypothetical sphere, which contains Sun and Earth at the center and the circumference of the sphere, respectively. The solar flux at the circumference of that hypothetical sphere is

$$F_s = \frac{E_s}{4\pi d^2}, \tag{1.3}$$

Solving above equation, we obtain $F_s = 1370$ Wm^{-2}. It is the amount of energy that normally falls on a unit area of the Earth's orbit per second when the earth is

at its mean distance from the Sun, known as the *solar constant*. This radiation is received by the $4\pi R_E^2$ surface area of the Earth. Thus the fraction of solar constant that is received by the per unit area of the Earth surface is

$$\frac{F_s \times \pi R_E^2}{4\pi R_E^2} = \frac{1370}{4} \sim 342 \;\; Wm^{-2}. \tag{1.4}$$

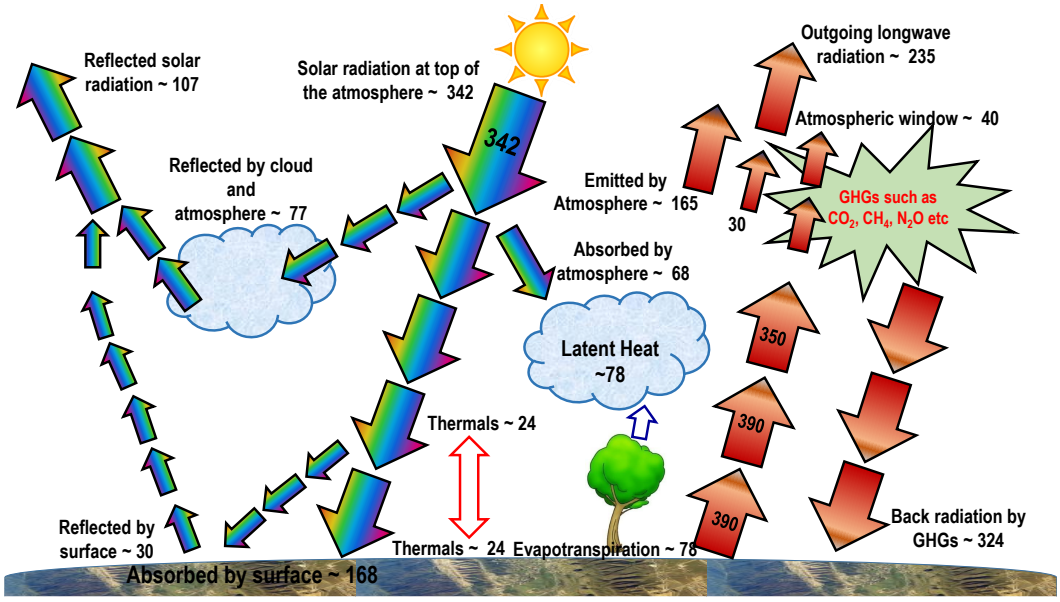

Figure 1.3: Schematic diagram of the energy budget of the Earth's atmosphere. Left part of figure shows the incoming energy flux from the Sun at Earth's surface, while the outgoing energy flux emitted from Earth's surface is shown on the right of figure. These energy fluxes are given in Wm^{-2} and the numbers are taken from [6].

So the average energy from sunlight coming to the top of Earth's atmosphere is around 343 Wm^{-2} [6–8]. Figure 1.3 shows the complex exchange and the flow of global mean energy in the atmosphere. Out of the 343 Wm^{-2}, about 30% ($\sim$ 107 Wm^{-2} [10]) is reflected back to space due to the reflection by clouds, scattering by air molecules, scattering by atmospheric aerosol particles and reflection from surface. Remaining 235 Wm^{-2} is absorbed by the Earth's surface ($\sim$ 168 Wm^{-2}) and the atmosphere ($\sim$ 67 Wm^{-2}). Further, the Earth's surface returned energy to atmosphere in form of sensible heat, latent heat via water vapour, and thermal infrared radiation for maintaining the energy balance. The global mean Earth's surface temperature is about 288 K and according to the Ste-

fan Boltzmann law, the infrared radiative flux emitted at the surface is 390 Wm^2. This flux is substantially exceeds from the outgoing infrared flux of 235 Wm^{-2} at the top of the atmosphere [6–8]. The GHGs present between top of the atmosphere and Earth's surface are most responsible agents for this energy imbalance. They absorbs as well as emit IR radiation, but the net effect is the absorption of energy. This is because the GHGs are at lower temperatures than the Earth's surface and hence they emit IR radiation at a lower intensity than if they were at the temperature of the Earth's surface. This imbalance in the incoming and outgoing energy flux is mostly caused for keeping the surface temperature warm.

1.2.2 Greenhouse effect

A glasshouse stays warm because its walls are transparent for the visible solar radiation but opaque for the long wave radiation. Hence, glasshouses provide an effective surrounding for growing vegetables in a cooler place. The Earth's greenhouse effect work similarly. GHGs present in the atmosphere work as a glass wall. They allow the visible solar radiation and prevent some of the outgoing thermal radiation from existing by absorbing it and hence warm the Earth's temperature. Without the GHGs in the atmosphere, the thermal radiation will escape to the space and mean surface temperature of the Earth would have been about $-18°C$. "Greenhouse Effect" is the consequence of absorbing the thermal radiation emitted by the surface. H_2O and CO_2 are the most important natural greenhouse gases, without either one of them the Earth would have been frozen planet. The burdens of GHGs are increasing in the atmosphere due to human activities which lead to further increase in temperature [1].

The climate is influenced by GHGs on the basis of their three properties [11]. First, superposition of the thermal IR spectrum of GHGs molecules in the atmosphere with the emission spectrum of the Earth's surface. Second, an absorption cross section and ambient concentrations of molecules, which decide the amount of radiation that could be absorbed. Third, the atmospheric lifetime of GHG molecules, which will decide the duration of their effects on climate. If the atmo-

spheric lifetime of GHGs is significantly high, even if their emissions are stopped today, they will affect climate up to several years. These three properties determine which gas is the most important GHG.

The atmospheric layer above the Earth's surface allows to pass the solar radiation and absorbs a fraction f of radiation emitted by the Earth's surface due to the presence of GHGs. Suppose the temperature of Earth's surface is T_0 and atmospheric layer is T_1. By Stefan-Boltzmann law, the radiation flux emitted by the Earth's surface will be σT_0^4 and the radiation flux absorbed by the atmospheric layer will be $f\sigma T_0^4$. Rest of radiation $(1-f)\sigma T_0^4$ will lose in the space. By Kirchhoff's law, atmospheric layer will also emit $f\sigma T_1^4$ radiation in both upward and downward direction in order to maintain its thermal equilibrium. Using the energy balance equation (Incoming solar radiation = Outgoing Earth's surface emitted radiation), the global mean surface is obtained by solving the following equations [7],

$$\frac{F_S(1-A)}{4} = (1-f)\sigma T_0^4 + f\sigma T_1^4, \tag{1.5}$$

where A = 0.28, is called the planetary albedo. We know from energy balance equation $f\sigma T_0^4 = 2f\sigma T_1^4$. Putting this value in the above equation and rearranging the equation, we get

$$T_0 = \left[\frac{F_S(1-A)}{4\sigma\left(1-\frac{f}{2}\right)}\right]^{\frac{1}{4}}. \tag{1.6}$$

After solving above equation, the global mean surface temperature is obtained as 288 K, corresponding to $f = 0.77$.

The spectrum measured at the top of the atmosphere (the radiation emitted by lower atmosphere and the Earth's surface) can be characterized by a superimposition of black-body spectra for different temperatures ranging from 200 to 320 K, depending on the wavelength region. Figure 1.4 shows the energy spectrum (dotted line) of a black body at these temperatures as well as the wavelength distribution of radiation (solid line) at the top of the atmosphere as measured

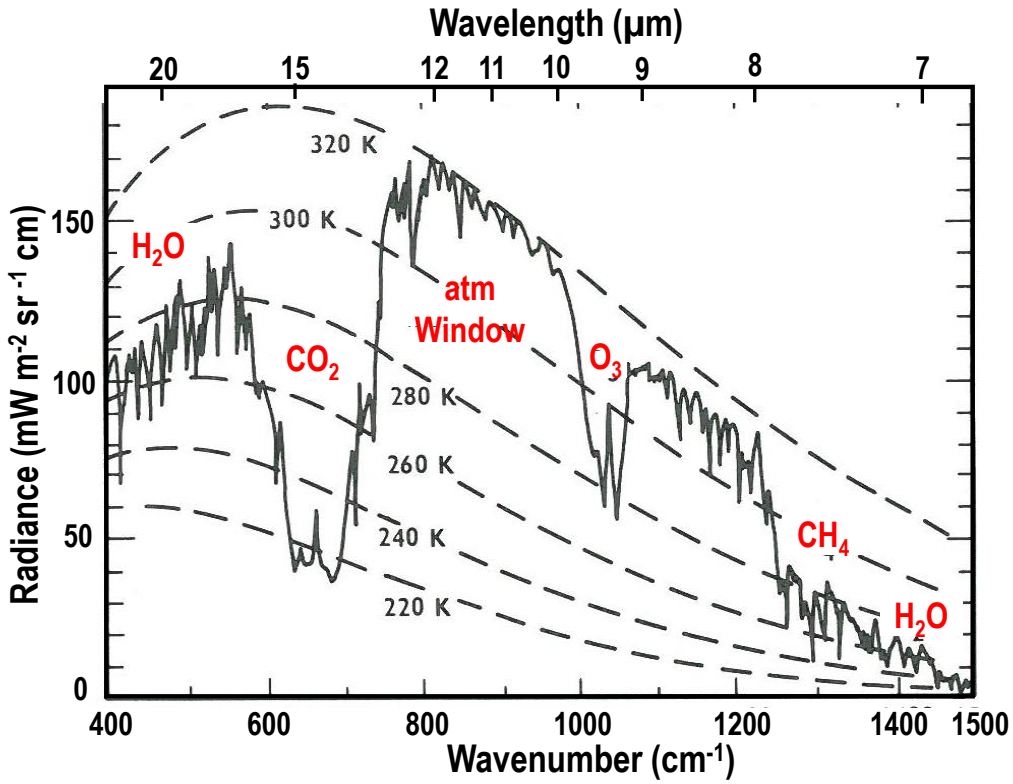

Figure 1.4: Solid line shows the distribution of IR spectrum, measured from the space using NASA IRIS D spectrometer over the hot Sahara desert. The superimposed dotted lines show the black body curves at different temperatures. Adapted from [12].

by the satellite instrument (NASA IRIS D spectrometer). The dips in the IR radiation show the attenuation due to the GHGs such as CO_2, H_2O and O_3. The Earth's emission spectra peaks at a wavelength of about 10 μm, tails extend down to a wavelength of about 5 μm and out of the microwave region ($\lambda > 100$ μm). The key point to note is that the region where most of terrestrial emission occurs ($7 - 13$ μm) is weakly absorbed by most important GHG CO_2 in the atmosphere but strongly absorbed by non-CO_2 GHGs such as O_3, CH_4, N_2O and the chloroflurocarbons. Since the concentration of non-CO_2 GHGs are very low as compared to CO_2, 80% of this radiation lost into the space. This is known as "atmospheric window" region. CO_2 strongly absorb the 15 μm emitted from the Earth's surface, but this band is close to the saturations due to its high concentration [6]. Hence, future warming will not linearly depends on further increase in atmospheric CO_2 concentrations, but will significantly affected by levels of GHGs,

which strongly absorbed the atmospheric window region of emitted radiation by Earth's surface.

1.3 Budget of direct and indirect Greenhouse Gases

The global flux of CO_2, CH_4 and CO are calculated by two approaches, namely "top-down" and "bottom-up". Top-down approach is based on the atmospheric inversion models including atmospheric transport models (which are constrained by their atmospheric observations), prior estimates of fluxes, and their uncertainties. This approach has limited insight into the underlying processes when different sources overlap in the same region. The bottom-up approach estimates the flux from the process based models, inventories and chemistry climate models (CCMs) estimating the levels of hydroxyl radicals (OH) and its chemistry in the atmosphere. The bottom-up models and inventories are not independent from inversions, because they are used as a prior spatial and temporal distribution of the CO_2, CH_4 and CO emissions in inversion study. The inversion study uses the atmospheric observations to partially correct the prior emissions.

1.3.1 CO_2 budget

Human activities have influenced CO_2 cycle for hundreds of years through agriculture, forestry, trade and energy use in industry and transport. However, only over the past two or three centuries these activities have become sufficiently widespread and far reaching to match the great forces of the natural world. The CO_2 cycle is a biogeochemical process through which CO_2 exchange occurs between major pools, including CO_2 in the atmosphere; oceans (surface, deep waters and marine sediments), in terrestrial ecosystems, rivers and estuaries, and in fossil carbon [4]. The exchange of CO_2 contents between different reservoirs depends on diverse response and feedback mechanism which reflect natural dynamics and human activity. Figure 1.5 shows the global carbon budget averaged for the

period of the last decade (2005 – 2014).

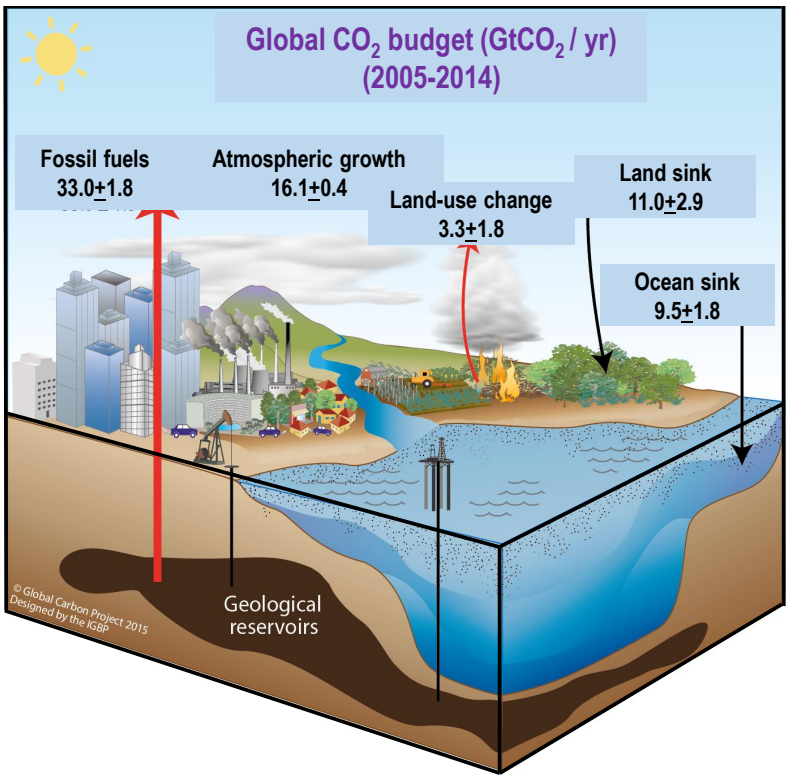

Figure 1.5: A schematic diagram of the overall perturbation of global CO_2 cycle caused by anthropogenic activities, averaged globally for the decade 2005-2015. All fluxes are in unit of Gigatonne CO_2 yr^{-1} ($GtCO_2$ yr^{-1}) with $\pm$ 1σ uncertainties. The uncertainties reflect the current capacity to characterise the annual estimates of each component of the global carbon budget. 1 Gigatonne = 1×10^{15} g. This figure is adapted from [13].

Anthropogenic flux

The anthropogenic sources of CO_2 consist mainly of the fossil fuel emissions and land use change. Any fossil fuel burned in the presence of O_2 will emit CO_2 significantly according to the following equations.

$$CH_n + (1 + n/4)O_2 \longrightarrow CO_2 + (n/2)H_2O \tag{1.7}$$

The global CO_2 emissions from fossil fuel is calculated from the energy consumption data, collected and archived by several organizations. Details of the calculation are discussed by [14]. The land-use changes include the CO_2 fluxes from deforestation, afforestation, logging (forest degradation and harvest activity), shifting cultivation (cycle of cutting forest agriculture and then abandoning), and regrowth of forest. Some of these activities consist emissions of CO_2 and some consists uptake of CO_2. The CO_2 flux consists the net sum of all anthropogenic activities. The emissions of CO_2 from land-use change (mainly deforestation), are based on the combined evidence from land-cover-change data, fire activity associated with deforestation, and dynamic global vegetation models. The cumulative anthropogenic CO_2 emissions from 1870 to 2015, are estimated to be 555 ± 55 PgC (2035 ± 205 $PgCO_2$), out of which fossil fuel combustion and cement production contributed about 75% (365 ± 30 PgC) and land use change (including deforestation, afforestation and reforestation) contributed about 25% (180 ± 80 PgC) [4]. During the last decade ($2005 - 2014$; Figure 1.5), about 91% of total CO_2 emissions were caused by fossil fuel and industry (33.0 ± 1.8 $GtCO_2$ yr^{-1}), and 9% of land-use change (3.3 ± 1.8 $GtCO_2$ yr^{-1}).

Oceanic flux

The oceans act as a large sink of atmospheric CO_2 [4]. The sink of CO_2 in ocean is driven by two processes [15, 16]: (1) Solubility pump, and (2) Biological pump. The exchange of CO_2 between the atmosphere and oceanic surface due to solubility pump, is driven by the CO_2 partial pressure difference across the air and sea interface. For example, the net flow of atmospheric CO_2 in the ocean will take place if the partial pressure of CO_2 in the atmosphere is greater than that of ocean surface. After entering CO_2 into sea water, the following chemical reactions take place.

$$CO_2 + H_2O \longrightarrow HCO_3^- + H^+, \tag{1.8}$$

$$HCO_3^- \longrightarrow H^+ + CO_3^{2-}. \tag{1.9}$$

The dissolved CO_2 in the oceans occurs in three main forms: bicarbonate (HCO_3^-) ions, carbonate ions (CO_3^{2-}) and same as in CO_2 form. About 90% inorganic

carbon in the oceans is in the form of HCO_3^-, about 10% is in the form of CO_3^{2-}, and less than 1% are in the form of CO_2 [4]. The low partial pressure of CO_2 in the oceanic surface water allows to diffuse large amount of CO_2 into the sea. The amount of CO_2 that diffuses and dissolves in the sea surface water also depends on wind, sea surface mixing, and the temperature of the water. The sink of CO_2 through the biological pump is driven by oceanic biology which sequestrates CO_2 from the atmosphere to the deep sea. The phytoplankton in the uppermost sunlit layer of the ocean form their food by consuming atmospheric CO_2 using photosynthesis processes. This processes is responsible for about 80% of total oceanic sink of CO_2. Further, CO_2 is also biologically fixed in the form of calcium carbonate ($CaCO_3$) by construction of calcareous skeletons, through the following net reaction.

$$Ca^{2+} + 2HCO_3^- \longrightarrow CaCO_3 + H_2O + CO_2. \tag{1.10}$$

Some of the skeletons end up in the deep ocean through sinking dead micro-organisms. The formation and sinking of $CaCO_3$ create an alkalinity gradient from surface to deep, which serves to raise the partial pressure of dissolved CO_2 in surface water and actually raise atmospheric levels. The mean ocean CO_2 sink (S_{OCEAN})) estimates are based on observations from the 1990s, while the oceanic models are used for calculating the annual anomalies and trends [4]. For the period of last decade ($2005 - 2014$), it is observed that the ocean is absorbing atmospheric CO_2 at a rate of 9.5 ± 1.8 $GtCO_2$ per year, thus removes about 26% of total CO_2 emitted to the atmosphere each year (Figure 1.5, [13]) and hence, mitigates the harmful impact of CO_2 on climate.

Biospheric flux

The terrestrial biosphere is the main natural CO_2 reservoir. It contains carbon in organic compounds in vegetation living biomass (450 to 650 PgC, [4]) and in dead organic matter in litter and soils by acquiring CO_2 at the time of photosynthesis. CO_2 uptake from the atmosphere from plant photosynthesis (Gross Primary production (GPP), 123 ± 8 GtC yr^{-1}, [17]) is the main natural process

that removes a significant amount of atmospheric CO_2 by the following reaction.

$$6CO_2 + 6H_2O + \text{photons} \longleftrightarrow C_6H_{12}O_6 + 6O_2, \tag{1.11}$$

The reverse of above equation also occurs, which is known as respiration. In this process CO_2 is released back to the atmosphere (118.7 GtC yr^{-1}, [4]) as per the following reaction.

$$C_6H_{12}O_6 + 6O_2 \longleftrightarrow 6CO_2 + 6H_2O + \text{heat} \tag{1.12}$$

The time scale of CO_2 fixed into plants and then release back into the atmosphere by autotrophic (plant) and heterotrophic (soil microbial and animal) respiration varies from 1 year to 100 years. The large photosynthesis reaction occurs mostly during the growing season, whereas respiration occurs nearly year-round. The greater land ecosystems in the Northern Hemisphere (NH) impart a characteristic "sawtooth" seasonal cycle in atmospheric CO_2 [18]. Recent measurements show that the seasonal amplitude of atmospheric CO_2 in the northern hemisphere has increased since 1960 due to the additional increases in the summertime uptake of CO_2 derived from the ecological changes in boreal and temperate forests [19]. The net sink of CO_2 in terrestrial vegetation and soils (S_{LAND}) is estimated by the difference (Fossil fuel emissions + Land-use emissions − (Atmospheric growth rate + Oceanic sink)) of the other terms of the global carbon budget. During the last decade ($2005-2014$), the average S_{LAND} is estimated to be 11 $\pm$ 2.9 $GtCO_2$ yr^{-1} 1.5).

Growth rate of atmospheric CO_2

The atmospheric global growth rate of CO_2 is calculated based on the average of multiple stations selected from the remote sites mostly from the marine boundary layer with well-mixed layer [20]. The mean atmospheric growth rate of CO_2 is observed 16.1 $\pm$ 0.4 $GtCO_2$ yr^{-1} (or 4.4 $\pm$ 0.1 GtC yr^{-1} using using 1 ppm CO_2 = 2.12 GtC) in last decade ($2005-2014$) [13].

1.3.2 CH_4 budget

The major CH_4 sources include natural biogenic sources (such as wetlands, termites, and very small from the oceans), anthropogenic sources (such as rice paddy, ruminant livestock (such as cows), landfills and waste) and other sources (such as extraction and use of fossil fuel, biomass burning) [21] and [22]. The biogenic CH_4 is produced from organic matter under low oxygen conditions by the fermentation processes of microbes.

Table 1.1: The annual global fluxes of CH_4 from different reservoirs (atmosphere, hydrates on land, hydrates in the ocean floor and gas reserves) estimated for the period of 2000-2009. The values inside the bracket represent the minimum and maximum range of fluxes. All fluxes are in the unit of Teragrams CH_4 yr^{-1} (Tg CH_4 yr^{-1}). 1 Teragrams = 1×10^{12} g. The numbers are adapted from [22].

Sources	CH_4 fluxes in Tg CH_4 yr^{-1} for the period of 2000-2009	
	Top-down	Bottom-up
Natural wetlands	175 [142-208]	217 [177-284]
Other natural sources (Fresh water, wild animals, wild fires, termites, geological, hydrates, permafrost)	43 [37-65]	131[61-200]
Sum of the natural sources	218 [179-273]	347 [238-484]
Agriculture and waste	209 [180-241]	200 [187-224]
Biomass Burning (incl. biofuels)	30 [24-45]	35 [32-39]
Fossil fuels	96 [77-123]	96 [85-105]
Sum of the anthropogenic sources	335 [273-409]	331 [304-368]
Sum of all sources	**548 [526-569]**	**678 [542-852]**
Chemical loss	518 [510-538]	604 [483-738]
Soil loss	32 [26-42]	28 [9-47]
Sum of all sinks	**540 [514-560]**	**632 [592-785]**

Table 1.1 shows estimates of CH_4 budget based on the "top-down" and "bottom-

up" approaches [22]. The top-down or inversion base estimate shows the CH_4 fluxes in the range of 142-208 Tg CH_4 yr^{-1} from natural wetlands, 180-241 Tg CH_4 yr^{-1} from agriculture and waste emissions, 77-123 Tg CH_4 yr^{-1} from fossil fuel related emissions. The bottom up approach shows about 20% higher estimation of total fluxes than the inversion based estimate. The bottom-up approach shows the CH_4 fluxes in the range of 177-284 Tg CH_4 yr^{-1} from natural wetland emissions, 187-224 Tg CH_4 yr^{-1} from agriculture and waste (rice, animals and waste), 85-105 Tg CH_4 yr^{-1} from fossil fuel related emissions, 61-200 Tg CH_4 yr^{-1} from other natural emissions including geological, termites and fresh water emissions, and 32-39 Tg CH_4 yr^{-1} comes from biomass and biofuel burning. This approach shows overall about 50 to 65% of CH_4 emissions are contributed by human activities and the remaining are contributed by natural sources. In India, the agriculture and waste emissions are largest regional emission sources of CH_4 and contribute about 27 and 22 Tg CH_4 per year from top-down and bottom-up approaches, respectively due to extensive rice agricultural and livestock industries [22]. However, per capita CH_4 emission in India is about 35% of those in developed countries. Emissions from the rice cultivation has a seasonal dependence which peak during monsoon (June-July-August) when a majority of rice is grown and rainfall occurs [23]. Indo Gangetic Plain (IGP) and Southern peninsular India are associated with the region of highest rice yield. The OH radicals, mostly in the troposphere, account for about 90% of the global CH_4 sink. There are small sinks of CH_4 such as soils, reaction with Cl radicals and atomic oxygen (O^1[D]) in the stratosphere and reaction with Cl radicals from sea salt in the marine boundary layer [24]. The following chemical reactions are mostly responsible for the removal of CH_4 in the atmosphere.

$$CH_4 + OH \rightarrow CH_3 + H_2O \quad (k_{OH} = 2.5 \times 10^{-12}\exp(-1775/T), \tag{1.13}$$

$$CH_4 + O^1D \rightarrow \text{Products} \quad (k_{OH} = 1.5 \times 10^{-10}), \tag{1.14}$$

$$CH_4 + Cl \rightarrow CH_3 + HCl \quad (k_{OH} = 7.3 \times 10^{-12}\exp(-1280/T). \tag{1.15}$$

where k_{OH} temperature dependent reaction rate constant (in cm^3 $molecule^{-1}$ s^{-1}) and taken from Sander et al., [25].

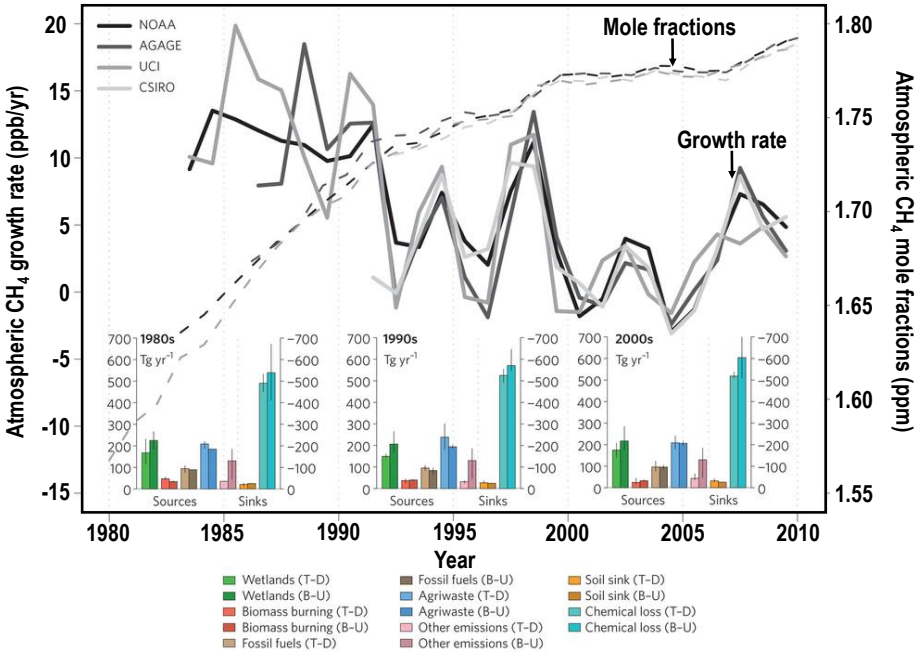

Figure 1.6: Variations in the atmospheric mixing ratios (dashed lines) and growth rate (solid lines) of CH_4, using the collected data from different NOAA, AGAGE, UCI and CSIRO networks. The bar chart denotes the budget of CH_4 from top-down (T-D, light-coloured bars) and bottom up (B-U, dark-coloured bars) approaches. The error bars represent the spread between minimum and maximum. This diagram is adapted from [22].

The accumulation of CH_4 in the atmosphere derived from the balance between sources and sinks of CH_4 in the atmosphere. Substituting the total emissions and total sinks numbers in a global mass balance equation for atmospheric CH_4, we get the average accumulation or growth rate in the atmosphere. The inversion and bottom-up approaches show the imbalance of about 6 and 50 Tg CH_4 yr^{-1}, respectively average for the period of 2000-2009. Atmospheric observation of CH_4 mixing ratios show the average increase about 2.2 ppb each year during the time period 2000-2009 [26]. The growth rate of CH_4 is not consistent. The past three decades have witnessed a large year-to-year fluctuations in the growth rate of atmospheric CH_4. The surface measurements from four networks: National Oceanic and Atmospheric Administration (NOAA) [26], Advanced Global Atmospheric Gases Experiment (AGAGE) [27], Commonwealth Scientific and In-

dustrial Research Organization (CSIRO) [28] and University of California, Irvine (UCI) [29] show consistent change in the global growth rate of annual CH_4 mixing ratios (Figure 1.6). These observation data sustained increase in atmospheric CH_4 levels in the 1980s (by an average of 12± 6 ppb yr^{-1}) but the growth rate slowed at the beginning of 1990s (by an average 6 ± 8 ppb yr^{-1}), plateaued from 1999 to 2006 (CH_4 levels reached 1.77 ± 2 ppm). Various studies have suggested that a reduction of anthropogenic emitting activities (such as coal mining, gas industry..etc) [29,30], significant and small change in OH mixing ratio [27], reduced emission from rice paddies [31] and stable microbial and fossil fuel emission from 1990 to 2005 could be the possible factors for the fluctuating trend of atmospheric CH_4 [32]. After 7 years ($1999-2006$) of a steady-state mixing ratios of CH_4, the CH_4 increase has resumed [27] with an increased emission of 21 Tg CH_4 yr^{-1} and 18 Tg CH_4 yr^{-1}, estimated by the inversions study during 2007 and 2008, respectively as compared to the period of $1999-2006$ [33]. The observed positive anomaly of CH_4 is contributed by the tropical wetland emissions (share about ∼2/3) and from high latitude wetlands (∼25%) [33,34].

There are still large uncertainties associated with the estimated regional fluxes of CH_4. These could be due to several factors, as discussed by Kirschke et.al [22]. First, mapping of natural wetlands is poor which should be improved, since the inter-annual changes in CH_4 emissions are mostly dominated by wetland emissions which are too uncertain. Second, the regional emissions and processes of CH_4 are poorly constrained by atmospheric observations in top-down models. Third, the trend of emission from specific sources are still uncertain, which demands for the improvement in land-surface models and improvement in anthropogenic inventories. Fourth, there are large uncertainties in quantification of transport and chemistry errors in the atmospheric chemistry transport models used in the inversion studies. These errors can be minimized by the comparisons of model simulations with the observations representing from different areas of the world.

1.3.3 CO budget

Carbon monoxide (CO) is an important pollutant in the troposphere, which affects atmospheric chemistry through it influence on O_3 [35–37]. CO does not absorb the IR radiation emitted by Earth's surface to be counted as a direct GHG, but it affects the atmospheric burden of GHGs such as O_3 and CH_4 [35,36] and hence, contribute in the positive radiative forcing ($\sim 0.23 \pm 0.7$ Wm^{-2} [1]). Overall, the tropospheric burden of CO is governed roughly half by the oxidation of hydrocarbons mainly due to the CH_4 oxidation and half by the direct surface emissions from incomplete combusted fuels [38]. The surface emission sources include fossil fuel, biofuel, wildfire and agricultural biomass burning [39].

Table 1.2: Global and South Asian emissions of CO from different sources. This data is taken from Emission Database for Global Atmospheric Research (EDGAR) version 3.2FT2000 [40].

Sources	CO fluxes in TgCO/yr	
	Global	South Asia
Fossil Fuel burning	243.2	19.1
Industrial processes	34.5	1.4
Biofuel Burning	250.3	103.9
Biomass Burning	435.8	32.6
Agricultural processes and waste handling	20.2	3.2
Total	**983.89**	**160.13**

The Emission database for Global Atmospheric Research (EDGAR) version 3.2FT2000 estimated that the global anthropogenic emission of CO is about 984 Tg yr^{-1} for the year 2000 with biomass, biofuel and fossil fuel burnings accounting for 44%, 25% and 25%, respectively [40]. The South Asian region is highly influenced by the incomplete combustion processes, especially by biofuel burning in cook stoves and contributes about 16% to global CO emissions (Table 1.2). Out of this 16%, biofuel burning, biomass burning, and fossil fuel burning contributes

around 65%, 20% and 12%, respectively (Table 1.2). India is the largest contributors of CO emission in South Asia and second largest in Asia due to its large population, accompanied by rapid industrialization, urbanization, infrastructure development and agricultural development [41]. Bottom-up inventories of CO indicate an increase of about 33% in India during 2000-2008 due to the rapid growth in these sectors in the past decade. Total CO emission in 2008 for India was 61.8 Tg, the majority of which is governed by the domestic sector (59%) and road transport sector (20%) [42]. The major sink of CO is the reaction with OH radicals and surface deposition by soil uptake [6].

1.4 Tools for studying the effects of GHGs on Earth's climate

Climate metrics are the important tools for quantifying and comparing the impacts of various anthropogenic emissions on Earth's climate. They are also useful in comparing different emissions for their impacts. Radiative forcing (RF) and Global warming potentials (GWP) are two important climate metrics, being used in climate policy and management related activity. The brief descriptions about these metrics are given in the following sections.

1.4.1 Radiative Forcing (RF)

Radiative forcing generally refers to the radiative perturbation due to change in the levels of GHGs, aerosol, change in cloud cover and several other perturbing agents which directly or indirectly influence the Earth's radiation budget. Radiative forcing represents the net change in energy flux escaping to the space due to a change in the atmospheric mixing ratios of radiatively active species (GHGs, aerosol, etc.) relative to 1750. Suppose the increase in abundance of GHG enhance the absorption efficiency from f to Δf. As discussed in Section 1.2.2, the outgoing flux emitted from the Earth's surface in radiative equilibrium is $\left[1 - \frac{f}{2}\right] \sigma T_o^4$. Due to change in the radiative efficiency of the atmosphere after increasing the levels of GHGs, the outgoing flux of Earth's emitted radiation will

be $\left[1-\frac{f+\Delta f}{2}\right]\sigma T_o^4$. Suppose radiative perturbation is ΔF and by definition, it can be defined as [7]

$$\left[1-\frac{f}{2}\right]\sigma T_o^4 - \left[1-\frac{f+\Delta f}{2}\right]\sigma T_o^4 = \frac{\Delta f}{2}\sigma T_o^4. \tag{1.16}$$

This perturbation will allow to reach a new equilibrium, where the surface temperature changes by $T + \Delta T_0$. Hence the new radiative equilibrium will be

$$\frac{F_S(1-A)}{4}F = \left[1-\frac{f+\Delta f}{2}\right]\sigma(T_0+\Delta T_0)^4, \tag{1.17}$$

After solving the above equation and using the approximation $(T_0+\Delta T_0)^4 = T_o^4 + 4T_o^3\Delta T_0)$, we obtained the linear relationship between the change in temperature due to the increasing amount of GHGs and RF.

$$\Delta T_0 = \lambda \Delta F \tag{1.18}$$

where $\lambda = \frac{1}{4\left(1-\frac{f}{2}\right)\sigma T_o^3}$ is known as the climate sensitivity parameter. Substituting the numerical values of σ, T_0 and f, we get $\lambda = 0.3$ $\mathrm{Km^2W^{-1}}$. Figure 1.7 shows the RF of different radiatively active species as given in IPCC, 2013 report [1] over the period of $1750-2011$. A positive value means net warming while negative value means cooling of the Earth's surface temperature. It clearly shows that the CO_2 and CH_4 are the two most potent radiative forcing agents which together contribute about 80% to recent warming of the globe.

Figure 1.7 also shows the confidence levels for the change in RF of different agents from the industrial era to the year of 2011. The confidence level depends on the evidence (robust, medium and limited) and agreement (high, medium and low). The evidence depends on our understanding of the processes causing the forcing. It is determined based on the consistency of results for a particular forcing agent provided by observations and modelling simulations. For robust evidence, the observations and modelling results are consistent while medium evidence can be assigned in cases where observations and modelling provided a diversity of results and hence not a consistent picture for the RF agent. The evidence to be limited only those cases where model study in some cases indicate

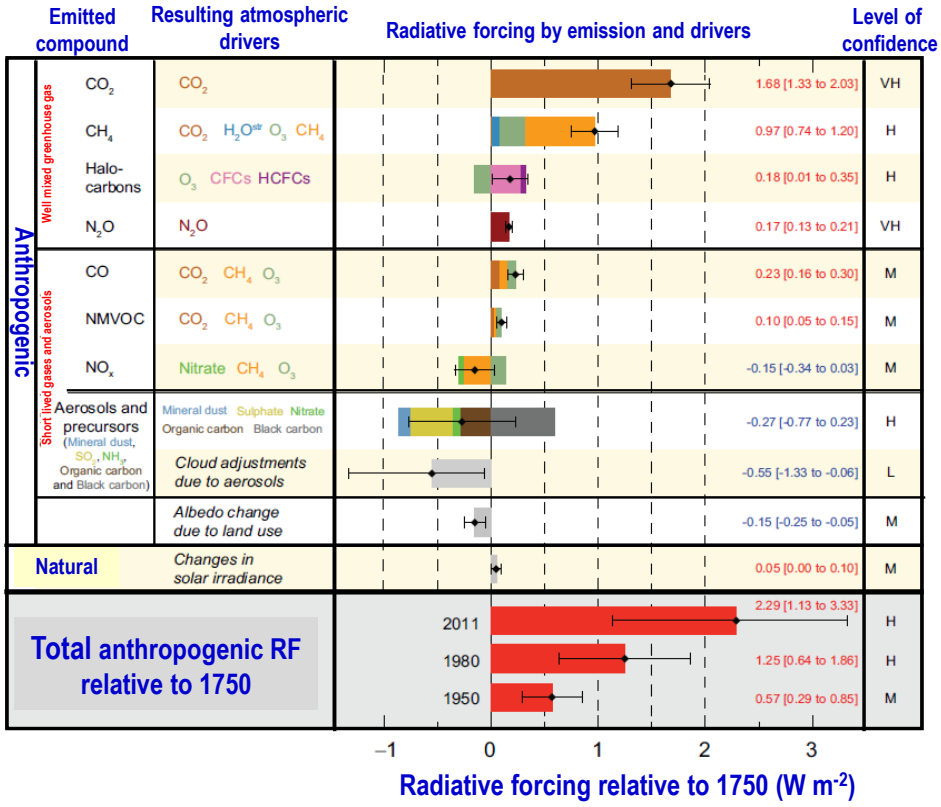

Figure 1.7: The estimates of global mean radiative forcing (RF) from different drivers of the climate change for the year of 2011, relative to 1750. The natural and anthropogenic substances and processes that alter the Earth's energy budget are known as the drivers of climate change. The error bar represents $\pm$ 1σ uncertainties. Source: [1].

changes, but direct observations are scared. The well mixed GHGs (such as CO_2, N_2O, CH_4 etc.) have robust evidence since they have well defined links between their atmospheric levels from the preindustrial era based on their high precision measurements and radiative effect. However, the existence of the influence of aerosol on cloud cover has limited evidence. The agreement is a qualitative judgment of the difference between the various estimates for a particular RF agent. The well mixed GHGs have high agreement since the relative uncertainties in the RF estimates are much smaller than for the other RF agents. The cause of low agreement is either due to the large diversity in estimates of the magnitude of the forcing or from the fact that the method to estimate the forcing has a large

uncertainty.

1.4.2 Global Warming Potential (GWP)

The next important climate metrics is global warming potential (GWP), which is an important index to compare the potential of trapping heat by certain mass of different GHGs relative to that of similar mass of CO_2 in the atmosphere for a specified time period. It depends on the heat absorbing ability of each gases as compared to CO_2, as well as the amount removed of each gas from the atmosphere over the given time periods. It is defined as the time-integrated RF from the instantaneous release of unit mass of any GHGs relative to the RF of the same mass of the reference gas. The GWP depends on the absorption of IR by certain GHGs and their atmospheric lifetimes. The GWP is determined by the following equation [1]:

$$GWP_i = \frac{\int_0^H RF_i(t)c_i dt}{\int_0^H RF_{CO_2}(t)c_{CO_2} dt} \tag{1.19}$$

where i denote the gas of interest, H is the time horizon for integration, RF is the radiative forcing for i and CO_2 and c is the remaining mass of i and CO_2 over time after the initial pulse emission. Table 1.3 shows the GWP values for different GHGs.

Table 1.3: GWPs and lifetimes of different GHGs from 2013 IPCC [1]. CO_2 has GWP value 1.

Gas	Lifetime (years)	GWP time horizon	
		20 years	100 years
CH_4	12.4	86	34
N_2O	121.0	268	298
HFC-134a (Hydro-fluorocarbon)	13.4	3790	1550
CFC-11 (Chlorofluorocarbon)	45.0	7020	5350
CF_4	50000.0	4950	7350

1.5 Indian GHGs measurements and need for further study

The prediction of future climate change and its feedback rely on our ability to quantify fluxes of the two major GHGs, CO_2 and CH_4 at local, regional and global scales. Though the scientific level of understanding of global warming due to these GHGs is significantly high (as discussed in Section 1.4.1), the regional scale (e.g. sub-continent and country level) fluxes of GHGs are uncertain, especially over the South Asian region; i.e., the estimated uncertainty is larger than the value itself [21, 43]. One of the major sources of these large uncertainties is the lack of spatial and temporal observations of these gases.

The first time series observations of CO_2, CH_4, CO and other greenhouse gases over India started in 1993, at a cleaner coastal site Cape Rama near Goa by Physical Research Laboratory (PRL), Ahmedabad in collaboration with Commonwealth Scientific and Industrial Research Organization (CSIRO) Australia and National Institute of Oceanography (NIO), Goa [44]. After that, several other groups have initiated similar measurements of surface level greenhouse gases [45–48]. Most of these measurements are made at weekly or fortnightly time intervals or at lower frequency. These data are very useful for several studies, like analyzing the seasonal cycle, growth rate, and estimating the regional (subcontinental) carbon sources and sinks after combining their mixing ratios with inverse modelling and atmospheric tracer transport models. However some important studies, like their diurnal variations, temporal covariance etc, are not possible from these measurements due to their limitations. Analysis of temporal covariance of atmospheric mixing processes and variation of fluxes on shorter time scales, e.g., sub-daily, is essential for understanding local to urban scale CO_2 flux variations [49–54]. The continuous measurements are useful since they consist of information about mixing ratio variability, including the diurnal and synoptic variations, containing signatures of local and regional CO_2 fluxes. Two aircraft based measurements programs, namely, Civil Aircraft for the Regular Investiga-

tion of the atmosphere Based on an Instrument Container (CARIBIC) [55] and the Comprehensive Observation Network for TRace gases by AIrLiner (CONTRAIL) [56] have provided important first look on the South Asian CO_2 budget, but these data have their own limitations [57–59].

Along with the need for atmospheric measurements for predicting the future levels of major GHGs, quantifying the components of anthropogenic emissions of CO_2 is similarly important for providing independent verification of future emission mitigation activities. The proposed strategy for quantification of the anthropogenic component of CO_2 emissions is to measure simultaneously the anthropogenic tracers [60,61]. Improved observational constraints on anthropogenic emissions will derive meaningful information on the biospheric flux estimate of CO_2. CO can be used as a surrogate tracer for detecting and quantifying anthropogenic emissions from burning processes, since it is a major product of incomplete combustion [60, 61]. The correlation slope between the atmospheric variations of CO and CO_2 can be used to quantify the fossil fuel contribution, distinguish between different burning processes or to determine the burning efficiency and the overall trend of anthropogenic emissions of CO in that city [60, 62–64]. The CO:CO_2 ratios are higher for low combustion sources (e.g. Forest fires) and lower for good or efficient combustion sources [61,65]. Further, the CO:CO_2 ratios can be used for estimating the total emission of CO over an urban area provided the total CO_2 emission is known in that area [62, 66]. Hence, the information about CO:CO_2 ratio will be helpful to understand the effects on the CO emissions after adopting the newer vehicular technologies and new cleaner emission norms and finally will be beneficial for reducing the uncertainties in CO emission inventories.

Apart from understanding of urban CO_2 emissions, there is also a need for understanding the nature of regional biospheric flux of CO_2, since its seasonal cycle (growing phase to dying phase) regulate significantly the atmospheric mixing ratios of CO_2. Understanding the nature of regional biospheric flux is important to

predict the future levels of CO_2 and hence future climate also. Inverse modelling is a well known approach for estimating the regional fluxes of CO_2 from the in-situ measurements together with an atmospheric chemistry-transport model (CTM). Hence, high quality measurements of GHGs combined with CTM simulations will provide a great opportunity to understand the characteristics of regional fluxes in relation with human activities and natural climate. However, the global models running at coarse horizontal resolution (grid size $>$ 40000 km^2) often suffer from under-prediction of the diurnal and seasonal variations in CO_2 at surface level in a strong source region [67, 68]. The vertical distributions of CO_2 contain the information about its regional signature, as against the surface level measurements, which are affected by local emissions. Thus, the vertical profile measurements in the free troposphere are extremely useful for learning about the regional emissions, transport effects and to improve/verify the estimates of regional budgets based on inverse modelling of measurements at surface stations [69].

India is the second largest populous country in the world and rapid socioeconomic development and urbanization have made it the third largest world's GHG emitter next to China and USA (EDGAR v4.2; CDIAC - [70]). However, this region is quite void in terms of continuous measurement of major GHGs such as CO_2, CH_4 etc. As discussed above, though some measurements have been done, but detailed measurements focusing on the urban variability and source studies are still not on record. The region is also void in terms of the vertical measurements of these gases.

1.6 Outline of the thesis

This thesis work is mostly focuses on the urban variability and emission characteristics of two most important GHGs, CO_2 and CH_4. For accomplishing this work, simultaneous measurements of CO_2 and CH_4 have been made along with the anthropogenic tracer CO using laser based cavity ring down spectroscopy

technique (CRDS) over Ahmedabad, a western urban region of India during November, 2013-July, 2015. The collected measurements of CO_2 and CH_4 are further compared with the available simulations of the chemical-transport models from different groups. The study of the tropospheric distributions of CO_2 and CO is also done using aircraft measurements and satellite measurements, respectively, as well as model simulations also. The following describes the chapter organization of the thesis.

Chapter 2 describes the methodological part of this work. It starts from the discussion of measurement principle of CO_2, CH_4 and CO instrument, based on the cavity ring down spectroscopic (CRDS) technique as well as the calibration protocols for making measurements at Ahmedabad. It also discusses about another measurement technique of CO_2 i.e., non dispersive infra red (NDIR) technique, used in the airborne measurements of CO_2 made by Japanise team under the CONTRAIL project. Remote sensing measurement technique of CO by MOPITT satellite are also discussed in brief. Furthermore, the used model simulations from JAMSTEC Japan, LSCE, France and Max Planck Germany, are described at the end of this chapter along with different validation statistical metrics.

Chapter 3 demonstrates the potential of simultaneous CO_2 and CO measurements for understanding the emission characteristics of CO_2 on diurnal and seasonal scales over an urban region Ahmedabad. Further, to understand the dominating factors responsible for the CO_2 variations on seasonal timescale, CO_2 measurements are compared with the atmospheric general circulation model (AGCM)-based chemistry- transport model (ACTM) simulations. In addition, the results suggest that the Carnegie-Ames-Stanford Approach (CASA) model for biospheric flux, under-predicts the seasonal amplitude observed in the observations.

Chapter 4 is focused on the tropospheric distributions of CO_2 over Delhi and

CO over five selected urban regions (Delhi, Dibrugarh, Ahmedabad, Hyderabad and Trivandrum) of India using Aircraft and satellite data, respectively. Further CO_2 and CO observations are also compared with the model simulations for checking the ability of models in capturing the observations of these gases where large scale transport and regional sources mostly control the levels of these gases.

Chapter 5 gives insight into the emission characteristics of second most important GHGs CH_4 over Ahmedabad. Further, simulations from two chemistry-transport models are also compared with the observed concentrations of CH_4. The comparisons suggest that the afternoon mixing ratios of CH_4 have the potential to represent foot print of emission of larger area and hence this data can be used in regional and global CH_4 inversion study with some caution.

Chapter 6 summarizes the main findings and contributions of this thesis with the future prospectives.

Chapter 2

Methodology

The accurate knowledge about the changes in the levels of greenhouse gases (GHGs) are important to mitigate their emissions as well as to predict and control the future global climate change. Therefore, precise and accurate measurements of these gases are important for understanding the phenomenon from emission processes to climate change. The net change in atmospheric levels of CO_2 and CH_4 are very small percentage (0.5% for CO_2 and 0.2% of CH_4) of their nominal concentration levels [71]. The World Meteorological Organization (WMO) has provided a framework for the measurements of atmospheric GHGs and suggested that the measurement uncertainty be less than $\pm$ 0.1 ppm for CO_2 and $\pm$ 2 ppb for CH_4. Infrared spectroscopy is a powerful tool for making the measurements of GHGs at prescribed accuracy and high frequency. It is based on the wavelength-dependent absorption of light and make use of the fact that each gas molecule has unique inherent property which define their absorption characteristics at a particular wavelength to a certain degree depending on its concentrations. These absorption lines are known as "fingerprint spectra". In present work, we have used two IR absorptions based techniques for collecting the atmospheric measurements of CO_2, CH_4, and CO. Further, we have also used the remote sensing measurements for studying the tropospheric distributions of CO and atmospheric chemistry transport models. The following sections give the highlights about the methodology for making atmospheric measurements as well as the basic details about the used photochemical models for accomplishing this thesis work.

2.1 In-situ measurement techniques

In the present work, we have used two different analyzers, based on two distinct detection techniques namely, Non Dispersive Infrared (NDIR) technique and Cavity Ring Down Spectroscopic (CRDS) technique. The NDIR technique based analyzer is used for making the aircraft measurements of CO_2 over Delhi while the CRDS technique based analyzer is used for making the ground-based measurements of CO_2, CH_4 and CO at Ahmedabad. Before going into the details of these techniques, we first will describe the "Beer Lambert Law", which enables to achieve the quantitative analysis for measuring the concentrations of atmospheric trace constituents based on their fingerprint spectra [72].

The spectroscopic measurements of any trace gas are accomplished by measuring the absorption of the light fraction at any wavelength passing through the gas medium. Beer Lambert's Law quantifies this phenomenon. It states that the rate of decrease in the intensity of the incident radiation as it passes through an absorbing medium is proportional to the initial intensity of the beam, concentration of the absorbing species, and path length traveled by the beam. Suppose the light beam with intensity I_o enters the absorbing medium and travels a path length L. So, the final intensity of light leaving that medium will be

$$I(\lambda) = I_0(\lambda) exp(-\sigma(\lambda) N L) \tag{2.1}$$

Where N is the molecular density (molecules/cm^3), L is beam path length (in cm) and $\sigma(\lambda)$ is absorption cross section of molecule (cm^2/molecules). Beer-Lambert law provides a linear relationship between the absorbance (A = log $\left(\frac{I_o(\lambda)}{I(\lambda)}\right)$) of a molecule to the concentration (C) and the path length (L) of the sample. However, under certain circumstances this linear relationship breaks down and gives non-linear relationship. Hence, the following conditions need to be fulfilled in order for BeerâĂŹs law to be valid.

1. The incident radiation strictly should be monochromatic.

2. The interaction medium must be homogeneous.

3. The interacting medium must not scatter the radiation.

4. The incident radiation must follow the linear path.

5. The incident light should not change the internal characteristics of the interacting atoms, since such effects will deplete the lower level and possibly give rise to stimulated emission.

2.1.1 NDIR technique

Non-dispersive infrared (NDIR) gas sensing is one of the most widely used standard techniques for measuring the concentrations of CO_2 in the atmosphere. The Licor spectrometer (LI-7000) based on this technique works by measuring the intensity of light absorbed by the sample. Figure 2.1 shows the schematic of the detection system of NDIR technique. The system consists of three basic components, an IR source; two cells (one containing the gas of interest and other a reference gas (non-absorbing gas)) and a detector. The IR source (a tungsten filament) transmits energy in the sample cell and reference cell. A bandpass optical filter (4.255 μm band for CO_2) is used in front of the detector (lead selenide) to provide the rejection of IR radiation outside the desired band. After passing from both the cells, the radiation at the detector is measured. The difference in signals received from both the cells measured by the detector is used to compute the absorption by Beer-Lambert law:

$$\frac{I_1}{I_2} = exp(-\sigma LN) \tag{2.2}$$

where L is the optical path length (length of the cell is about 15.2 cm), I_1 is the intensity measured after the sample cell and I_2 is the intensity measured after the reference cell.

NDIR technique has extraordinary accuracy and precision for making high frequency measurements of CO_2 in the atmosphere. However, the real-time continuous detection and quantification of CO_2 from this technique is little challenging. The analyzer based on this technique suffers from non-linear response to the

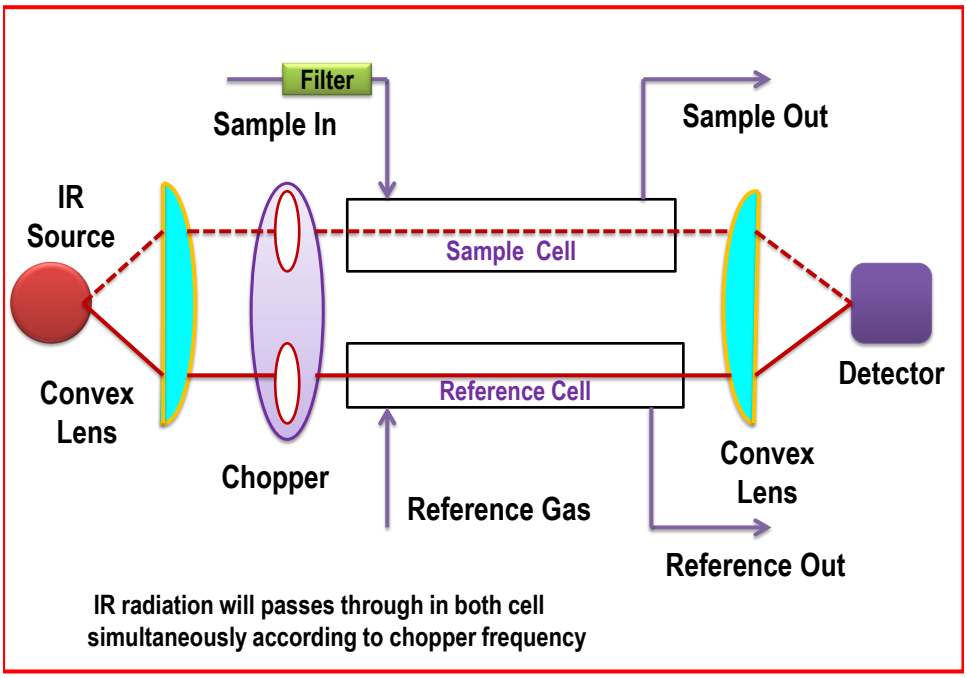

Figure 2.1: Schematic of NDIR technique based CO_2 analyzer. Adapted from the Licor manual.

target gas, an undesirable cross-sensitivity to water vapour concentration and susceptible to drift over time and temperature. The zero drift is $\pm$ 0.3 ppm per degree centigrade change in temperature. Therefore, to ensure the desired precision and accuracy of measurement, substantial sample conditioning and post-processing of data are needed in addition to frequent (hourly) instrument calibration using internationally recognized gas standard.

2.1.2 CRDS technique

This technique was developed by O'Keefe and Deacon in 1988 [73]. CRDS provides a promising approach with little efforts for making both high-precision and high frequency observations, by creating long path length over which a laser pulse can decay. The long path lengths are achieved by multiple reflections of a laser pulse between highly reflective mirrors and are desirable because they increase the sensitivity of the measurements making it possible to measure very low concentrations of gases. The following three main characteristics make this technique

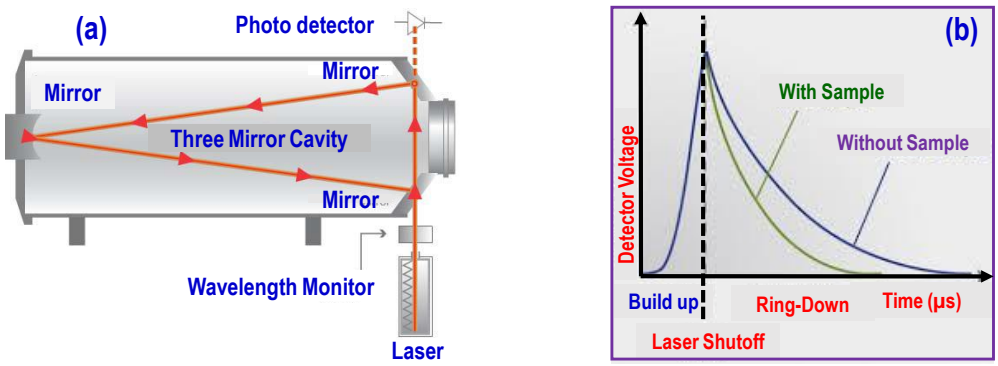

Figure 2.2: (a) Schematic of the measuring principle of CRDS based analyzer. (b) The response of detector with and without sample inside the instrument. Adapted from the Picarro official website.

unique and highly usable than other conventional techniques [74–76].

1. It provides a very long interaction path length (about 20 km) between the sample and the incident wavelength, by utilizing a 3-mirror configuration, which enhances its sensitivity over other conventional technique NDIR.

2. The ability to isolate a single spectral feature with a resolution of 0.0003 cm^{-1}, due to its operating low pressure ($\sim$ 140 Torr) which ensures that the peak height or area is linearly proportional to the concentration.

3. The measurements of trace gases using this technique are achieved by measuring the decay time of light intensity inside the cavity while the conventional optical absorption spectroscopy technique is based on magnitude and absorption of light intensity. Hence, the final concentrations will be insensitive to the pulse to pulse variations in the laser intensity and thus increases the accuracy of measurements. Furthermore, there is no need of frequent zeroing and span calibration in this technique.

The schematic diagram of CRDS technique is shown in Figure 2.2a. The main parts of the instrument based on this techniques are tunable diode laser, an optical cavity [formed by three highly reflective mirrors (Reflectivity R > 99.97 %) separated by a distance d], wavelength monitor and a photo-detector.

The laser is tuned by changing its input voltage and current at four wavelengths i.e., 1.603, 1.659, 1.565 and 1.651 μm for measuring CO_2, CH_4, CO and H_2O, respectively. Light from a semiconductor diode laser is coupled into a stable high finesse non confocal optical cavity, containing analyte gas. When the optical frequency matches the resonant frequency of the cavity, energy builds up in the cavity. Laser gets switched off as energy build-up complete inside the cavity. The laser pulse is reflected many times back and forth between the mirrors inside the optical cavity, which results in interaction path length with sample of about 20 Km. At each pass when the pulse is reflected back from mirror, a small fraction of light exit from the third mirror due to finite mirror transmittance. A photo-diode detector is positioned behind the mirror measuring this transmitted light, the signal decay is then analyzed. The time at which the light intensity inside the cavity decreases to 1/e of it's initial value is called the ring down time (denoted by τ). The ring down time will be high and dominated by mirror loss when the wavelength of injected light does not match with the absorption feature of any gas present inside the cavity. Figure 2.2b shows a profile of light intensity as a function of time in a CRDS cavity. The decay of intensity of light pulse can be denoted from Beer's law

$$I(t) = I_0 exp\left(\frac{-t}{\tau}\right). \tag{2.3}$$

Where t is the time and τ is characteristic decay time constant in μs, known as ring down. Differences in light intensity that might be present between laser pulses do not affect analysis because only the decay is analyzed, not the magnitude of intensity. The ring-down for the cavity without the sample is given by

$$\tau_0 = \frac{L}{cn \ln R}. \tag{2.4}$$

where R is mirror reflectivity, n is number of mirrors, c is speed of light and L is round trip cavity length in cm. This measurement provides the zero absorption baseline. Since R is close to unity ≈ 0.99, so we can approximate $\ln R$ = 1-R and the above equation can be written as

$$\tau_0 = \frac{L}{cn(1-R)}. \tag{2.5}$$

In the presence of absorbing gas species the ring down time will be

$$\tau = \frac{L}{c\left[n(1-R) + L\alpha(\nu)\right]}. \tag{2.6}$$

Where $\alpha(\nu)$ is the molecular absorption coefficient of the absorber present over a path length inside the cavity and can be determined by the product of frequency dependent absorption cross section (σ) in cm^2 $molecule^{-1}$ with number density (N).

$$\alpha(\nu) = N \times \sigma. \tag{2.7}$$

The absorbance spectrum is calculated from the following standard equation

$$\alpha(\nu_j) = \frac{1}{c}\left[\frac{1}{\tau(\nu_j)} - \frac{1}{\tau_0(\nu_j)}\right]. \tag{2.8}$$

where j is corresponds to different wavelengths. The absorption cross section of a molecular species is known for a particular wavelength. Hence, the concentrations of GHGs are calculated by measuring the changes in the ring-down time.

2.2 Effect of water vapor on CO_2 measurements

Water vapor affects the measurements of CO_2 by diluting its mole fractions in the air and by broadening the spectroscopic absorption lines of other gases. For the use of atmospheric models and comparison between stations, the dry concentration is important since at constant pressure dilution decreases the trace gas concentration with increasing the levels of water vapor concentration. Figure 2.3 shows that the dilution range of CO_2 varies from 6 to 11 ppm when the water vapor varies from 8000 ppm to 13,000 ppm. The water vapor range under 100 ppm will restrict dilution at 0.04 ppm. Dilution errors are the largest source of error in the CO_2 measurements.

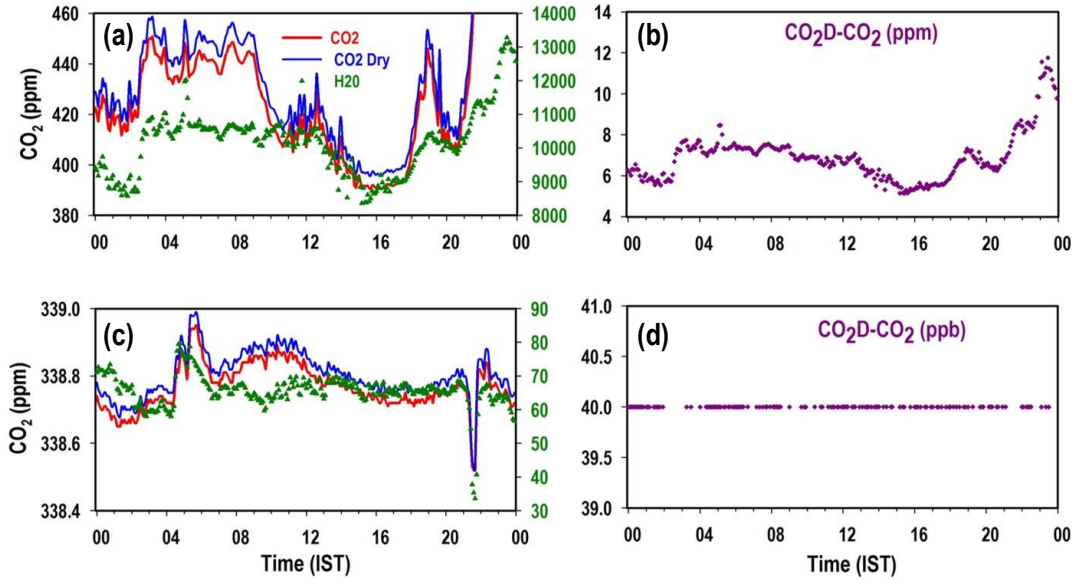

Figure 2.3: Effect of water vapor on the CO_2 measurements. The red line in left figures shows the wet CO_2 mixing ratio while blue line shows the mixing ratio of CO_2 after removing the effect of water vapor. Green line shows the corresponding levels of water vapour. Figures on right show the difference between dry and wet CO_2 mixing ratios for different ranges of water vapour mixing ratios.

2.3 Experimental setup

Brief descriptions of the experimental setups for ground based measurements and airborne measurements will be discussed in following sections.

2.3.1 Ground based measurements of CO_2, CH_4 and CO

The CRDS analyzer (Picarro G2401) for the simultaneous measurements of CO_2, CH_4, CO and H_2O was installed at PRL, Ahmedabad in November, 2013. Figure 2.4 shows the schematic diagram of the measurement system consisting of the analyzer, moisture removal system and the calibration set up. Atmospheric air is sampled continuously from the terrace of the building (50 meter above the ground level) through a teflon tube (1/4-inch outside diameter) using a pump located after the optical cavity of instrument. The air intake is capped with an inverted teflon funnel conical beaker to prevent liquid water from entering the sample line. The air passes through a glass manifold (where excess moisture is removed

during high humidity condition), a 5 μm PTFE (polytetrafluoroethylene) filter (for removal of dust particles) and another moisture removal system consisting of a 50-strand Nafion dryer (for removing the moisture to the level of 0.04% (400 ppm) mole fraction of H_2O) [77].

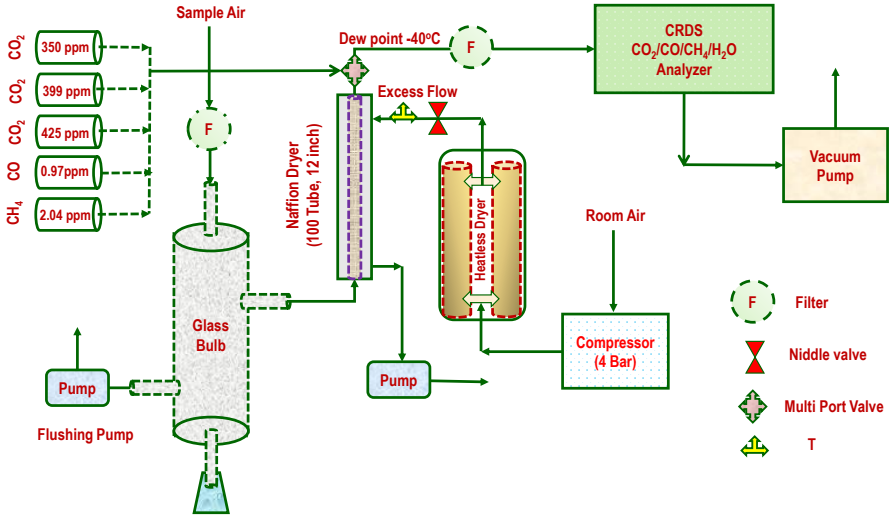

Figure 2.4: Schematic of the measurement system in PRL. A Nafion dryer has been introduced in the inlet of instrument for removing water vapour from the ambient air. The calibration mixtures (three) from NOAA, USA are used to calibrate CO_2 measurements and two calibration mixtures each from Linde, UK are used to calibrate CH_4 and CO measurements.

Although, the instrument has ability to correct for the water vapour interferes by using experimentally derived water vapor correction algorithms [78], but it has an absolute H_2O uncertainty of $\sim$ 1% [75] and can introduce a source of error using a single water vapor correction algorithm [79]. This error can be minimized by either generating the correction coefficients periodically in the laboratory or by removing the water vapour from the sample air. Conducting the water vapor correction experiment is a bit tricky and needs extra care as discussed by [79]. Hence, we prefer to remove water vapour from the sample air. Nafion dryer contains a bunch of semi-permeable membrane tubing separating an internal sample gas stream from a counter sheath flow of dry gas in stainless steel

outer shell. The partial pressure of water vapour in the sheath air should be lower than the sample air for effectively removing the water vapour from the sample air. A heatless dryer generates dry air using a 4 bar compressor (KNF, MODEL: NO35ATE) which is used as a sheath flow in Nafion dryer. This setup dries the ambient air near to 0.03% (300 ppm) concentration of H_2O. The instrument is connected with the calibration mixtures and sample inlet via a multi port valve system. The measurements stopped from March, 2014 to June,2014 due to some technical problem in instrument.

Instrument Tests

The instrument is calibrated for CO_2 by three calibration mixtures (350.67 ± 0.02 (ND50573), 399.68 ± 0.01 (ND50582) and 426.20 ± 0.01 (ND50090) ppm) from NOAA, USA and for CH_4 (2.04 ppm (LL-50186)) and CO (970 ppb (LL-74774)) by two separate calibration mixtures from Linde, UK. An additional secondary standard tank (CO_2: 338 ppm, CO: 700 ppm) is used to determine the precision of the instrument. The secondary standard values are calibrated using the primary standards and CO_2, CH_4 and CO mole fraction values are assigned to the cylinder. To determine the precision and drift, a target gas is measured by instrument for 24 hours. To insure the stabilization, we exclude the first hour data.

For calculating the precision, we take the average and standard deviations of 5 min data for respective gases which is shown in Figure 2.5. For CO_2, CO and CH_4 , for 5 minute data, precision were found as 0.015, 0.005 and 0.0006 ppm respectively within ± 1σ. Maximum drift for 24 hours has been calculated by subtracting the maximum and minimum value of 5 minute average which were found to be 0.2, 0.015 and 0.005 ppm respectively for CO_2, CO and CH_4. The linearity of the instrument for CO_2 measurements has been checked by using three calibration standards (350.67 ppm, 399.68 ppm and 426.20 ppm) of CO_2. All gases were passes for one hour. First 10 min and last 5 min data were removed for avoiding the stabilization problems.

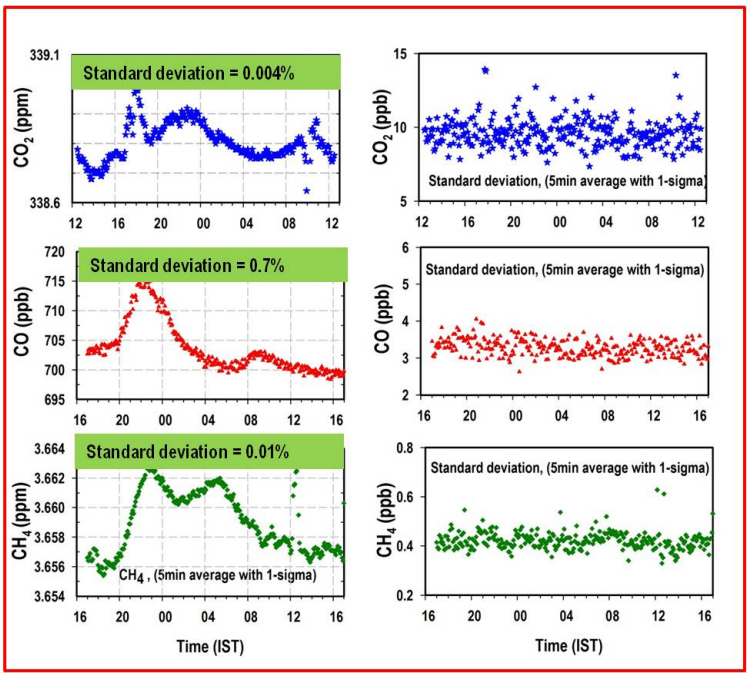

Figure 2.5: The precision and drift tests for CRDS based instrument for the 24 hour period. Left figures show the 5 min averaged values while right figures show the 5 min standard deviations corresponding to different gases.

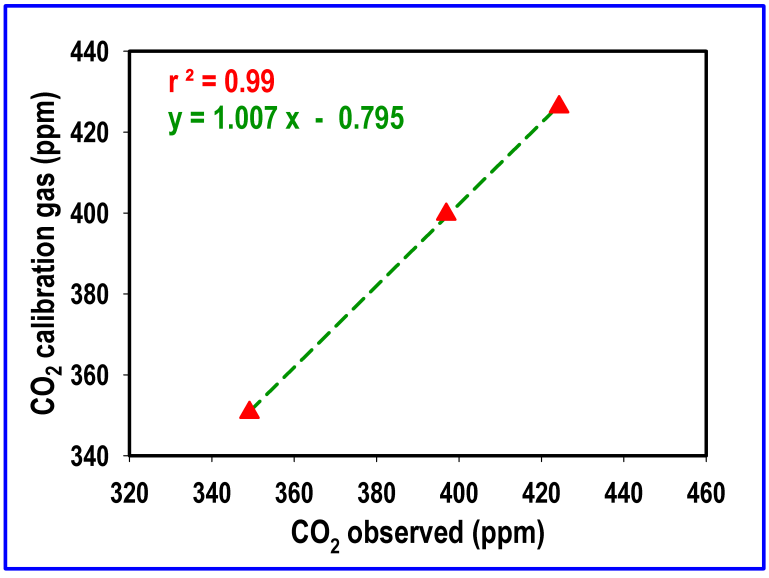

Figure 2.6: Calibration curve for the Picarro analyzer for CO_2 measurements, using three known standards of CO_2 from NOAA, USA.

Figure 2.6 shows the result of the linearity assessments. The linearity tests

were conducted very frequently and the slope is found in the range of 0.99 - 1.007 ppm with correlation coefficient (r^2) of about 0.999.

2.3.2 Airborne measurements of CO_2

This study also analyses the vertical distributions of CO_2 from the Campaign based vertical profiles measured over Delhi in 2010, 2011 and 2012 using the Continuous CO_2 Measuring Equipment (CME) on-board a Japan Airline (JAL) passenger aircraft by the CONTRAIL project [56]. CME contains non-dispersive infrared (NDIR) based analyzer (LI-840, LI-COR Inc.) and assembly of components to maintain the precision and calibration of the instrument. CME was installed on several aircrafts operated by JAL as part of the second phase of this program in 2005. The air is drawn by a pump from the intake port and analysed for CO_2 using the analyzer. The analyzer is calibrated frequently during the flight using two calibration gases. The measurement precision is estimated to be 0.1 ppm. All these actions are performed automatically using an on-board controller.

2.4 Remote sensing measurements of CO

In order to study the tropspheric distributions of CO, this study uses Level 3 V6 monthly mean gridded ($1^o \pm 1^o$ resolution) CO products from Measurements of Pollution in the Troposphere (MOPITT) for a period of 14 years (January, 2001 - December, 2014) at 9 pressure levels between 900 hPa and 100 hPa [80]. MOPITT is an eight channel nadir looking gas correlation radiometer, on-board the NASA EOS Terra satellite, which was placed in a near polar sun-synchronous orbit at an altitude of 705 km in December 1999. The MOPITT algorithms estimate three products Thermal IR (V6-TIR), Near IR (V6-NIR) and Thermal and Near IR Joint (V6-TIR/NIR). They have their own advantages and disadvantages as discussed by [81, 82]. The bias in TIR products varies from 9% at 900 hPa to 3.4% at 200 hPa [82]. Low radiance bias correction factors exhibit minimal influence of a variety of potential bias sources including errors in instrumental specifications, forward model errors, spectroscopy errors, and geophysical

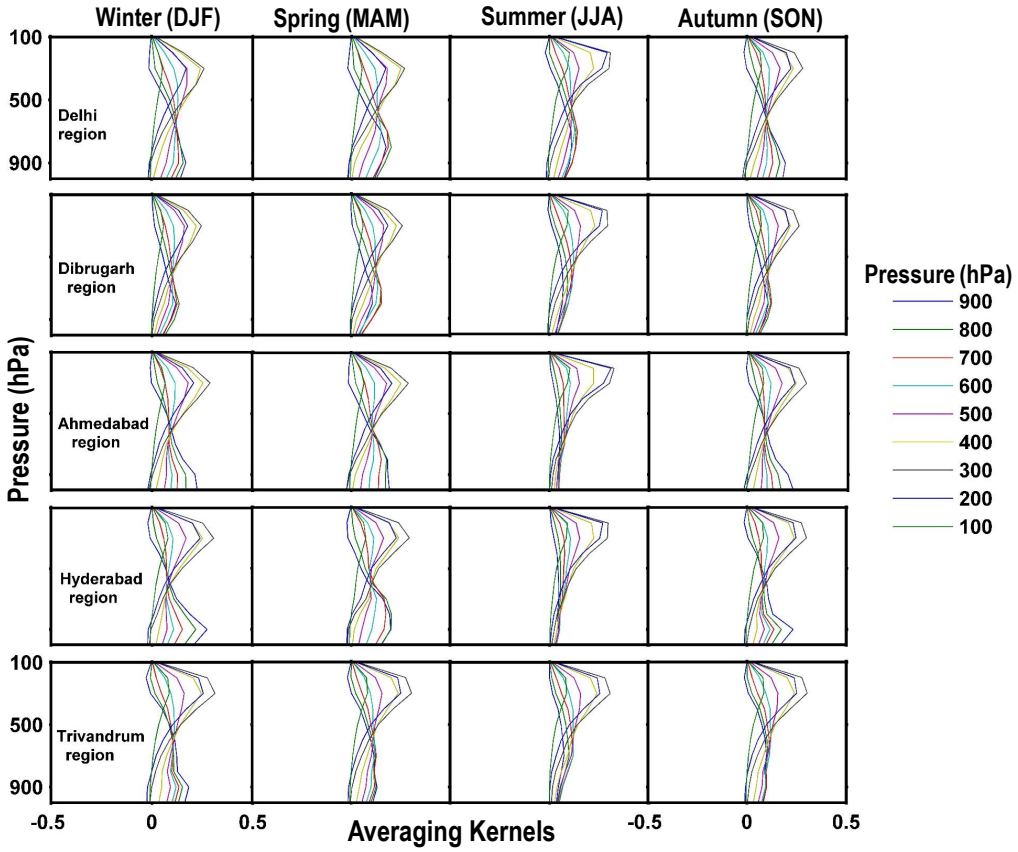

Figure 2.7: Climatological seasonal mean (period January, 2001 - December, 2014) of MOPITT averaging kernels at different pressure levels over all the regions in India. Different colours show distinct pressure levels in hPa.

errors on the retrieved CO data. Therefore, we used the V6-TIR products for this study which is mostly focused on the transport effects on CO mixing ratio at upper tropospheric level. For avoiding the dominance of a priori profiles, we use only those profiles, which have Degrees of Freedom (DOF) for signal greater than 1.2. As a result of applying this filter, we did not get monthly profiles for one or two months over some of the regions of study.

Before making the use of retrieved data for the study, it is very necessary to check the data consistency with the sensitivity of MOPITT retrievals. Hence, for checking the sensitivity of CO profiles over study regions, we took the climatological mean of averaging kernel profiles at different pressure levels for the four different seasons from January, 2001 to December, 2014 (Figure 2.7). In general,

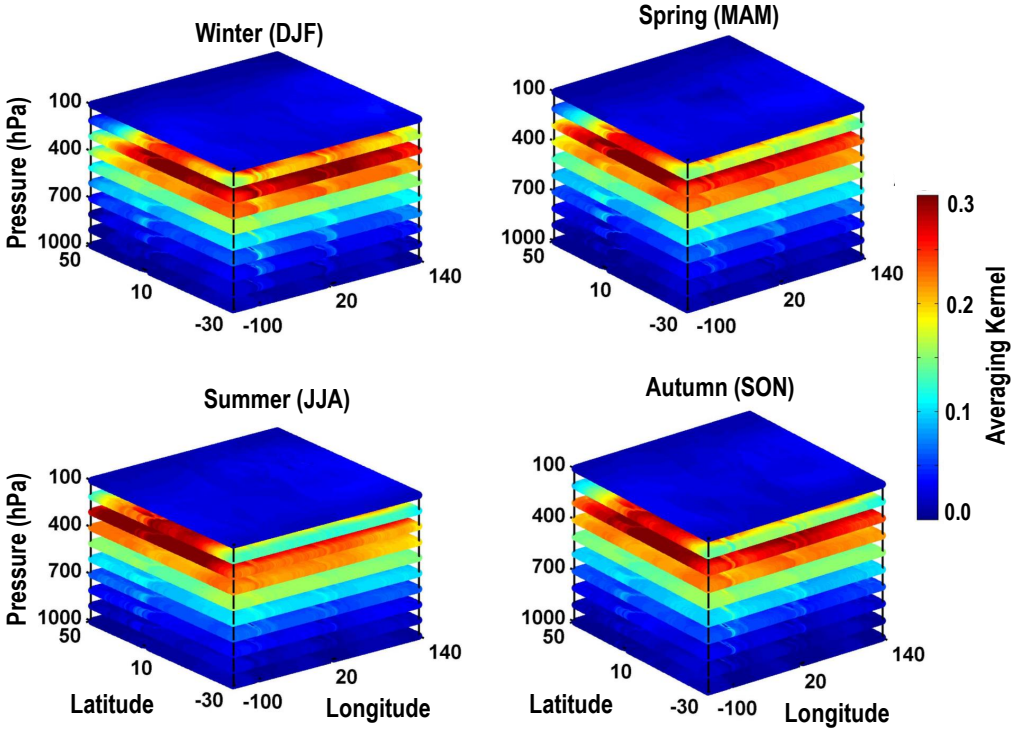

Figure 2.8: Climatological seasonal mean (during January, 2001 - December, 2014) of MOPITT averaging kernels at 300 hPa level over different latitudes (30^{o}S - 50^{o}N) and longitudes (100^{o}W - 140^{o}E) during winter (DJF), spring (MAM), summer (JJA) and autumn (SON). The color bar shows the magnitude of averaging kernels at this pressure level.

over all study regions, the averaging kernels show the significant retrieval sensitivity at each height in all seasons except summer. The retrieval sensitivity has been observed very good during all the four seasons in the upper tropospheric (300-200 hPa) levels. We have discussed also about the effects of long-range transport at 300 hPa, over all the study regions in Section 4.2.4. So for dealing with the long-range transport, the retrieval sensitivity of CO over the transport pathways at 300 hPa is also studied. We took the latitude-longitude slab (30^{o}S - 50^{o}N, 100^{o}W - 140^{o}E) mostly covering the transport pathways of CO and plotted the climatology of averaging kernels over this selected region as shown in Figure 2.8. It illustrates the significant information content in the MOPITT V6 retrievals over selected regions in all the four seasons at 300 hPa. Although, the magni-

tude of averaging kernels matrix is slightly lower over oceanic and some other regions, it has nicely captured the broad features at these levels. As suggested by Rodgers [83], the "area" of the averaging kernel rows (i.e., the sum of all elements of a particular row in the averaging kernel (AK) matrix) can be thought of as a rough measure of the fraction of the retrieval which comes from the data, rather than the a priori. In other words, if the AK row sum for a particular retrieval level is much less than 1, the retrieval is dominated by the a priori. As the AK row sum approaches 1, the a priori contribution becomes smaller and smaller. Our main focus of this study is on the seasonal cycle of CO at 900 hPa and 300 hPa. Hence, we calculate the fraction of the retrieval using this method at 900 hPa and 300 hPa during different seasons and observed that the smaller contributions from a-priori at these levels over all the study regions.

2.5 Description of the photochemical-transport models

Generally two types of 3-D numerical models are used to understand the atmospheric processes and the temporal variations of atmospheric constituents. One is the general circulation models (GCM) and another type is chemistry transport model (CTM). GCM simulates the climate in a statistical sense but not in weather sense for a particular year. These models solve the equations for conservation of momentum, energy and water. The concentrations of atmospheric species mainly affected by their emissions sources, chemical and natural sinks, transport and deposition. The numerical models which simulate the variability in space and time of these species using meteorological information and emission information from different inventories, are known as the chemical transport models (CTMs). These models are widely used for interpreting atmospheric observations and understanding different processes. The meteorological data simulated by the GCMs can be used as an meteorological input in CTMs to simulate the atmospheric composition for past and future climate. We have used the coupled GCM and CTM model simulations in this study whose basic descriptions are given below.

2.5.1 ACTM model for CO_2

This study uses the Center for Climate System Research/National Institute for Environmental Studies/Frontier Research Center for Global Change (CCSR/NIES/FRCGC) atmospheric general circulation model (AGCM)-based chemistry- transport model (ACTM). The model is nudged with reanalysis meteorology using Newtonian relaxation method. The U and V components of horizontal winds are used from the Japan Meteorological Agency Reanalysis (JRA-25) [84]. The model has $1.125^o \times 1.125^o$ horizontal resolution (T106 spectral truncation) and 32 vertical sigma-pressure layers up to about 50 km. Three components namely anthropogenic emissions, monthly varying ocean exchange with net uptake and terrestrial biospheric exchange of surface CO_2 fluxes are used in the model. The fossil fuel emissions for the model simulations are taken from Emission Database for Global Atmospheric Research (EDGAR) v4.2 FT2010 inventory (http://edgar.jrc.ec.europa.eu) for the year of 2010. Air-sea fluxes from [85] have been used for the oceanic CO_2 tracer. The oceanic fluxes are monthly and are linearly interpolated between mid-months. The terrestrial biospheric CO_2 tracers are provided from the Carnegie-Ames-Stanford-Approach (CASA) process model [86], after introducing a diurnal variability using 2 m air temperature and surface short wave radiation from the JRA-25 as per [87]. The ACTM simulations has been extensively used in TransCom CO_2 model inter-comparison studies [67, 68].

2.5.2 ACTM model for CH_4

This study uses CH_4 simulations from an atmospheric general circulation model (AGCM) -based CTM (ACTM) of Center for Climate System Research/National Institute of Environmental Studies/Frontier Research Center for Global Change (CCSR/NIES/FRCGC) [88] for the year of 2014. It simulates atmospheric CH_4 concentrations at hourly time interval with a spatial resolution of $2.8^o \times 2.8^o$ (T42 spectral truncations). It consists of 67 vertical sigma-pressure levels from surface to about 90 km. The model transport is nudged with horizontal winds (U and V) and temperature at 6-hourly interval from the Japan Meteorological

Agency reanalysis fields, version JRA-25 [84]. The model transport and chemistry are validated and used in several studies [89,90]. The a-priori anthropogenic emissions namely, agricultural soils, agricultural waste burning, energy manufacturing transformation, enteric fermentation, fossil fuel fires, fugitive from solid, oil production and refineries, gas production and distribution, industrial process and production use, road transportation, solid waste disposal and waste water are from Emission Database for Global Atmospheric Research (EDGAR) v4.2 FT2010 (http://edgar.jrc.ec.europa.eu) database. Anthropogenic emissions for 2010-2014 are kept constant at the level of 2010 due to unavailability of data. The a-priori wetlands and rice paddies emissions are based on the VISIT terrestrial ecosystem model simulations for 2000-2013 [91], biomass burning emissions are from GFED version 3.2 [92], termites emissions from [93] and marine emission are based on [94].

2.5.3 LMDz-OR-INCA model for CH_4

This study also uses simulations of CH_4 from the chemical transport model LMDz-OR-INCA, run by LSCE, France group [95]. This model couples a general circulation model developed at the Laboratorie de Météorologie Dynamique (LMD) [96]), a global chemistry and aerosol model INCA (Interactions between Chemistry and Aerosols [97,98]) and a global land surface model ORCHIDEE (Organizing Carbon and Hydrology in Dynamic Ecosystems [99]). LMDz uses the finite volume transport scheme for calculating turbulent mixing in the planetary boundary layer (PBL), deep convection and large-scale advection of tracers. The INCA model is used to simulate the distribution of aerosols and gaseous reactive species in the troposphere. INCA prepares the surface and in situ emissions, calculates dry deposition and wet scavenging rates, and integrates in time the mole fractions of atmospheric species with a time step of 30 min. INCA is coupled online to the LMDz General Circulation Model (GCM) to account, with different degrees of complexity, for climate chemistry interactions. LMDz is coupled with the ORCHIDEE dynamic global vegetation model or soil/atmosphere exchanges of water and energy but not for biogenic CO_2 or VOC fluxes. Together, these

three models form the LMDz-OR-INCA model. The model has fixed horizontal resolution of 2.5^o in longitude and 1.27^o in latitude (144 $\times$ 142) and the zoom version has the same number of grid boxes, but a resolution of $0.66^o \times 0.51^o$ for the region of 50^oE - 130^oE and 0^oN - 55^oN covering India and China. The vertical resolutions of both the versions consists of 19 sigma-pressure layers extending from the surface up to about 3.8 hPa. The spacings between two successive layers are not symmetrical and, correspond to a vertical resolution of about 300 - 500 m in the planetary boundary layer (with the first level at about 70 m height) and to a resolution of about 2 km at the tropopause (with 7 - 9 levels located in the stratosphere) [97]. The meteorological data for this model are the 6 hourly reanalysis data taken from the European Centre for Medium-range Weather Forecasting (ECMWF) operational forecast model. The time step of model output is hourly. The anthropogenic emissions (industry, fossil fuel, and industrial biofuel) are based on the inter-annually varying anthropogenic emissions obtained from the EDGAR v4.2 FT2010 database. The climatologically varying CH_4 emissions from wetlands are based on the scheme developed by [100], biomass burning emissions are based on the GFED v3.0 product (http://www.globalfiredata.org/data.html) developed by [101], termite emissions are based on [102], ocean emissions are based on [103] and soil sinks are based on [104]. Note that the seasonal variation of rice emissions is imposed by distributing the yearly values as given in [105]. Due to unavailability of anthropogenic emissions for the period of 2011-2014 and biomass burning emission for the period of 2012-2014, data for the years of 2010 and 2011 have been used to represent these emissions respectively. The mole fractions of CH_4 are simulated over the period 2000 - 2014 with zoom grids and extracted. The study uses the zoomed simulations of CH_4 over study location for the year of 2014.

2.5.4 MOZART model for CO

The MOZART-4 (Model for Ozone And Related Tracers, version 4) is an off-line three dimensional global chemical transport model which includes comprehensive tropospheric chemistry, simulating 85 gas phase species, 12 bulk aerosol species,

157 gas-phase and 39 photolysis reactions [106]. The model has been simulated at a horizontal resolution of 2.8^o latitude by 2.8^o longitude with 28 sigma pressure levels extending from surface up to 2 hPa. The input data for meteorological fields have been taken from National Center for Environmental Prediction (NCEP) reanalysis dataset. Anthropogenic emissions (dominated by fossil fuel combustion and biofuel burning) are taken from the Precursors of Ozone and their Effects in the Troposphere (POET) inventory for the year 2000 gridded at $1^o \times 1^o$ resolution [107]. Further, Regional Emission inventory in Asia (REAS) [108] has been used to update the anthropogenic emissions of CO and NOx over Asia for the year 2006. The GFEDv2.0 product is used for biomass burning emissions [101]. More details about the MOZART can be found in [109]. In this study we have used the average monthly climatology for the period of January, 2002 - December, 2007.

2.5.5 EMAC model for CO

The ECHAM5/MESSy2 Atmospheric Chemistry (EMAC) model is a numerical chemistry and climate simulation system that includes sub-models describing tropospheric and middle atmospheric processes and their interaction with oceans, land and human influences [110]). It uses the second version of the Modular Earth Submodel System (MESSy2) to link multi-institutional computer codes. The core atmospheric model is the 5^{th} generation European Centre Hamburg general circulation model (ECHAM5, [111]. For the present study, we applied EMAC (ECHAM5 version 5.3.02, MESSy version 2.24) in the T42L90MA-resolution, i.e. with a spherical truncation of T42 (corresponding to a quadratic Gaussian grid of approximately 2.8^o by 2.8^o in latitude and longitude) with 90 vertical hybrid pressure levels up to 0.01 hPa ($\sim$ 80 km altitude). The model simulation is described in [112] with the only difference of the usage of the ACCMIP emissions data for anthropogenic emissions for the year 2000 [113] and the GFEDv3.1 for biomass burning emissions [101], the last dataset with inter-annual variability. The meteorological data has been taken from the ECMWF operational forecast model [114]. The model has been extensively evaluated for CO [115–117]. In this study, we have used the average monthly climatology for the period of January,

2001 - December, 2008.

2.6 Statistical metrics for checking model performances

This section consider the appropriate parameters for determining the model bias and error. For assessing the model performance we use five statistical metrics, namely coefficient of determination (r^2), mean bias (MB), modified and normalized mean bias (MNMB), absolute and percentage value of root mean square error (RMSE). These metrics are used in several studies for evaluating the performance of atmospheric models [118–121]. The coefficient of determination provides the information about strength of linear association between model and observations and simply calculated as:

$$r^2 = \left[\frac{\Sigma_{i=1}^{N}(X_{obs,i} - \overline{X}_{obs})(X_{model,i} - \overline{X}_{model})}{\sqrt{\Sigma_{i=1}^{N}(X_{obs,i} - \overline{X}_{obs})^2}\sqrt{\Sigma_{i=1}^{N}(X_{model,i} - \overline{X}_{model})^2}} \right] \tag{2.9}$$

where $X_{obs,i}$ and $X_{model,i}$ represent the i^{th} observed and model values while $\overline{X_{obs}}$ and $\overline{X_{model}}$ indicate the average values in the observation and model. The r^2 can have values between 0 and 1.

The MB shows the average deviations between estimated and observed values and thus provides the information about the absolute bias (over-prediction and under-prediction) of the model. The positive and negative values of MB will indicate overestimation and underestimation of any variable by the model. The range of MB varies from -∞ to ∞. It is defined as

$$MB = \frac{1}{N}\Sigma_{i=1}^{N}(X_{model,i} - X_{obs,i}) \tag{2.10}$$

The normalised approach provides errors in a relative sense, which is easier to understand without knowing about the concentration range and unit of the species. MNMB is a measure of the estimation bias error, which allows analyzing symmetrically how the model overestimates or underestimates with respect to

observed values. It varies from -200% to 200% and can be computed using the following formula:

$$MNMB = \frac{2}{N}\Sigma_{i=1}^{N}\left(\frac{X_{model,i} - X_{obs,i}}{X_{model,i} + X_{obs,i}}\right) \tag{2.11}$$

The RMSE represents the standard deviations of the differences between model values and observed values. It encapsulates the typical magnitude of average error produced by the model. But without knowing about the range of the species we can not conclude that the error is large or small. Hence, we calculate percentage RMSE (%RMSE) also. Both RMSE and %RMSE will provide the information about the closeness of model values and observed values and defined as follows:

$$RMSE = \sqrt{\frac{1}{N}\Sigma_{i=1}^{N}(X_{model,i} - X_{obs,i})^2} \tag{2.12}$$

$$\%RMSE = \frac{1}{\overline{X}_{obs}}\sqrt{\frac{1}{N}\Sigma_{i=1}^{N}(X_{model,i} - X_{obs,i})^2} * 100 \tag{2.13}$$

The range of RMSE varies from 0 to ∞ while %RMSE varies from 0 to 100.

Chapter 3

Study of CO_2 and CO over an urban location

India is the second largest populous country in the world having about 1.3 billion inhabitants. Rapid socioeconomic developments and urbanization have made it the third largest CO_2 emitter next to China and USA since 2011, but it ranks at 137^{th} level based on the per capita emission rate of CO_2 (EDGAR v4.2; CDIAC - [70]). For example, in 2010 India's emission rate was 2.2 ton CO_2 eq/capita while the developed countries like USA, Russia and UK had emission rates of about 21.6, 17.6 and 10.9 ton CO_2 eq/capita, respectively (EDGAR v4.2). The budgets of these gases on regional as well as global scales can be estimated by bottom-up and top down approaches. However, large uncertainties are associated in the GHGs budgets over South Asia, especially over India than for other continents. Based on the atmospheric CO_2 inversion using model calculations, Patra et al., [21] found that the biosphere in South Asia acted as the net CO_2 sink during 2007-2008 and estimated CO_2 flux of about -104 ± 150 TgC yr^{-1}. Further, based on the bottom-up approach, Patra et al., [21] gave an estimate of biospheric flux of CO_2 of about -191 ± 193 TgC yr^{-1} for the period of 2000-2009. Both of these approaches show the range of uncertainty $100-150\%$. One of the major sources of these large uncertainties is the lack of spatial and temporal observations of these gases [21, 122].

Furthermore, quantifying the components of anthropogenic emissions is also important for providing independent verification of future emission mitigation activities. Urban regions have large emissions of fossil-fuel CO_2, and hence measurements over these regions provide excellent target from both atmospheric and policy perspectives. The combination of CO_2 and CO measurements allow the quantification of the anthropogenic component of CO_2 [60,62–64]. In addition, local source patterns can be identified by the combination of CO and CO_2 measurements since different combustion processes have different emission ratios [60,61]. Therefore, continuous atmospheric measurements of CO_2 and CO can help to distinguish between anthropogenic and biospheric influences on observed CO_2 variations as well as understanding of their dominant regional emission sources. Further, the CO and CO_2 correlation slope can be used for calculating the total emissions of CO over the study region which will be helpful for reducing the uncertainties in the emission inventories of CO [61]. Several ground based and aircraft based studies, aimed at measurements of urban and regional mixing ratios of CO_2 and their relationships to the mixing ratios of CO in the context of categorizing the region wise dominant sources influencing the species, have been done from different parts of world [60–63]. However, this type of study has not been performed in India except recently reported results from weekly samples for three Indian sites by [48]. Herein lies the importance of the present study in this chapter, which will focus on the variability in CO_2 mixing ratios along with the anthropogenic tracer CO over an urban region.

Simultaneous continuous measurements of CO_2 and CO from an urban site Ahmedabad, located in the western India, are utilized under this chapter for studying the temporal variations (diurnal and seasonal) of both gases, their emissions characteristics on diurnal and seasonal scale using their mutual correlations, estimating the contribution of vehicular and biospheric emission components in the diurnal cycle of CO_2 using the ratios of CO to CO_2 and rough estimate of the annual CO emissions from study region. Finally, the measurements of CO_2 have been compared with simulations using an atmospheric chemistry-transport model

to discuss roles of various processes contributing to CO_2 mixing ratios variations.

3.1 Site description, local emission sources and meteorology

The measurement facility is housed inside the campus of the Physical Research Laboratory (PRL), situated in the western part of Ahmedabad (23.03°N, 72.55°E, 55 m AMSL) in the Gujarat state of India (Figure 3.1). It is a semi-arid, urban region in western India, having a variety of large and small scale industries (textile mills and pharmaceutical production facilities) in eastern and northern outskirts. The institute is situated about $15-20$ km away from these industrial areas. The western part is dominated by the residential areas. The city has a population of about 5.6 million (Census India, 2011) and has large number of automobiles (about 3.2 million), which are increasing at the rate of about 10% per year. Most of the city buses and auto-rickshaws (three-wheelers) use compressed natural gas (CNG) as a fuel. The transport-related activities are the major contributors of various pollutants [123]. The Indo-Gangetic Plain (IGP) is situated in the north-east of Ahmedabad, which is very densely populated region and has high levels of pollutants emitted from various industries and power plants along with anthropogenic emissions from burning of fossil fuels and traditional biofuels (wood, cow-dung cake etc). The Thar Desert and the Arabian Sea are situated in the northwest and southwest of Ahmedabad, respectively.

Figure 3.2 shows average monthly variability of temperature, relative humidity (RH), wind speed based on data taken from Wunderground (www.wunderground.com), rainfall from Tropical Rainfall Measuring Mission (TRMM) and planetary boundary layer (PBL) height from the Modern-Era Retrospective Analysis for Research and Applications (MEERA). The wind rose plot shows the surface level wind speed and direction during different seasons over Ahmedabad in 2014. Large seasonal variations are observed in the wind speed and direction over Ahmedabad.

During summer (June - July - August), the inter-tropical convergence zone

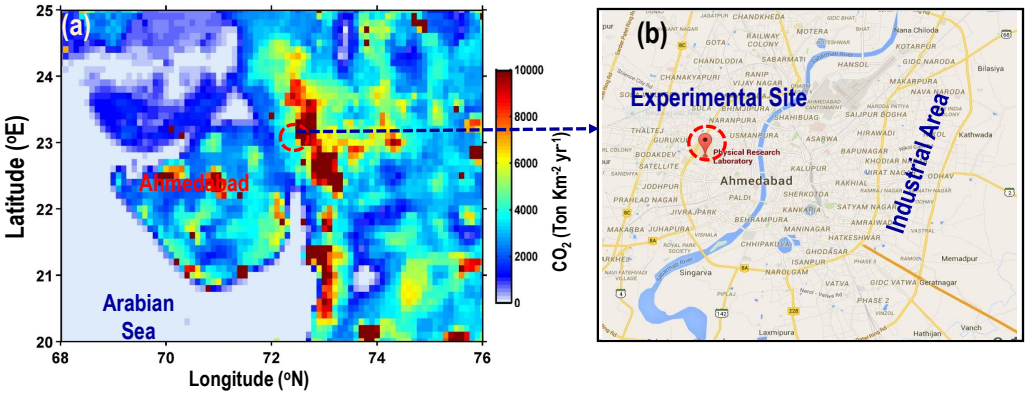

Figure 3.1: (a) Spatial distribution of total anthropogenic CO_2 emissions from Emission Database for Global Atmospheric Research (EDGAR) version 4.2 inventory over Ahmedabad and surrounding regions. (b) The Ahmedabad city map showing location of the experimental site (PRL).

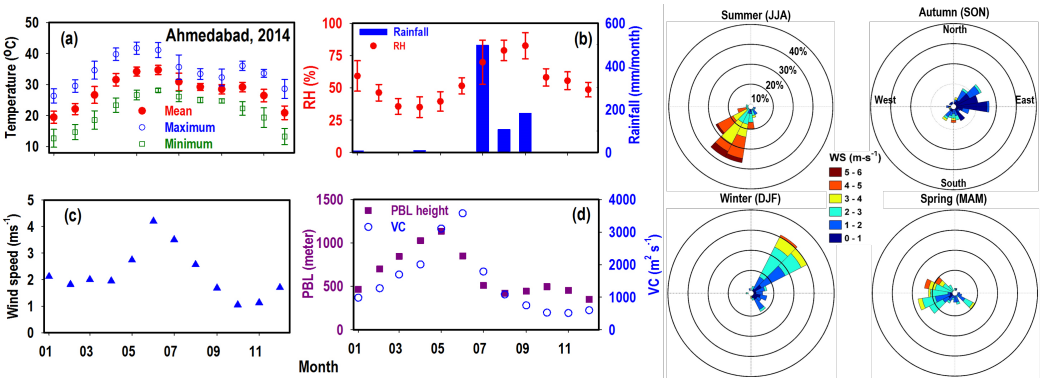

Figure 3.2: (Left panel: a-d) Monthly average temperature with monthly maximum and minimum value, relative humidity (RH), rainfall, wind speed, planetary boundary layer (PBL) height and ventilation coefficient (VC) over Ahmedabad during the year of 2014. Temperature, RH and wind speed are taken from Wunderground weather (*www.wunderground.com*) while rainfall and PBL height data are used from Tropical Rainfall Measuring Mission (TRMM) satellite and MEERA reanalysis data. (Right panel) Wind rose plots for Ahmedabad for the four seasons of 2014 using daily average data from Wunderground.

(ITCZ) moves northward across India. It results in the transport of moist and cleaner marine air from the Arabian Sea and the Indian Ocean to the study location by south-westerly winds, or the so-called southwest monsoon (summer

monsoon). The first shower due to the onset of the southwest monsoon occurs in July and it retreats in the mid of September over Ahmedabad. Due to heavy rain and winds mostly from oceanic region, RH shows higher values in July, August and September. Highest RH of about 83% is observed in September. The long-range transport of air masses from the north-eastern part of the Asian continent starts to prevail over Indian region when ITCZ moves back southward in September and October. These months are regarded as transition period for the summer. During autumn (September-October-November), the winds are calm and undergo a change in their direction from south west to north east. When the transition of winds takes placed from oceanic to continental region in October, the air gets dryer and RH decreases until December. The winds are north easterly during winter (December- January - February) and transport pollutants mostly from continental region (IGP region). During pre-monsoon season (March - April - May), winds are north-westerly and little south-westerly which transport mixed air masses from continent and oceanic regions. The average wind speed is observed higher in June and July while lower in October and March when transition of wind starts from oceanic to continental and continental to oceanic, respectively. The monthly averaged temperature starts increasing from January and attains maximum (34.6 $\pm$ 1.4°C) in June, followed by a decrease until September and temperature is slightly warmer in October compared to the adjacent months. The monthly variation in PBL height closely resembles with the temperature pattern. Maximum PBL height of about 1130 m is found in June and it remains in the lower range at about 500 m during July to January. The ventilation coefficient (VC) is obtained by multiplying wind speed and PBL height which gradually increases from January to attain the maximum value in June and the lowest values of VC are observed in October and November.

3.2 Measurement technique

Simultaneous measurements of CO_2 and CO have been made using a state-of-the-art laser based cavity ring down spectroscopy (CRDS) technique (Picarro-G2401

analyser) at Ahmedabad, an urban site in western India, from November 2013 to June 2015 with a break during March - June 2014. The ambient air is drawn in through a 1/4-inch teflon tube. The sample air passes through a glass manifold (where excess moisture is removed during high humidity condition), a 5 μm PTFE (polytetrafluoroethylene) filter (for removal of dust particles) and another moisture removal system consisting of a 50-strand Nafion dryer (for removing the moisture to the level of 0.04% (400 ppm) mole fraction of H_2O). Detail of the measurements and calibration procedures are discussed in Chapter 2.

3.3 Time series analysis

Figures 3.3a and 3.3b show the time series of 30 minute average CO_2 and CO mixing ratios for the period of November, 2013 - February, 2014 and July, 2014 to June, 2015. The mixing ratios of both gases exhibit large synoptic variability because the site is close to anthropogenic sources such as vehicular emissions, industrial emissions etc. The mixing ratios and variability of both gases are lowest in the month of July and August. Maximum scatter in the mixing ratios and several plumes of very high levels both gases have been observed from October, 2014 until mid-March 2015. Almost all plumes of CO_2 and CO are one to one correlated and are found during evening rush hours and late nights due to calm winds and common emission sources. Figures 3.3e and 3.3f show the variations of CO_2 and CO mixing ratios with wind speed and direction for the study period except July, August and September due to non-availability of wind data. Most of the high and low mixing ratios of both these gases are found to be associated with low and high wind speeds. There is no specific direction for high levels of these gases. This probably indicates the vehicular emission is an important contributor to the local emissions since the measurement site is surrounded by city roads.

Figures 3.3c and 3.3d show the probability distributions or frequency distributions of CO_2 and CO mixing ratio during the study period. The frequency distribution of CO_2 shows almost normal distribution while CO shows skewed to-

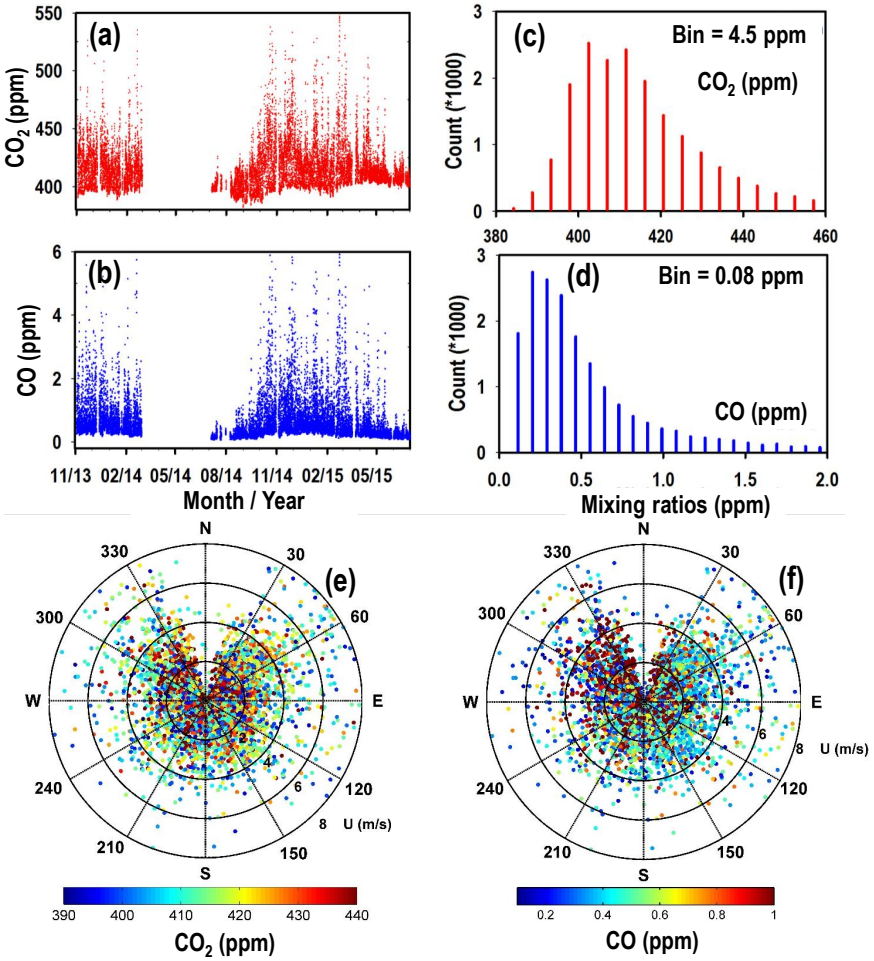

Figure 3.3: (a and b) Time series of 30 minute average values CO_2 and CO measured at Ahmedabad for the study period. (c and d) The frequency distribution in CO_2 and CO mixing ratios at the intervals of 4.5 ppm and 80 ppb, respectively for the study period using 30 minute mean of both gases. (e and f) The polar plots show the variation of 30 minute averaged CO_2 and CO at this site with wind direction and speed during the study period except July, August and September due to unavailability of meteorology data.

wards right (lower mixing ratios). This is because, natural cycle of the biosphere (photosynthesis and respiration) along with some common controlling factors (local meteorology and anthropogenic sources), affects significantly the levels of CO_2. The control of the boundary layer is common for the diurnal variations of these species because of their chemical lifetimes are longer (> months) than the timescale of PBL height variations ($\sim$ hrs). However, biospheric fluxes of CO_2

can have strong hourly variations. During the study period the CO_2 mixing ratios varied between $382-609$ ppm, with 16% of data lying below 400 ppm, 50% lying in the range $400-420$ ppm, 25% between $420-440$ ppm and 9% in the range of $440-570$ ppm. Maximum frequency of CO_2 is observed at 402.5 ppm during the study period. The CO mixing ratios are found in the range of $0.07-8.80$ ppm with almost 8% data lies below the most probable frequency of CO at 0.2 ppm, while 70% data lies between the mixing ratios of 0.21 ppm and 0.55 ppm. Only 8% data lies above the mixing ratio of 1.6 ppm and rest of 14% data lies between 0.55 and 1.6 ppm. The annual mean mixing ratios of CO_2 and CO are found to be 413.0 ± 13.7 ppm and 0.50 ± 0.37 ppm, respectively, after removing outliers beyond 2σ values.

3.4 Seasonal patterns of CO_2 and CO

The seasonal cycles of CO_2 and CO are mostly governed by the strength of emission sources, sinks and transport patterns. Although they follow almost identical seasonal patterns but the factors responsible for their seasonal behaviors are distinct as for the diurnal variations. We calculate the seasonal cycle of CO_2 and CO using two different approaches. In first approach, we use monthly mean of all data and in the second approach we use monthly mean for afternoon period ($1200-1600$ hrs) only. The seasonal cycle from first approach will depict the combined influence of local emissions (mostly) as well as that of large scale circulation. The second approach removes the auto-covariance by excluding CO_2 and CO data mainly affected by local emission sources and represent seasonal cycles at the well mixed volume of the atmosphere. The CO_2 time series is de-trended by subtracting a mean growth rate of CO_2 observed at Mauna Loa (MLO), Hawaii ($155.62°W$, $19.48°N$), i.e., 2.13 ppm yr^{-1} or 0.177 ppm $month^{-1}$ (www.esrl.noaa.gov/gmd/ccgg/trends/) for clearly depicting the seasonal cycle amplitude. Figure 3.4a and 3.4b show the variations of monthly average mixing ratios of CO_2 and CO using all daily ($0-24$ hr) data and afternoon (1200-1600 hrs) data collected during the study period.

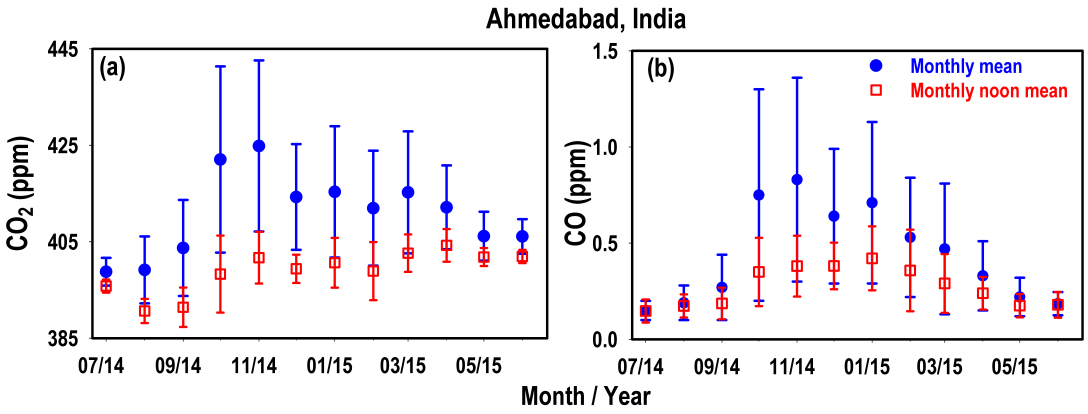

Figure 3.4: The seasonal variations of CO_2 and CO at Ahmedabad, India from July, 2014 to June, 2015 using their monthly mean mixing ratios. The blue dots and red rectangles show the monthly average mixing ratios of these gases for the total (0-24 hrs) and noon time (1200-1600 hrs) data, respectively with $\pm$ 1σ spread.

Both average mixing ratios (total and noon time) of CO_2 exhibit strong seasonal cycle, but show distinct patterns (occurrence of maxima and minima) to each other. This difference occurs because seasonal cycle of CO_2 from all data is mostly governed by the ventilation and large scale circulation while the seasonal cycle from noon time mean mixing ratio is mostly related to the seasonality of vegetation activity. The total and noon time mean mixing ratios of CO show almost similar pattern and evince that the seasonal cycle of CO_2 from the afternoon mean is mostly controlled by the biospheric productivity, since biospheric cycle does not influence CO mixing ratio directly. In general, total mean values of CO_2 and CO are observed lower in July having mixing ratio 398.78 $\pm$ 2.8 ppm and 0.15 $\pm$ 0.05 ppm, respectively. A sudden increase in the total mean of both gases is observed from September to October and maximum mixing ratios of CO_2 and CO are observed to be 424.9 $\pm$ 17.0 ppm and 0.83 $\pm$ 0.53 ppm, respectively, during November. From January to June the total mean mixing ratio of CO_2 decreases from 415.3 $\pm$ 13.6 to 406.1 $\pm$ 3.0 ppm and total mean mixing ratio of CO decreases from 0.71 $\pm$ 0.22 to 0.18 $\pm$ 0.06 ppm. During summer months predominance of south-westerly winds which bring cleaner air from the

Arabian Sea and the Indian Ocean over to Ahmedabad and high VC (Figure 3.2) are responsible for the lower mixing ratio of total mean of both the gases. CO_2 and CO mixing ratios are also at their seasonal low in the northern hemisphere due to net biospheric uptake and seasonally high chemical loss by reaction with OH, respectively. In addition, deep convections in the southwest monsoon season efficiently transport the Indian emission (for CO, hydrocarbons) or uptake (for CO_2) signals at the surface to the upper troposphere, resulting lower mixing ratios at the surface in the summer compared to the winter months [57, 124–127]. During autumn and early winter (December), lower VC values cause trapping of anthropogenically emitted CO_2 and CO. This is the major cause for high CO_2 and CO mixing ratios during this period. The north-easterly winds bring very high levels of pollutants from IGP region and could additionally enhance the levels of CO_2 and CO during these seasons (autumn and winter). Higher VC and predominance of comparatively less polluted mixed air masses from oceanic and continental region results in the lower total mean mixing ratios of both the gases.

We have found significant differences which are observed in the afternoon mean mixing ratios of CO_2 as compared to daily mean. The first distinct feature is that significant difference of about 5 ppm is observed in the afternoon mean of CO_2 mixing ratio from July to August as compared to difference in total mean mixing ratio about $\sim$0.38 ppm for the same period. Significant difference in the afternoon mixing ratios of CO_2 from July to August is mainly due to the increasing sink by net biospheric productivity after the Indian summer monsoon rainfall. Another distinct feature is that the daily mean mixing ratio of CO_2 is found highest in November while the afternoon mean mixing ratio of CO_2 attains maximum value (406 ± 0.4 ppm) in April. Prolonged dry season combined with high daytime temperature (about 41°C) during April-May make the tendency of ecosystem to become moderate source of carbon exchange [57] and this could be responsible for the elevated mean noon time mixing ratios of CO_2.

The average amplitude (max - min) of the annual cycle of CO_2 is observed

around 13.6 and 26.07 ppm from the afternoon mean and total mean, respectively. Different annual cycles and amplitudes have been observed from other studies conducted over different Indian stations. Similar to our observations of the afternoon mean mixing ratios of CO_2, maximum values are also observed in April at Pondicherry (PON,12.0°N, 79.8°E, 20 m a.s.l: also known as Puducherry) and Port Blair (POB, 11.6°N, 92.7°E, 20 m a.s.l) with amplitude of mean seasonal cycles about 7.6 ± 1.4 and 11.1 ± 1.3 ppm respectively [48]. Cape Rama (CRI, 15°N, 74°E, 60 m a.s.l), a costal site on the south-west coast of India show the seasonal maxima one month before our observations in March annual amplitude about 9 ppm [44]. The Sinhagad (SNG, 18.4°N, 73.8°E, 1312 m a.s.l) site located over the Western Ghats Mountains, show very larger seasonal cycle with annual amplitude about 20 ppm [47]. The amplitude of mean annual cycle at the free tropospheric site Hanle (HLE, 32.7°N, 78.9°E, 4500 m a.s.l) at altitude of 4500 m is observed to be 8.2 ± 0.4 ppm, with maxima in early May and the minima in mid-September [48]. Distinct seasonal amplitudes and patterns are due to differences in regional controlling factors for the seasonal cycle of CO_2 over these locations, e.g., the HLE is remotely located from all continental sources, POB site is sampling predominantly marine air, CRI observes marine air in the summer and Indian flux signals in the winter, and SNG represents a forested ecosystem. These comparisons show the need for CO_2 measurements over different ecosystems for constraining its budget.

The annual amplitude in the afternoon and daily mean CO mixing ratios is observed to be about 0.27 and 0.68 ppm, respectively. The mean annual cycles of CO over PON and POB show the maxima in the winter months and minima during summer months same as our observations with annual amplitudes of 0.078 ± 0.01 and 0.144 ± 0.016 ppm, respectively. So the seasonal levels of CO are affected by large scale dynamics which changes air masses from marine to continental and vice versa and by photochemistry. The amplitudes of annual cycle at these locations differ due to their climatic conditions and sources/sinks strengths.

3.5 Diel cycle

The diurnal patterns for all months and seasons are produced by first generating the time series from the 15 min averages and then averaging the individual hours for all days of the respective month and season. The values beyond $\pm 2\sigma$ standard deviations from the mean are considered as an outliers and not included in the final mean.

3.5.1 Diel cycle of CO_2

Figure 3.5 shows the diurnal cycle of CO_2 during all the four seasons. In general, the diurnal pattern shows two peaks during morning (0700-0800 hrs) and evening time (2000-2200 hrs) along with dip during afternoon hours (1500-1700 hrs). All times are in Indian Standard Time (IST), which is 5.5 hrs ahead of Greenwich Mean Time (GMT). CO2 concentrations decreases rapidly after morning rush hours (0700-0800 hrs) due to its uptake by the plants during active photosynthesis process as well as the higher depth of atmospheric mixing. During monsoon and autumn season, comparatively lower concentrations indicate that the higher uptake of CO_2 during afternoon hours. The CO_2 levels start increasing after 1600 hrs and peaked around 2100 hrs, which are mainly due to the rush hour vehicular emissions and less dilution due to the lower depth of atmospheric mixing. Comparative levels of CO_2 during evening rush hours except summer confirm separately the major influence from the similar sources (vehicular emission) in its levels which do not show large variability as in post-midnight hours, which will be discussed later. There are many interesting features in the 0000-0800 hrs period. Concentrations of CO_2 start decreasing from 0000 hrs to 0300 hrs and afterwards increases until 0600 and 0700 hrs during summer and autumn. In subsequent section, in contrarory to this, the main anthropogenic tracer CO shows a continuous decline in its level during all the seasons from mid night to early morning and hence, indicate that there is enough vertical mixing of low CO air from above that once CO source is turned off. CO_2 uptake during monsoon seasons depleated the entire mixed layer due to the active vegetation and when the

low CO_2 air residual layer mixes after turning But in case of CO_2, higher respiration by the biosphere is mainly responsible for the increase in CO_2 levels during night hours. During the winter and spring seasons, concentrations of CO_2 during night hours are almost constant and small increase is observed only from 0600 to 0800 hrs during the winter season. The constant levels of CO_2 at night hours during these seasons gives the evidence of a continued but weak source (such as respiration) in order to offset dilution of mixing of low CO_2 air from aloft. Dry soil conditions could be one the possible caused for weak respirations. No peak during morning hours is observed in spring. Distinct timings for the occurrence of the morning peak during different seasons is generally related to the sunrise time, which reinforce the evolutions of PBL height and photosynthesis process. The sunrise occur at 0555-0620 hrs, 0620-0700 hrs, 0700-0723 hrs and 0720-0554 hrs during summer, autumn, winter and spring, respectively. During spring and summer, rush hour starts after sunrise, so the vehicular emissions occur when the PBL is already high and photosynthetic activity has started. But in winter and autumn, rush hour starts parallely with the sunrise, so the emissions occur when the PBL is low and concentration build up is much strong in these seasons than in spring and summer seasons.

The diurnal amplitude is defined as the difference between the maximum and minimum concentrations of CO_2 in the diurnal cycle. The amplitudes of monthly averaged diurnal cycle of CO_2 from July, 2014 to May 2015 are shown in Figure 3.5b. The diurnal amplitude shows large month to month variation with increasing trend from July to October and decreasing trend from October onwards. Lowest diurnal amplitude of about 6 ppm is observed in July while highest amplitude about 51 ppm is observed in October. The amplitude does not change much from December to March and is observed in the range of 25-30 ppm. Similarly from April to May the amplitude also varies in a narrow range from 12 to 15 ppm. The jump in the amplitude of CO_2 diurnal cycle is observed highest (around 208%) from July to August. This is mainly due to significant increase of biospheric productivity from July to August after the rains in Ahmedabad. It is

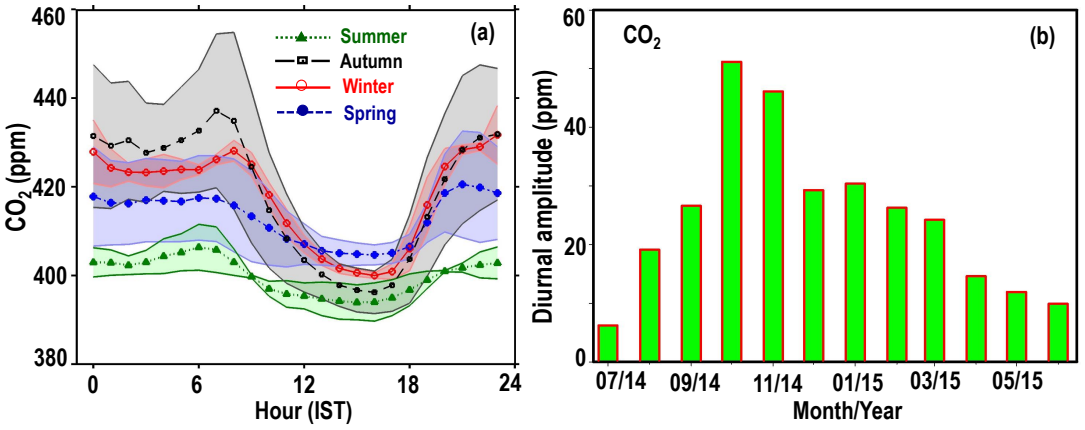

Figure 3.5: (a) Average diurnal variation of CO_2 over Ahmedabad during all the four seasons. (b) Monthly variation of average diurnal amplitude of CO_2 from July, 2014 to June, 2015. All times are in Indian Standard Time (IST), which is 5.5 hrs ahead of Greenwich Mean Time (GMT).

observed that during July the noon time CO2 levels are found in the range of 394-397 ppm while in August the noon time levels are observed in the range of 382-393 ppm. The lower levels could be due to the higher PBL height during afternoon and cleaner air, but in case of CO (will be discussed in next section), average day time levels in August are higher than in July. It rules out that the lower levels during August are due to the higher PBL heightand presence of cleaner marine air, and confirms the higher biospheric productivity during August.

The monthly average diurnal cycles of the biospheric net primary productivity from CASA model for Ahmedabad and for the year of 2014 are shown Figure 3.6. The details of CASA flux are given in the Section 2.5. It is observed that the model shows higher biospheric productivity in September and October while the observations are suggesting higher productivity in August. This indicates that the CASA model is not able to capture the signal of higher biospheric productivity for Ahmedabad and need to be improved. Similar discrepancy in the timing of maximum biospheric uptake is also discussed earlier by [57] using inverse model CO_2 fluxes an2 diurnal cycle is observed highest (around 208%) from July to August. This is mainly due to significant increase of biospheric productivity from July to d CASA biospheric fluxes.

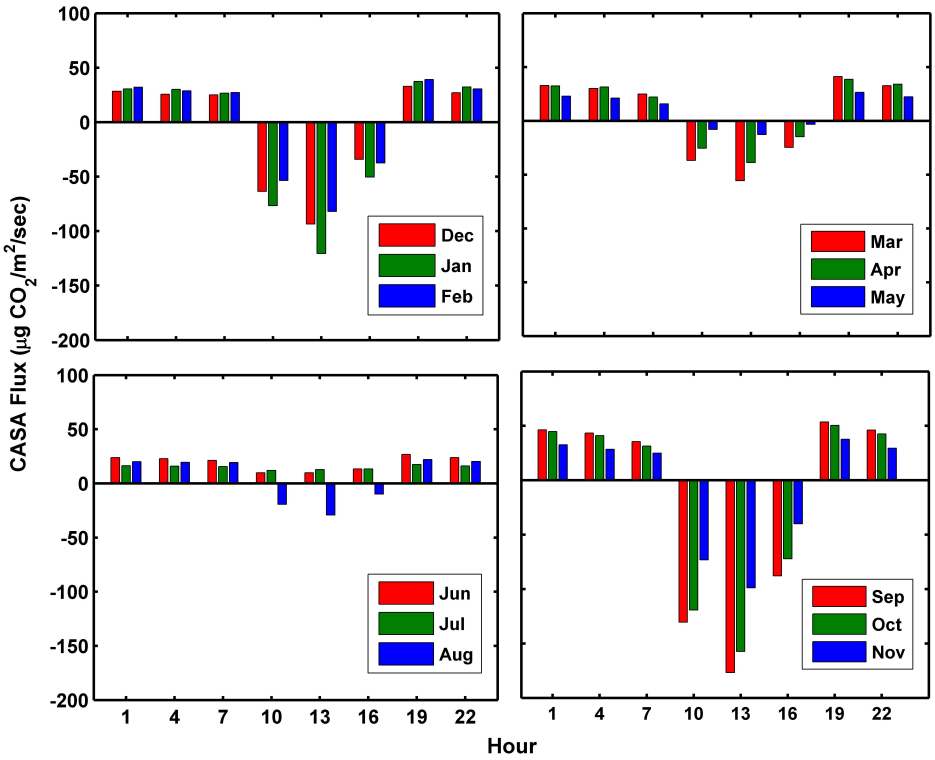

Figure 3.6: Diurnal variation of the biospheric flux from the CASA ecosystem model, averaged for the year of 2014 during all the four seasons.

Near surface diurnal amplitude of CO_2 has been documented in humid sub-tropical Indian station Dehradun (30.3°N, 78.0°E, 435 m a.s.l) and a dry tropical Indian station Gadanki (13.5°N, 79.2°E, 360 m a.s.l) [46]. In comparison to Ahmedabad, both these stations show distinct seasonal change in the diurnal amplitude of CO_2. The maximum CO_2 diurnal amplitude of about 69 ppm is observed during the summer season at Dehradun, whereas maximum of about 50 ppm during autumn at Gadanki.

3.5.2 Diel cycle of CO

Figure 3.7a shows seasonally averaged diurnal variation of CO. In general, the mean diurnal cycles of CO during all the seasons show lower mixing ratios during noon (1200-1700 hrs) and two peaks, one in the morning (0800-1000 hrs) and other in the evening (2000-2200 hrs). This cycle exhibits the same pattern as the

mean diurnal cycle of traffic flow, with maxima in the morning and at the end of the afternoon, which suggests the influence of traffic emissions on CO measurements. Along with the traffic flow, PBL dynamics also plays a critical role in governing the diurnal cycle of CO. The amplitudes of the evening peaks in diurnal cycles of CO are always greater than the morning peaks. It is because the PBL height evolve side by side with the morning rush hours traffic and hence increased dilution while during evening hours PBL height decrease along with evening time rush hours traffic and favors accumulation of pollutants until the late evening under the stable PBL conditions. The noon time minima is mostly associated with the dilution by the higher boundary layer hight. The controll of the chemical loss of CO by OH radicals can be neglected on its diurnal cycle due to higher lifetime of CO ranging from 1 to 3 months. The peaks during morning and evening rush hours, minima during afternoon hours in CO diurnal cycle during all the seasons are similar as in CO_2. However, there are a few noticeable differences in the diurnal cycles of both the gases. The first noticeable difference is that the CO morning peak appears later than CO_2 peak. This is because as discussed earlier with sunrise time, PBL height starts evolve and same time photosynthesis process also get started and hence CO_2 morning peak depends on the sunshine time. But in case of CO, timing of the morning peak mostly depends on the rush hour traffic and is consistent at $0800 - 1000$ hrs in all seasons. The second noticeable difference is the afternoon mixing ratios of CO show little seasonal spread as compared to the afternoon mixing ratios of CO_2. Again, this is due to the biospheric control on the mixing ratio of CO_2 during the afternoon hours of different seasons while CO levels are mainly controlled by the dilution during these afternoon hours. The third noticeable difference is that the levels of CO decrease very fast after evening rush hour in all seasons while this feature is not observed in case of CO_2 since respiration during night hours contributes to the levels of CO_2. The average morning ($0800 - 0900$ hrs) peak values of CO are observed minimum (0.18 ± 0.10 ppm) in summer and maximum (0.72 ± 0.16 ppm) in winter while its evening peak shows minimum value (0.34 ± 0.14 ppm) in summer and maximum (1.60 ± 0.74 ppm) in autumn. The changes in CO mixing

ratios show large fluctuations from morning peak to afternoon minima and from afternoon minima to evening peak. From early morning maxima to noon minima, the changes in CO mixing ratios are found in the range of 20 - 200% while from noon minima to late evening maxima the changes in CO mixing ratios are found in the range of 85% to 680%. Similar diurnal variations with two peaks have also been observed in earlier measurements of CO as well as NOx at this site [128].

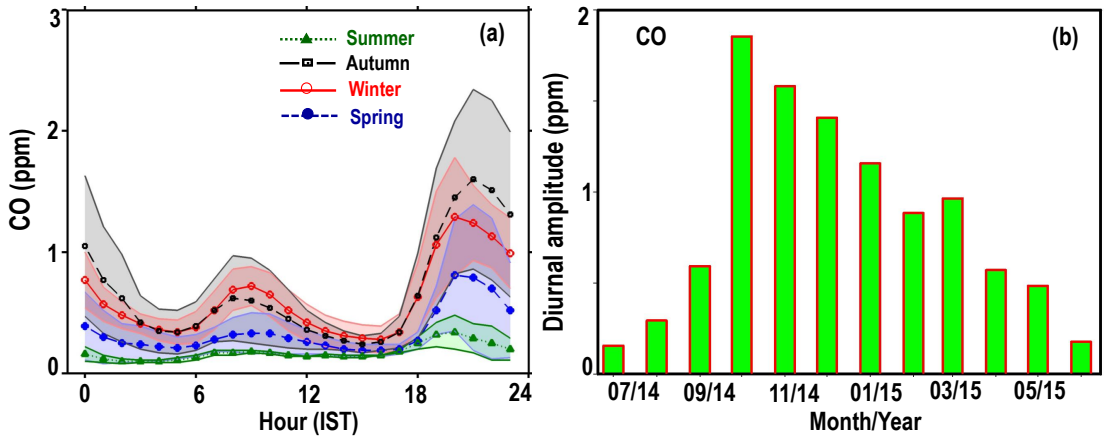

Figure 3.7: (a) Average diurnal variation of CO over Ahmedabad during all the four seasons. (b) Monthly variation of the diurnal amplitude of CO.

The evening peak contributes significantly to the diurnal amplitude of CO. The largest amplitude in CO cycle is observed in autumn (1.36 ppm) while smallest amplitude is observed in summer (0.24 ppm). The diurnal amplitudes of CO are observed to be about 1.01 and 0.62 ppm, respectively, during winter and spring. The monthly diurnal cycle of CO (Figure 3.7b) shows minimum (0.156 ppm) amplitude in July and maximum (1.85 ppm) in October. After October the diurnal amplitude keep on decreasing till summer. The evening peak contributes significantly to the diurnal amplitude of CO. The largest amplitude in CO cycle is observed in autumn (1.36 ppm) while smallest amplitude is observed in summer (0.24 ppm). The diurnal amplitudes of CO are observed to be about 1.01 and 0.62 ppm, respectively, during winter and spring. The monthly diurnal cycle of CO (Figure 3.7b) shows minimum (0.156 ppm) amplitude in July and maximum

(1.85 ppm) in October. After October the diurnal amplitude keep on decreasing till summer.

3.6 Correlation between CO and CO_2

The relationships of CO to CO_2 can be useful for investigating the CO source types and their combustion characteristics in the city region of Ahmedabad. For correlations study, in principle the baseline levels to be removed from the measured mixing ratios. Although, the most ideal case of determining the background levels are the continuous measurement of respective gases at a cleaner site. But due to unavailability of measurements at cleaner sites, we use the 5^{th} percentile value of CO_2 and CO for each day as a background for corresponding day. The excess CO_2 ($CO_{2(exc)}$) and CO ($CO_{(exc)}$) above the background for Ahmedabad city, are determined for each day after subtracting the background mixing ratios from the hours of each day ($CO_{2(exc)}$ = $CO_{2(obs)}$ - $CO_{2(bg)}$, $CO_{(exc)}$ = $CO_{(obs)}$ - $CO_{(bg)}$).

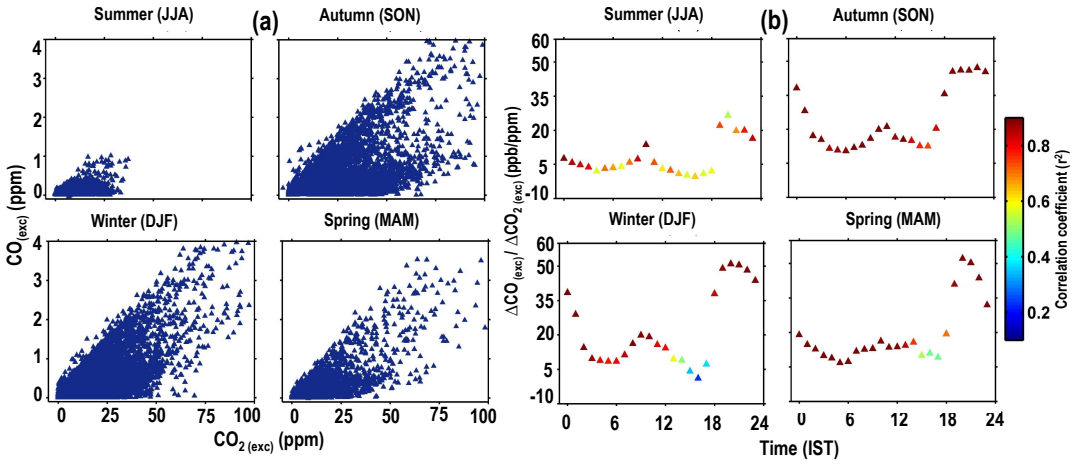

Figure 3.8: (a) Correlation of excess CO above background ($CO_{(exc)}$) with the excess CO_2 above background ($CO_{2(exc)}$) during all the four seasons using 30 minutes averaged data. (b) The diurnal variation of the $\Delta CO_{(exc)}/\Delta CO_{2(exc)}$ slopes during all the four seasons. The colour bar in this plot shows the correlation coefficient (r^2) for corresponding time.

We use robust regression method for the correlation study. It is an alternative to least squares regression method and more applicable for analysing time series data with outliers arising from extreme events (http://www.ats.ucla.edu/stat/ stata /dae/rreg.htm). Figure 3.8a illustrates the correlations between $CO_{(exc)}$ and $CO_{2(exc)}$ for the four seasons. The impact of the possible sources of CO and CO_2 varies from month to month and hence season to season. The lowest correlation ($r^2 = 0.39,\ p = 0.0001$) is observed during summer, with a $\Delta CO_{(exc)}/\Delta CO_{2(exc)}$ ratio of 0.6 $\pm$ 0.1 ppb/ppm. Lowest correlation suggest that different mechanisms control the levels of CO and CO_2 during the summer season. As discussed previously, higher biospheric productivity during this season mostly controls the CO_2 mixing ratios while CO mixing ratios are mostly controlled by the long range transport and higher loss due to OH. Highest correlation ($r^2 = 0.76,\ p < 0.0001$) with $\Delta CO_{(exc)}/\Delta CO_{2(exc)}$ ratio of 8.4 $\pm$ 0.2 ppb/ppm is observed during spring season. As seen previously that the diurnal cycle of CO_2 is not significantly removed by the biosphere during spring with lower draw down in daily CO_2. Along with this, higher VC during this season will result in very fast mixing. Therefore, very fast mixing will mostly regulate their relative variation and hence, will results higher correlation in this season. Other factors like soil and plant respiration during this period may also control CO_2 mixing ratios due to which the correlation coefficient is not equal to 1. The ratio of $\Delta CO_{(exc)}/\Delta CO_{2(exc)}$ is estimated to be 8.5 $\pm$ 0.15 ppb/ppm ($r^2 = 0.52$) and 12.7 $\pm$ 0.2 ppb/ppm ($r^2 = 0.55$) in autumn and winter, respectively. Relatively higher ratios during winter than other three seasons indicates contribution of CO emission from additional biofuel burning sources. The winter time ratio is similar to the airmass influenced by both fossil fuel and biofuel emissions as discussed by [48] over PON. Using CARIBIC observations, [129] also reported the $\Delta CO/\Delta CO_2$ ratio in the range of $15.6 - 29.3$ ppb/ppm from the airmass influenced by both biofuel and fossil fuel burning in the Indo-Chinese Peninsula. Further, $\Delta CO/\Delta CO_2$ ratio is also observed of about 13 ppb/ppm in South-east Asian outflow in February-April, 2001 during the TRACE-P campaign and suggest the combined influence of fossil fuel and biofuel burning [130]. The narrow range of the ratios from autumn to spring

(8.4 - 12.7 ppb/ppm) suggests that the dominance of common and local emission sources during these seasons, and this range is correspond to the range of anthropogenic combustion sources (10-15 ppb/ppm) in developed countries [131–133].

Table 3.1: Emission ratios of CO/CO_2 (ppb/ppm), derived from emission factors (gases emitted (in grams) per kilogram of fuel burned).

Biomass burning	Transport		Industry	Domestic	
Crop-residue[a,b,c]	Diesel[d,e,f]	Gasoline[d,f]	Coal	Coal[d,f]	Biofuel[c,d]
45.7 – 123.6	8.6 – 65.2	33.5	23.5 – 40.4	53.3 – 62.2	52.9 – 98.5

[a] [134]; [b] [135]; [c] [65]; [d] [136]; [e] [137]; [f] [138]

The $\Delta CO_{(exc)}/\Delta CO_{2(exc)}$ slope and their correlation may depend on the time of the day due to the variation in different controlling factors on their levels. Hence, we computed the diurnal cycle of $\Delta CO_{(exc)}/\Delta CO_{2(exc)}$ slope for all the seasons by binning the data for both hour and month (3 month × 24 hrs) as shown in Figure 3.8b. The colours indicate the correlation coefficients (r^2) for respective hour. These ratios do not reflect the diurnally varying PBL height, but rather the diurnally varying mix of fossil fuels and biogenic sources. The $\Delta CO_{(exc)}/\Delta CO_{2(exc)}$ slopes show very distinctive diurnal variation, being higher ($30 - 50$ ppb/ppm) in the evening rush hours with very good correlation ($r^2 > 0.85$) and lower ($5 - 20$ ppb/ppm) in the afternoon hours with lower correlation ($r^2 = 0.5-0.6$) during all the four seasons. Negative and lower slopes in afternoon hours during summer season indicate the higher biospheric productivity during this period. The slopes and their correlations are fairly comparable for all the four seasons in the evening rush hours which indicate stronger influence of common emission sources. Slopes during this time can be considered as fresh emissions since dilution and chemical loss of CO can be considered negligible for this time. These observed ratios are much lower than ratios related to domestic sources but are similar transport sector mostly dominated from gasoline combustion (Table 3.1). Except summer, the overall ratios in all four seasons were found in the range of 10-25 ppb/ppm during the daytime and 10-50 ppb/ppm during nighttime.

3.7 Top-down CO emissions from observations

If the emissions of CO_2 are known for study locations, the emissions of CO can be estimated by multiplying the correlation slopes and molecular mass mixing ratios [62, 66]. Final emissions of CO will depend on choosing the values of correlation slopes. The slopes should not be biased from particular local sources, chemical processing and PBL dynamics. We exclude summer data as the CO_2 variations mainly depend on the biospheric productivity during this season. As discussed previously, the morning and evening rush hours data are appropriate for tracking vehicular emissions, while the afternoon data are affected by other environmental factors, e.g., the PBL dynamics, biospheric activity and chemical process. The stable, shallow nighttime PBL accumulates emissions since the evening and hence the correlation slope for this period can be used as a signature of the city's emissions. Hence, we calculate the slopes from the data corresponding to the period of $2300 - 0500$ hrs. Additionally, slopes for morning hours ($0600 - 1000$ hrs), afternoon hours ($1100 - 1700$ hrs), and night hours ($1800 - 0600$ hrs) are also used for estimating the CO emissions to study the difference in the estimation of CO emissions due to choice of different times for slopes. The CO emission (E_{CO}) for Ahmedabad is calculated using the following formula,

$$E_{CO} = \left(\alpha_{CO} \frac{M_{CO}}{M_{CO_2}} \right) E_{CO_2}, \tag{3.1}$$

Where, α_{CO} is the correlation slope of $CO_{(exc)}$:$CO_{2(exc)}$ in ppb/ppm, M_{CO} is the molecular mass of CO in g/mol, M_{CO_2} is the molecular mass of CO_2 in g/mol and E_{CO_2} is the CO_2 emission in Gigagram (Gg) over Ahmedabad. The Emission Database for Global Atmospheric Research (EDGAR) version 4.2 emission inventory reported an annual emissions of CO_2 at $0.1° \times 0.1°$ for the period of $2000 - 2008$ (http://edgar.jrc.ec.europa.eu/overview.php). It reported an annual CO_2 emission of 6231.6 Gg CO_2 year^{-1} by EDGARv4.2 inventory over the box $72.3° <$ longitude $< 72.7°$E, $22.8° <$ latitude $< 23.2°$N) which contain Ahmedabad coordinates in the center of the box. We assume that the emissions of CO_2 are linearly changing with time and using increasing rate of emission from 2005 to 2008, we extrapolate the emission of CO_2 for 2014 over same area. The bottom-

up CO_2 emission for the Ahmedabad is thus estimated of about 8368.6 Gg for the year of 2014. Further, for comparing the estimated emission with inventory emissions we extrapolated the CO emissions also for the year of 2014 using same method applied as for CO_2. We assumed the same slopes for the year of 2008 and calculate CO emission for that year also. The slope values for different time period, estimated and inventory emissions of CO using different values of slope are given in Table 3.2.

Table 3.2: Estimates of the CO emission for the year of 2014 using the CO_2 emission from EDGARv4.2 emission inventory (http://edgar.jrc.ec.europa.eu/overview.php) over the box (22.8° < latitude < 23.2°N, 72.3° < longitude < 72.7°E) and $CO_{(exc)}$:$CO_{2(exc)}$ slopes observed from different time periods dataset. The correlation coefficient for corresponding slopes are given inside the bracket in slope column. Monsoon data are not included for calculating slopes.

Time (IST)	Slope (ppb/ppm) Correlation coefficient (r^2)	EDGAR Emissions (Gg)		Estimated Emissions (Gg)
		CO_2	CO	
2300 - 0500 hrs	13 ± 0.14 (0.71)	8368.6	45.3	69.2 ± 0.7
0600 - 1000 hrs	11.4 ± 0.19 (0.56)			60.7 ± 1.0
1100 - 1600 hrs	14.9 ± 0.19 (0.61)			79.3 ± 1.0
1800 - 0500 hrs	34.6 ± 0.37 (0.58)			184.2 ± 1.9
Full day (24 hr)	10.8 ± 0.09 (0.53)			57.5 ± 0.5

The correlation between $CO_{(exc)}$ and $CO_{2(exc)}$ for the period of $2300-0500$ hrs is very tight and slope for this period can be considered for estimating the fossil fuel CO emissions for Ahmedabad. Using this slope and based on CO_2 emissions from EDGAR inventory, the estimated fossil fuel emission for CO is observed 69.2 ± 0.7 Gg for the year of 2014. The EDGAR inventory underestimates the emission of CO as they give the estimate about 45.3 Gg extrapolated for 2014.

The slope corresponding to the night hours (1800 – 0600 hrs) give the highest estimate of CO. Using all combinations of slopes, the derived CO emissions are always higher than the bottom-up EDGAR emission inventory.

3.8 Diurnal tracking of CO_2 emissions

CO has virtually no natural sources in an urban environments except oxidation of hydrocarbons. As we discussed earlier that incomplete combustion of fossil fuels is the main sources of CO in urban environments and therefore can be used as a surrogate tracers to attribute CO_2 enhancements to fossil fuel combustion on shorter timescale. Several studies have demonstrated that the ratio of the excess mixing ratios of CO and CO_2 in background mixing ratios can be used to determine the fraction of CO_2 from fossil fuels and validated this method using carbon isotope ($\Delta^{14}CO_2$) measurements [52, 60, 63, 139, 140]. This quantification technique is more practical, less expensive and less time consuming in comparison to the $^{14}CO_2$ method [141]. For performing this analysis, the background mixing ratios of CO and CO_2 and the emission ratio of CO/CO_2 from anthropogenic emissions are required. The methods for calculating the background mixing ratios of CO_2 and CO are already discussed in Section 3.6.

Figure 3.9a shows the excess diurnal variations of CO_2 above the background levels during different seasons. As discussed in the previous section, the vehicular emissions are major emission sources over the study locations. For calculating the emission ratio of CO/CO_2 from the vehicular emissions, we used the evening time (1900-2100 hrs) mixing ratios of $CO_{2(exc)}$ and $CO_{(exc)}$ for whole study period since correlation for this period is very high. The other reason for choosing this time is that there is insignificant contribution of biospheric in CO_2 and no chemical loss of CO. We assume that negligible influence of other sources (open biomass burning, oxidation of hydrocarbons) during this period. The emission ratio for this time is calculated to about 47 ± 0.27 ppb CO/ppm CO_2 with very high correlation (r^2 = 0.90) (Figure 3.9b) after excluding those data points, corresponding for

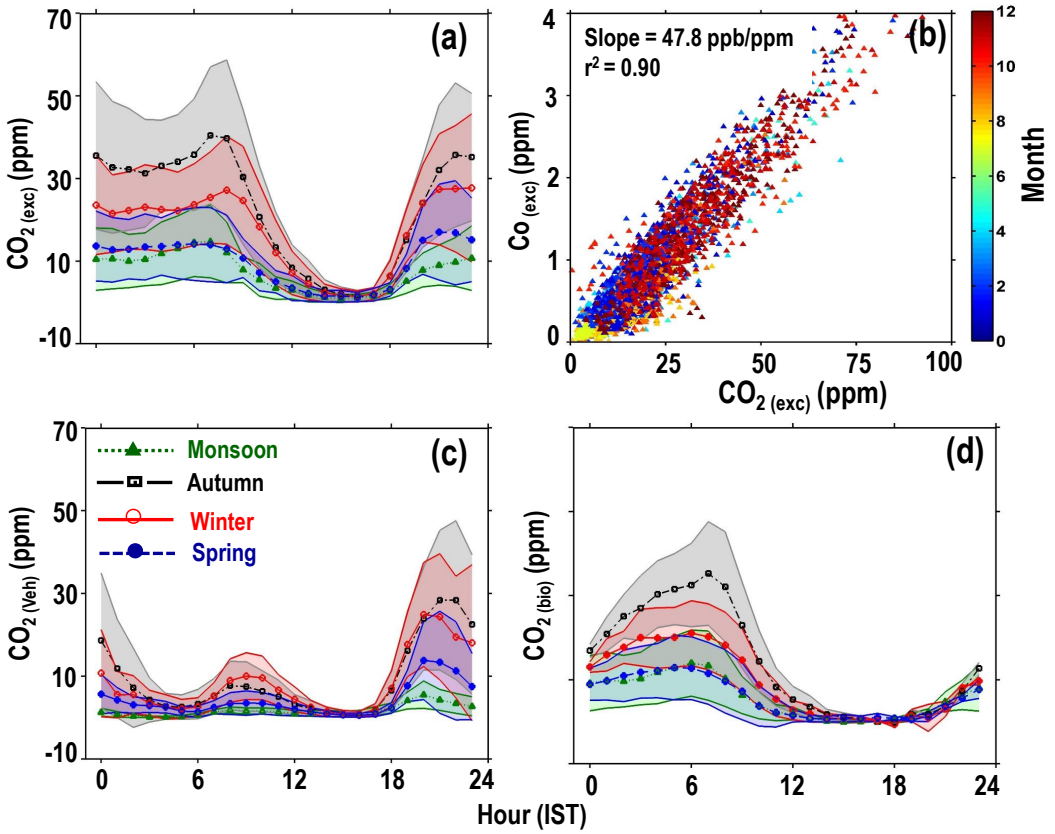

Figure 3.9: (a) Diurnal cycle of excess CO_2 over background levels during all the four seasons. (b) Correlation between excess CO and CO_2 for evening hours (1800-2100 hrs) during the study period. Contributions of fossil fuel (c) and biosphere (d) in the diurnal variation of excess CO_2 in all the four seasons.

which the mean wind speed is greater than 3 ms^{-1} for avoiding the effect of fast ventilation and transport from other sources. The tight correlation imply that there is not a substantial difference in the emission ratio of these gases during the measurement period from November, 2013 to June, 2015. $CO_{2(exc)}$ and $CO_{(exc)}$ will be poorly correlated with each other if their emission ratio varies largely with time, assuming the correlation is mainly driven by emissions. Since this ratio is mostly dominated by the transport sector, this analysis will give mainly the fraction of CO_2 from the emissions of transport sector. We define it as $R_{CO/CO_{2(Veh)}}$. The standard deviation, which is very small, shows the uncertainty associated with slope. The contribution of transport sector ($CO_{2(Veh)}$) in the diurnal cycle of CO_2 is calculated using following formula.

$$CO_{2(Veh)} = \frac{CO_{(obs)} - CO_{(bg)}}{R_{CO/CO_{2(Veh)}}} \tag{3.2}$$

where $CO_{(obs)}$ is the observed CO mixing ratio and $CO_{(bg)}$ is the background mixing ratio of CO. Uncertainty in the $CO_{2(Veh)}$ is dominated by the uncertainty in the $R_{CO/CO_{2(Veh)}}$ and by the choice of $CO_{(bg)}$. The uncertainty in $CO_{2(Veh)}$ due to the uncertainty in the $R_{CO/CO_{2(Veh)}}$ is about 0.5% or 0.27 ppm and can be considered negligible. As discussed in Section 2.3.1, the uncertainty in the measurements of $CO_{(bg)}$ is very small and also can be considered negligible. Further, the contributions of CO_2 from other major sources are calculated by subtracting the $CO_{2(Veh)}$ from the excess mixing ratios of CO_2. These sources are those sources which do not emit significant amount of CO and can be considered mostly as natural sources (respiration), denoted by $CO_{2(bio)}$.

The average diurnal cycles of CO_2 above its background for each seasons are shown in (Figure 3.9a). The diurnal pattern of $CO_{2(Veh)}$ (Figure 3.9c) reflects the pattern like CO, because we are using constant $R_{CO/CO_{2(Veh)}}$ for all seasons. Overall, this analysis suggests that the anthropogenic emissions of CO_2 from transport sectors during early morning from 0600 to 1000 hrs varied from 15 to 60% (4-15 ppm). During afternoon hrs (1100 – 1700 hrs), the vehicular emitted CO_2 varied from 20 to 70% (1 – 11 ppm) and during evening rush hours (1800-2200 hrs), it varies from 50 to 95% (2-44 ppm). During night/early morning hours (0000-0700 hrs) respiration contributes from 8 to 41 ppm of CO_2 (Figure 3.9d). The highest contributions from 18 to 41 ppm are observed in the autumn from the respiration sources during night hours, since there is more biomass during this season after the South Asian summer monsoon. During afternoon hours, lower biospheric component of CO_2 could be due to a combination of the effects of afternoon anthropogenic emissions, biospheric uptake of CO_2 and higher PBL height.

3.9 Model - Observations comparison of CO_2

In this section, we compared the CO_2 observations with the ACTM model simulated CO_2. The model descriptions has been discussed in Chapter 2. The comparison results are discussed in following sections.

3.9.1 Diel cycle comparision

We first evaluate the ACTM in simulating the mean diurnal cycle of CO_2 over Ahmedabad by comparing model simulated surface layer mean diurnal cycle of CO_2. The atmospheric mixing ratios of CO_2 are calculated by adding the anthropogenic component, oceanic component, biospheric component from CASA process model. Figure 3.10a and Figure 3.10b show the residuals (hourly mean - daily mean) of diurnal cycles of CO_2 based on the observations and model simulations, respectively.

The model shows very little diurnal amplitude as compared to observational diurnal amplitude. Larger differences and discrepancies in night time and morning CO_2 mixing ratios between the model and observations might be contributed by diurnal cycle of the anthropogenic fluxes from local emissions and biospheric fluxes, and uncertainties in the estimation of PBL height by the model. Hence, there is a need for efforts in improving the regional anthropogenic emissions as well as module for estimating the PBL height. It may be pointed out that the model's horizontal resolution ($1.125^\circ \times 1.125^\circ$) is coarse for analysing local scale observations. However, the model is able to capture the trend of the diurnal amplitude, highest in autumn and lowest in summer. Figure 10c shows better agreement ($r^2 = 0.56$) between the monthly change in modelled and observational diurnal amplitude of CO_2 from monthly mean diurnal cycle however, the slope ($m = 0.17$) is very poor. We include the diurnal amplitudes of CO_2 for November and December, 2013 also for improving the total number of data points. The model captured the spread in the day time mixing ratio of CO_2 from summer to spring with a difference that model shows lower mixing ratio of CO_2 during

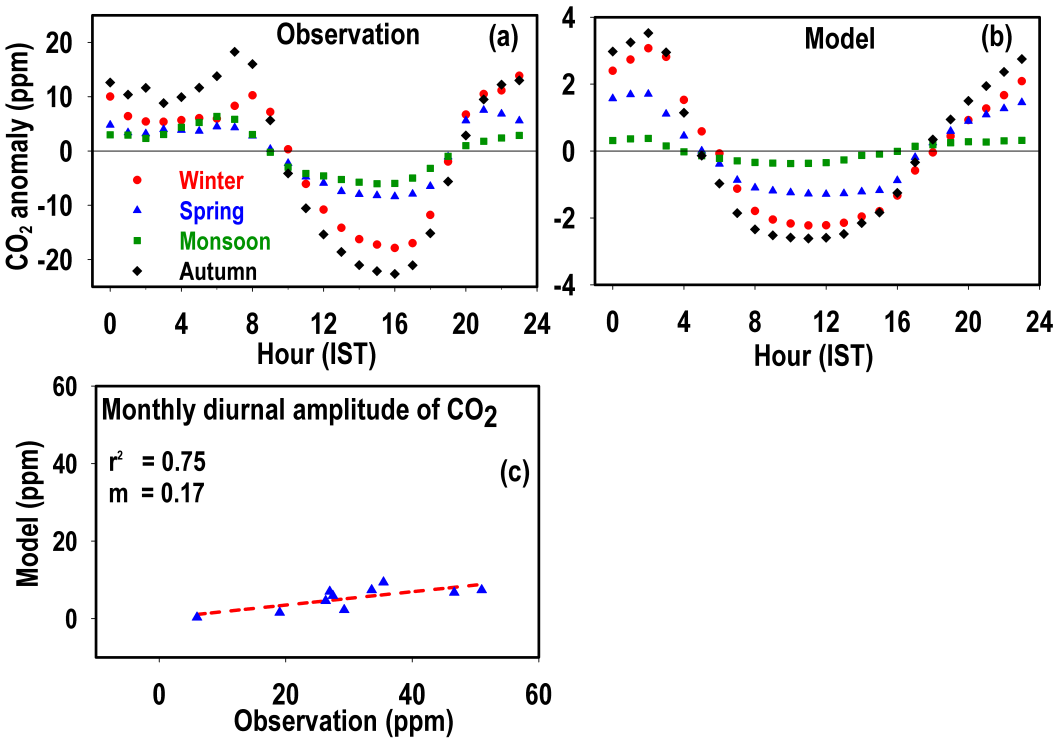

Figure 3.10: Anomaly of the diurnal cycle of CO_2 (in ppm) for (a) observations and (b) modal simulation over Ahmedabad in all the four seasons. Please note that the scales of model and observational diurnal cycles are different. (c) Correlation between observed and model simulated monthly mean diurnal cycle amplitudes.

noon hours in autumn while observations show lowest in summer. Most of the atmospheric CO_2 uptake occur following the Southwest monsoon season during July-September [57] and as a consequences we observe the lowest CO_2 mixing ratio during the from the measurements during this season. But the model is not able to capture this feature since CASA biospheric flux (Figure 3.6) shows highest productivity in autumn and hence lowest mixing ratios of CO_2 in autumn during daytime. This also suggest that there is a need for improving the biospheric flux for this region. It is to be noted that CASA model used a land use map corresponding the late 1980s and early 1990s, which should be replaced by rapid growth in urbanised area in Ahmedabad (area and population increased by 91% and 42%, respectively, between 1990 and 2011). The model resolutions may be another factor for discrepancy. As shown by Ballav et.al. [142], a regional model WRF-CO_2 is able to capture both diurnal and synoptic variations at two closely

spaced stations within 25 km. Hence, the regional models could be helpful for capturing these variabilities.

3.9.2 Seasonal cycle comparison

Figure 3.11a shows the performance of ACTM simulating mean seasonal cycle of CO_2 over Ahmedabad by comparing model simulated mean surface seasonal cycle of CO_2. As discussed previously, the data is not available for the period of March - June, 2014. For visualizing the compleate seasonal cycle of CO_2, we include the monthly mean mixing ratios of CO_2 of the year of 2015, in place of data gap period. The seasonal cycles are calculated after subtracting the annual mean from each month, and corrected for growth rate using the observations at MLO (using same de-trending method discussed in Section 3.4). For comparison, we used the seasonal cycle calculated from afternoon time average monthly mixing ratios, since model is not able to capture the local fluctuations and produce better agreements when boundary layer is well mixed. In Table 3.3 we present the summary of the comparisons of model and observations. The model reproduces the observed seasonal cycle in CO_2 fairly well but with low seasonal amplitude about 4.15 ppm compared to 13.6 ppm observed. Positive bias during summer depicts the underestimation of biospheric productivity by CASA model. The highest root mean square error is observed to be 3.21% during summer. For understanding the role of biosphere, we also compared the seasonal cycle of CO_2 from noon time mean data with the seasonal cycle of CO_2 fluxes over South Asia region which is taken from the [57] where they calculated it using a inverse model with including CARIBIC data and shifted a sink of 1.5 PgC yr^{-1} sink from July to August and termed it as "TDI64/CARIBIC-modified". Positive and negative values of flux show the net release and net sink by the land biosphere over the South Asia. This comparison shows almost one to one correlation in the monthly variation of CO_2 and suggest that the lower levels of CO_2 during July, August and higher level in April are mostly due to the moderate source and sink of South Asian ecosystem during these months, respectively. Significant correlation ($r = 0.88$) between South Asian CO_2 fluxes and monthly mean CO_2 data for day time only

suggest that the day time levels of CO_2 are mostly controlled by the seasonal cycle of biosphere (Figure 3.11b).

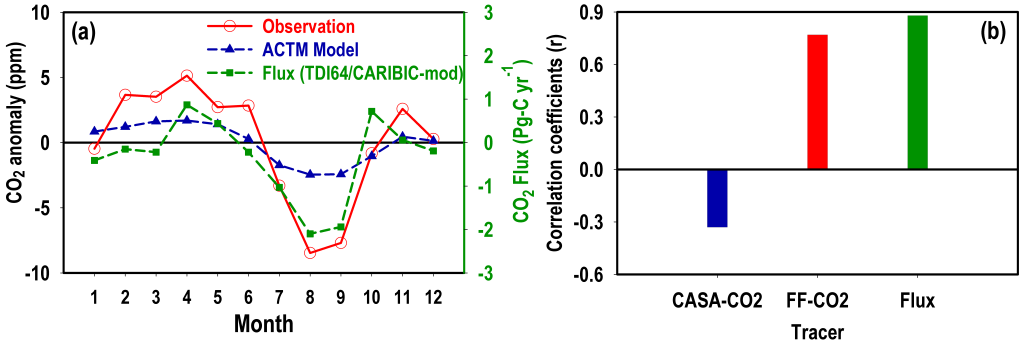

Figure 3.11: (a) The red circles and blue triangles show the mean seasonal cycles of CO_2 (in ppm) using afternoon values only, calculated from measurements and the model over Ahmedabad. The green rectangles show the seasonal cycles of CO_2 flux over South Asia, calculated from TDI64/CARIBIC-modified inverse model as given in [57]. (b) Blue bar and red bar show the correlation coefficient (r) of model CO_2 mixing ratio of biospheric tracer and fossil fuel tracer component with observed mixing ratios of CO_2 taking the entire annual time series of daily mean data, respectively. The green bar shows the correlation coefficient between the monthly residuals of afternoon mean only and the CO_2 flux over South Asia.

Separate correlation between individual tracers of model and observed data has been studied to investigate the relative contribution of individual tracer component in the CO_2 variation (Figure 3.11b). We did not include the oceanic tracer and observed CO_2 correlation result, since no correlation has been observed between them. The comparison is based on daily mean of entire time series. Correlation between biospheric tracers and observed CO_2 have been found negative. This is because during growing season biospheric sources act as a net sink for CO_2. Correlation of observed CO_2 with fossil fuel tracer has been observed fairly well ($r = 0.75$). Hence, individual tracers correlation study also give the evidence of the overall dominance of fossil flux in overall mixing ratios of CO_2 over Ahmedabad for entire study period, and by assuming fossil fuel CO_2 emission we can derive meaningful information on biospheric uptake cycle.

Table 3.3: Model performance metrics used to quantify the level of agreement between model simulations and observations. These statistics are based on hourly values in each day.

Parameter	Winter	Autumn	Monsoon	Annual
MB (ppm)	−2.72	12.64	−2.45	2.27
FGE (%)	0.96	3.12	2.0	1.76
RMSE (ppm)	5.21	12.82	9.14	8.60
RMSE (%)	1.27	3.21	2.20	2.09

This study suggests that the model is able to capture seasonal cycle with lower amplitude for Ahmedabad. However, the model fails to capture the diurnal variability since local transport and hourly daily flux play important roles for governing the diurnal cycle and hence there is a need for improving these features of the model.

3.10 Highlights

We report simultaneous in-situ measurements of CO_2 and CO mixing ratios in the ambient air at Ahmedabad, a semiarid urban region in western India using laser based CRDS technique during November, 2013 - June, 2015 with a gap from March, 2014 to June, 2014. The observations show the range of CO_2 mixing ratios from 382 to 609 ppm and CO mixing ratios from 0.07 to 8.8 ppm, with the average of CO_2 and CO to be 416 ± 19 ppm and 0.61 ± 0.6 ppm, respectively. The highest mixing ratios of both the gases are recorded for lower ventilation and for winds from north-east direction, representing CO_2 and CO transported from anthropogenic sources. The lowest mixing ratios of both the gases are observed for higher ventilation and for the south-west direction, where air travels from the Indian Ocean. Along with these factors, the biospheric seasonal cycle (photosynthesis outweighs respiration during growing season and reverse during fall season) also controls the seasonal cycle of CO_2. The lowest day time CO_2

mixing ratios ranging from 382 to 393 ppm in August, suggest for the stronger biospheric productivity during this month over the study region, in agreement with an earlier inverse modelling study. This is in contrast to the terrestrial flux simulated by the CASA ecosystem model, showing highest productivity in September and October months. Hence, the seasonal cycles of both the gases reflect the seasonal variations of natural sources/sinks, anthropogenic emissions and seasonally varying atmospheric transport. The annual amplitudes of CO_2 variation after subtracting the growth rate based on the Mauna Loa, Hawaii data are observed to be about 26.07 ppm using monthly mean of all the data and 13.6 ppm using monthly mean of the afternoon period (1200-1600 hrs) data only. Significant difference between these amplitudes suggests that the annual amplitude from afternoon monthly mean data only does not give true picture of the variability. It is also to be noted that most of the CO_2 measurements in India are based on day time flask samplings only.

Significant differences in the diurnal patterns of CO_2 and CO are also observed, even though both the gases have major common emission sources and effects of PBL dynamics and advection. Differences in their diurnal variability is probably the effect of terrestrial biosphere on CO_2 and chemical loss of CO due to reaction with OH radicals. The morning and evening peaks of CO are affected by rush hours traffic and PBL height variability and occur almost same time throughout the year. However, the morning peaks in CO_2 changes its time slightly due to shift in photosynthesis activity according to change in Sun rise time during different seasons. The amplitudes of annual average diurnal cycles of CO_2 and CO are observed about 25 and 0.48 ppm, respectively (Table 3.4). Both gases show highest amplitude in autumn and lowest in summer.

The availability of simultaneous and continuous measurements of CO_2 and CO have made it possible to study their correlations during different times of the day and during different seasons. The minimum value of slope and correlation coefficient of 0.8 ± 0.2 ppb/ppm and 0.62, respectively are observed in summer. During other three seasons, the slopes vary in narrow range (Table 3.4) and in-

Table 3.4: Summary of results for the study period. The "exc" refer to the excess mixing ratios of CO_2 and CO after subtracting the background mixing ratios.

Period	Mean (ppm)		Diurnal amplitude (ppm)		Correlation $CO_{(exc)}$:$CO_{2(exc)}$	
	CO_2	CO	CO_2	CO	Slope (ppb/ppm)	Correlation coefficient (r^2)
Monsoon	400.3 ± 6.8	0.19 ± 0.13	12.4	0.24	0.6 ± 0.1	0.39
Autumn	419.6 ± 22.8	0.72 ± 0.71	40.9	1.36	8.5 ± 0.2	0.52
Winter	417.2 ± 18.5	0.73 ± 0.68	31.7	1.01	12.7 ± 0.2	0.55
Spring	415.4 ± 14.8	0.41 ± 0.40	15.9	0.62	8.4 ± 0.1	0.76
Annual	413.0 ± 13.7	0.50 ± 0.37	25.0	0.48	8.3 ± 0.7	0.62

dicate about the common emission sources of CO during these seasons. These slopes lie in the range (10 -15 ppb/ppm) of anthropogenic sources in developed countries, e.g., Japan. This suggest that the overall emissions of CO over Ahmedabad are mostly dominated by the anthropogenic (fossil fuel) combustion. These slopes also show significant diurnal variability having lower values (about 5-20 ppb/ppm) during noon hours and higher values (about 30-50 ppb/ppm) during evening rush hours with highest correlation (r>0.9). This diurnal pattern is similar to the traffic density and indicate the strong influence of vehicular emissions in the diurnal pattern of CO. Further, using the slope from the evening rush hours (1800-2200 hrs) data as vehicular emission ratios, the contributions of vehicular emissions and biospheric emissions in the diurnal cycle of CO_2 have been segregated. At rush hours, this analysis suggests that 90-95% of the total emissions of CO_2 are contributed by vehicular emissions. Using the relationship, the CO emission from Ahmedabad has been estimated. In this estimation, fossil fuel derived emission of CO_2 from EDGAR v4.2 inventory is extrapolated linearly from 2008 to 2014 and it is assumed that there are no year-to-year variations in the land biotic and oceanic CO_2 emissions. The estimated annual emission CO for Ahmedabad is estimated to be 69.2 ± 0.7 Gg for the year of 2014. The extrapolated CO emission from EDGAR inventory for 2014 shows a value smaller than this estimate by about 52%.

The observed results of CO_2 are also compared with an atmospheric general circulation model based chemistry transport model simulated CO_2 mixing ratios. The model captures some basic features like the trend of diurnal amplitude, seasonal amplitude etc, qualitatively but not quantitatively. The model captures the seasonal cycle fairly good but the amplitude is very less as compared to the observations. Similarly, performance of the model capturing the change in monthly averaged diurnal amplitude is quite good ($r^2 = 0.56$), however the slope is very poor. We also examined the correlation between the hourly averaged observed CO_2 and tracer of fossil fuel from model simulation and found fairly good correlation between them, which suggests that the overall levels of CO_2 over Ahmedabad are mostly controlled by the fossil fuel combustion throughout the year, while biosphre controlls mostly the day time levels of CO_2.

Chapter 4

Tropospheric distributions of CO_2 and CO

As discussed in the previous chapter, measurements of surface level CO_2 and CO over an urban region are very useful for understanding the nature of their dominant emissions sources and subsequently also helpful for the purpose of mitigation polices. The natural fluxes of CO_2 are about an order of magnitude higher than the anthropogenic ones, they get more or less balanced seasonally while the latter accumulates. Hence, better understanding about the regional biospheric fluxes of CO_2 play a crucial role in predicting the future levels of CO_2 and hence future climate also. However, the regional scale (e.g. sub-continent and country level) fluxes of GHGs are uncertain especially over the South Asian region; i.e., the estimated uncertainty is larger than the value itself [21, 43]. The main reasons for these uncertainties are the limited measurements of CO_2 over these regions. The inverse modelling approach is well known for estimating fluxes of greenhouse gases from the in-situ measurements together with an atmospheric chemistry-transport model (CTM). The consistency of estimated flux depends on the accuracy of observations and ability of CTM to simulate atmospheric processes. Therefore, high quality continuous measurements of GHGs combined with CTM simulations provide a great opportunity to understand the characteristics of regional biospheric fluxes of CO_2. The CTM model running at coarse horizontal resolution (grid size $> 2^\circ \times 2^\circ$) often suffer from under-prediction of the diurnal

and seasonal variations in CO_2 at surface level in a strong source region [67,68]. The free tropospheric distributions of CO_2 contain the information about its regional signature, as against the surface level measurements, which are affected by local emissions. Thus, the vertical profile measurements in the free troposphere are extremely useful for learning about the regional emissions, transport effects and to improve/verify the estimates of regional budgets based on inverse modelling of measurements at surface stations [69].

CO is one of the most important atmospheric pollutants, responsible for the 75% sink of hydroxyl radicals (OH) and thereby affecting the oxidizing capacity of the troposphere as well as contributing to the overall positive radiative forcing (0.23 ± 0.7 Wm^{-2}) by affecting the concentrations of GHGs such as CH_4 and O_3 [35,36]. Being an important precursor of tropospheric O_3, it greatly influences the air quality. The mean atmospheric lifetime of CO varies from a few weeks in lower troposphere to about 3 months in upper troposphere. Due to its long lifetime, it can get transported globally, but does not become evenly mixed in the troposphere. This makes CO an excellent tracer to study the long range transport of pollutants in the atmosphere [143,144]. Therefore vertical measurements of CO will be helpful for constraining the skill of long transport of global chemistry models.

Systematic and accurate vertical profile measurements of CO_2 are not available over India except for the recent measurements over Delhi (also known as New Delhi) by the CONTRAIL (Comprehensive Observation Network for Trace gases by Airline) program. The only other measurements of CO_2 in the troposphere over the Indian region are from the CARIBIC (Civil Aircraft for the Regular Investigation of the Atmosphere Based on Instrument Container) program [55]. While the CARIBIC measurements are based on flask air sampling at the floating altitude of commercial aircrafts, the recent CONTRAIL measurements are continuous covering full flight tracks including ascends and descends. This study presents results of CO_2 measurements based on the CONTRAIL tropospheric

data over Delhi for the years 2007, 2010 and 2011 along with model simulations. We use the 14 years (January, 2001 to December, 2014) MOPITT satellite retrievals for vertical distribution of CO. The details about the measurement and used model configurations for this study have been discussed in Chapter 2.

4.1 Tropospheric distribution of CO_2 over Delhi

The following sections give description and local meteorology of the site, tropospheric distribution of CO_2 over Delhi with a focus on its vertical gradient in different seasons, seasonal cycle at different tropospheric altitudes and finally comparison of the observed features with an atmospheric chemistry model.

4.1.1 Site description

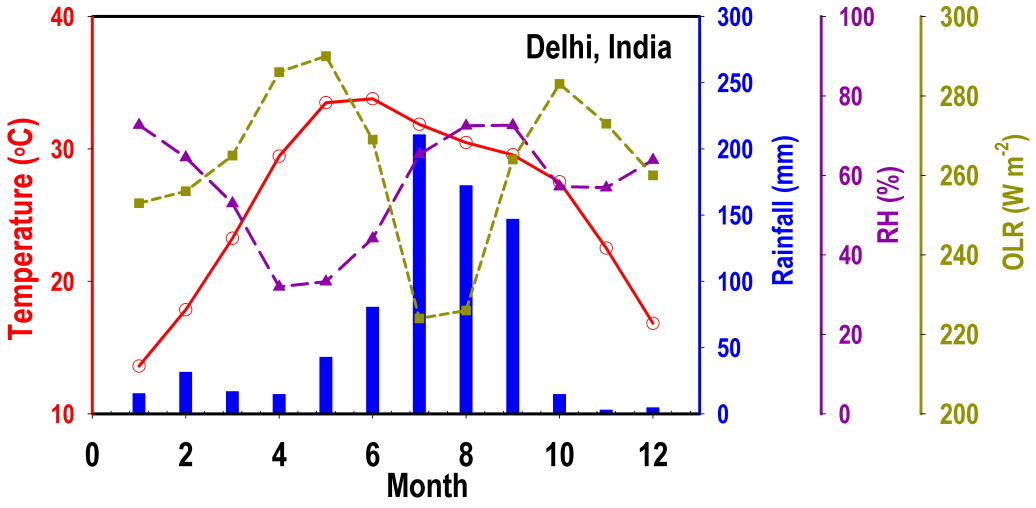

Figure 4.1: The average monthly variation of temperature (red circle), rainfall (blue bar), relative humidity (RH: mergenta triangle) and outgoing longwave radiation (OLR: yellow square) over Delhi based on their monthly climatology (January, 2002 - December, 2011). The temperature and relative humidity data are taken from Wunderground ($http://www.wunderground.com$), rainfall data is taken from Tropical Rainfall Measuring Mission (TRMM) satellite and outgoing longwave radiation (OLR) data is taken from National Centers for Environmental Prediction (NCEP) reanalysis.

Delhi (28.4°N, 77.2°E, 213 m AMSL), the capital of India having population of about 11 million in 2011 ($http://www.census2011.co.in/city.php$), is a major metropolis city in northern India. Large scale industries and three coal power plants are running in Delhi. It shows the typical features of humid subtropical climate, which is characterized by intensely hot summers and cold winters. The rain is brought by the southwest monsoon in the mid of June and continues till the end of September ranging from 80 mm (in June) to 210 mm (in July). The monsoon causes higher RH values (average around $65\% - 72\%$) during this period. The average annual rainfall is approximately 714 mm. The air is driest during April and May (average RH around 32%). Heavy fog during mild winter (starts in late November and peaks in January) is responsible for higher RH ($62\% - 72\%$) during this period (Figure 4.1). The average temperature shows a strong variability (higher value of about 33°C in May-June and lower about 13°C in January) over Delhi. The OLR shows lowest value during monsoon and indicate for the deep convection during this season.

4.1.2 Vertical distribution of CO_2

This section discusses about the seasonally varying tropospheric distributions of CO_2 over Delhi for the years of 2007, 2010 and 2011 using aircraft measurements from the CONTRAIL program and seasonally averaged model simulations. Profile data are available from about 0.7 km height to about 11 km whenever a Japan AirLines aircraft equipped with the CONTRAIL instrumentation comes to Delhi. All data are binned for every 200 m and average CO_2 mixing ratios are calculated. These individual profiles have been used to calculate average profiles for the four seasons, Winter (DJF), Spring (MAM), Summer (JJA) and Autumn (SON) of each year. Data for May and July months are not available for 2007 and 2010 respectively. Similar procedure has been used to calculate season average profiles from the model simulated concentrations at the observation site.

Figure 4.2a-c shows the seasonal-mean vertical profiles of CO_2 over Delhi from

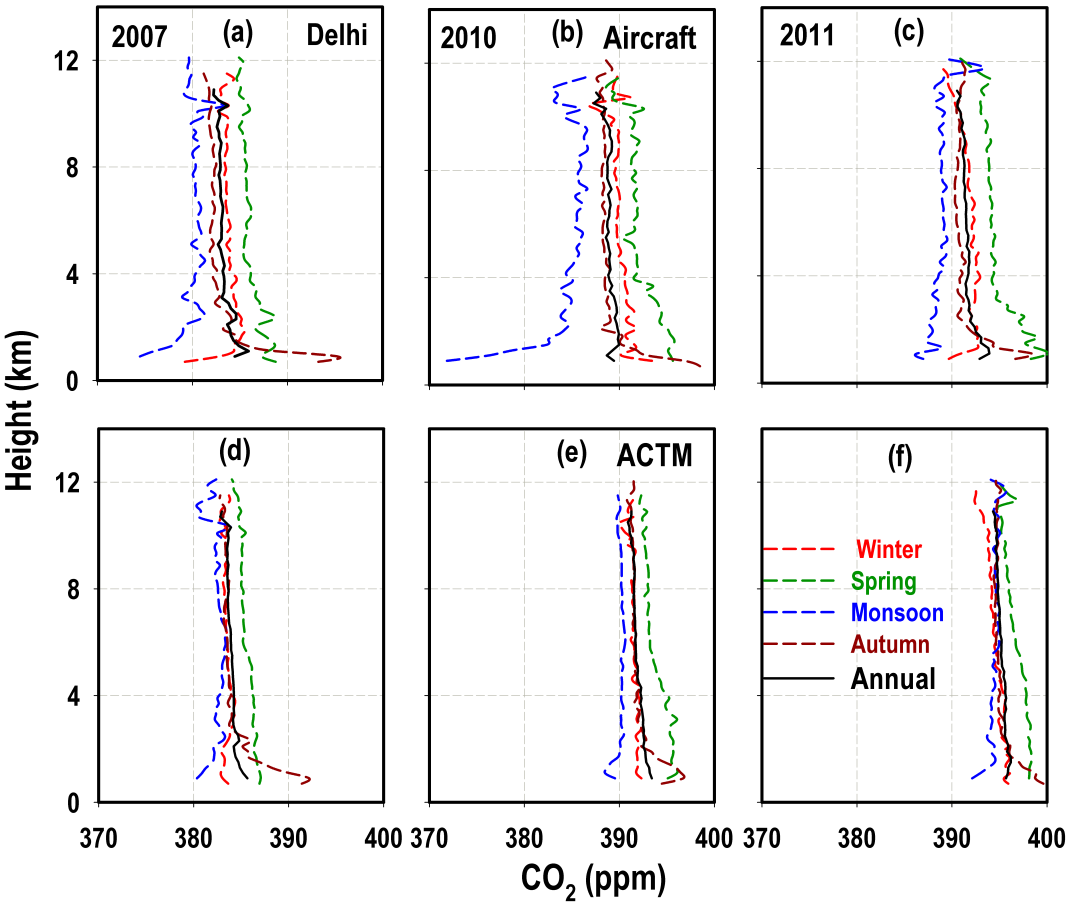

Figure 4.2: Vertical distributions of CO_2 during different seasons over Delhi, India for the years 2007, 2010 and 2011 using aircraft measurements from the CONTRAIL (Comprehensive Observation Network for Trace gases by Airline) program and ACTM simulations.

the CONTRAIL data. The observed profiles show large seasonal variability. Most of the profiles show almost constant vertical profiles in the 2 to 10 km height of the free troposphere. The monsoon season profiles show lowest CO_2 values as compared to other seasons in the troposphere. There is also a sharp increase in CO_2 mixing ratios from the lowest height around 1 km but this increase is slower above about 2 km height. Further, this effect of increase is strong during 2010. Low CO_2 in the lower height (<2 km height) is caused by the effect of strong biospheric productivity during the monsoon period [57] along with the dominance of cleaner air from oceanic region. On the contrary, the autumn profiles show a sharp decrease in CO_2 levels from about 1 to about 2 km height. This could

be due to a shallow boundary layer during this season and the fact that total emissions exceed terrestrial biospheric uptake. This decrease continues till about 8 km but at a slower rate. The free tropospheric values are higher during autumn as compared to the monsoon values for all the three years. These average profiles in the winter season do not show much variability except below about 1 km in the troposphere. CO_2 levels during winter are slightly higher than those in the autumn season in the free troposphere (altitude >2 km). Highest levels of CO_2 are observed at all the altitudes in the spring season as compared to all other seasons in all the three years. This is expected due to dry season and respiration dominating the uptake due to photosynthesis. The mixing ratio of CO_2 also decreases with height but the change is slower as compared to autumn season. It could be due to the higher atmospheric mixing during this period. The CO_2 levels of the average profiles for each year are in between autumn and winter seasons. The model average CO_2 profiles also show similar feature. The observed increase rate of CO_2 over Delhi in the free troposphere is about 2.04 ppm yr^{-1} during this period (2007-2011). This is similar to the increase rate observed at other Indian stations like Hanle: 2.1 ppm yr^{-1} and Pondicherry: 1.7 ppm yr^{-1}; [48]) as well as at Mauna Loa, USA: 2.13 ppm yr^{-1}).

Figure 4.2d-f also shows the ACTM model simulated averaged seasonal profiles of CO_2. The model results are sampled for the day and hour of observation over Delhi. The model profiles for each season for these three years also show similar trend as observed with lowest values in monsoon and highest in the spring season. The model is able to capture higher CO_2 values in the lowest height (<2 km) but it does not capture such sharp change in this height range during monsoon. Also the spread in the free troposphere during all these seasons is much lower than the observations. The index of agreement (r^2) between observed profiles and model simulated profiles shows that the model has good skill in simulating the vertical variations during autumn, winter and spring (r^2 = 0.65 - 0.90) but poor in simulating during monsoon variability (r^2 = 0.45 - 0.50).

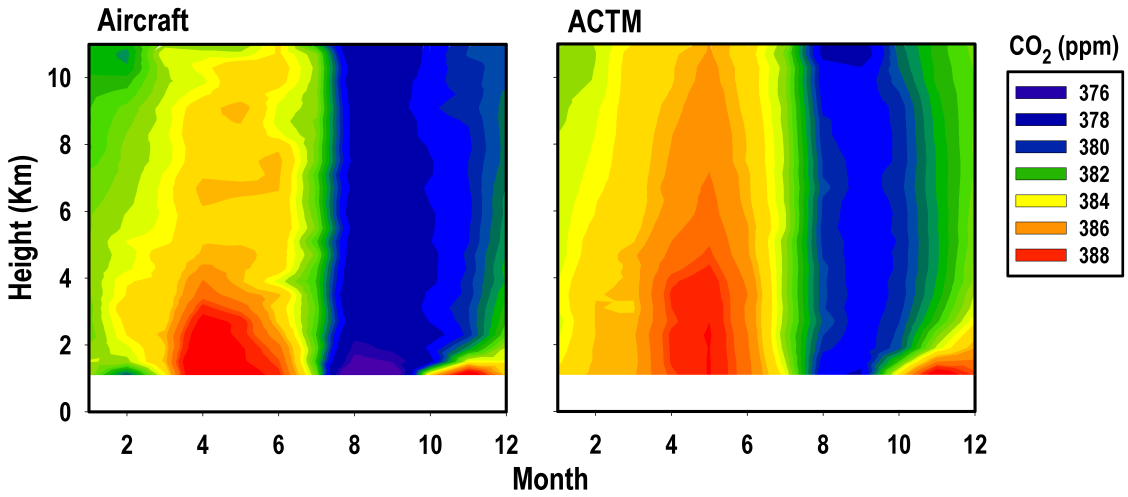

Figure 4.3: The aircraft based and ACTM simulated monthly average distributions of CO_2 from 1 km to 11 km over Delhi, India for the years 2007, 2010 and 2011. The monthly average is calculated after removing the trend for each month data of all the three years.

Variations of CO_2 in the troposphere based on average monthly values at 200 m intervals for all the years of 2007, 2010 and 2011 are shown in Figure 4.3. Before averaging the monthly mixing ratios of CO_2 for the years of 2007, 2010 and 2011, the CO_2 monthly averaged values are detrended by subtracting a global mean growth rate of CO_2 observed at Mauna Loa (MLO), Hawaii, i.e., 2.13 ppm yr^{-1} or 0.177 ppm/month (www.esrl.noaa.gov/gmd/ccgg/trends/) for clearly depicting the seasonal cycle amplitude. This detrending is needed for making complete seasonal cycle from CONTRAIL measurements with data gaps in some of the months of these years. The contour plot shows lower vertical gradient in CO_2 mixing ratios during the spring months (March-May) below 4 km. It indicates higher atmospheric mixing during this season. The model partially captures this feature and shows mixing with a lower decreasing trend throughout the troposphere during this period. From November to February the model shows higher levels above 2 km as compared to the observations. In a nutshell, the ACTM model is able to capture the general features of CO_2 distributions including the vertical propagation of seasonal cycle of CO_2, however the CO_2 concentrations above 2 km altitude are overestimated mostly during winter. In

addition, the model shows higher vertical upward transport during spring and monsoon. These features of ACTM simulations could be due to coarse model resolution ($\sim 2.8 \times 2.8$ deg), and lack of observational data to constrain the surface fluxes by inversion [57].

4.1.3 Seasonal variation of CO_2

The atmospheric CO_2 is taken by plants to conduct photosynthesis. Each year, during the growing phase of terrestrial vegetation, considerable amount of CO_2 is taken up from the atmosphere and it is returned to the atmosphere through the respiration or through the decay of the plants. Hence, the growing and decaying cycle of terrestrial vegetation predominantly creates a seasonal variation in the atmospheric CO_2 concentrations. The oceanic flux component does not show strong seasonal variation compared to the terrestrial biosphere, and the emissions due to fossil fuel burning and cement production are typically aseasonal, particularly in the regions of tropical climate.

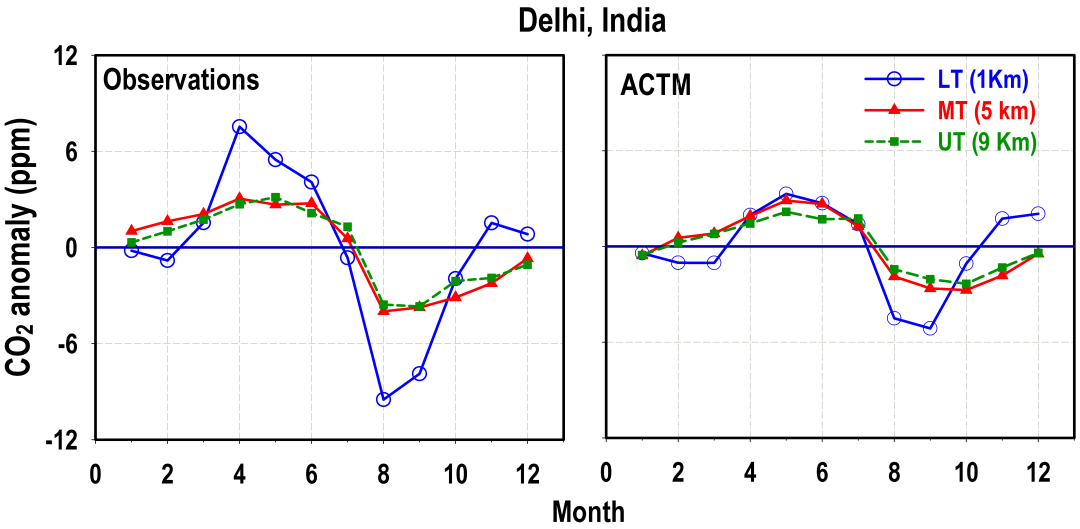

Figure 4.4: The annual variations of CO_2 at different tropospheric heights over Delhi, India average for the years 2007, 2010 and 2011 using aircraft measurements from the CONTRAIL (Comprehensive Observation Network for Trace gases by Airline) program and model simulations.

After averaging the monthly mixing ratios of CO_2, the monthly anomaly has been calculated by subtracting the annual average from monthly mean values. Figure 4.4 shows the averaged seasonal cycle of CO_2 at different tropospheric region (lower troposphere (LT; at 1 km), middle troposphere (MT; at 5 km) and upper troposphere (UT; at 9km)) using the aircraft measurements and model simulations. A strong seasonal variation is observed in CO_2 in the LT height. The CO_2 levels start increasing from February to April, thereafter start decreasing, attains lowest mixing ratios in month of August. After August, again CO_2 levels start increasing. It is mainly due to the seasonal change in the South Asian ecosystem production. It acts as a moderate source of carbon during April-May and weak sink in December-January due to the prolonged dry season combined with a rapid rise in air temperature. From June onwards, arrival of monsoon rainfall causes higher ecosystem production and hence CO_2 levels sharply decreases. In the MT and UT the low levels are observed till the month of October and further higher peak is observed during the period of May-June.

Table 4.1: Modified Normalized Mean Bias (MNMB) of ACTM relative to aircraft observations over Delhi.

Region	MNMB in %			
	Winter	Spring	Monsoon	Autumn
LT $(1-1.5$ km)	0.4	-0.2	1.34	0.1
MT $(1.5-6$ km)	0.3	-0.3	1.0	0.7
UT $(6-10$ km)	0.4	0.3	0.9	0.7

The model is able to capture the seasonal cycle of CO_2 at LT height, but the maxima and minima are shifted by about one month. This discrepancy has been discussed in [57,77] and they attribute this underestimation mostly to uncertainties in the terrestrial biospheric fluxes. The model also largely underestimates the annual amplitude (maximum - minimum). The observation and the model shows annual amplitudes at LT to be 17.0 ppm and 8.3 ppm respectively. It is to be noted that amplitude of decreasing phase of vegetation is higher than the

amplitude of increasing phase. As we move from LT to MT and UT, the annual amplitude decreases significantly but annual cycle remains same except little shift in peak from April to May. At both height regions (MT and UT) seasonal cycles closely match with the model simulated seasonal cycles. Both observations and model show higher correlations at MT and UT heights ($r^2 = 0.86$) as compared to LT height. Table 4.1 shows the statistical parameters for model validation, i.e., modified normalized mean bias (MNMB) of ACTM Model relative to aircraft observations. The MNMB is observed highest during monsoon season at all heights while lowest is observed in winter season. Overall bias is observed lowest and equal in MT and UT height. It reflects that the observations at MT and UT heights are more reliable for validating the coarse resolutions model.

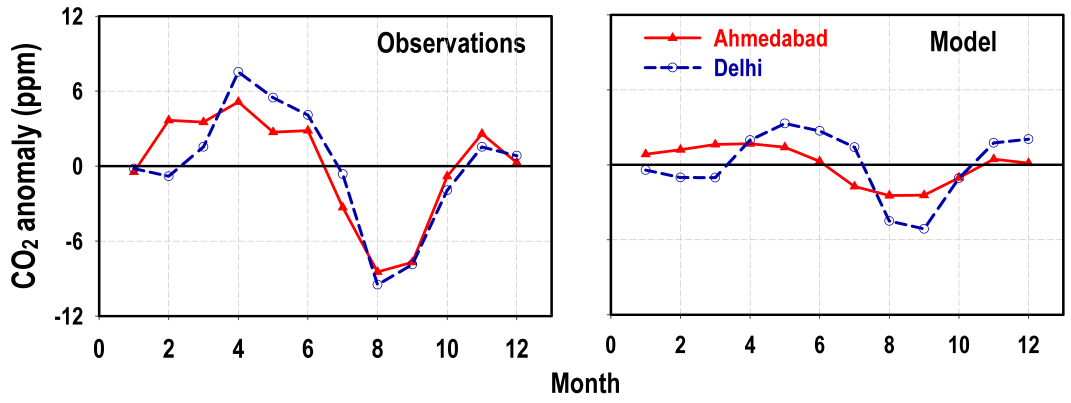

Figure 4.5: The annual variations of CO_2 over Delhi and Ahmedabad from observations and model (ACTM) simulations. The annual cycle over Delhi is calculated using monthly average mixing ratios of CO_2 for the years 2007, 2010 and 2011 after removing the trend from the monthly mean values, while the annual cycle of CO_2 over Ahmedabad is calculated using the afternoon mean mixing ratios of CO_2 for the year of 2014. More details about Ahmedabad seasonal cycle of CO_2 have been discussed in Chapter 3.

Further, we compare the averaged seasonal cycle of CO_2 over Delhi ($\sim$ 1 km) with the seasonal cycle of surface level CO_2 at Ahmedabad (Figure 4.5). Both seasonal cycles almost show one to one correlation; maximum mixing ratios in April and minimum in August. The observed annual amplitude at Delhi about

3 ppm higher than the annual amplitude observed at Ahmedabad. It suggests that the ecosystem around Delhi experiences stronger seasonal climate variation (peak-to-trough temperature, in particular) as compared to the ecosystem around Ahmedabad. Over both locations, ACTM model largely underestimates the seasonal amplitudes as well as shows the discrepancy in capturing higher and lower mixing ratios of CO_2 in its annual cycle.

4.1.4 Effect of rainfall on seasonal distribution of CO_2

It is very well known that soil water and atmospheric CO_2 are two essential components for the growth of vegetation. Therefore, there could be a connection between rainfall which is significant source of water for terrestrial biosphere and atmospheric CO_2 [57]. In this section, we discuss about the link between amount of rainfall and lower tropospheric levels of CO_2 over Delhi.

The southwest monsoon winds, bring significant rainfall during southwest monsoon months from June to September. In order to study the connection between precipitation and CO_2 uptake by plant, we choose two years; 2010 and 2011, since the rainfall amount varies significantly in these two successive years. We choose the annual cycle at 1 km, since this altitude remains always within the boundary layer and hence the annual cycle reflects the effect of local activities. To understand the terrestrial CO_2 sources and sinks, the basic way is to compare or subtract the background concentration either from the free troposphere or from a remote background site [145]. Concentrations higher than background indicate a source and those lower indicate a sink. We take the monthly mean concentration of CO_2 at 8 km altitude as background for 1 km height for corresponding month and subtract CO_2 concentration at 8 km altitude from 1 km altitude for each month. Relation between precipitation and biospheric uptake of atmospheric CO_2 is well reflected in the annual cycle of CO_2 in both the years (Figure 4.6a). During the monsoon month of 2010, the precipitation is observed higher as compared to that in 2011 (Figure 4.6b). Figure 4.6a shows that, in the month of June, 2011 the precipitation was about 150 mm higher than the June

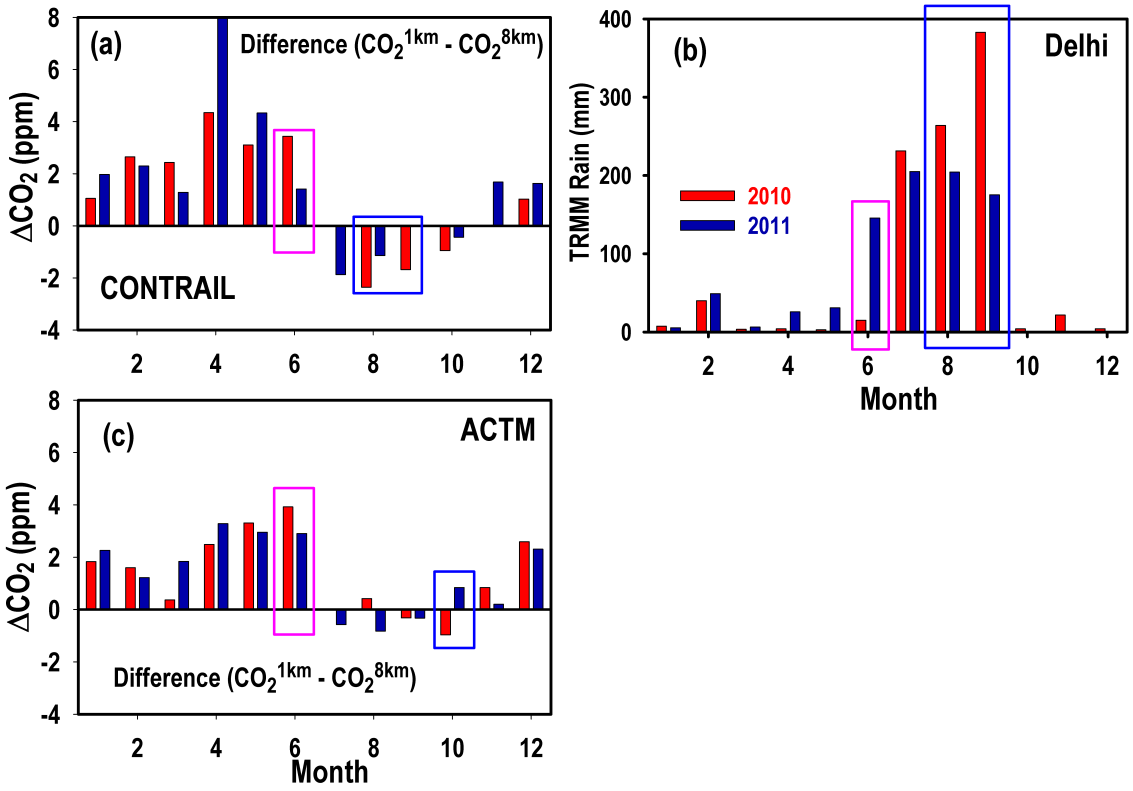

Figure 4.6: (a) Seasonal variation of excess CO_2 concentrations at 1 km altitude for the years of 2010 and 2011 over Delhi. The excess concentrations of CO_2 are calculated at this height by subtracting the monthly concentrations of CO_2 at 8 km altitude. (b) Monthly variation of precipitation over Delhi from the Tropical Rainfall Measuring Mission (TRMM) rainfall data for the years of 2010 and 2011. (c) Seasonal variation of excess CO_2 concentration, simulated from the atmospheric chemistry transport model (ACTM) for 2010 and 2011.

month of 2010 and hence the CO_2 levels are observed about 2 ppm lower due to significant uptake in June of 2011 as compared to CO_2 levels in this month of the year of 2010. Again, significant rain fall during August and September months of 2010 have reduced the CO_2 levels by about 1 ppm and 1.7 ppm respectively as compared to the year of 2011. Thus, the summer monsoon is most important for providing water for vegetation during this season as well as soil moisture for the rest of season. Therefore, the level of precipitation is important for vegetation, agriculture as well as removing the CO_2 from the atmosphere by plants. We also calculate the annual cycle of CO_2 for both the years from ACTM model (Figure

4.6c). The model is not able to capture the effect of rainfall in the uptake of CO_2 for the year of 2010 because the monthly total CASA fluxes did not vary between years. The model-observations agreement depends greatly on the surface fluxes incorporated in the ACTM. Hence, like the previous model-observations comparison over Ahmedabad (in Chapter 3), this comparison also suggests additional improvement of the ecosystem model CASA, which produces a much weaker seasonal cycle.

4.2 Tropospheric distribution of CO

So far we have discussed about the tropospheric distributions of CO_2 over Delhi. Now we will discussed the tropospheric distributions of CO from satellite based measurements over different regions of India including Delhi also. These selected urban regions have very different ecosystems in India.

4.2.1 Sites descriptions and meteorology

Figure 4.7 shows locations of the study regions in the map of India. Table 4.2 shows the grid size used for extracting the CO data from MOPITT retrievals as well as the geographical information and population residing in the major cities inside the grid boxes. We have already discussed about the local meteorology over Delhi in Section 4.1.1. Hence, here we will discuss about the local meteorology over the remaining study regions.

Dibrugarh, a small city located in the northeast part of India, is a rural, continental site. It has a humid subtropical climate with extremely wet summers and relatively dry winters. Ahmedabad, a densely populated (5.5 million), industrialized, metropolitan city located in western India. Large scale industries like textile, automobile etc. are located in and around Ahmedabad. The city has a 400 MW coal fired power plant. Ahmedabad has a hot semi-arid climate. Hyderabad, an urban city in central India, lies in the northern part of the Deccan Plateau. It

Figure 4.7: Study locations for the vertical distributions of CO, marked by circles. This map is taken from the Google.

Table 4.2: Details of major cities inside the latitude and longitude grid box taken for the study. Altitudes of corresponding cities are above mean sea level (AMSL). Population details are taken from the Indian census of 2011 (*http* : *//www.census*2011.*co.in/city.php*)

Locations	Lat,Long (°N,°E)	Lat-span (°N)	Long-span (°E)	Altitude (m, AMSL)	Population (Million)
Delhi	28.4, 77.2	27.5-29.5	76.5-78.5	213	11.07
Dibrugarh	27.5, 95.0	26.5-28.5	93.5-95.5	108	0.13
Ahmedabad	23.0, 72.5	22.5-24.5	71.5-73.5	55	5.5
Hyderabad	17.4, 78.5	16.5-18.5	77.5-79.5	542	6.8
Trivandrum	8.6, 77.0	7.5-9.5	76.5-78.5	10	3.3

is a densely populated (6.8 million in 2011) city and its outskirts are covered by large industrial sectors of metal, paints, tanning and pharmaceuticals. It has a tropical wet and dry climate bordering on a hot semi-arid climate. Trivandrum (also known as Thiruvananthapuram) is a tropical coastal city, located on the west coast of India and bounded by the Arabian Sea to its west and the Western Ghats to its east on the southern tip of the Indian peninsula. The city has a population of around 3.3 million according to the census of 2011. It has a climate

that borders between a tropical savanna climate and a tropical monsoon climate. Hence, it does not experience distinct seasons. Average variability of surface air temperature, relative humidity, rainfall and OLR are shown in Figure 4.8.

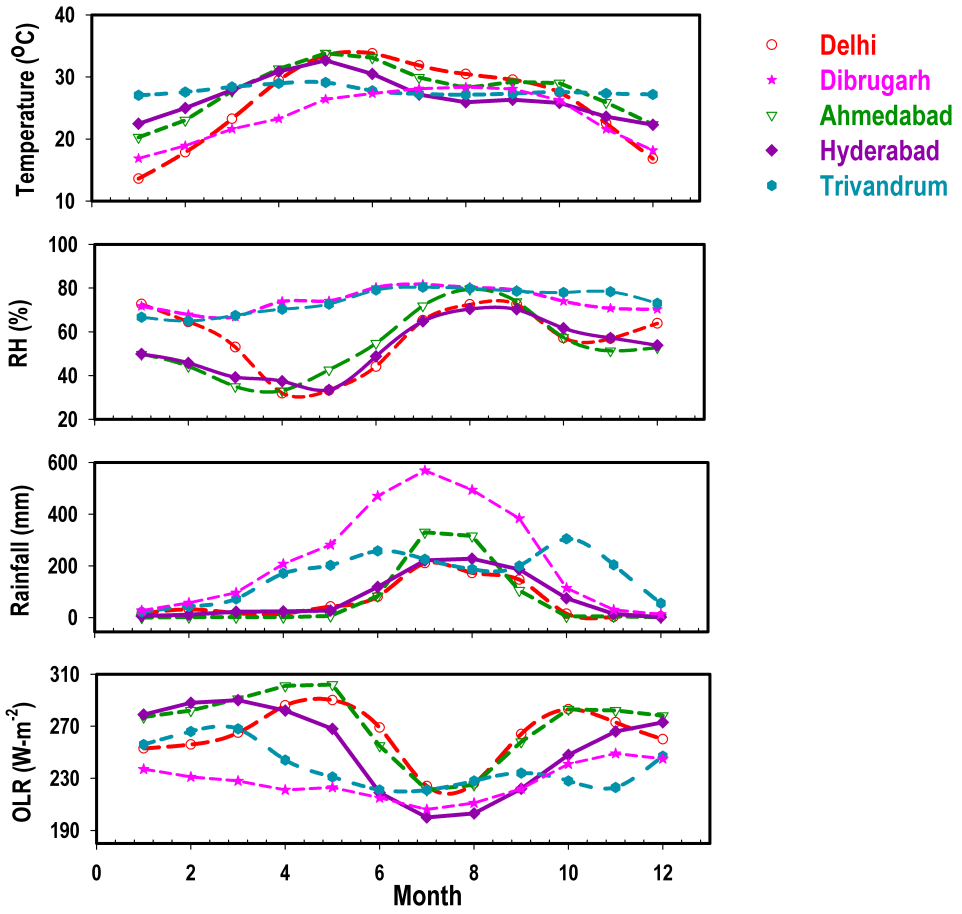

Figure 4.8: Seasonal variations of temperature, rainfall, relative humidity (RH) and OLR, based on their monthly climatology (2002-2011) over CO study regions. The temperature and relative humidity data are taken from "Wunderground" (*http* : *//www.wunderground.com*), rainfall data is taken from Tropical Rainfall Measuring Mission (TRMM) satellite and OLR data is taken from National Centers for Environmental Prediction (NCEP) reanalysis.

4.2.2 Vertical distribution of CO

Average seasonal vertical distributions of CO from 900 hPa to 100 hPa based on all the data from 2001 to 2014 for all the five regions are shown in Figure 4.9. The seasons discussed in this section and further sections are correspond to the

northern hemispheric or boreal seasons. In general, highest CO mixing ratio are observed at 900 hPa in all the seasons except monsoon over most of the regions, due to upward air motion and cleaner marine air. However, the vertical variability is very different from place to place and from season to season. The opposite seasonal cycle mixing ratios of CO at 300-200 hPa during monsoon are observed higher than the mixing ratio at 900 hPa.

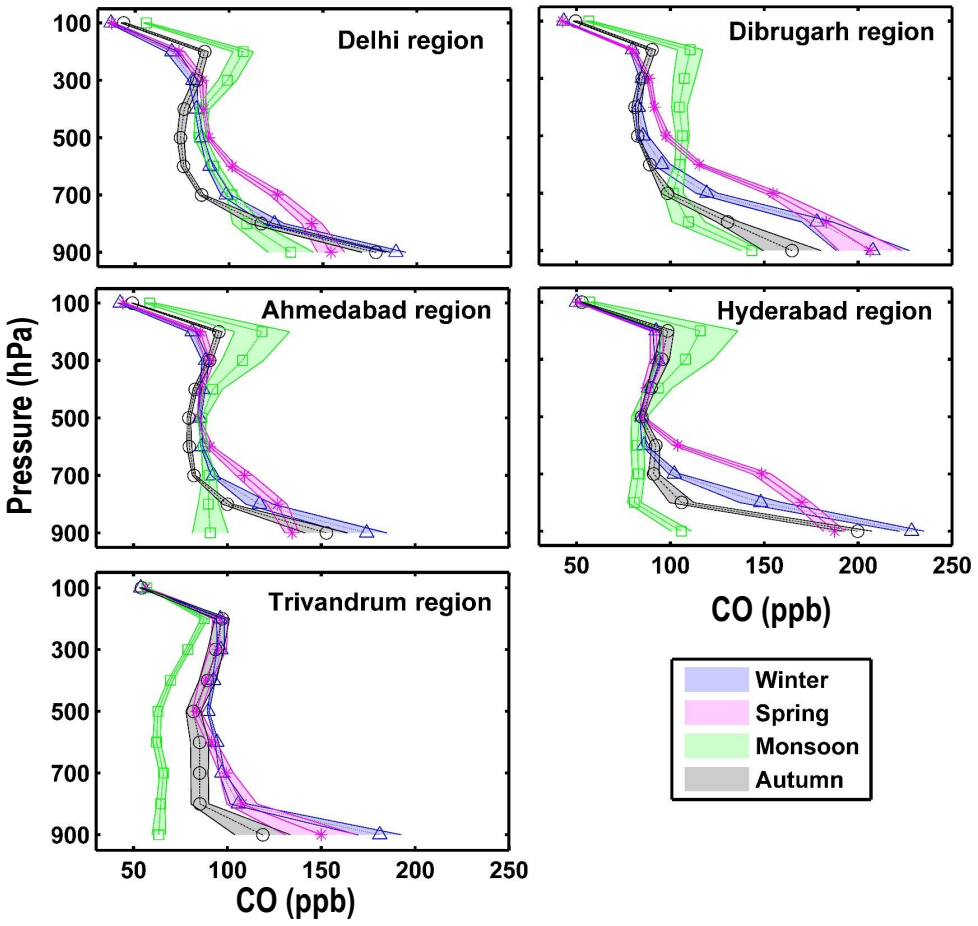

Figure 4.9: The seasonal climatology (2001-2014) of vertical profiles of CO over all the study regions from MOPITT satellite. The blue triangles show the winter (DJF), magenta stars show spring (MAM), green rectangles show monsoon (JJA) and grey circles show the autmn seasons. The CO mixing ratios are given in ppb. The shaded area shows the $\pm$ 1σ standard deviation of corresponding levels.

CO mixing ratios are highest in the winter closely followed during autumn and lowest in the monsoon at 900 hPa over Delhi region. Higher values of CO

during winter are due to shallow planetary boundary layer (PBL). It decreases with height from 900 hPa to 100 hPa during winter and spring, however, we find a decrease in concentrations from 900 hPa to around 500 hPa and an increase at pressures lower than 500 hPa (300-200 hPa) in autumn and monsoon, with the highest values around 200 hPa during monsoon. The vertical gradient is found to be lowest in monsoon as compared to other seasons. It shows comparatively fast mixing over Delhi during this season. CO mixing ratios decrease faster above 200 hPa in all the four seasons. The mixing ratios at 100 hPa have minimum variability (low standard deviation).

CO distribution over Dibrugarh region shows similar variability but the mixing ratios are almost comparable during winter and spring followed by autumn and lowest in the monsoon. Its concentrations in this region are dominated by biomass burning, which is higher in the spring. The shallow boundary layer could be responsible for higher CO during winter. During spring, higher CO levels are observed from surface to 600 hPa in comparison to other seasons which may be due to higher mixing of surface polluted air up to this height due to higher boundary layer height. The monsoon profile corresponds to only one month profile (for 14 year period= mean of $14\times1 = 14$ profiles) due to unavailability of retrieval data and shows almost comparable CO mixing ratio from 800 hPa to 200 hPa. It indicates the uniform and higher mixing due to the deep convection during this season. The mixing ratio in monsoon at 200 hPa is highest compared to other seasons.

Vertical distribution of CO over Ahmedabad region shows similar features as observed over Delhi. Its values at 900 hPa during winter are higher than in other seasons (90 - 152 ppb). One notable change is that, its levels at 300 - 200 hPa are higher than the surface mixing ratio during monsoon. Its profile during monsoon does not show significant decreasing trend (86 to 92 ppb) with height up-to 400 hPa and thereafter it starts increasing and gets peaked (118 ± 14 ppb) at 200 hPa. This indicates that the mixing is stronger, which transports the surface CO

very fast up to higher pressure level. The peak mixing ratio in monsoon at 200 hPa is observed higher than other study regions except Hyderabad. Significant peak in CO at 300-200 hPa is observed during autumn as well. Concentrations of CO over Hyderabad at 900 hPa during winter and autumn are significantly higher than over other study regions. The decreasing slope from 900 hPa to 700 hPa is observed highest during winter in comparison to other seasons. It could be mainly due to shallow boundary layer during this season. It also shows very weak vertical gradient during monsoon from 800 hPa to 400 hPa just like over Ahmedabad. Further, a peak of CO is observed at 200 hPa, which is comparatively higher than the value of CO at 900 hPa during monsoon. In addition to this, the CO profiles also show significant increase at 200 hPa in other three seasons.

Vertical distribution of CO over Trivandrum region shows distinct features as compared to other study regions. The CO profiles show almost negligible vertical gradient from 800 hPa to 500 hPa in all the four seasons, which reflect the dominance of vertical mixing up to this height. Above 500 hPa, the CO mixing ratios start increasing up to 200 hPa in all the four seasons. CO peaks during spring, winter and autumn dominant over the monsoon peak at 200 hPa. It is totally an opposite feature than over other study regions, where monsoon peak dominates over other seasons.

4.2.3 Seasonal Cycle: Amplitude and Inter-annual Variability

The seasonal cycle of CO is governed mainly by three processes: emissions, transport (advection and convection) and chemistry. The nature of seasonal variation is not consistent and vary from station to station and with height. Figure 4.10 shows the climatological mean seasonal variations of CO at 900 hPa and 300 hPa along with climatological mean pseudo CO retrievals by MOZART and EMAC models for the common period of January, 2001 to December 2007. The CO levels around 900 hPa are mostly affected by surface emissions while around 300 hPa,

are mostly affected by transport (convection as well as advection). In order to quantify the average seasonal cycles and inter-annual variability of CO at 900 hPa and 300 hPa, we calculate the metrics of seasonal cycle amplitude (A, root mean square amplitude of the annual cycle), and inter-annual variability (V, RMS of the standard deviations of the 12 months around the annual cycle) at 900 hPa and 300 hPa. These parameters (A, V) are estimated according to the procedure followed by [146].

$$A = \sqrt{\frac{1}{12}\sum_{m}(\xi_m - \bar{\eta})^2}, \tag{4.1}$$

where ξ_m is mean seasonal cycle and $\bar{\eta}$ is the arithmetic mean of ξ_m, which can be defined as

$$\xi_m = \frac{1}{n}\sum_{y}\xi_m^y, \tag{4.2}$$

$$\bar{\eta} = \frac{1}{12}\sum_{m}\xi_m^y. \tag{4.3}$$

The inter-annual variability in seasonal cycle can be represented as RMS of the standard deviations of 12 months in the annual cycle

$$V = \sqrt{\frac{\sum_{m}\sum_{y}(\xi_m^y - \xi_m)^2}{\sum_{m} n_m}}. \tag{4.4}$$

These results are given in Table. 4.3 for the selected pressure levels (900 and 300 hPa). For the purpose of broad classification, [146] defined distinctly seasonal and mostly inter-annual cases as those where $A > 1.5V$ and $V > 1.5A$ respectively.

In general, the mean seasonal cycle of CO shows higher levels in winter months and lower levels in monsoon months at 900 hPa. Higher levels in winter are due to the lower boundary layer height and due to decreased loss with OH radicals [147]. In addition to this, all study regions are mostly influenced by polluted continental

Table 4.3: Seasonal cycle amplitude (A) and inter-annual variability (V) metrics of CO in ppb as discussed in the text for selected pressure levels and for all the regions.

Regions	900 hPa	300 hPa
Delhi	$A = 25 \quad V = 15$	$A = 10 \quad V = 9.8$
Dibrugarh	$A = 26 \quad V = 14$	$A = 8 \quad V = 9$
Ahmedabad	$A = 36 \quad V = 17$	$A = 7 \quad V = 14$
Hyderabad	$A = 49 \quad V = 20$	$A = 10 \quad V = 13$
Trivandrum	$A = 47 \quad V = 13$	$A = 5 \quad V = 12$

air masses during this season. Hence, winter maxima is a combination of chemical, meteorological and transport factors. During summer, prevailing southwest monsoon over study regions, brings the cleaner air masses from the surrounding marine regions. It causes lower CO at 900 hPa during this season over all the study regions. The CO levels over Delhi and Dibrugarh during monsoon months are observed higher as compared to other study regions. This is because Ahmedabad, Hyderabad and Trivandrum regions are nearby the surrounded marine regions and get the cleaner marine air mass, while Delhi and Dibrugarh regions are farthest from marine regions and mostly influenced by marine and continental mixed air mass during monsoon. Trivandrum region exhibits lowest CO levels during monsoon, because south-west monsoon first hits Trivandrum. Dibrugarh shows higher CO mixing ratio during March also in comparison to other study regions. It is mainly caused by the biomass burning over north-east India which is a major controlling factor in the seasonal variation of CO over this region [148, 149]. All study regions show distinct seasonal behaviour at 900 hPa. Hyderabad and Trivandrum show comparable higher seasonal cycle, with root mean square amplitudes of 49.2 and 47.2 ppb respectively at this pressure level.

In contrary to 900 hPa, observations at 300 hPa show higher CO mixing ratios in monsoon months and lower in boreal winter months, over Delhi, Dibrugarh and Ahmedabad (Figure 4.10). Delhi region shows CO peak in the month of July, Dibrugarh and Ahmedabad show in the month of August. Surprisingly, Trivan-

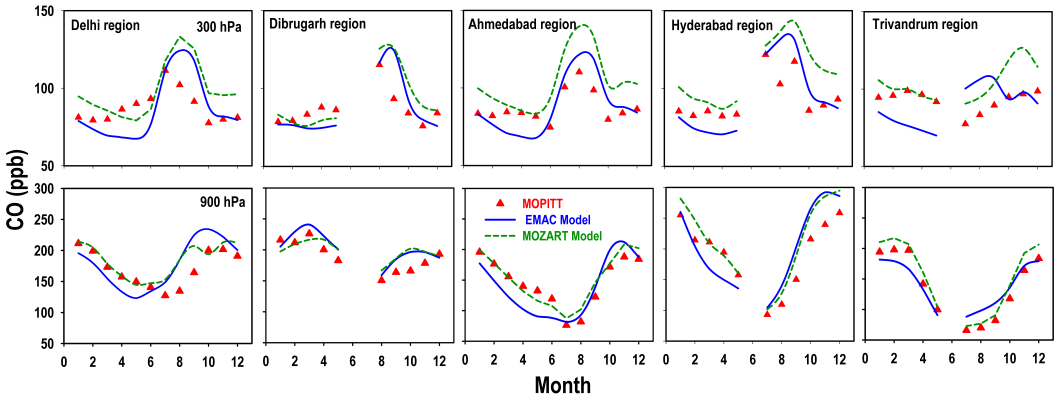

Figure 4.10: Seasonal variations of CO at 900 hPa and 300 hPa from MOPITT satellite, MOZART and EMAC models using 7 years monthly climatology (2001-2007) over all the study regions. The mixing ratios are given in ppb. The annual cycles from both models represent pseudo retrievals, which are obtained using the mixing ratios from both the models and MOPITT averaging kernels and the a-priori profiles. Red triangles show MOPITT CO mixing ratios while green dash lines and solid blue lines correspond to MOZART and EMAC simulated CO respectively.

drum does not show this feature. Hyderabad does not show any clear picture and behaves like a transition region for winds and shows two peaks in the month of July and September. Kar et al., [124] also observed a development of plume of high CO mixing ratios in July over north and east of the Indian subcontinent, which reaches its maximum intensity in August. This plume is associated with the trapping of the convectively uplifted pollutants from the Indian and Chinese regions in the so - called Tibetan anticyclone [150]. Higher levels of CO at upper tropospheric heights during monsoon over the Indian subcontinent have also been discussed in several other studies [58,125,126,151]. During September, the plume moves equator ward to Southeast Asia and subsequently dissipates. The plume mostly covers the Delhi, Dibrugarh, Ahmedabad and Hyderabad regions during its development phase and hence responsible for higher CO levels over these regions during July and August. During the dissipating time, the plume touches Hyderabad region and hence cause for higher levels of CO during September over Hyderabad at 300 hPa [124]. Trivandrum region shows minima in monsoon at 300 hPa, which is a totally different feature than over other regions. Convection

as well as advection due to the long range transport control the seasonal cycle of CO at 300 hPa at most of the study regions and will be discussed in Section reftransport. The seasonal amplitude at this pressure level is found higher over Delhi and Hyderabad region (A = 10 ppb and 9.5 ppb respectively). In contrary to 900 hPa, the annual variability dominates on the seasonal variability at 300 hPa over all of the study regions. Mostly inter-annual behaviour dominates at 300 hPa over Ahmedabad, Hyderabad and Trivandrum.

4.2.4 Long-range transport of CO in the upper troposphere

Figure 4.11 shows contour plot of vertical distributions of CO over all the study regions based on monthly averaged climatology for the period of 2001-2014. As mentioned previously, we averaged only those data points which have daytime DFS values are greater than 1.2 and hence, using this filtering criteria some monthly profiles get removed. In view of this, there are no profiles of CO for May and July over Dibrugarh and for May over Ahmedabad and Hyderabad. This contour plot is slightly different than the contour in Figure 4.14 due to distinct time period. High levels of CO are observed in the 300 - 200 hPa region mostly during Asian summer monsoon over all the regions except Trivandrum. In fact, lower levels of CO are observed at this height range during monsoon over Trivandrum. CO levels are highest (122 ppb) over Delhi in July and over Ahmedabad in August (131 ppb) at 200 hPa. It could be due to the pollutants carried aloft by deep convection activity over India and China and trapped within the anticyclonic wind during the Asian summer monsoon as discussed earlier. Higher levels of CO are also observed over Hyderabad, Trivandrum and partially over Ahmedabad in the height range of 300 -200 hPa during other seasons as well. The rest of the study regions Delhi and Dibrugarh which represent northern and eastern regions of India, do not show this feature. Since there is no direct emission sources of CO except the photochemical production of CO at this height region (300 - 200 hPa), it could be due to transport from some intense source regions of CO.

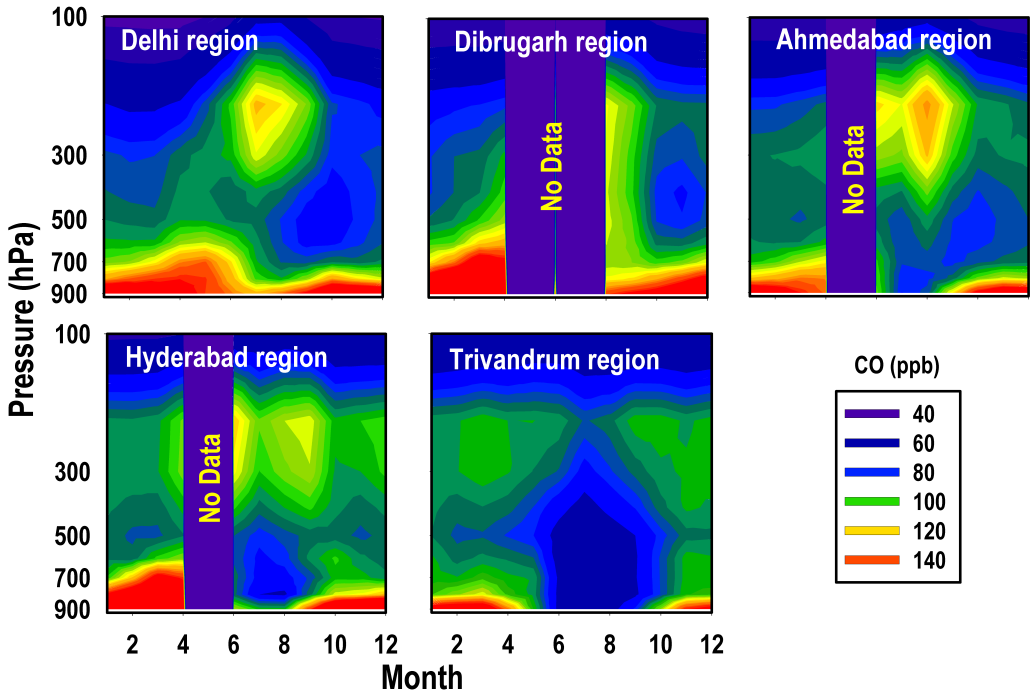

Figure 4.11: CO distribution in the troposphere average for the period of 14 years (2001-2014) of MOPITT monthly climatology over all the study regions. The colours denote the range of CO mixing ratios in ppb.

Further, the 12 year seasonal climatology (January, 2001 - December, 2012) of fire counts detected by the MODIS have been employed (see Figure 4.12a), to investigate the effect of seasonal variations in fires on climatological CO levels. It clearly shows that the widespread burning occurs during winter over Central Africa, northern parts of South America, Thailand and Myanmar. The major fire activities occur in S-SE Asia (India, Thailand, Myanmar, Vietnam etc.) and in Central Africa in spring. During monsoon it shifts towards South Africa and Central South America while during autumn major fire activities occur over Central South America, Central and South Africa and Northern Australia and Indonesia. The biomass burning activities emit huge amounts of CO over these regions during these periods. OLR values are lower (< 240 W m^{-2}) over fire active regions, which indicate about the deep convection during these seasons. The emitted CO from these fire active regions get lifted up rapidly by deep convection process.

Climatology of global distribution of CO at 300 hPa (Figure 4.12b) clearly

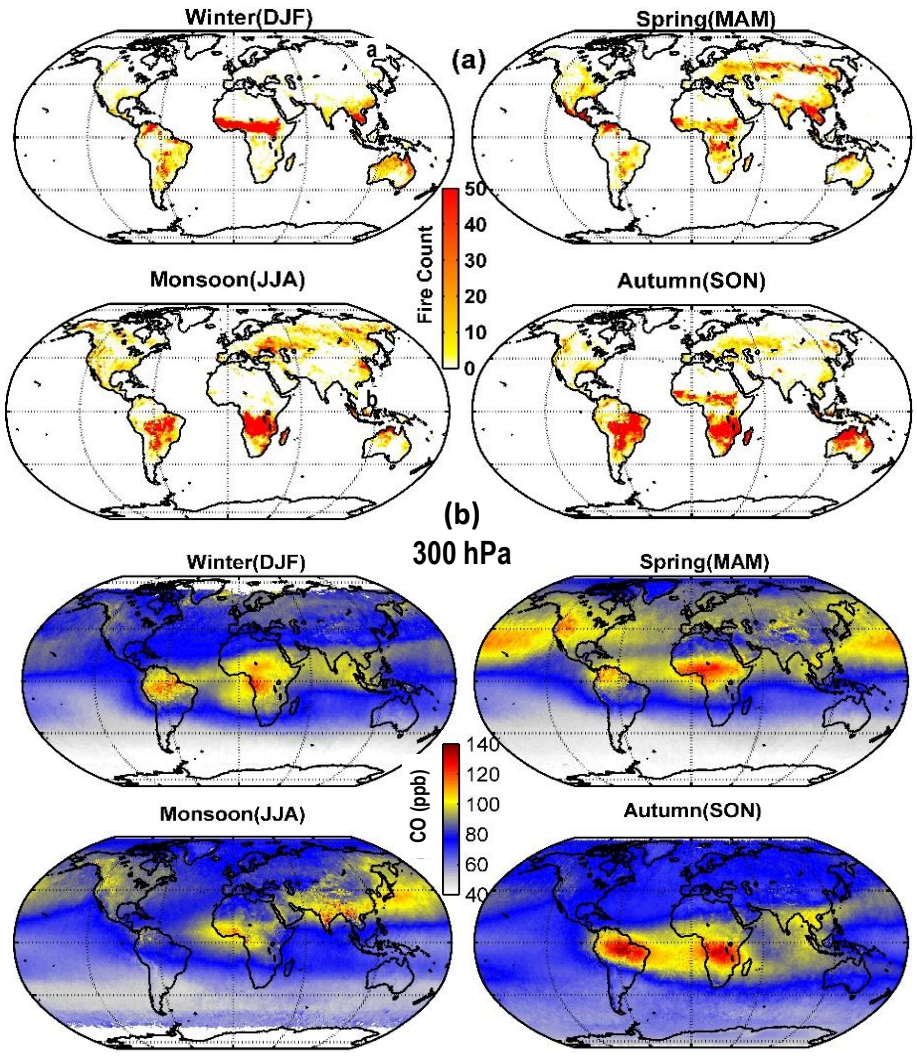

Figure 4.12: (a) The longterm (January, 2001 to December, 2012) seasonal average of fire counts from MODIS satellite. (b) The lower four plots show the 14 years (2001-2014) climatology of MOPITT CO mixing ratios (in ppb) at 300 hPa height for all the four seasons.

shows that most of the major hot spots of CO are those regions where biomass burnings are intense at surface. These plots also confirm the convection over these regions independently. Once the surface CO reaches at 300 hPa, it starts advecting by strong winds at this height. Most of southern parts of India have higher levels of CO at this pressure level in all the seasons (Figure 4.12b).

The 7 day kinematic back trajectories (Figure 4.13) are computed for 10 km ($\sim$ 300 hPa) altitude using the Hybrid Single Particle Lagrangian Integrated

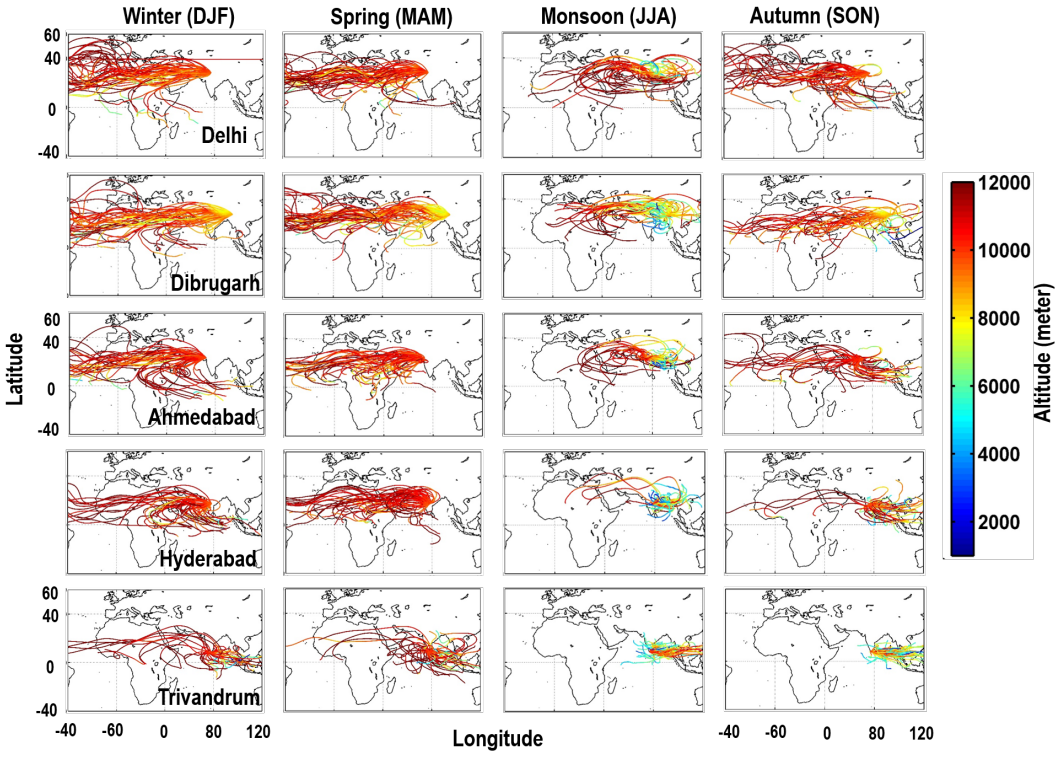

Figure 4.13: The 7 day air mass back trajectories using HYSPLIT model at 10 km altitude (nearer to 300 hPa) over all the study regions during the four seasons. The altitude of these trajectories is shown by the colour bar. The trajectories are calculated corresponding to MOPITT overpass time over equatorial region (1030 GMT = 1600 IST) for alternate days (started from 1st January) for the years of 2002 and 2012 (approx. 365 trajectories over each study region).

Trajectory Model (HYSPLIT) (http://ready.arl.noaa.gov/HYSPLIT.php) for the alternate days of the years of 2002 and 2012. The trajectories are calculated corresponding to the MOPITT overpass time over equatorial region at 1600 IST. The air-mass over all the study regions spend almost 90% time between 9-12 km except monsoon. During monsoon, the trajectories are mostly originating from the lower altitudes. The trajectories over Delhi and Dibrugarh during winter, spring and autumn are coming mostly from the northern parts of Africa which is the desert region. During monsoon these trajectories are confined over the Asian region due to anticyclonic circulations. However, during spring, the back trajectories over Ahmedabad are mostly coming from the central African region bringing higher levels of CO. During autumn part of the trajectories are coming from cen-

tral Africa and part from SE-Asia bringing higher levels of CO over Ahmedabad. The monsoon trajectories are similar to those over Delhi and Dibrugarh regions. Over Hyderabad, back trajectories during winter and spring show mostly their origins from the fire active region of central Africa. Therefore, during these two seasons, the long-range transport of polluted air from these fire active regions could enhance CO levels at 300 hPa over Hyderabad also. On the other hand, the trajectories for the autumn are confined comparatively in a smaller region due to low wind speed and indicate the transport of mixed air from SE-Asia and the Arabian Sea. Although no major fire counts have been observed over SE-Asia during autumn in the range of back trajectories but CO levels are already higher at 300 hPa over Thailand, Myanmar and Indian Oceanic region (Figure 4.12b), mostly due to the vertical transport of CO enriched air mass due to biomass burning over Indonesia [152].

Trivandrum has different wind patterns at 300 hPa than over other regions. Here, mostly the winds are coming from the east direction during all the seasons. The 7 day back trajectories do not have specific direction during winter and spring. As seen in Figure 4.13, these trajectories cover large parts of south India and south-east Asian region including Thailand and Myanmar. Hence, higher levels of CO over Thailand and Myanmar due to fires there, could be responsible for higher levels of CO over Trivandrum during winter and spring. During monsoon and autumn, the trajectories show clearly their origins from the south-east Asian region. However, there are no fire in SE-Asian region in the monsoon. As discussed earlier, higher levels of CO during autumn could be due to fires over the Indonesia region. Along with it, deep convection during autumn over Trivandrum may also contribute to the high CO values at 300 hPa.

4.2.5 Comparison with model simulations

This section presents the comparison of monthly climatology of MOPITT CO with two chemistry-transport models (MOZART and EMAC) simulated CO climatology from January, 2001 to December, 2007. The satellite retrievals cannot

be compared directly with model simulations, since satellite retrieval depends on the a priori information of retrieved gas and relative sensitivity of the retrievals to different pressure levels in the atmosphere. Thus, the modelled profiles are transformed first to the so called âĂIJpseudo-retrievalâĂİ. The MOPITT averaging kernel A_{MOPITT} and the a priori constraint vector P^a_{MOPITT} are applied to the models (MOZART and EMAC) CO profiles P_{MODEL} to obtained the pseudo retrievals of model profiles using the following equation as discussed in [80] and in [117]

$$P^{pr}_{Model} \equiv P^a_{MOPITT} + A_{MOPITT}(P_{MODEL} - P^a_{MOPITT}) \tag{4.5}$$

where P^a_{MOPITT}, A_{MOPITT} and P_{MODEL} represents the MOPITT 'a-priori' profile, averaging kernel matrix and Model simulated CO profiles respectively. In order to make the comparison of seasonal profiles of CO with MOZART and EMAC model simulated CO profiles, we have calculated the modified normalized mean biases (MNMB), in order to take account of asymmetry between the cases of under and over prediction, which is already discussed in Chapter 2. Figure 4.10 shows the seasonal cycle of CO at 900 hPa and 300 hPa from MOPITT observations and model simulations. At 900h hPa, both the models reproduce fairly well seasonal pattern and amplitude of CO over all the study regions. The model simulations are very close to the observations during winter and spring months with a difference that EMAC mostly underestimates (MNMB varies from 5% to 20%) and MOZART mostly overestimates the observations (MNMB varies from -1% to -15%). During monsoon and autumn months, the mixing ratios of CO are overestimated by both the models (MNMB varies from -5% to -35%).

Over Delhi region, both the models show one month lag in the increasing phase of CO seasonal cycle at 900 hPa level. MOPITT CO data show increase after July while models show increase in June. In March, the significant increase in the levels of CO over Dibrugarh region which is due to the impact of extensive biomass burning in eastern Indian region, is captured well by both models simulations. The model's simulated and observed CO are very close to each other

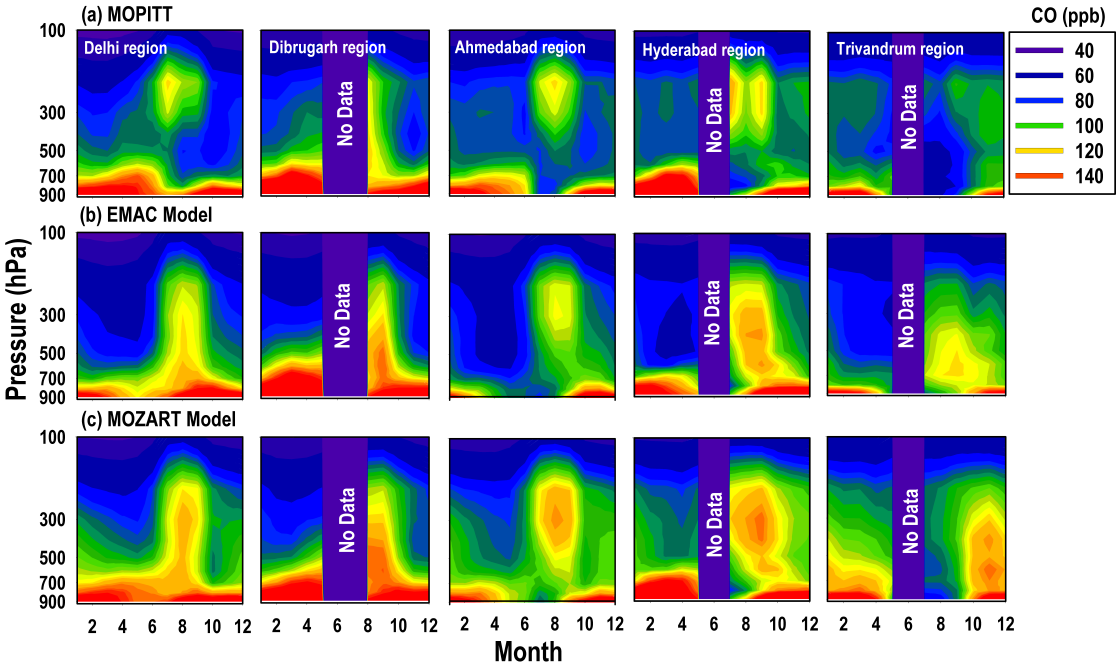

Figure 4.14: Comparison of CO contours from MOPITT satellite, and pseudo retrievals of EMAC and MOZART models using the 7 years monthly climatology (from 2001 to 2007) over all the study regions. The pseudo retrievals are calculated using model simulations and MOPITT averaging kernels and a-priori profiles.

over Ahmedabad and Trivandrum regions. At 300 hPa, the seasonal pattern is again fairly reproduced by both the models over all the study regions except Trivandrum. In this altitude region, the models mostly underestimate (MNMB in the range of 2-30% in different locations) in comparison to lower altitude region. Generally, the models capture the peak during monsoon months quiet well but with a lag of one or two months. Over Trivandrum, the EMAC results show a peak during monsoon months while observations and MOZART do not show any peak during these months. The seasonal pattern by MOZART is captured very well at this height. CO contour plots based on the MOPITT and the pseudo-retrieval profiles from both the models for all the five regions are shown in Figure 4.14. This figure clearly shows that both models reproduce very well monsoon high at 300 hPa altitude region due to the deep convection, while the vertical gradients are partially captured by both models during all seasons. Overall both the models capture significantly the higher levels of CO over Ahmedabad, Hyderabad and Trivandrum regions during autumn seasons, which are mostly due

to the long-range transport of CO from Africa and SE-Asia as discussed in the previous section. It seems that basic transport patterns in the troposphere are simulated well by both the models.

4.3 Highlights

In this chapter we discussed the vertical distributions of CO_2 using aircraft based measurements from CONTRAIL program for 3 years period over Delhi. Further, the distributions of CO_2 during different seasons are compared with an ACTM model and finally the effect of rainfall on the lower tropospheric levels of CO_2 is discussed. This chapter also discusses the role of long range transport over different Indian regions using the 14 years tropospheric CO data from the MOPITT satellite measurements. The following salient points are extracted from this study.

1. The CO_2 profiles show lower values below about 1 km height during the south-west monsoon season compared to the middle and upper troposphere. This is due to net uptake of CO_2 during the monsoon season and net emission during other seasons.

2. The amplitude of seasonal variability in CO_2 shows direct, but a delayed link with the strength of Indian summer monsoon rainfall in Delhi. The model simulations are more close to the observations in the upper troposphere (3-8 km) as compared to lower troposphere (below 3 km).

3. A comparison between the observed and model simulated seasonal cycle of CO_2 shows that the model simulations are more close to the observations in the upper troposphere (3-8 km) as compared to lower troposphere (below 3 km). Furthermore, like to surface observations of CO_2 at Ahmedabad, the model also shows a 1 month shift in the minima of CO_2 seasonal cycle over Delhi, which suggests again the need for improvement in the biospheric flux from CASA model.

4. Highest CO mixing ratios are observed in the winter (DJF) at 900 hPa over all the study regions due to the shallow boundary layer and possibly due to reduced chemical destruction as well. Dibrugarh region, shows higher CO in the spring (MAM) season as compared to all the study regions due to dominating contribution from biomass burning in that region. Lowest mixing ratios at this pressure level are observed during the summer monsoon (JJA) over all the regions. This is mainly due to the sweeping of Indian region by cleaner marine air mass carried by the south-west Indian monsoon. The CO levels over Delhi and Dibrugarh during monsoon are observed higher and over Trivandrum lowest in comparison to other study regions. This is because Delhi and Dibrugarh gets mixed air mass of continental and oceanic origin and Trivandrum gets direct from the Indian Ocean at 900 hPa.

5. We observe a reversal in the vertical decreasing trend above the height of 500 hPa with a peak around 300 - 200 hPa height region. Further, it is noted that this peak level is highest during monsoon at all the regions except Trivandrum. This is likely due to convection of polluted air getting trapped in the anticyclonic wind system. Higher levels of CO in this pressure range are also observed in other seasons over Ahmedabad, Hyderabad and Trivandrum. This has not been reported so far in the literature to the best of our knowledge. The 7 day back trajectories calculated using HYSPLIT model show the transport from biomass burning affected regions of central Africa and SE- Asia.

6. Unlike to CO_2 seasonal cycle in the lower troposphere (in PBL) and upper troposphere over Delhi, where the seasonal phase remains same, CO shows opposite seasonal cycles in the lower troposphere (900 hPa) and upper tropospheric height (300 hPa) with lower values during monsoon at 900 hPa and higher values at 300 hPa, over all the study regions except Trivandrum, which highlights the role of deep convection during monsoon and effects of long-range transport during other seasons.

7. Monthly climatology of satellite data have been compared with the clima-

tology simulated using MOZART and EMAC models. The models are able to capture the broad features like seasonal variability at 900 hPa, peak at 300 hPa during Asian summer monsoon due to the deep convection and vertical gradients.

Chapter 5

Methane characteristics at an urban location

Atmospheric CH_4 is the second major human-linked GHG after carbon dioxide (CO_2) and contributes about one-fifth to the increase in radiative forcing since 1750 [1]. Besides its role in climate, it plays a central role in both tropospheric and stratospheric chemistry [153, 154]. The atmospheric mixing ratios of CH_4 have increased by 150% from ∼0.7 ppm to ∼1.8 ppm during 1750 - 2011 [[3], Please see NOAA/AGAGE websites for recent data], with large year-to-year fluctuations in its growth rate. The past three decades have witnessed an increasing atmospheric CH_4 in the 1980s but the growth rate slowed in the beginning of 1990s, plateaued from 1999 to 2006 [30] and since 2007 the CH_4 burden (total amount of CH_4 in the air) has resumed [27, 34]. The reason for these observed changes still remains uncertain due to the limited understanding of what controls atmospheric CH_4 budget. CH_4 has shorter lifetime (about 9 years) than CO_2 (about 120 years), and many other GHGs; thus a reduction in its anthropogenic emission (∼ 64% of current global total CH_4 emissions [22]) would be an effective way of abating global warming in the near future. The urban areas are significant emitters of CH_4 per capita as compared to the rural areas due to economic activity and hence measurements over these regions are helpful for understanding the nature of dominant emission sources and subsequent planning for mitigation policies. India is a very fast developing country and rapid growth in industrial, transportation

and agricultural activities have led to the emission of several trace gases including CO_2, CH_4 into the atmosphere [41, 108]. Time series measurements of CH_4 in India began with low frequency flask measurements collected biweekly from Cape Rama since the year of 1993 [44] and afterwards measurements also started from three new stations: Hanle, Pondicherry and Port Blair since the year of 2000 [44]. Furthermore, the measurements of CH_4 mixing ratios from a high-altitude hill station in the eastern Himalayas started from December 2011 to February 2013 employing gas chromatographic (GC) technique at the sampling frequency of 10 -15 minutes [155]. None of these measurements represent the urban emissions. To realize the need of the study over urban areas, this chapter presents the results of CH_4 measurements over an urban location in western India i.e., Ahmedabad. It discusses the temporal variability of CH_4 along with the estimation of its total emissions over Ahmedabad. Further, these observations of CH_4 are compared with simulations of two global chemistry transport models (CTMs) from which we show that the resulting measurements could provide important constraints for its top-down emission estimations.

5.1 Measurement technique

The atmospheric mixing ratios of CH_4 are measured in the dried air stream using CRDS technique based analyzer (Picarro-G2401). The ambient air is drawn in through a 1/4-inch Teflon tube with a pump attached at the end of the instrument. The air intake is capped with an inverted Teflon funnel conical beaker to prevent liquid water from entering the sample line. The sample air passes through a glass manifold (where excess moisture is removed during high humidity condition), a 5 μm PTFE (polytetrafluoroethylene) filter (for removal of dust particles) and another moisture removal system consisting of a 50-strand Nafion dryer (for removing the moisture to the level of 0.04% mixing ratio of H_2O). More details about the instrument setup and its calibration procedure have been already described in Chapter 2.

5.1.1 Time series analysis

The time series of CH_4 is calculated using 30 minute average of every second data for each day (Figure 5.1, blue triangles). We also derive the 5^{th} percentile lowest values of CH_4 data for each day (over 24 hours window; red circles in Figure 5.1). These values are considered as "background mixing ratios" of CH_4 for corresponding days, since these levels are minimally influenced by the local emission sources [156]. Further, on the basis of wind direction during different seasons [157], the wind regimes are divided in three categories; 1. When air masses over the study location originated from the south west direction (clean oceanic air), 2. When air masses mostly originated from northeast (continental air) and 3. North-west-south directions (continental and oceanic regime mixed).

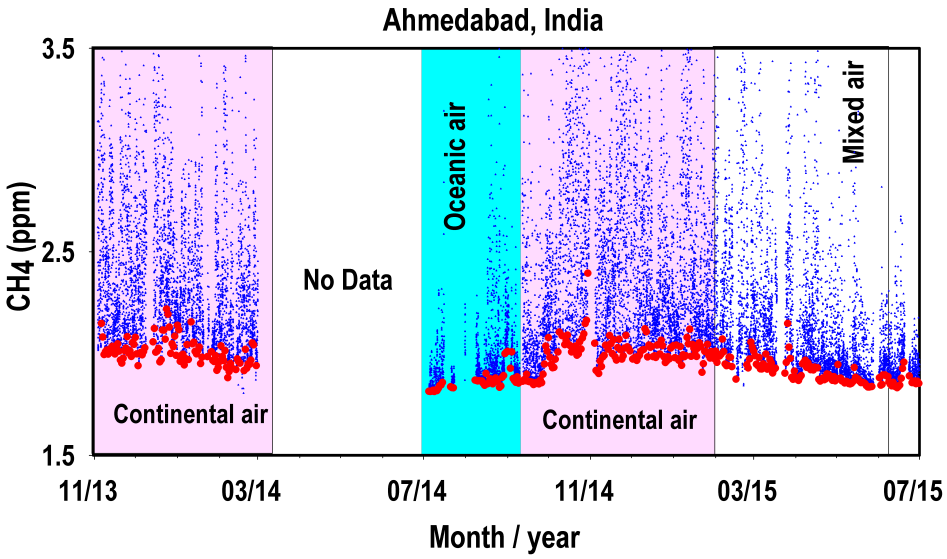

Figure 5.1: Blue triangles show the time series of CH_4 mixing ratios at Ahmedabad for the period of November, 2013 - February, 2014 and July, 2014 - June, 2015 using 30 minute average mixing ratios. Red circles show the 5^{th} percentile mixing ratios of CH_4 for each day corresponding to same period. The shaded background shows the dominance of air originated from different regions, classified based on the prevailing wind direction over the study location.

The CH_4 time series shows large day-to-day variations during the study period. The highest and lowest mixing ratios of CH_4 during this period are observed

to be 10.50 and 1.80 ppm, respectively with a mean of 2.30 ± 0.58 ppm. Higher levels as well as higher variability of CH_4 are found during October to March, corresponding to the period when the station is influenced by continental airmass (Figure 5.1). Local meteorology also plays an important role in determining the distribution of trace gases via dispersion and accumulation of these gases. Further, the scatter plot (not shown here) shows a significant negative correlation between observed wind speed and CH_4 mixing ratios. The mixing ratios of CH_4 were elevated (>2.40 ppm) under calm winds (<3 m s^{-1}) due to accumulation of local pollution. Typically, the calm wind and strong temperature inversion provide a favorable condition for the accumulation of air pollutants in the planetary boundary layer (PBL). In the stronger wind regimes (> 3 m s^{-1}), the impact of dilution due to mixing with regional background air occurs. Most of the lower mixing ratios in the high wind speed regimes were measured during the daytime. It shows that CH_4 levels are mostly controlled by local meteorology and emissions in Ahmedabad. The frequency distribution of CH_4 time series during the study period shows that 63.7% of the observations are below 2.10 ppm and 93.3% are below 3.00 ppm. Maximum occurrence is in the range of $1.80 - 2.35$ ppm contributing to 74.5% of total observations followed by CH_4 values in the ranges of $2.50 - 2.97$ and $3.00 - 4.00$ ppm contributing to 18.8% and 5.3%, respectively. There are 224 events during this period of observations, when CH_4 mixing ratios are observed higher than 4.00 ppm and occasionally CH_4 mixing ratios as high as 10.00 ppm are also observed. Higher plumes indicate strong emission sources of CH_4 in and around Ahmedabad. Maximum frequency of CH_4 occurs at 2.08 ppm. The background mixing ratio of CH_4 also exhibits higher seasonal variability, which is probably due to changes in large scale circulation patterns during different seasons. On the average, the observational site shows higher mixing ratios of CH_4 when air masses are of continental origins and loaded with pollutants on their trajectory to Ahmedabad and it observes lower mixing ratios, when the wind direction shifts from continental to oceanic region. The mixing ratios of CH_4 progressively decrease when wind speed start increasing and air masses originate from mixed regime (continental as well as oceanic regions).

5.2 Seasonal cycle of CH_4

Like in Chapter 3, seasonal cycle of CH_4 is calculated using monthly averages of all the data and using monthly averages of afternoon period (1200−1600 hrs) data only. In both the cases, values beyond mean ± 2σ are considered outliers and not included in monthly average calculations. The afternoon average monthly mixing ratios of CH_4 will be used to compare its seasonal amplitude with other available measurements over the Indian and surrounded regions, which are based on weekly flask samples collected during noon hours.

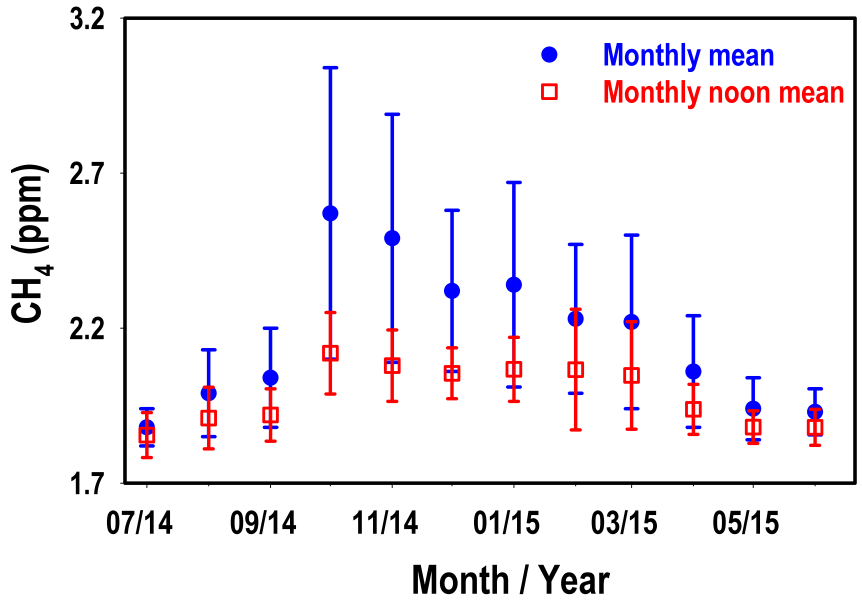

Figure 5.2: Seasonal variations of CH_4 using total (24 hrs) data and afternoon data (1200 -1600 hrs) only, for the period of 2014-2015.

Figure 5.2 shows the monthly variations of CH_4 from July, 2014 to July, 2015. The total mean (all 24 hours value) mixing ratios of CH_4 attain minimum levels in July (1.88 ± 0.60 ppm) and peak in October (2.57 ± 0.47 ppm). Afterwards, the mixing ratio of CH_4 starts decreasing and continue till the end of May. The afternoon mean mixing ratios of CH_4 also show minima in July and maxima in October, but later its mean levels remain almost constant till March and then suddenly starts decreasing. These lower and higher mixing ratios of CH_4 mostly

correspond to the changing seasonal wind patterns from continental to oceanic and oceanic to continental, respectively. Clear change in wind patterns in the lower atmosphere over Ahmedabad has been shown in [158]. It is expected that CH_4 emissions peak in summer monsoon due to highest biogenic production in wet seasons, but the influence of the lower background mixing ratios resulting from the transport of southern hemispheric marine air over India, is compensating the effects of increased emissions. Along with it, the persistent large-scale deep convection over the Indian subcontinent, which rapidly transports the low-level air to higher altitudes and hence depletes the mixing ratios at the surface level. The evidence of higher CH_4 mixing ratios at the upper tropospheric level due to deep convection during monsoon is also observed from the aircraft flask measurements over India by the Civil Aircraft for the Regular Investigation of the atmosphere Based on an Instrument Container (CARIBIC) project [59, 127]. Along with these two main factors, increased loss from OH radicals could be another important factor responsible for lower CH_4 mixing ratio during the summer monsoon. After monsoon, due to waterlogged, and flooded landfills and waste, the biogenic emissions increase. The satellite observations over India show that the waterlogged areas increase nearly threefold from the beginning to the end of the monsoon resulting in increased wetland CH_4 emissions [159]. The VC is lower during October, which does not allow efficient dispersion of city emissions and accumulation takes place. During autumn and winter, the winds are from the IGP region, which is one of the most important regions for rice growing mainly in the Kharif season (May to October) and the Rabi season (November to April). The agricultural practices over this region contribute largely in the anthropogenic biogenic emissions of CH_4 since rice cultivation produces large emissions of CH_4. The winds from these regions may contribute additionally to the higher mixing ratios of CH_4 over the measurement site during this period. The VC values are high, and mixed air masses from both continental and oceanic regions reach the study location during spring. This combined effect results in lower levels of CH_4 during spring.

5.3 Comparison of seasonal cycle with other sites

This section gives the comparison of the annual cycle of CH_4 at Ahmedabad (from midday observations) with few other sites; Hanle (HLE, 32.7°N, 78.9°E, 4500 m a.s.l), Cape Rama (CRI, 15°N, 74°E, 60 m a.s.l), Pondicherry (PON, 12.0°N, 79.8°E, 20 m a.s.l), Port Blair (POB, 11.6°N, 92.7°E, 20 m a.s.l) and Seychelles (SEY, 5°S, 55°E, 3 m a.sl). The observations at HLE, PON and POB are corresponding to the period of 2007-2011, while Cape Rama and Seychelles observations are corresponding to the year of 1999 and 2014, respectively. More details about these observations can be found in [44] and [48]. Since the measurement periods are different, in order to make comparison, we calculate the monthly residuals by subtracting the annual mean from the monthly means over each site. Figure 5.3 shows the CH_4 seasonal variations observed at Ahmedabad compared with these stations. For the sake of completeness, we include the monthly mean of March-June data for the year of 2015, since these months data are not available for the year of 2014 at Ahmedabad. This comparison shows the combined role of emissions and seasonal transport pattern change. All stations except Hanle (a free troposphere station) show similar seasonal pattern with the lowest mixing ratios observed in summer period (JJA) and highest observed in autumn (SON) and winter (DJF) periods.

Figure 5.4 shows the wind patterns during boreal winter (DJF), spring (MAM), summer (JJA) and autumn (SON) seasons. These sites are clearly under the influence of north-east and south-west monsoon during winter and summer, respectively. During spring and autumn, no clear directions of winds are observed and local winds are dominating. During winter, Ahmedabad, CRI, PON and POB observe air mass directly from the Indian subcontinent, which is one of the CH_4 emission hot spots due to large livestock population and rice cultivation [160,161]. The summer high values at HLE are observed because the emission signal from the Indian subcontinent are transported vertically due to the deep convection [48] over this location. SEY is located in the intertropical convergence zone (ITCZ) during boreal winter period which separates this site from Southern Hemispheric

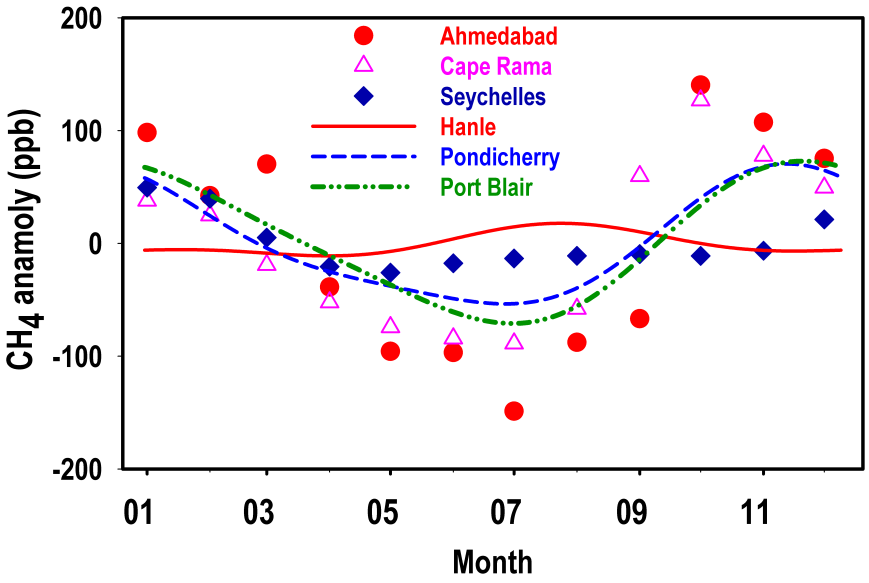

Figure 5.3: Seasonal variations of CH_4 over different locations in and around India. Monthly anomaly is calculated after subtracting the annual mean from the monthly average mixing ratios of CH_4. The data for Cape Rama has been taken from [44], while Hanle, Pondicherry and Port Blair data have been used from [48]. Seychelles data are from NOAA [34].

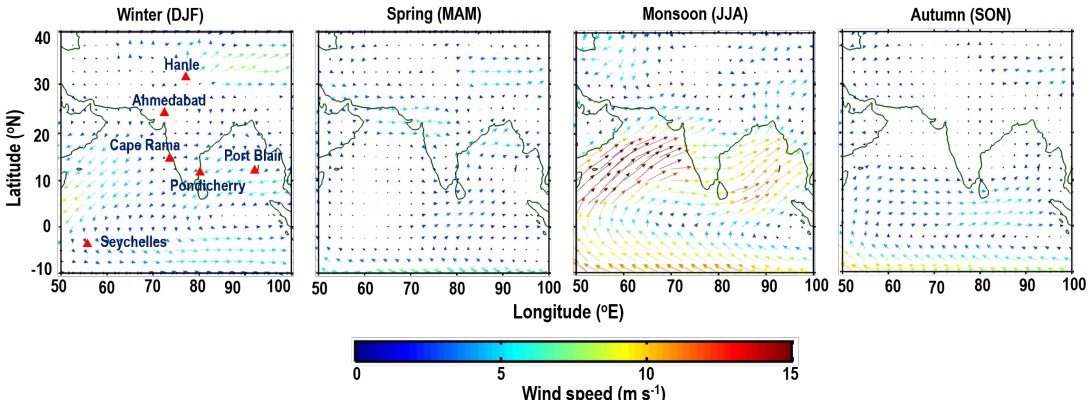

Figure 5.4: Climatology (2009 - 2014) of seasonal wind pattern over Indian and surrounding regions. The colours denote the wind speed in m s^{-1}. The triangles show different stations used for comparison with Ahmedabad. The wind fields have been taken from National Centers for Environmental Prediction (NCEP) reanalysis dataset.

(SH) air and hence air mass from the Indian and other continental regions can cause higher levels of CH_4 during this season. SEY also shows smaller increasing

trend from May to August as compared to other study locations, which is due to the influence of the Southern Hemispheric (SH) air at this site, when ITCZ is located over India.

5.4 Diurnal variation of CH_4

The diurnal cycles are calculated by averaging the CH_4 mixing ratios at hourly intervals from all the collected data every second for different seasons. Figure 5.5 shows seasonally averaged diurnal variation of CH_4 (values beyond mean $\pm$ 2σ are treated as outliers and not included in seasonal averaging).

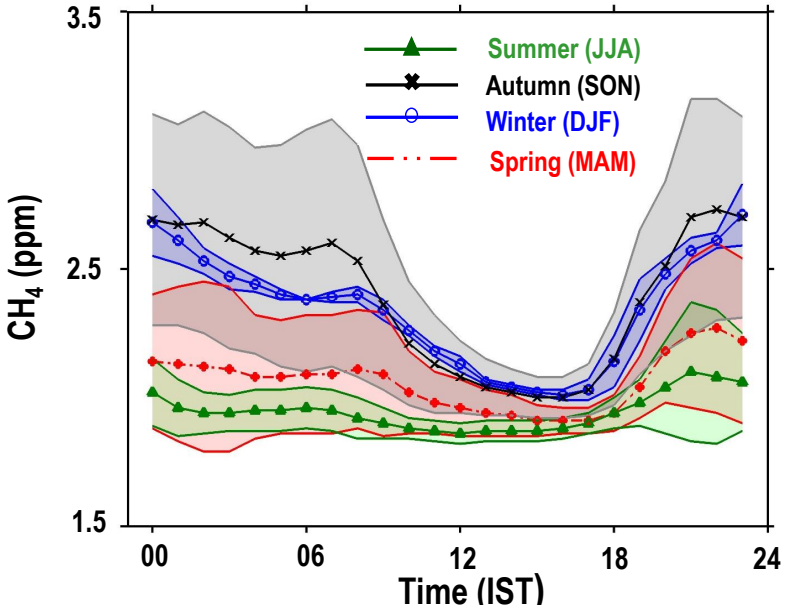

Figure 5.5: Diurnal variation of CH_4 over Ahmedabad during all the four seasons.

In general two peaks, one in the morning (0700 - 0900 hrs) and second in the evening (2000 - 2300 hrs) are observed in all the 4 seasons. In the summer and spring seasons, the morning peak is not obvious. After the morning peak, CH_4 starts decreasing up to 1600 hrs. The minimum levels in the afternoon are mostly caused by the increasing mixing volume due to the expanded boundary layer height. After this minimum around 1600 hrs, the CH_4 mole mixing ratios increase till 2200 hrs. Major emission sources of CH_4 (wetlands, rice agriculture, landfills, waste dump and industrial emissions) are relatively constant throughout a day.

Leaks from CNG filling stations and from the CNG vehicles due to lower engine efficiency may also contribute to CH_4 emissions. The double peaks variations during the morning and evening rush hours have also been observed for other urban pollutants such as carbon monoxide and nitrogen oxide [77,123]. However, given that vehicular exhausts are not a large emission source of CH_4 and its major sources are constant, the elevated levels during the evening and late night hours and depleted levels during afternoon hours, reflect the characteristics of change in the PBL depths throughout the day. The diurnal amplitude is observed minimum (0.24 ppm) in monsoon and maximum (0.73 ppm) in autumn. During winter and spring it is observed to be about 0.70 and 0.36 ppm, respectively.

5.5 Correlation analysis

Correlation studies of CH_4 with CO and CO_2 are useful to investigate the contributions from different source sectors [62,156]. In this study we focus on local to regional emission sources, and for that reason it is necessary to remove the background levels of these gases from their time series. The excess mixing ratios of each of these gases, ΔX_{exc}, above the background mixing ratios are

$$\Delta X_{exc} = [X] - [X]_o \tag{5.1}$$

where $X = CO_2$, CO and CH_4, and $[X]_o$ denotes the background mixing ratio of X. The method to define background CH_4 concentrations is also applied to obtain the background of CO_2 and CO for each day distributions [156]. Slopes and correlation coefficients are calculated using the robust regression linear fit method since the slopes and the correlation estimated from this model are not significantly affected by outliers (http://www.ats.ucla.edu/stat/stata/dae/rreg.htm). The 30 minute average data are used for the correlation study on diurnal, seasonal and yearly scale. We denote $CH_{4(exc)}$:$CO_{2(exc)}$ and $CH_{4(exc)}$:$CO_{(exc)}$ correlation slopes by $\Delta CH_{4(exc)}/\Delta\ CO_{2(exc)}$ and $\Delta CH_{4(exc)}/\Delta CO_{(exc)}$, respectively. The characteristics of these slopes are discussed in the following sections..

5.5.1 CH_4-CO correlation

Figure 5.6a shows the scatter plots of CH_4 and CO for all the four seasons. Significant correlations have been observed between CH_4 and CO. Highest correlation ($r^2 = 0.83$) is observed during spring while almost comparable correlations have been observed during monsoon ($r^2 = 0.72$), autumn ($r^2 = 0.69$) and winter ($r^2 = 0.67$). $\Delta CH_{4(exc)}/\Delta CO_{(exc)}$ slopes show highest values in monsoon and autumn. It might be due to higher emissions of CH_4 from the biogenic sources (wetland and rice paddies) in hot and humid monsoon season (e.g., [162]) and significantly faster chemical loss of CO by OH radicals during this season, since the reaction rate of CO with OH is 24 times faster than the reaction rate of CH_4 with OH. Higher $\Delta CH_{4(exc)}/\Delta CO_{(exc)}$ ratios during monsoon are also reported over different Indian stations [48] and over the western North Pacific regions [133]. The $\Delta CH_{4(exc)}/\Delta CO_{(exc)}$ slopes are found in the range of $0.32 - 0.38$ ppm/ppm during all the four seasons at Ahmedabad ($r^2 \sim 0.80$). These slopes are higher than those for biomass/biofuel burning air masses and close to the values for airmass impacted by the anthropogenic emissions [65, 129, 133, 163, 164]. The observed range of slopes lies in the range observed by several ground based studies ($0.3-1.6$ ppm/ppm) and aircraft campaigns ($0.3 - 0.8$ ppm/ppm) [48, 129, 133, 164].

The diurnal patterns of $\Delta CH_{4(exc)}/\Delta CO_{(exc)}$ slope (Figure 5.6; right 4 panels) also shows very distinct patterns from previous patterns of diurnal slopes of CH_4 and CO_2. The slope starts increasing from midnight (0000 hrs) to early morning (0500-0600 hrs) and afterwards decreases very fast up to 1500-1600 hrs. After 1600 hrs, it remains relatively constant till midnight hours and its values are observed in the range of $0.3 - 1.3$ ppm/ppm in all the seasons. CO mixing ratios sharply decrease from midnight to early morning due to slow down in the intensity of its major emission source (vehicular emission) [77] but CH_4 does not show this sharp decrease, since vehicular emissions are not the major source of CH_4, hence these two processes are accountable for the increasing slope. On the other hand, the slope is low during evening hours due to the higher evening traffic and parallely decreasing boundary layer height, which cause prominent increase in the

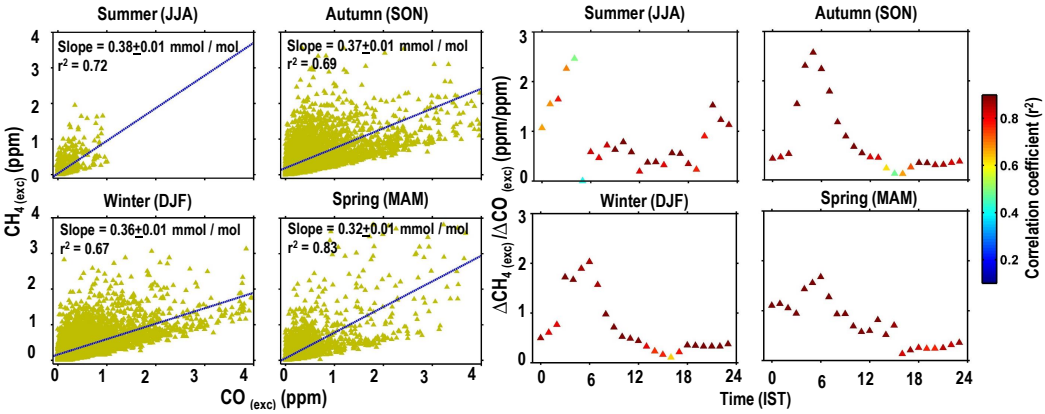

Figure 5.6: Left panel) Correlation of $CH_{4(exc)}$ with CO_{exc} during all the four seasons. "Exc" in the subscript of both gases denotes the excess mixing ratio after subtracting background from each data. Each data point is averaged for 30 minute. Right panel) Diurnal variation of the $\Delta CH_{4(exc)}/\Delta CO_{(exc)}$ slopes during different seasons. The colour code shows the strength of correlations.

CO emissions as compared to CH_4. The diurnal pattern of $\Delta CH_{4(exc)}/\Delta CO_{(exc)}$ slope suggests that the CH_4 mixing ratios do not get affected significantly by the vehicular emissions over the study locations. It shows a significant peak in the morning hours ($0500-0600$ hrs) during all the seasons. The slope is found to be in the range of $0.5-2.5$ ppm/ppm from midnight to early morning during all the four seasons. Most of the higher values are observed during night hours during monsoon, autumn and winter, mainly due to continuous emission of CH_4 from biogenic sources trapped in the lower nocturnal boundary layer. Except monsoon, the $\Delta CH_4/\Delta CO$ slopes do not show any significant change from afternoon to midnight hours and their values are observed in the range of $0.3-1.3$ ppm/ppm. Therefore, this analysis using tracer-tracer slopes suggests that CH_4 has constant diurnal source over this location and its diurnal pattern is mostly controlled by the change in the boundary layer height from day to night.

5.5.2 CH_4-CO_2 correlation

Figure 5.7 (left 4 panels) shows the scatter plots of CH_4 and CO_2 for the different seasons. Significant correlations between $CH_{4(exc)}$ and $CO_{2(exc)}$ are observed during all the seasons except summer. Even though both gases have distinct sources

and sinks (CH_4 loss by photochemistry and CO_2 removal by photosynthesis), but their atmospheric lifetimes are much longer than the timescales for mesoscale transport and therefore behave like inert tracers in the planetary boundary layer. The atmospheric processes in the boundary layer result in mixing on relatively short time scales, even if they are emitted from different emission sources. Several studies also show the tight correlation between $CH_{4(exc)}$ and $CO_{2(exc)}$ measured in different source regions [62, 66, 165, 166]. The $\Delta CH_{4(exc)}/\Delta CO_{2(exc)}$ slope shows seasonal variations. The slope is observed lowest to be 4.4 ± 0.15 ppb/ppm ($r^2 = 0.68$) during summer and may be attributable mainly due to the CO_2 biospheric flux uptake in summer. During autumn and winter this slope values have been observed to be similar, 16.3 ± 0.12 ppb/ppm ($r^2 = 0.80$), and 16.9 ± 0.09 ppb/ppm ($r^2 = 0.82$), respectively. The narrow range of slopes suggest for constant co-located urban emission sources of CH_4 during these periods as well as dormant of biospheric activity as compared to summer season [167]. The slope decreases (13.8 ± 0.08 ppb/ppm, $r^2 = 0.83$) in the spring season as compared to autumn and winter season, which could be due to becoming the biosphere as net source of CO_2 due to higher atmospheric temperature as discussed in Chapter 3 and in [77].

The observed monsoon slope at Ahmedabad is closed to the slope calculated from aircraft measurements (6.70 ± 0.01 ppb/ppm) during the California Research at the Nexus of Air Quality and Climate Change (CalNex) field campaign in May-June, 2010 period [166] and slope (7.8 ± 0.8 ppb/ppm) calculated using ground-based Fourier Transform Spectrometer (FTS) in Southern California, USA [62]. The flask measurements over other stations of India show the slopes in the range of $6.7 - 45.7$ ppb/ppm [48]. The magnitude of observed slopes are less than the slope calculated from CARABIC observations in the upper troposphere of the Indian region. CARIBIC observations show a negative correlation (Slope = -21.0 ± 1784.0 ppb/ppm) during July-September, 2008 and positive correlation (Slope = 23.5 ± 41.4 ppb/ppm) during January-March, 2012 over India, south of 20°N.

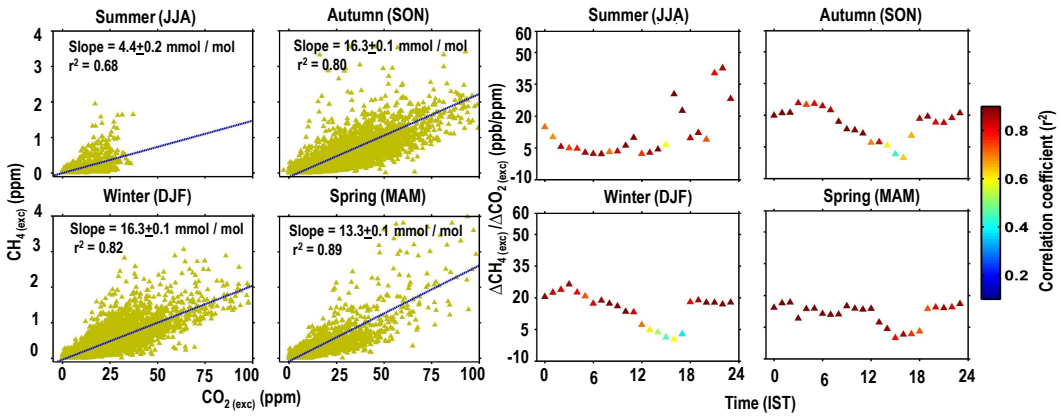

Figure 5.7: Left panel) Correlation of $CH_{4(exc)}$ with $CO_{2(exc)}$ during all the four seasons. Each data point is averaged for 30 minute. "Exc" in the subscript of both gases denote the excess mixing ratio after subtracting background from each data. Right panel) Diurnal variation of $\Delta CH_{4(exc)}/\Delta CO_{2(exc)}$ slopes during all the four seasons. The colour bar shows the strength of correlation for corresponding time.

The diurnal pattern of $\Delta CH_{4(exc)}/\Delta CO_{2(exc)}$ slope shows almost identical patterns in autumn, winter and spring (Figure 5.7). The diurnal pattern of $\Delta CH_{4(exc)}/\Delta CO_{2(exc)}$ slope shows almost identical patterns in autumn, winter and spring. Higher values of slope with comparatively less variation are found during late evening to early morning hours. These values are found to be in the range of 15-22 ppb/ppm. The mixing layer depth decreases from evening to early morning hours and accumulates the pollutants within the boundary layer. Almost comparable slopes for this period suggest that the diurnal variation of CH_4 is mostly governed by the boundary layer dynamics during these seasons. The slope decreases very fast from morning to evening hours due to the increase in mixed layer depth. The $\Delta CH_{4(exc)}/\Delta CO_{2(exc)}$ slopes are found to be in the range of $0.5 - 12$ ppb/ppm during noon hours. During these hours, poor correlations indicate dominance of different controlling factors for the distributions CH_4 and CO_2 mixing ratios. This slope shows a distinct diurnal pattern and correlation during monsoon. During afternoon, the negative value in the monsoon is due to the contribution of enhanced biospheric uptake and biogenic emissions of CO_2 and CH_4, respectively. As mentioned earlier, CARABIC flask measurements over India also show a negative correlation between CH_4 and CO_2 in the upper tro-

pospheric height ($10 - 12$ km) during July - September, 2008 and suggest for strong uptake of CO_2 by the terrestrial biosphere with an increase of biogenic CH_4 emissions during this period.

5.6 Comparison with model simulations

This section presents comparisons of ACTM and LMDz-OR-INCA models simulated CH_4 with the surface observations over this study region for the year of 2014. We calculate the mean diurnal cycle of CH_4 in each season for both the models using same method discussed in Section 5.4 and compare with the observations. The noon time observed mixing ratios of CH_4 are well captured by both the models. However, both models are not able to capture the morning and evening features of the diurnal cycle, which is mostly due to the change in the boundary layer height and slight change in the strength of local emission sources (Figure 5.8). This could be due to the transport in the models which are too coarse to represent the vertical diffusion during the evening and night hours, when there is very low mixing due to the stratification of the low atmosphere. The uncertainties in the local fluxes could be another factor for these differences. It suggests that afternoon mean observations are representative of the regional background concentrations and have larger footprint area, which is more comparable to the model grids of both the models. Hence, in order to well simulate the mixing ratio over an urban region, there is a need for higher resolution transport model (including higher resolution meteorological data and flux data) than the present ones to account for the local sources and physical/dynamical processes. On the other hand, these comparisons also suggest that data should be filtered for regional background for using the station data in inversions of global or regional CH_4 budgets.

The day to day variabilities based on daily mean data of CH_4 for afternoon period only are reproduced better by both the models, however overall ACTM has a higher bias than LMDz model. Note here that the horizontal resolution of

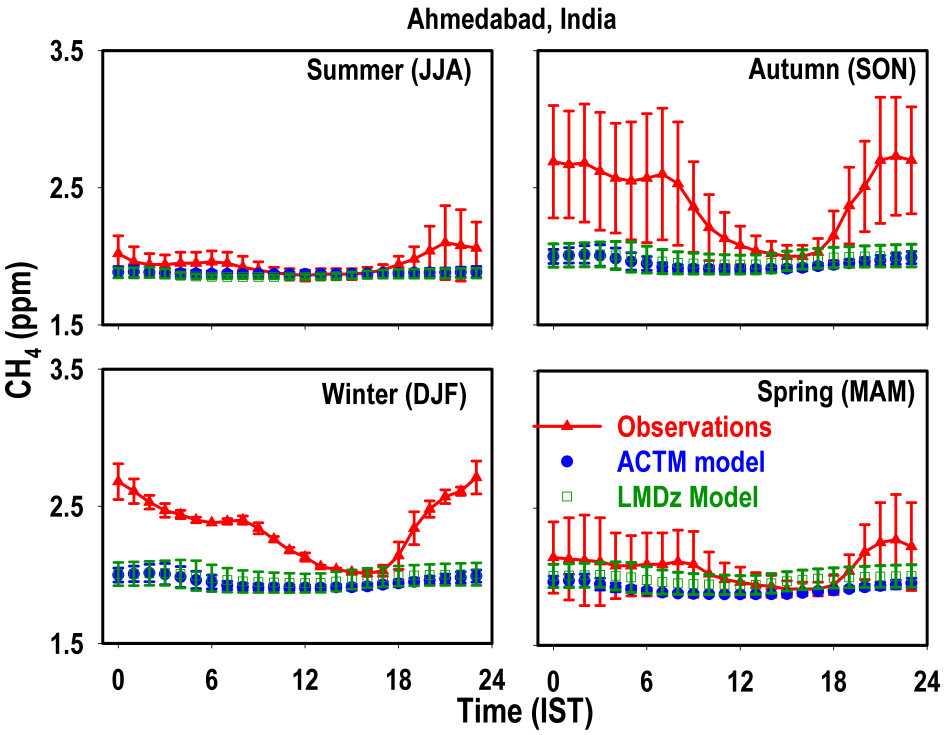

Figure 5.8: The diurnal variations of the observed CH_4 (in red circle), ACTM (blue circle) and LMDz (in green rectangle) model simulated CH_4 over Ahmedabad using hourly mean mixing ratios of CH_4 during all the four seasons. The bars show corresponding 1σ spread.

Table 5.1: Statistical comparison of simulated and measured CH_4 to quantify the level of agreement between ACTM/LMDz model simulations and observations.

Parameter	Winter	Autumn	Monsoon	Annual
MB (mmol mol^{-1})	$-0.1/-0.1$	$-0.1/-0.1$	$-0.1/-0.1$	$-0.1/-0.1$
MNMB (%)	$-4.1/-1.2$	$-4.5/-3.2$	$-0.7/-0.3$	$-3.6/-1.9$
RMSE (mmol mol^{-1})	0.1/0.1	0.2/0.1	0.1/0.1	0.2/0.1
RMSE (%)	5.3/3.6	7.1/5.4	3.1/2.4	5.9/4.4

LMDz (0.66×0.51 deg) is finer than that of ACTM (∼2.8×2.8 deg). Higher short-term mixing ratios, originate mainly due to plumes from local point sources are not captured by the models because many of the large sources of urban types, such as waste dumps, dairy farm and fuel burning, are located well within one grid-box (>60×60 km^2) of both the models. Further, seasonal cycle of CH_4 is calculated

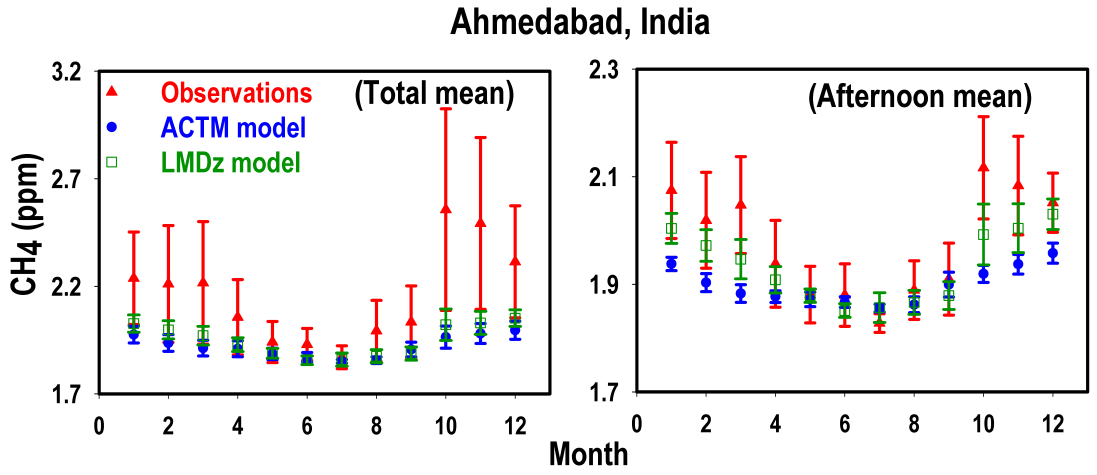

Figure 5.9: The left plot shows the monthly variation of observed CH_4 (in red triangle) with ACTM (in blue circle) and LMDz model (in green rectangle) simulations using the monthly averaged data for the year of 2014. The right plot shows the monthly variation of CH_4 using the corresponding monthly averaged data for the afternoon period (1200 - 1600 hrs) over Ahmedabad.

using the monthly mean of all data (24 hours×30 days) (Left panel of Figure 5.9) and monthly mean of afternoon period (1200-1600 hrs*30 days) data only (Right panel of Figure 5.9). For the sake of completeness, we include the monthly mean of March-June data for the year of 2015, since these months data are not available for the year of 2014. The seasonal patterns of CH_4 are reproduced fairly well by both the models, however seasonal amplitudes (max - min) from total monthly mean data are 78% and 71% underestimated by ACTM and LMDz, respectively. The seasonal amplitudes (max - min) of observations, ACTM simulation and LMDz simulation from monthly mean (afternoon mean) are found to be 0.69 ppm (0.29 ppm), 0.15 ppm (0.10 ppm), and 0.20 ppm (0.18 ppm), respectively. Both the models capture very effectively the sudden increase in the mixing ratio of CH_4 from September to October. The seasonal variations as well as annual variation of different statistical metrics are shown in Table 5.1. These models underestimate the observed CH_4 mixing ratio throughout the study period with MB ranging from -0.01 to -0.09 ppb/ppm during all the seasons. Both the model's underestimate the total mean having minimum bias of about -0.3% in July and maximum of about -26% in October. This large difference is resulting from models inability

to simulate the local features of short-term high concentrations. As discussed in Section 5.2, the maximum influence from local emissions are observed more often during the autumn. Further, these models also underestimate the monthly mean observed mixing ratios of CH_4 for afternoon period, but the bias reduces very significantly (to about 40%) compare to the all-day means. ACTM largely underestimates the observations from October to March as compared to LMDz. From April to September, when high atmospheric mixing nullify the dominance of local influence, both models show very close agreement with the observations. MNMB, RMSE, and RMSE (%) also show similar seasonal variability and are estimated to be about -0.2 to -4.5%, 0.1 to 0.2 ppb/ppm, and 2.4 to 7.1%, respectively. It could be concluded that observations during afternoon period are representative of regional background concentrations and the footprint area is large enough (up to the ACTM grid) to be well captured by both models.

5.7 Top-down CH_4 emissions

This section describes how we have used the CH_4 time series to estimate its total average emission for Ahmedabad are using"top-down" approach. It is based on the correlation slope of CH_4 and CO_2 mixing ratios above the background and total CO_2 emissions from EDGARv4.2 inventory. This approach relies on the fact that both CH_4 and CO_2 are non-reactive on the time scale of dispersion from their respective sources and the total CO_2 emission based on EDGAR v4.2 emission map is correct [168]. This method of estimating the emissions of CH_4 does not require that both gases originate from same sources or even that emissions are geographically collocated [165]. When the lifetimes of both gases are long as compared to their mixing time in the atmosphere, being emitted from different sources will nonetheless be well correlated. Both gases are well mixed before reaching the sampling location as discussed in the previous section and thus the slope of regression of the mixing ratios of CH_4 and CO_2 allows to scale the local CH_4 emissions to the local CO_2 emissions. Further, we restrict ourselves for using only night time slope (1900 - 0500 hrs) in order to keep only signal strongly

influenced by local sources.

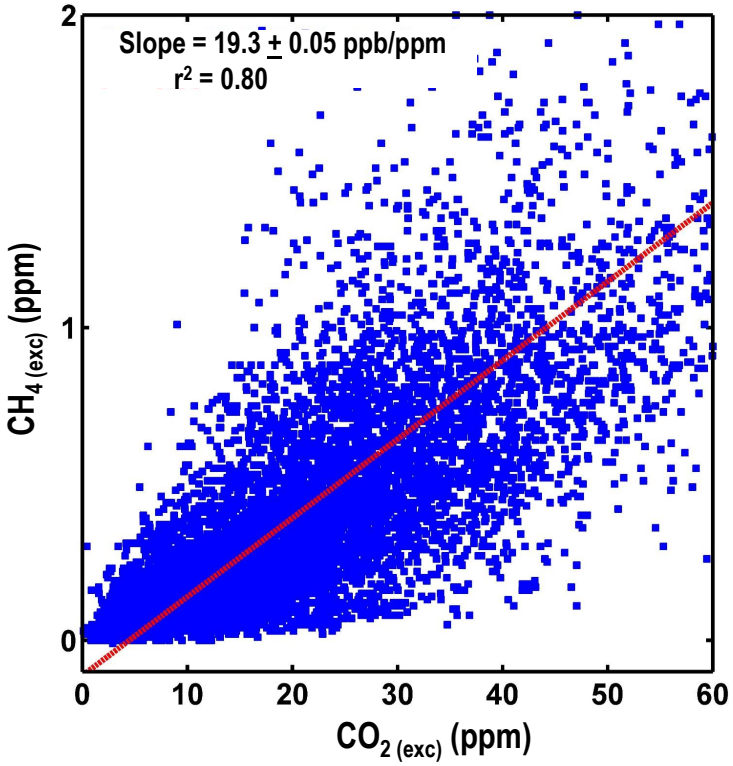

Figure 5.10: The correlation between excess $CH_{4(exc)}$ and $CO_{2(exc)}$ mixing ratios during the night hours (1900 – 0500 hrs) of whole study period at Ahmedabad. The excess mixing ratios are calculated after subtracting the background mixing ratios.

EDGAR inventory emissions are limited up to the year of 2008 only. For scaling the 2008 emissions to the 2014, we use the increasing rate of both gases from 2005 to 2008, and then linearly extrapolated the emissions. Emissions of CO_2 and CH_4 in Ahmedabad are estimated by summing 0.1 degree spatial resolution emissions by EDGARv4.2 inventory over the box (22.8<latitude<23.2, 72.3<longitude<72.7) which contain Ahmedabad coordinates in the center of the box. It is also assumed that, there are no inter-annual variations in the terrestrial biospheric and oceanic CO_2 fluxes from 2008 to 2014. The CO_2 emission for 2008 given by the inventory for the Ahmedabad region is about 6231 Gg yr^{-1} and the extrapolated emission is calculated to be 8368 Gg yr^{-1} for the year of 2014. Similarly, the CH_4 emissions for 2008 and 2014 from the inventory are about 29.8 and 32.0 Gg yr^{-1}, respectively. CH_4 emission is calculated from CO_2 emissions

using the following formula discussed in several studies [62, 66, 165, 168].

$$E_{CH4} = \left(\alpha_{CH_4} \frac{M_{CH_4}}{M_{CO_2}} \right) E_{CO_2} \tag{5.2}$$

where E_{CH_4} is the emission of CH_4 from Ahmedabad, α_{CH_4} is the correlation slope of CH_4 to CO_2 in ppb/ppm, M_{CH_4} is the molecular mass of CH_4 in g/mol, M_{CO_2} is the molecular mass of CO_2 in g/mol and E_{CO_2} is the CO_2 emission in Gg over Ahmedabad. We calculate α from the correlation between night time data of CH_4 and CO_2, which is observed to be 19.3 $\pm$ 0.05 ppb/ppm as seen in Figure 5.10. Using Equation 5.2, we infer the CH_4 emissions of about 58 Gg for the year of 2014. The computed emissions of CH_4 reveal an underestimate for Ahmedabad emissions by 81% by EDGARv4.2 inventory. Due to unavailability of the uncertainty in EDGAR CO_2 emissions over study regions, we can not compute the uncertainty in calculated emissions from this uncertainty. Further, for making sensitivity study we also calculate the emissions using whole data which is observed to be about 46 Gg for the same period.

5.8 Highlights

In view of the importance of measurements over urban region, simultaneous measurements of CH_4 with CO_2 and CO have been made in Ahmedabad, an urban site in the western India, using a highly sensitive laser based cavity rind down spectrometer from November, 2013 - July, 2015. These results have been analysed to study the seasonal and diurnal characteristics of CH_4, its possible emission sources, total emission of CH_4 and comparison of CH_4 with two atmospheric chemistry transport models simulation. The salient features extracted from this study are following.

1. Strong seasonal cycle of CH_4 is observed due to strong influences of seasonal varying transport pattern and the ventilation coefficient (VC) over study location. During summer (JJA), the south-west monsoon wind caries clear air mass from oceanic regions to the study location and cause minimum mixing ratios of CH_4 (average to be 1.94 $\pm$ 0.10 ppm) while the northeasterly

continental winds and lower ventilation coefficient together are responsible for the higher mixing ratios of CH_4 (average to be 2.30 ± 0.28 ppm) during autumn (SON) season. The annual amplitude (max (in October) - min (in July)) of CH_4 is observed to be 0.69 ppm.

2. The results also show a strong diurnal cycle of CH_4. In general, lower and higher levels of CH_4 are observed in the afternoon hours and evening and night hours, respectively. The diurnal cycle of CH_4:CO correlation slope indicates that the diurnal cycle of CH_4 is mostly controlled by varying mixing volume from day to night.

3. Inter-correlations of CH_4 with simultaneously measured CO_2 and CO have been used to understand the dominating emission source of CH_4. The narrow range in CH_4:CO_2 and CH_4:CO slopes during autumn and winter indicate for the constant emission source of CH_4 over the study location. The CH_4:CO slope indicates dominance of anthropogenic sources of CH_4 during the study period. Further, the correlation slope between CH_4 and CO_2 combined with CO_2 emissions from EDGARv4.2 is used to compute emissions of CH_4 for Ahmedabad. The computed emissions of CH_4 overestimate the EDGARv4.2 emissions by 81%.

4. Two state-of-the-art general circulation based chemistry-transport models (ACTM and LMDz-OR-INCA) have been used to simulate the temporal variability of tropospheric CH_4 at Ahmedabad for the year of 2014. The simulated results indicate that both the models have a good ability for simulating the seasonal variation of CH_4. However, bias analysis indicates that the observations are under-predicted by both the models. The underestimation of the observations by the models could be due to the model representation error and possible missing of several sources of CH_4 in the emission inventories used. The ACTM shows large bias as compared to the LMDz-OR-INCA model. The bias for the seasonal cycle calculated using all data is observed large as compared to the seasonal cycle calculated using the monthly mean for afternoon ($1200 - 1600$ hrs) period only. It suggests

that during this period, observations are regionally representative and can be well captured by both global and regional transport models and thus can be potentially utilized for global and regional inversions.

Chapter 6

Summary and future perspectives

The substantial increase in the atmospheric concentrations of greenhouse gases (GHGs) such as carbon dioxide (CO_2), methane (CH_4), nitrous oxide (N_2O) etc, since the commencement of industrial era (crica 1750), is recognized to be the most significant contributor to the global climate change. The concentrations of CO_2 and CH_4 in 2014 have exceeded their preindustrial levels by almost 40% (278 to 397 ppm) and 150% (722 to 1842 ppb), respectively [1], and are still rising at an alarming rate of 2.08 ppm CO_2 yr^{-1} during $2005 - 2014$ [13] and about 5 ppb CH_4 yr^{-1} since 2007 [34]. This increase in their concentrations is caused by the human activities, which are known to produce CO_2 from fossil fuel combustion, cement production, deforestation, and CH_4 from mainly agriculture, livestock, energy production and waste management. Though, the scientific level of understanding of global climate change due to the GHGs is significantly high, the regional scale (e.g. sub-continent and country level) budget (i.e., sources and sinks flux) of GHGs are uncertain especially over the South Asian region; i.e., the estimated uncertainty is larger than the value itself [21, 43]. The resulting uncertainties could be minimized by making measurements of greenhouse gases (GHGs) over different ecosystems and further compared them with the simulations from respective chemistry transport models (CTMs), which will helpful for reducing the model uncertainties. Future projection of regional climate depends greatly on the understanding of regional budget of CO_2, CH_4 and other GHG's, as well as their future levels at reduced uncertainty in CTMs. Monitoring atmo-

spheric CO_2 and CH_4 concentrations on a continuous basis was initiated about the International Geophysical Year ($1957 - 1958$). Until about 2010, majority of such observations have been performed in rural and remote background sites, because the main purpose of these has been to record global/hemispheric mean concentrations and to estimate GHGs sources and sinks for continental scale regions. On the other hand, during the last few decades industrialization and rapid urbanization have accelerated around the world. Urbanization causes about 70% of CO_2 emissions and significant amount of anthropogenic CH_4 emissions from the urban areas in South Asia. These emissions from urban areas are projected to increase further over the coming decades. Therefore, for understanding the emissions growth and verifying the mitigation policies, there is an urgent need for monitoring the GHGs emissions over urban areas.

The anthropogenic emissions of GHGs have been increasing dramatically over Indian region due to rapid growth in economy, industries, transportation and urbanization. However, the region is void in terms of high quality continuous measurements of CO_2 and CH_4. Though some measurements have been done, detailed and well documented measurements focusing on the urban variability and sources are still not on record. This study mostly focuses on the surface measurements of CO_2 and CH_4 concentrations in combination with the anthropogenic emission tracer CO and their comparisons with the simulations from available CTMs over an urban site (Ahmedabad) in western India. Furthermore, the vertical distribution of CO_2 using available aircraft data over Delhi and satellite data of CO in the troposphere over five selected regions in India along with their comparisons with CTMs are also presented in this study.

6.1 Summary of results

High-frequency atmospheric surface measurements of CO_2, CH_4 and CO have been made using highly sensitive laser based cavity ring down spectrometer at

Ahmedabad, an urban site in western India from November, 2013 to June, 2015 with a break during March - June, 2014. The observed results show the range of CO_2 concentrations from 382 to 609 ppm, CH_4 concentrations from 1.80 to 10.50 ppm and CO concentrations from 0.07 to 8.8 ppm, with the average values of CO_2, CH_4 and CO to be 416 ± 19 ppm, 2.30 ± 0.58 ppm and 0.61 ± 0.6 ppm respectively. The lower level of CO_2 and CH_4 concentrations matches well with background level of 397 ppm and 1.84 ppm, respectively. These observations show highest concentrations corresponding to lower ventilation and for winds from north-east direction, representing CO_2, CH_4 and CO transported from anthropogenic sources. Seasonally low concentrations of CO_2, CH_4 and CO are influenced by the air mass from the cleaner marine region. Along with these factors, the influence of biospheric seasonal cycle (photosynthesis outweighs respiration during growing season and reverse during fall season) is also observed in the seasonal cycle of CO_2. Lowest day time CO_2 concentrations ranging from 382 to 393 ppm in August, suggest for the stronger biospheric productivity during this month over the study region, in agreement with an earlier inverse modelling study. This does not match with the terrestrial flux simulated by the Carnegie-Ames-Stanford Approach (CASA) ecosystem model, showing highest productivity in September and October months. Hence, the seasonal cycles of these gases reflect the seasonal variations of natural sources/sinks, anthropogenic emissions and seasonally varying atmospheric transport. The annual amplitudes of CO_2, CH_4 and CO variations are observed to be about 26.07 ppm, 0.69 ppm and 0.68 ppm, respectively using monthly mean of all the data and 13.6 ppm, 0.26 and 0.27, respectively using monthly mean of the afternoon period (1200-1600 hrs) data only. Significant differences between these amplitudes suggest that the annual amplitude from afternoon monthly mean data only does not give true picture of the variability. It is to be noted that most of the CO_2 and CH_4 measurements in India except the present data are based on day time flask samplings only. The results also show considerably strong diurnal cycles of CO_2, CH_4 and CO with significant differences reflecting variability in local sources, sinks and atmospheric stability. Differences in their diurnal variability are mainly caused by the addi-

tional effect of terrestrial biosphere on CO_2. The morning and evening peaks of CO are affected by rush hours traffic and planetary boundary layer (PBL) height variability and occur almost same time throughout the year. However, the morning peaks in CO_2 changes its time slightly due to shift in photosynthesis activity according to change in sun rise time during different seasons. The diurnal pattern suggests that the CH_4 mixing ratios do not get affected significantly by the vehicular emissions over the study locations and mostly controlled by the evolution of the atmospheric boundary layer along with constant emissions sources throughout the day.

Inter-species correlations on diurnal and seasonal basis have provided information about possible variations/categories of their sources and sinks. Significant spreads during monsoon and other three seasons are observed in their correlation slopes. The minimum values of observed slopes and correlation coefficients are observed in summer. During other three seasons, the slopes vary in narrow range and indicate about the constant, common and collocated local emission sources of these gases during these seasons. The slope values indicate the dominance of anthropogenic sources of these gases during the study period. Furthermore, the covariation of CO and CO_2 is used to differentiate anthropogenic and biospheric components of the diurnal cycle of CO_2 and it is found that there is significant contribution of biospheric respirations and anthropogenic emissions in late night (0000-0500 hrs) and evening rush hours (1800-2200 hrs) respectively. Using the slopes of CH_4 and CO_2 correlation as well of CO and CO_2 correlation, CH_4 and CO emissions for Ahmedabad have been estimated. In this estimation, fossil fuel derived emission of CO_2 from EDGAR v4.2 inventory is extrapolated linearly from 2008 to 2014 and it is assumed that there are no year-to-year variations in the land biotic and oceanic CO_2 emissions. The estimated annual emissions of CH_4 and CO for Ahmedabad are found to be 81% and 52% higher than the EDGAR emissions, respectively.

The observed results of CO_2 are also compared with an chemistry transport

model (i.e., JAMSTECs ACTM) simulated CO_2 concentrations for the year of 2014. The model captures some basic features like the trend of diurnal amplitude, seasonal amplitude etc, qualitatively but not quantitatively. The model captures the seasonal cycle fairly well but the amplitude is very less as compared to the observations. The correlation between model and observations demonstrate that the seasonal cycle of day time concentrations of CO_2 is mostly governed by the seasonal cycle of terrestrial biosphere, while overall concentrations are due to the fossil fuel combustion. The mixing ratios of CH_4 are also compared with two state-of-the-art general circulation based chemistry-transport models (JAMSTECs ACTM and LSCE's LMDz-OR-INCA) to study temporal variability for the year of 2014. The simulated results indicate that both the models have a good ability for simulating the seasonal variation of CH_4. However, bias analysis indicates that the observations are under-predicted by both the models. The underestimation of the observations by the models could be due to the model representation error and possible missing of several sources of CH_4 in the emission inventories used. The ACTM shows large bias as compared to the LMDz-OR-INCA model. The bias for the seasonal cycle calculated using all the observed data is found large as compared to the seasonal cycle calculated using the monthly mean for afternoon (1200 - 1600 hrs) period only. It suggests that during this period, observations are regionally representative and can be well captured by both global and regional transport models and thus can be potentially utilized for global and regional inversions.

The vertical distribution of CO_2 over Delhi from CONTRAIL program has been studied to understand its variability in the troposphere. While monsoon period profiles show lower values below about 1 km height, these profiles during other seasons show higher values of CO_2. This is due to net uptake of CO_2 during the monsoon season and net emission during other seasons. The amplitude of seasonal variability in CO_2 shows direct link with the strength of rainfall in Delhi. The measurements show stronger seasonal cycle of CO_2 in the boundary layer as compared to the seasonal cycle in the free troposphere due to its local/regional

influence. A comparison between the observed and model simulated seasonal cycle of CO_2 shows that the model simulations are more close to the observations in the upper troposphere ($3-8$ km) as compared to lower troposphere (below 3 km). Furthermore, unlike surface observations at Ahmedabad, the model also shows a 1 month shift in the minima of CO_2 seasonal cycle over Delhi, which suggests again the need for improvement in the biospheric flux from CASA model.

Average seasonal distributions of CO in the troposphere over five different regions in India based on MOPITT data show very large variability with height, seasons as well as from region to region. A significant increase in the mixing ratios of CO has been observed in the 300-200 hPa region in all the four seasons over the study regions. While it is due to strong convection during the monsoon season, long range transport from the biomass burning regions of Central Africa and East Asia is found to contribute to this increase during other seasons particularly over Ahmedabad and other study regions south of it. Unlike to CO_2 seasonal cycle in the lower troposphere (in PBL) and upper troposphere over Delhi, where the seasonal phase remains same, CO shows opposite seasonal cycles in the lower troposphere (900 hPa) and upper tropospheric height (300 hPa) with lower values during monsoon at 900 hPa and higher values at 300 hPa, over all the study regions except Trivandrum, which highlights the role of deep convection during monsoon and effects of long-range transport during other seasons. Simulations from two photochemical-transport models (MOZART and EMAC) are able to capture these CO variations.

6.2 Scope for future work

Continuing these measurements at Ahmedabad for long period will be helpful to study the trend of anthropogenic emissions over this region. Although all urban areas tend to be large carbon emitters, their emission footprints can vary significantly. Emissions in some cities are dominated by large industries (e.g.,

Mumbai, Kolkata, Mexico), or vehicular emissions (e.g., Delhi, Los Angeles), or natural gas infrastructures (e.g., Hazira, Dahej), which leak methane. These source of emissions can be quantitatively segregated from simultaneous measurements of the isotopic composition of CO_2 and CH_4. Burning of fossil fuels produce CO_2 containing no Radiocarbon ($\Delta^{14}C$) due to its short half-life of 5730 years, compared to the formation of fossil fuels [60, 63]. Using this unambiguous fact, radiocarbon ($\Delta^{14}C$) measurements are very helpful for providing a quantitative proportions of CO_2 resulting from fossil fuel combustions and biospheric respirations. Furthermore, the ratio of stable isotope measurements of CO_2 ($\frac{\delta^{13}C}{\delta^{12}C}$) are very useful for separating the emissions from natural gases and petroleum combustion using the fact that the natural gases have typically lower ratio than that of petroleum [60, 139, 169, 170]. Similarly, the biogenic sources (such as wetlands, agriculture, waste management) tends to deplete $^{13}CH_4$ (i.e. diminish the $\frac{\delta^{13}C}{\delta^{12}C}$ ratio in atmospheric CH_4) in the atmosphere, while fossil fuel, biomass burning emissions, as well as all the CH_4 sinks enriched $^{13}CH_4$ in the atmosphere [3, 171]. Hence, a bigger network (covering various ecosystem) of high quality simultaneous measurements of these gases and their isotopes along with their model simulations, is needed to elucidate more accurate distribution of emissions and source categories. More importantly, the measurement systems should be run continuously over multiple years for tracking the changes associated with their levels, anthropogenic activities and effects of emission mitigation policies.

As discussed earlier, regional quantification of the budgets of CO_2 and CH_4 using inverse models rely highly on simulations of these gases from global transport model at coarse resolution. However, simulated fluxes are associated with high degree of uncertainties due to the errors associated with the dynamics of the transport models. Hence, in order to incorporate the sub grid scale processes, inverse models need to run at regional scales. For this, high resolutions regional forward transport models need to be run for simulating high frequency concentrations of CO_2 and CH_4 as well as meteorology [54, 172]. Hence, the simulations of CO_2 and CH_4 from regional forward transport models such as WRF-CO_2,

WRF-CH_4 in combinations with their atmospheric measurements from different ecosystems will provide their budget at with improved uncertainties and hence will place a significant contribution for the global carbon cycle research. Accurate knowledge of the emissions and sources of the whole suite of the GHGs will be needed for fulfilling the mitigation polices as well as the projection of future climate.

Bibliography

[1] G. Myhre, D. Shindell, F. Breon, W. Collins, J. Fuglestvedt, J. Huang, D. Koch, J. Lamarque, D. Lee, B. Mendoza, T. Nakajima, A. Robock, G. Stephens, T. Takemura, and H. Zhang, *Anthropogenic and Natural Radiative Forcing* (Cambridge University Press, Cambridge, United Kingdom and New York, NY, USA, 2013), book section 8, pp. 659–740.

[2] J. R. Petit, J. Jouzel, D. Raynaud, N. I. Barkov, J.-M. Barnola, I. Basile, M. Bender, J. Chappellaz, M. Davis, G. Delaygue, M. Delmotte, V. M. Kotlyakov, M. Legrand, V. Y. Lipenkov, C. Lorius, L. PEpin, E. Ritz, C. Saltzman, and M. Stievenard, Nature **399**, 429–436 (1999).

[3] D. F. Ferretti, J. B. Miller, J. W. C. White, D. M. Etheridge, K. R. Lassey, D. C. Lowe, C. M. M. Meure, M. F. Dreier, C. M. Trudinger, T. D. van Ommen, and R. L. Langenfelds, Science **309**, 1714–1717 (2005).

[4] P. Ciais, C. Sabine, G. Bala, L. Bopp, V. Brovkin, J. Canadell, A. Chhabra, R. DeFries, J. Galloway, M. Heimann, C. Jones, C. LeÂăQueÌĄreÌĄ, R. Myneni, S. Piao, and P. Thornton, *Carbon and Other Biogeochemical Cycles* (Cambridge University Press, Cambridge, United Kingdom and New York, NY, USA, 2013), book section 6, pp. 465–570.

[5] D. T. Shindell, G. Faluvegi, D. M. Koch, G. A. Schmidt, N. Unger, and S. E. Bauer, Science **326**, 716–718 (2009).

[6] J. Seinfeld and S. Pandis, *Atmospheric Chemistry and Physics* (John Wiley and Sons: New York, 1998).

[7] D. Jacob, *Introduction To Atmospheric Chemistry and Physics* (Princeton university press: Princeton, New Jersey, 1999).

[8] G. Brasseur and S. Solomon, *Aeronomy of the Middle Atmosphere* (Springer Netherlands, 2005).

[9] J. Holton, *Encyclopedia of atmospheric sciences*, vol. 5 (Academic Press: Amsterdam, 2003).

[10] V. Ramanathan, R. D. Cess, E. F. Harrison, P. Minnis, B. R. Barkstrom, E. Ahmad, and D. Hartmann, Science **243**, 57–63 (1989).

[11] A. R. Ravishankara, Y. Rudich, and D. J. Wuebbles, Chemical Reviews **115**, 3682–3703 (2015).

[12] R. A. Hanel, B. J. Conrath, V. G. Kunde, C. Prabhakara, I. Revah, V. V. Salomonson, and G. Wolford, Journal of Geophysical Research **77**, 2629–2641 (1972).

[13] C. Le Quéré, R. Moriarty, R. M. Andrew, J. G. Canadell, S. Sitch, J. I. Korsbakken, P. Friedlingstein, G. P. Peters, R. J. Andres, T. A. Boden, R. A. Houghton, J. I. House, R. F. Keeling, P. Tans, A. Arneth, D. C. E. Bakker, L. Barbero, L. Bopp, J. Chang, F. Chevallier, L. P. Chini, P. Ciais, M. Fader, R. A. Feely, T. Gkritzalis, I. Harris, J. Hauck, T. Ilyina, A. K. Jain, E. Kato, V. Kitidis, K. Klein Goldewijk, C. Koven, P. Landschützer, S. K. Lauvset, N. Lefèvre, A. Lenton, I. D. Lima, N. Metzl, F. Millero, D. R. Munro, A. Murata, J. E. M. S. Nabel, S. Nakaoka, Y. Nojiri, K. O'Brien, A. Olsen, T. Ono, F. F. Pérez, B. Pfeil, D. Pierrot, B. Poulter, G. Rehder, C. Rödenbeck, S. Saito, U. Schuster, J. Schwinger, R. Séférian, T. Steinhoff, B. D. Stocker, A. J. Sutton, T. Takahashi, B. Tilbrook, I. T. van der Laan-Luijkx, G. R. van der Werf, S. van Heuven, D. Vandemark, N. Viovy, A. Wiltshire, S. Zaehle, and N. Zeng, Earth System Science Data **7**, 349–396 (2015).

[14] R. J. Andres, T. A. Boden, F.-M. Bréon, P. Ciais, S. Davis, D. Erickson, J. S. Gregg, A. Jacobson, G. Marland, J. Miller, T. Oda, J. G. J. Olivier,

M. R. Raupach, P. Rayner, and K. Treanton, Biogeosciences **9**, 1845–1871 (2012).

[15] B. A. Seibel and P. J. Walsh, Science **294**, 319–320 (2001).

[16] K. Caldeira and M. E. Wickett, Nature **425**, 365–365 (2003).

[17] C. Beer, M. Reichstein, E. Tomelleri, P. Ciais, M. Jung, N. Carvalhais, C. RÃűdenbeck, M. A. Arain, D. Baldocchi, G. B. Bonan, A. Bondeau, A. Cescatti, G. Lasslop, A. Lindroth, M. Lomas, S. Luyssaert, H. Margolis, K. W. Oleson, O. Roupsard, E. Veenendaal, N. Viovy, C. Williams, F. I. Woodward, and D. Papale, Science **329**, 834–838 (2010).

[18] C. D. Keeling, Tellus **12**, 200–203 (1960).

[19] H. D. Graven, R. F. Keeling, S. C. Piper, P. K. Patra, B. B. Stephens, S. C. Wofsy, L. R. Welp, C. Sweeney, P. P. Tans, J. J. Kelley, B. C. Daube, E. A. Kort, G. W. Santoni, and J. D. Bent, Science **341**, 1085–1089 (2013).

[20] A. P. Ballantyne, C. B. Alden, J. B. Miller, P. P. Tans, and J. W. C. White, Nature **488**, 70–72 (2012).

[21] P. K. Patra, J. G. Canadell, R. A. Houghton, S. L. Piao, N.-H. Oh, P. Ciais, K. R. Manjunath, A. Chhabra, T. Wang, T. Bhattacharya, P. Bousquet, J. Hartman, A. Ito, E. Mayorga, Y. Niwa, P. A. Raymond, V. V. S. S. Sarma, and R. Lasco, Biogeosciences **10**, 513–527 (2013).

[22] S. Kirschke, P. Bousquet, P. Ciais, M. Saunois, J. G. Canadell, E. Dlugokencky, P. Bergamaschi, D. Bergmann, D. Blake, L. Bruhwiler, P. Cameron Smith, S. Castaldi, F. Chevallier, L. Feng, A. Fraser, M. Heimann, E. Hodson, S. Houweling, B. Josse, P. Fraser, P. Krummel, J. Lamarque, R. Langenfelds, V. Le Quere, C. Naik, S. O'Doherty, P. Palmer, I. Pison, D. Plummer, B. Poulter, R. Prinn, M. Rigby, B. Ringeval, M. Santini, M. Schmidt, D. Shindell, I. Simpson, R. Spahni, L. P. Steele, S. Strode, K. Sudo, S. Szopa, G. R. van der Werf, A. Voulgar-

akis, M. van Weele, R. Weiss, J. Williams, and G. Zeng, Nature Geosci **6**, 813–823 (2013).

[23] S. Hayashida, A. Ono, S. Yoshizaki, C. Frankenberg, W. Takeuchi, and X. Yan, Remote Sensing of Environment **139**, 246 – 256 (2013).

[24] W. Allan, H. Struthers, and D. C. Lowe, Journal of Geophysical Research: Atmospheres **112** (2007). D04306.

[25] S. Sander, R. R. Friedl, D. M. Golden, M. J. Kurylo, G. K. Moortgat, H. Keller-Rudek, P. H. Wine, A. R. Ravishankara, C. E. Kolb, M. J. Molina, B. J. Finlayson-Pitts, R. E. Huie, and V. L. Orkin, JPL Publication (2006).

[26] E. J. Dlugokencky, E. G. Nisbet, R. Fisher, and D. Lowry, Philosophical Transactions of the Royal Society of London A: Mathematical, Physical and Engineering Sciences **369**, 2058–2072 (2011).

[27] M. Rigby, R. G. Prinn, P. J. Fraser, P. G. Simmonds, R. L. Langenfelds, J. Huang, D. M. Cunnold, L. P. Steele, P. B. Krummel, R. F. Weiss, S. O'Doherty, P. K. Salameh, H. J. Wang, C. M. Harth, J. MÃijhle, and L. W. Porter, Geophysical Research Letters **35** (2008). L22805.

[28] R. J. Francey, L. P. Steele, R. L. Langenfelds, and B. C. Pak, J. Atmos. Sci. **56**, 279–285 (1999).

[29] I. J. Simpson, S. A., M. P., S. Meinardi, L. Bruhwiler, N. J. Blake, D. Helmig, F. S. Rowland, and D. R. Blake, Nature **488**, 490–494 (2012).

[30] E. J. Dlugokencky, S. Houweling, L. Bruhwiler, K. A. Masarie, P. M. Lang, J. B. Miller, and P. P. Tans, Geophysical Research Letters **30** (2003). 1992.

[31] F. Kai, S. Tyler, J. Randerson, and D. R. Blake, Nature **476**, 194–197 (2011).

[32] I. Levin, C. Veidt, B. H. Vaughn, G. Brailsford, T. Bromley, R. Heinz, D. Lowe, J. B. Miller, C. Posz, and J. W. C. White, Nature **486** (2012).

[33] P. Bousquet, B. Ringeval, I. Pison, E. J. Dlugokencky, E.-G. Brunke, C. Carouge, F. Chevallier, A. Fortems-Cheiney, C. Frankenberg, D. A. Hauglustaine, P. B. Krummel, R. L. Langenfelds, M. Ramonet, M. Schmidt, L. P. Steele, S. Szopa, C. Yver, N. Viovy, and P. Ciais, Atmospheric Chemistry and Physics **11**, 3689–3700 (2011).

[34] E. J. Dlugokencky, L. Bruhwiler, J. W. C. White, L. K. Emmons, P. C. Novelli, S. A. Montzka, K. A. Masarie, P. M. Lang, A. M. Crotwell, J. B. Miller, and L. V. Gatti, Geophysical Research Letters **36**, n/a–n/a (2009). L18803.

[35] P. J. Crutzen, M. G. Lawrence, and U. Poschl, Tellus A **51**, 123–146 (1999).

[36] J. Lelieveld, F. J. Dentener, W. Peters, and M. C. Krol, Atmospheric Chemistry and Physics **4**, 2337–2344 (2004).

[37] G. P. Brasseur, M. Schultz, C. Granier, M. Saunois, T. Diehl, M. Botzet, E. Roeckner, and S. Walters, J. Climate **19**, 3932–3951 (2006).

[38] P. Bergamaschi, R. Hein, M. Heimann, and P. J. Crutzen, Journal of Geophysical Research: Atmospheres **105**, 1909–1927 (2000).

[39] M. G. Lawrence and J. Lelieveld, Atmos. Chem. Phys. **10**, 11017–11096 (2010).

[40] J. G. J. Olivier, J. A. Van Aardenne, F. J. Dentener, V. Pagliari, L. N. Ganzeveld, and J. A. H. W. Peters, Environmental Sciences **2**, 81–99 (2005).

[41] H. Akimoto, Science **302**, 1716–1719 (2003).

[42] J. Kurokawa, T. Ohara, T. Morikawa, S. Hanayama, G. Janssens-Maenhout, T. Fukui, K. Kawashima, and H. Akimoto, Atmospheric Chemistry and Physics **13**, 11019–11058 (2013).

[43] P. Peylin, R. M. Law, K. R. Gurney, F. Chevallier, A. R. Jacobson, T. Maki, Y. Niwa, P. K. Patra, W. Peters, P. J. Rayner, C. Rödenbeck, I. T. van der Laan-Luijkx, and X. Zhang, Biogeosciences **10**, 6699–6720 (2013).

[44] S. K. Bhattacharya, D. V. Borole, R. J. Francey, C. E. Allison, L. P. Steele, P. Krummel, R. Langenfelds, K. A. Masarie, Y. K. Tiwari, and P. Patra, Current Science **97** (2009).

[45] P. Mahesh, N. Sharma, V. Dadhwal, P. Rao, B. Apparao, A. Ghosh, K. Mallikarjun, and M. Ali, Journal of Earth Science and Climatic Change **5**, – (2014).

[46] N. Sharma, V. Dadhwal, Y. Kant, P. Mahesh, K. Mallikarjun, H. Gadavi, A. Sharma, and M. Ali, Air, Soil and Water Research **7**, 61–68 (2014).

[47] Y. K. Tiwari, R. K. Vellore, K. R. Kumar, M. van der Schoot, and C.-H. Cho, Science of The Total Environment **490**, 570 – 578 (2014).

[48] X. Lin, N. K. Indira, M. Ramonet, M. Delmotte, P. Ciais, B. C. Bhatt, M. V. Reddy, D. Angchuk, S. Balakrishnan, S. Jorphail, T. Dorjai, T. T. Mahey, S. Patnaik, M. Begum, C. Brenninkmeijer, S. Durairaj, R. Kirubagaran, M. Schmidt, P. S. Swathi, N. V. Vinithkumar, C. Yver Kwok, and V. K. Gaur, Atmospheric Chemistry and Physics **15**, 9819–9849 (2015).

[49] R. Ahmadov, C. Gerbig, R. Kretschmer, S. Koerner, B. Neininger, A. J. Dolman, and C. Sarrat, Journal of Geophysical Research: Atmospheres **112** (2007). D22107.

[50] G. Pérez-Landa, P. Ciais, G. Gangoiti, J. L. Palau, A. Carrara, B. Gioli, F. Miglietta, M. Schumacher, M. M. Millán, and M. J. Sanz, Atmospheric Chemistry and Physics **7**, 1851–1868 (2007).

[51] B. M. Briber, L. R. Hutyra, A. L. Dunn, S. M. Raciti, and J. W. Munger, Land **2**, 304 (2013).

[52] M. Lopez, M. Schmidt, M. Delmotte, A. Colomb, V. Gros, C. Janssen, S. J. Lehman, D. Mondelain, O. Perrussel, M. Ramonet, I. Xueref-Remy, and P. Bousquet, Atmospheric Chemistry and Physics **13**, 7343–7358 (2013).

[53] L. Ammoura, I. Xueref-Remy, V. Gros, A. Baudic, B. Bonsang, J.-E. Petit, O. Perrussel, N. Bonnaire, J. Sciare, and F. Chevallier, Atmospheric Chemistry and Physics **14**, 12871–12882 (2014).

[54] S. Ballav, P. K. Patra, Y. Sawa, H. Matsueda, A. Adachi, S. Onogi, M. Takigawa, and U. De, J. Earth System Sci. **in press** (2015).

[55] C. A. M. Brenninkmeijer, P. Crutzen, F. Boumard, T. Dauer, B. Dix, R. Ebinghaus, D. Filippi, H. Fischer, H. Franke, U. Frieβ, J. Heintzenberg, F. Helleis, M. Hermann, H. H. Kock, C. Koeppel, J. Lelieveld, M. Leuenberger, B. G. Martinsson, S. Miemczyk, H. P. Moret, H. N. Nguyen, P. Nyfeler, D. Oram, D. O'Sullivan, S. Penkett, U. Platt, M. Pupek, M. Ramonet, B. Randa, M. Reichelt, T. S. Rhee, J. Rohwer, K. Rosenfeld, D. Scharffe, H. Schlager, U. Schumann, F. Slemr, D. Sprung, P. Stock, R. Thaler, F. Valentino, P. van Velthoven, A. Waibel, A. Wandel, K. Waschitschek, A. Wiedensohler, I. Xueref-Remy, A. Zahn, U. Zech, and H. Ziereis, Atmospheric Chemistry and Physics **7**, 4953–4976 (2007).

[56] T. Machida, H. Matsueda, Y. Sawa, Y. Nakagawa, K. Hirotani, N. Kondo, K. Goto, T. Nakazawa, K. Ishikawa, and T. Ogawa, J. Atmos. Oceanic Technol. **25**, 1744–1754 (2008).

[57] P. K. Patra, Y. Niwa, T. J. Schuck, C. A. M. Brenninkmeijer, T. Machida, H. Matsueda, and Y. Sawa, Atmospheric Chemistry and Physics **11**, 4163–4175 (2011).

[58] T. J. Schuck, C. A. M. Brenninkmeijer, A. K. Baker, F. Slemr, P. F. J. von Velthoven, and A. Zahn, Atmospheric Chemistry and Physics **10**, 3965–3984 (2010).

[59] T. J. Schuck, K. Ishijima, P. K. Patra, A. K. Baker, T. Machida, H. Matsueda, Y. Sawa, T. Umezawa, C. A. M. Brenninkmeijer, and J. Lelieveld, Journal of Geophysical Research: Atmospheres **117** (2012). D19304.

[60] J. C. Turnbull, J. B. Miller, S. J. Lehman, P. P. Tans, R. J. Sparks, and J. Southon, Geophysical Research Letters **33** (2006).

[61] Y. Wang, J. W. Munger, S. Xu, M. B. McElroy, J. Hao, C. P. Nielsen, and H. Ma, Atmospheric Chemistry and Physics **10**, 8881–8897 (2010).

[62] D. Wunch, P. O. Wennberg, G. C. Toon, G. Keppel-Aleks, and Y. G. Yavin, Geophysical Research Letters **36** (2009).

[63] S. Newman, S. Jeong, M. L. Fischer, X. Xu, C. L. Haman, B. Lefer, S. Alvarez, B. Rappenglueck, E. A. Kort, A. E. Andrews, J. Peischl, K. R. Gurney, C. E. Miller, and Y. L. Yung, Atmospheric Chemistry and Physics **13**, 4359–4372 (2013).

[64] M. E. Popa, M. K. Vollmer, A. Jordan, W. A. Brand, S. L. Pathirana, M. Rothe, and T. Röckmann, Atmospheric Chemistry and Physics **14**, 2105–2123 (2014).

[65] M. O. Andreae and P. Merlet, Global Biogeochemical Cycles **15**, 955–966 (2001).

[66] K. W. Wong, D. Fu, T. J. Pongetti, S. Newman, E. A. Kort, R. Duren, Y.-K. Hsu, C. E. Miller, Y. L. Yung, and S. P. Sander, Atmospheric Chemistry and Physics **15**, 241–252 (2015).

[67] P. K. Patra, R. M. Law, W. Peters, C. RÃűdenbeck, M. Takigawa, C. Aulagnier, I. Baker, D. J. Bergmann, P. Bousquet, J. Brandt, L. Bruhwiler, P. J. Cameron-Smith, J. H. Christensen, F. Delage, A. S. Denning, S. Fan, C. Geels, S. Houweling, R. Imasu, U. Karstens, S. R. Kawa, J. Kleist, M. C. Krol, S.-J. Lin, R. Lokupitiya, T. Maki, S. Maksyutov, Y. Niwa, R. Onishi, N. Parazoo, G. Pieterse, L. Rivier, M. Satoh, S. Serrar, S. Taguchi, R. Vautard, A. T. Vermeulen, and Z. Zhu, Global Biogeochemical Cycles **22** (2008). GB4013.

[68] R. M. Law, W. Peters, C. RÃűdenbeck, C. Aulagnier, I. Baker, D. J. Bergmann, P. Bousquet, J. Brandt, L. Bruhwiler, P. J. Cameron-Smith, J. H. Christensen, F. Delage, A. S. Denning, S. Fan, C. Geels, S. Houweling, R. Imasu, U. Karstens, S. R. Kawa, J. Kleist, M. C. Krol, S.-J. Lin,

R. Lokupitiya, T. Maki, S. Maksyutov, Y. Niwa, R. Onishi, N. Parazoo, P. K. Patra, G. Pieterse, L. Rivier, M. Satoh, S. Serrar, S. Taguchi, M. Takigawa, R. Vautard, A. T. Vermeulen, and Z. Zhu, Global Biogeochemical Cycles **22** (2008). GB3009.

[69] B. B. Stephens, K. R. Gurney, P. P. Tans, C. Sweeney, W. Peters, L. Bruhwiler, P. Ciais, M. Ramonet, P. Bousquet, T. Nakazawa, S. Aoki, T. Machida, G. Inoue, N. Vinnichenko, J. Lloyd, A. Jordan, M. Heimann, O. Shibistova, R. L. Langenfelds, L. P. Steele, R. J. Francey, and A. S. Denning, Science **316**, 1732–1735 (2007).

[70] T. Boden, G. Marland, and R. Andres, Oak Ridge, Tenn., U.S.A. (2015).

[71] IPCC, *Summary for Policymakers* (Cambridge University Press, Cambridge, United Kingdom and New York, NY, USA, 2013), book section SPM, pp. 1–30.

[72] J. D. Ingle and S. R. Crouch, *Spectrochemical analysis* (Prentice-Hall, 1988).

[73] A. O′Keefe and D. A. G. Deacon, Review of Scientific Instruments **59**, 2544–2551 (1988).

[74] M. Bitter, S. M. Ball, I. M. Povey, and R. L. Jones, Atmospheric Chemistry and Physics **5**, 2547–2560 (2005).

[75] H. Chen, J. Winderlich, C. Gerbig, A. Hoefer, C. W. Rella, E. R. Crosson, A. D. Van Pelt, J. Steinbach, O. Kolle, V. Beck, B. C. Daube, E. W. Gottlieb, V. Y. Chow, G. W. Santoni, and S. C. Wofsy, Atmospheric Measurement Techniques **3**, 375–386 (2010).

[76] A. Karion, C. Sweeney, S. Wolter, T. Newberger, H. Chen, A. Andrews, J. Kofler, D. Neff, and P. Tans, Atmospheric Measurement Techniques **6**, 511–526 (2013).

[77] N. Chandra, S. Lal, S. Venkataramani, P. K. Patra, and V. Sheel, Atmospheric Chemistry and Physics Discussions **15**, 32185–32238 (2015).

[78] E. Crosson, Applied Physics B **92**, 403–408 (2008).

[79] L. R. Welp, R. F. Keeling, R. F. Weiss, W. Paplawsky, and S. Heckman, Atmospheric Measurement Techniques **6**, 1217–1226 (2013).

[80] M. N. Deeter, L. K. Emmons, G. L. Francis, D. P. Edwards, J. C. Gille, J. X. Warner, B. Khattatov, D. Ziskin, J.-F. Lamarque, S.-P. Ho, V. Yudin, J.-L. AttiÃľ, D. Packman, J. Chen, D. Mao, and J. R. Drummond, Journal of Geophysical Research: Atmospheres **108** (2003).

[81] M. Deeter *et al.*, Journal of Geophysical Research **118**, 6710–6725 (2013).

[82] M. N. Deeter, S. Martínez-Alonso, D. P. Edwards, L. K. Emmons, J. C. Gille, H. M. Worden, C. Sweeney, J. V. Pittman, B. C. Daube, and S. C. Wofsy, Atmospheric Measurement Techniques **7**, 3623–3632 (2014).

[83] C. D. Rodgers, *Inverse Methods for Atmospheric Sounding: Theory and Practice* (World Scientific Publishing Co. Pte. Ltd., 2000).

[84] K. Onogi, J. Tsutsui, H. Koide, M. Sakamoto, S. Kobayashi, H. Hatsushika, T. Matsumoto, N. Yamazaki, H. Kamahori, K. Takahashi, S. Kadokura, K. Wada, K. Kato, R. Oyama, T. Ose, N. Mannoji, and R. Taira, Journal of the Meteorological Society of Japan. Ser. II **85**, 369–432 (2007).

[85] T. Takahashi, S. C. Sutherland, R. Wanninkhof, C. Sweeney, R. A. Feely, D. W. Chipman, B. Hales, G. Friederich, F. Chavez, C. Sabine, A. Watson, D. C. Bakker, U. Schuster, N. Metzl, H. Yoshikawa-Inoue, M. Ishii, T. Midorikawa, Y. Nojiri, A. KÃűrtzinger, T. Steinhoff, M. Hoppema, J. Olafsson, T. S. Arnarson, B. Tilbrook, T. Johannessen, A. Olsen, R. Bellerby, C. Wong, B. Delille, N. Bates, and H. J. de Baar, Deep Sea Research Part II: Topical Studies in Oceanography **56**, 554 – 577 (2009).

[86] J. T. Randerson, M. V. Thompson, T. J. Conway, I. Y. Fung, and C. B. Field, Global Biogeochemical Cycles **11**, 535–560 (1997).

[87] S. C. Olsen and J. T. Randerson, Journal of Geophysical Research: Atmospheres **109** (2004). D02301.

[88] P. K. Patra, M. Takigawa, K. Ishijima, B. Choi, D. Cunnold, E. Dlugokencky, P. Fraser, A. Gomezpelaez, T. Goo, J. Kim, P. Krummel, F. Langenfelds, R.and Meinhardt, H. Mukai, S. Doherty, R. Prinn, P. Simmonds, P. Steele, Y. Tohjima, K. Tsuboi, K. Uhse, R. Weiss, D. Worthy, and T. Nakazawa, Journal of the Meteorological Society of Japan. Ser. II **87**, 635–663 (2009).

[89] P. Patra, S. Houweling, M. Krol, P. Bousquet, D. Belikov, D. Bergmann, H. Bian, S. Cameron, M. P. Chipperfield, K. Corbin, C. Fortems, A. Fraser, E. Gloor, P. Hess, A. Ito, S. R. Kawa, R. M. Law, Z. Loh, S. Maksyutov, L. Meng, P. I. Palmer, R. G. Prinn, M. Rigby, R. Saito, and C. Wilson, Atmospheric Chemistry and Physics **11**, 12813âĂŞ12837 (2011).

[90] P. K. Patra, M. C. Krol, S. A. Montzka, T. Arnold, E. L. Atlas, B. R. Lintner, B. B. Stephens, B. Xiang, J. W. Elkins, P. J. Fraser, A. Ghosh, E. J. Hintsa, D. F. Hurst, K. Ishijima, P. B. Krummel, B. R. Miller, K. Miyazaki, F. L. Moore, J. Muhle, R. G. O/′Doherty, S. Prinn, L. P. Steele, M. Takigawa, H. J. Wang, R. F. Weiss, S. C. Wofsy, and D. Young, Nature **513**, 219–223 (2014).

[91] A. Ito and M. Inatomi, Biogeosciences **9**, 759–773 (2012).

[92] G. R. van der Werf, J. T. Randerson, L. Giglio, G. J. Collatz, M. Mu, P. S. Kasibhatla, D. C. Morton, R. S. DeFries, Y. Jin, and T. T. van Leeuwen, Atmospheric Chemistry and Physics **10**, 11707–11735 (2010).

[93] I. Fung, J. Lerner, E. Matthews, M. Prather, L. Steels, and P. Fraser, Journal of Geophysical Research **96**, 13033–13065 (1991).

[94] H. W. Bange, T. G. Bell, M. Cornejo, A. Freing, G. Uher, R. C. Upstill-Goddard, and G. Zhang, Environmental Chemistry pp. 195–197 (2009).

[95] S. Szopa, Y. Balkanski, M. Schulz, S. Bekki, D. Cugnet, A. Fortems-Cheiney, S. Turquety, A. Cozic, C. DÃľandreis, D. Hauglustaine, A. Idelkadi, J. LathiÃĺre, F. Lefevre, M. Marchand, R. Vuolo, N. Yan, and J.-L. Dufresne, Climate Dynamics **40**, 2223–2250 (2013).

[96] F. Hourdin, I. Musat, S. Bony, P. Braconnot, F. Codron, J.-L. Dufresne, L. Fairhead, M.-A. Filiberti, P. Friedlingstein, J.-Y. Grandpeix, G. Krinner, P. LeVan, Z.-X. Li, and F. Lott, Climate Dynamics **27**, 787–813 (2006).

[97] D. A. Hauglustaine, F. Hourdin, L. Jourdain, M.-A. Filiberti, S. Walters, J.-F. Lamarque, and E. A. Holland, Journal of Geophysical Research: Atmospheres **109** (2004). D04314.

[98] G. A. Folberth, D. A. Hauglustaine, J. Lathière, and F. Brocheton, Atmospheric Chemistry and Physics **6**, 2273–2319 (2006).

[99] G. Krinner, N. Viovy, N. de Noblet-DucoudrÃĺ, J. OgÃľe, J. Polcher, P. Friedlingstein, P. Ciais, S. Sitch, and I. C. Prentice, Global Biogeochemical Cycles **19** (2005). GB1015.

[100] J. O. Kaplan, G. Folberth, and D. A. Hauglustaine, Global Biogeochemical Cycles **20** (2006).

[101] G. R. van der Werf, J. T. Randerson, L. Giglio, G. J. Collatz, P. S. Kasibhatla, and A. F. Arellano Jr., Atmospheric Chemistry and Physics **6**, 3423–3441 (2006).

[102] M. G. Sanderson, Global Biogeochemical Cycles **10** (1996).

[103] G. Lambert and S. Schmidt, Chemosphere **26**, 579 – 589 (1993).

[104] A. J. Ridgwell, S. J. Marshall, and K. Gregson, Global Biogeochemical Cycles **13**, 59–70 (1999).

[105] E. Matthews, I. Fung, and J. Lerner, Global Biogeochemical Cycles **5**, 3–24 (1991).

[106] L. K. Emmons, S. Walters, P. G. Hess, J.-F. Lamarque, G. G. Pfister, D. Fillmore, C. Granier, A. Guenther, D. Kinnison, T. Laepple, J. Orlando, X. Tie, G. Tyndall, C. Wiedinmyer, S. L. Baughcum, and S. Kloster, Geoscientific Model Development **3**, 43–67 (2010).

[107] C. Granier, A. Guenther, J. Lamarque, A. Mieville, J. Muller, J. Olivier, J. Orlando, J. Peters, G. Petron, G. Tyndall, and S. Wallens, available at http://www.aero.jussieu.fr/projet/ACCENT/POET.php. (2005).

[108] T. Ohara, H. Akimoto, J. Kurokawa, N. Horii, K. Yamaji, X. Yan, and T. Hayasaka, Atmospheric Chemistry and Physics **7**, 4419–4444 (2007).

[109] V. Sheel, L. K. Sahu, M. Kajino, M. Deushi, O. Stein, and P. Nedelec, Journal of Geophysical Research: Atmospheres **119**, 9123–9141 (2014).

[110] P. Jöckel, H. Tost, A. Pozzer, C. Bruhl, J. Buchholz, L. Ganzeveld, P. Hoor, A. Kerkweg, M. Lawrence, R. Sander, B. Steil, G. Stiller, M. Tanarhte, D. Taraborrelli, J. van Aardenne, and J. Lelieveld, Atmospheric Chemistry and Physics **6**, 5067–5104 (2006).

[111] E. Roeckner, R. Brokopf, M. Esch, M. Giorgetta, S. Hagemann, L. Kornblueh, E. Manzini, U. Schlese, and U. Schulzweida, Journal of Climate **19**, 2527–2550 (2006).

[112] P. Jöckel, A. Kerkweg, A. Pozzer, R. Sander, H. Tost, H. Riede, A. Baumgaertner, S. Gromov, and B. Kern, Geoscientific Model Development **3**, 717–752 (2010).

[113] J.-F. Lamarque, T. C. Bond, V. Eyring, C. Granier, A. Heil, Z. Klimont, D. Lee, C. Liousse, A. Mieville, B. Owen, M. G. Schultz, D. Shindell, S. J. Smith, E. Stehfest, J. Van Aardenne, O. R. Cooper, M. Kainuma, N. Mahowald, J. R. McConnell, V. Naik, K. Riahi, and D. P. van Vuuren, Atmospheric Chemistry and Physics **10**, 7017–7039 (2010).

[114] J. Lelieveld, C. Brühl, P. Jöckel, B. Steil, P. J. Crutzen, H. Fischer, M. A. Giorgetta, P. Hoor, M. G. Lawrence, R. Sausen, and H. Tost, Atmospheric Chemistry and Physics **7**, 1313–1332 (2007).

[115] A. Pozzer, P. Jöckel, H. Tost, R. Sander, L. Ganzeveld, A. Kerkweg, and J. Lelieveld, Atmospheric Chemistry and Physics **7**, 2527–2550 (2007).

[116] A. Pozzer, P. Jöckel, and J. Van Aardenne, Atmospheric Chemistry and Physics **9**, 9417–9432 (2009).

[117] J. Yoon and A. Pozzer, Atmospheric Chemistry and Physics **14**, 10465–10482 (2014).

[118] S. Han, Y. Kondo, N. Oshima, N. Takegawa, Y. Miyazaki, M. Hu, P. Lin, Z. Deng, Y. Zhao, N. Sugimoto, and Y. Wu, Journal of Geophysical Research: Atmospheres **114** (2009).

[119] N. Elguindi, H. Clark, C. Ordóñez, V. Thouret, J. Flemming, O. Stein, V. Huijnen, P. Moinat, A. Inness, V.-H. Peuch, A. Stohl, S. Turquety, G. Athier, J.-P. Cammas, and M. Schultz, Geoscientific Model Development **3**, 501–518 (2010).

[120] R. Kumar, M. Naja, G. G. Pfister, M. C. Barth, and G. P. Brasseur, Geoscientific Model Development **5**, 321–343 (2012).

[121] E. Cuevas, C. Camino, A. Benedetti, S. Basart, E. Terradellas, J. M. Baldasano, J.-J. Morcrette, B. Marticorena, P. Goloub, A. Mortier, A. Berjón, Y. Hernández, M. Gil-Ojeda, and M. Schulz, Atmospheric Chemistry and Physics Discussions **14**, 27797–27879 (2014).

[122] R. M. Law, P. J. Rayner, L. P. Steele, and I. G. Enting, Global Biogeochemical Cycles **16**, 1–1–1–18 (2002). 1053.

[123] C. Mallik, S. Lal, and S. Venkataramani, Journal of Atmospheric Chemistry pp. 1–22 (2015).

[124] J. Kar, H. Bremer, J. R. Drummond, Y. J. Rochon, D. B. A. Jones, F. Nichitiu, J. Zou, J. Liu, J. C. Gille, D. P. Edwards, M. N. Deeter, G. Francis, D. Ziskin, and J. Warner, Geophysical Research Letters **31** (2004).

[125] W. J. Randel and M. Park, Journal of Geophysical Research: Atmospheres **111** (2006).

[126] M. Park, W. J. Randel, L. K. Emmons, and N. J. Livesey, Journal of Geophysical Research: Atmospheres **114** (2009).

[127] A. K. Baker, T. J. Schuck, C. A. M. Brenninkmeijer, A. Rauthe-SchÃűch, F. Slemr, P. F. J. van Velthoven, and J. Lelieveld, Geophysical Research Letters **39** (2012). L10813.

[128] S. Lal, M. Naja, and B. Subbaraya, Atmospheric Environment **34**, 2713 – 2724 (2000).

[129] S. C. Lai, A. K. Baker, T. J. Schuck, P. van Velthoven, D. E. Oram, A. Zahn, M. Hermann, A. Weigelt, F. Slemr, C. A. M. Brenninkmeijer, and H. Ziereis, Atmospheric Chemistry and Physics **10**, 1649–1660 (2010).

[130] R. S. Russo, R. W. Talbot, J. E. Dibb, E. Scheuer, G. Seid, C. E. Jordan, H. E. Fuelberg, G. W. Sachse, M. A. Avery, S. A. Vay, D. R. Blake, N. J. Blake, E. Atlas, A. Fried, S. T. Sandholm, D. Tan, H. B. Singh, J. Snow, and B. G. Heikes, Journal of Geophysical Research: Atmospheres **108** (2003).

[131] P. Suntharalingam, D. J. Jacob, P. I. Palmer, J. A. Logan, R. M. Yantosca, Y. Xiao, M. J. Evans, D. G. Streets, S. L. Vay, and G. W. Sachse, Journal of Geophysical Research: Atmospheres **109** (2004).

[132] N. Takegawa, Y. Kondo, M. Koike, G. Chen, T. Machida, T. Watai, D. R. Blake, D. G. Streets, J.-H. Woo, G. R. Carmichael, K. Kita, Y. Miyazaki, T. Shirai, J. B. Liley, and T. Ogawa, Journal of Geophysical Research: Atmospheres **109** (2004).

[133] A. Wada, H. Matsueda, Y. Sawa, K. Tsuboi, and S. Okubo, Atmospheric Environment **45**, 2129 – 2137 (2011).

[134] R. Dhammapala, C. Claiborn, C. Simpson, and J. Jimenez, Atmospheric Environment **41**, 1512 – 1520 (2007).

[135] G. CAO, X. ZHANG, S. GONG, and F. ZHENG, Journal of Environmental Sciences **20**, 50 – 55 (2008).

[136] D. G. Streets, T. C. Bond, G. R. Carmichael, S. D. Fernandes, Q. Fu, D. He, Z. Klimont, S. M. Nelson, N. Y. Tsai, M. Q. Wang, J.-H. Woo, and K. F. Yarber, Journal of Geophysical Research: Atmospheres **108** (2003).

[137] O. SÃąnchez-Ccoyllo, R. Ynoue, L. Martins, R. Astolfo, R. Miranda, E. Freitas, A. Borges, A. Fornaro, H. Freitas, A. Moreira, and M. Andrade, Environmental Monitoring and Assessment **149**, 241–249 (2009).

[138] D. Westerdahl, X. Wang, X. Pan, and K. M. Zhang, Atmospheric Environment **43**, 697 – 705 (2009).

[139] I. Levin, B. Kromer, M. Schmidt, and H. Sartorius, Geophysical Research Letters **30** (2003). 2194.

[140] J. C. Turnbull, A. Karion, M. L. Fischer, I. Faloona, T. Guilderson, S. J. Lehman, B. R. Miller, J. B. Miller, S. Montzka, T. Sherwood, S. Saripalli, C. Sweeney, and P. P. Tans, Atmospheric Chemistry and Physics **11**, 705–721 (2011).

[141] F. R. Vogel, S. HAMMER, A. STEINHOF, B. KROMER, and I. LEVIN, Tellus B **62**, 512–520 (2010).

[142] S. Ballav, P. K. PATRA, M. TAKIGAWA, S. GHOSH, U. K. DE, S. MAKSYUTOV, S. MURAYAMA, H. MUKAI, and S. HASHIMOTO, Journal of the Meteorological Society of Japan. Ser. I **90**, 959–976 (2012).

[143] D. P. Edwards, L. K. Emmons, D. A. Hauglustaine, D. A. Chu, J. C. Gille, Y. J. Kaufman, G. PÃľtron, L. N. Yurganov, L. Giglio, M. N. Deeter, V. Yudin, D. C. Ziskin, J. Warner, J.-F. Lamarque, G. L. Francis, S. P. Ho, D. Mao, J. Chen, E. I. Grechko, and J. R. Drummond, Journal of Geophysical Research: Atmospheres **109** (2004).

[144] H. Sodemann, M. Pommier, S. R. Arnold, S. A. Monks, K. Stebel, J. F. Burkhart, J. W. Hair, G. S. Diskin, C. Clerbaux, P.-F. Coheur, D. Hurtmans, H. Schlager, A.-M. Blechschmidt, J. E. Kristjánsson, and A. Stohl, Atmospheric Chemistry and Physics **11**, 3631–3651 (2011).

[145] J. Lloyd, O. Kolle, H. Fritsch, S. R. de Freitas, M. A. F. Silva Dias, P. Artaxo, A. D. Nobre, A. C. de Araújo, B. Kruijt, L. Sogacheva, G. Fisch,

A. Thielmann, U. Kuhn, and M. O. Andreae, Biogeosciences **4**, 759–768 (2007).

[146] N. J. Livesey, J. A. Logan, M. L. Santee, J. W. Waters, R. M. Doherty, W. G. Read, L. Froidevaux, and J. H. Jiang, Atmospheric Chemistry and Physics **13**, 579–598 (2013).

[147] T. Holloway, H. Levy, and P. Kasibhatla, Journal of Geophysical Research: Atmospheres **105**, 12123–12147 (2000).

[148] K. P. Vadrevu, L. Giglio, and C. Justice, Atmospheric Environment **64**, 179 – 191 (2013).

[149] I. Girach and P. R. Nair, Atmospheric Environment **99**, 599 – 609 (2014).

[150] Q. Li, J. H. Jiang, D. L. Wu, W. G. Read, N. J. Livesey, J. W. Waters, Y. Zhang, B. Wang, M. J. Filipiak, C. P. Davis, S. Turquety, S. Wu, R. J. Park, R. M. Yantosca, and D. J. Jacob, Geophysical Research Letters **32** (2005).

[151] J. H. Jiang, N. J. Livesey, H. Su, L. Neary, J. C. McConnell, and N. A. D. Richards, Geophysical Research Letters **34** (2007). L18812.

[152] S. Srivastava and V. Sheel, Atmospheric Environment **67**, 53 – 62 (2013).

[153] P. J. Crutzen, Nature **350**, 380–382 (1991).

[154] R. J. Cicerone and R. S. Oremland, Global Biogeochemical Cycles **2**, 299–327 (1988).

[155] A. L. Ganesan, A. Chatterjee, R. G. Prinn, C. M. Harth, P. K. Salameh, A. J. Manning, B. D. Hall, J. Mühle, L. K. Meredith, R. F. Weiss, S. O'Doherty, and D. Young, Atmospheric Chemistry and Physics **13**, 10633–10644 (2013).

[156] D. E. J. Worthy, E. Chan, M. Ishizawa, D. Chan, C. Poss, E. J. Dlugokencky, S. Maksyutov, and I. Levin, Journal of Geophysical Research: Atmospheres **114** (2009). D10301.

[157] S. Lal, N. Chandra, and S. Venkataramani, Current Science **109** (2015).

[158] S. Lal, S. Venkataramani, N. Chandra, O. R. Cooper, J. Brioude, and M. Naja, Journal of Geophysical Research: Atmospheres **119**, 10012–10026 (2014). 2014JD021854.

[159] R. Agarwal and J. Garg, Current Science **96** (2012).

[160] K. Yamaji, T. Ohara, and H. Akimoto, Atmospheric Environment **37**, 4393 – 4406 (2003).

[161] X. Yan, H. Akiyama, K. Yagi, and H. Akimoto, Global Biogeochemical Cycles **23** (2009). GB2002.

[162] X. Yan, Z. Cai, T. Ohara, and H. Akimoto, Journal of Geophysical Research: Atmospheres **108** (2003). 4505.

[163] J. Muhle, C. A. M. Brenninkmeijer, T. S. Rhee, F. Slemr, D. E. Oram, S. A. Penkett, and A. Zahn, Geophysical Research Letters **29**, 16–1–16–4 (2002). 1910.

[164] Y. Xiao, D. J. Jacob, J. S. Wang, J. A. Logan, P. I. Palmer, P. Suntharalingam, R. M. Yantosca, G. W. Sachse, D. R. Blake, and D. G. Streets, Journal of Geophysical Research: Atmospheres **109** (2004). D15S16.

[165] P. O. Wennberg, W. Mui, D. Wunch, E. A. Kort, D. R. Blake, E. L. Atlas, G. W. Santoni, S. C. Wofsy, G. S. Diskin, S. Jeong, and M. L. Fischer, Environmental Science & Technology **46**, 9282–9289 (2012).

[166] J. Peischl, T. B. Ryerson, J. Brioude, K. C. Aikin, A. E. Andrews, E. Atlas, D. Blake, B. C. Daube, J. A. de Gouw, E. Dlugokencky, G. J. Frost, D. R. Gentner, J. B. Gilman, A. H. Goldstein, R. A. Harley, J. S. Holloway, J. Kofler, W. C. Kuster, P. M. Lang, P. C. Novelli, G. W. Santoni, M. Trainer, S. C. Wofsy, and D. D. Parrish, Journal of Geophysical Research: Atmospheres **118**, 4974–4990 (2013).

[167] Y. Tohjima, M. Kubo, C. Minejima, H. Mukai, H. Tanimoto, A. Ganshin, S. Maksyutov, K. Katsumata, T. Machida, and K. Kita, Atmospheric Chemistry and Physics **14**, 1663–1677 (2014).

[168] Y.-K. Hsu, T. VanCuren, S. Park, C. Jakober, J. Herner, M. FitzGibbon, D. R. Blake, and D. D. Parrish, Atmospheric Environment **44**, 1 – 7 (2010).

[169] S. Newman, X. Xu, K. R. Gurney, Y.-K. Hsu, K.-F. Li, X. Jiang, R. Keeling, S. Feng, D. O'Keefe, R. Patarasuk, K. W. Wong, P. Rao, M. L. Fischer, and Y. L. Yung, Atmospheric Chemistry and Physics Discussions **15**, 29591–29638 (2015).

[170] C. D. Keeling, Geochimica et Cosmochimica Acta **13**, 322 – 334 (1958).

[171] G. Monteil, S. Houweling, E. J. Dlugockenky, G. Maenhout, B. H. Vaughn, J. W. C. White, and T. Rockmann, Atmospheric Chemistry and Physics **11**, 9141–9153 (2011).

[172] C. Gerbig, A. J. Dolman, and M. Heimann, Biogeosciences **6**, 1949–1959 (2009).

List of Publications

Publications in Journals

1. **Chandra, N.,** S. Lal, S. Venkataramani, P. K. Patra and V. Sheel (2015), Temporal variations in CO2 and CO at Ahmedabad in western India, Atmos. Chem. Phys. Discuss., 15, 32185-32238, doi:10.5194/acpd-15-32185-2015.

2. **Chandra, N.,** S. Venkataramani, S. Lal, V. Sheel and A. Pozzer (2016), Effects of convection and long-range transport on the distribution of carbon monoxide in the troposphere over India., Atmospheric Pollution Res.(In press).

3. Lal, S., **N. Chandra**, and S. Venkataramani (2015): A study of CO_2 and related trace gases using a laser based technique at an urban site in western India, CURRENT SCIENCE, VOL. 109, NO. 11.

4. Mallik, C., **N. Chandra,** S. Venkataramani and S. Lal (2016), Variability of atmospheric carbonyl sulfide at a semi-arid urban site in western India, Sci Total Environ., doi: 10.1016/j.scitotenv.2016.02.014.

5. Lal, S., S. Venkataramani, **N. Chandra**, O. R. Cooper, J. Brioude, and M. Naja (2014), Transport effects on the vertical distribution of tropospheric ozone over western India, J. Geophys. Res. Atmos., 119,doi:10.1002/2014JD021854.

Publications under preparation

1. **Chandra, N.,** S. Lal, S. Venkataramani, P. K. Patra, M. Ramonet and X. Lin, Methane at Ahmedabad: Measurements and models comparison.

2. **Chandra, N.,** S. Lal, P. K. Patra and S. Venkataramani, Tropospheric distributions of CO_2 over Delhi: Airborne measurements and model simulations.

Atmos. Chem. Phys. Discuss., 15, 32185–32238, 2015
www.atmos-chem-phys-discuss.net/15/32185/2015/
doi:10.5194/acpd-15-32185-2015

Atmospheric Chemistry and Physics Discussions

Temporal variations in CO_2 and CO at Ahmedabad in western India

N. Chandra[1,2], S. Lal[1], S. Venkataramani[1], P. K. Patra[3], and V. Sheel[1]

[1]Physical Research Laboratory, Ahmedabad 380009, India
[2]Indian Institute of Technology, Gandhinagar 382355, India
[3]Department of Environmental Geochemical Cycle Research, JAMSTEC, Yokohama 2360001, Japan

Received: 29 September 2015 – Accepted: 4 November 2015 – Published: 17 November 2015

Correspondence to: S. Lal (shyam@prl.res.in)

Published by Copernicus Publications on behalf of the European Geosciences Union.

Abstract

About 70 % of the anthropogenic CO_2 is emitted from the megacities and urban areas of the world. In-situ simultaneous measurements of carbon dioxide (CO_2) and carbon monoxide (CO) have been made using a state-of-the-art laser based cavity ring down spectroscopy technique at Ahmedabad, an urban site in western India, from November 2013 to May 2015 with a break during March to June 2014. Annual average concentrations of CO_2 and CO have been found to be 413.0 ± 13.7 ppm and 0.50 ± 0.37 ppm respectively. Both the species show strong seasonality, with lower concentrations of 400.3 ± 6.8 ppm and 0.19 ± 0.13 ppm, respectively during the south-west monsoon, and higher values of 419.6 ± 22.8 ppm and 0.72 ± 0.68 ppm, respectively in autumn (SON). Strong diurnal variations are also observed for both the species. The common factors for diurnal cycles of CO_2 and CO are the vertical mixing and rush hour traffic, while the influence of biospheric fluxes is also seen in CO_2 diurnal cycle. Using CO and CO_2 covariation, we differentiate the anthropogenic and biospheric components of CO_2 and found that significant contributions of biospheric respiration and anthropogenic emission in the late night (00:00–05:00 IST) and evening rush hours (18:00–22:00 IST) respectively. We compute total yearly emission of CO to be 69.2 ± 0.07 Gg for the study region using the observed CO : CO_2 correlation slope and bottom-up CO_2 emission inventory. This calculated emission of CO is 52 % larger than the estimated emission of CO by the EDGAR inventory. The observations of CO_2 have been compared with an atmospheric chemistry transport model (i.e., ACTM), which incorporates various components of CO_2 fluxes. ACTM is able to capture the basic variabilities, but both diurnal and seasonal amplitudes are largely underestimated compared to the observations. We attribute this underestimation by model to uncertainties in terrestrial biosphere fluxes and coarse model resolution. The fossil fuel signal from the model shows fairly good correlation with observed CO_2 variations, which supports the overall dominance of fossil fuel emissions over the biospheric fluxes in this urban region.

1 Introduction

Carbon dioxide (CO_2) is the most important anthropogenically emitted greenhouse gas (GHG) and has increased substantially from 278 to 390 ppm in the atmosphere since the beginning of the industrial era (circa 1750). It has contributed to more than 65 % of the radiative forcing increase since 1750 and hence leads to the significant impact on the climate system (Ciais et al., 2013). Major causes of CO_2 increase are anthropogenic emissions, especially fossil fuel combustion, cement production and land use change. The cumulative anthropogenic CO_2 emissions from the preindustrial era to 2011, are estimated to be 545 ± 85 Pg C, out of which fossil fuel combustion and cement production contributed 365 ± 30 Pg C and land use change (including deforestation, afforestation and reforestation) contributed 180 ± 80 Pg C (Ciais et al., 2013). Land and oceans are the two important sinks of atmospheric CO_2, which remove about half of the anthropogenic emissions (Le Quéré et al., 2014). Though the global fluxes of CO_2 can be estimated fairly well, the regional scale (e.g. sub-continent and country level) fluxes are associated with quite high uncertainty especially over South Asian region; the estimation uncertainty being larger than the value itself (Patra et al., 2013; Peylin et al., 2013). Detailed scientific understanding of the flux distributions is needed for formulating effective mitigation policies (such as Kyoto Protocol). In inverse modelling, CO_2 flux is estimated from atmospheric CO_2 observations and using an atmospheric transport model. Therefore, it is necessary to measure CO_2 concentrations covering different ecosystems and geographical areas of the world, which unfortunately is not the case (Gurney et al., 2002).

Although, carbon monoxide (CO) is not a direct GHG but it affects climate and air quality through the formation of CO_2 and ozone (O_3). It affects the oxidizing capacity of the atmosphere through reaction with the free OH radicals. Additionally, CO can be used as a surrogate tracer for detecting and quantifying anthropogenic emissions from burning processes, since it is a major product of incomplete combustion (Turnbull et al., 2006; Wang et al., 2010). The vehicular emissions contribute large fluxes of CO_2 and

CO to the atmosphere in urban regions. The verification of future mitigation activities demand for quantifying the spatiotemporal distributions of these emissions. The CO emissions have large uncertainty as compared to CO_2, because its emission strongly depends on the combustion efficiency, the vehicle engine and their adopted technology as well as driving conditions. The correlation slope between the atmospheric variations of CO and CO_2 can be used to quantify the fossil fuel contribution, distinguish between different burning processes or to determine the burning efficiency and overall trend of anthropogenic emissions of CO in a city (Turnbull et al., 2006; Wunch et al., 2009; Newman et al., 2013; Popa et al., 2014). The $CO : CO_2$ ratios are higher for low combustion sources (e.g. forest fires) and lower for good or efficient combustion sources (Andreae and Merlet, 2001; Wang et al., 2010). Further, the $CO : CO_2$ ratio can be used for estimating the total emission of CO over an urban area provided the total CO_2 emission is known for that area. Hence, the information about $CO : CO_2$ ratio will be helpful to understand the effects on the CO emissions after adopting the newer vehicular technologies and new cleaner emission norms and finally will be beneficial for reducing the uncertainties in CO emission inventories. Several ground based and aircraft based correlation studies of $CO : CO_2$ have been done in the past from different parts of the world (Turnbull et al., 2006; Wunch et al., 2009; Wang et al., 2010; Newman et al., 2013) but such study has not been done in India except recently reported results from weekly samples for three Indian sites by Lin et al. (2015).

India is the second largest populous country in the world having about 1.3 billion inhabitants. Rapid socioeconomic developments and urbanization have made it the third largest CO_2 emitter next to China and USA since 2011 but it ranks at 137th level based on the per capita emission rate of CO_2 (EDGAR v4.2; CDIAC – Boden et al., 2015). For example, in 2010 India's emission rate was 2.2 t CO_2 eq capita^{-1} while the developed countries like USA, Russia and UK had emission rates of about 21.6, 17.6 and 10.9 t CO_2 eq capita^{-1} respectively (EDGAR v4.2). The budgets of these gases on regional as well as global scales can be estimated by bottom-up and top down approaches. Large uncertainties are associated in the GHGs budgets over South Asia,

especially over India than for other continents. Based on the atmospheric CO_2 inversion using model calculations, Patra et al. (2013) found that the biosphere in South Asia acted as the net CO_2 sink during 2007–2008 and estimated CO_2 flux of about $-104 \pm 150\,Tg\,C\,yr^{-1}$. Further, based on the bottom-up approach, Patra et al. (2013) gave an estimate of biospheric flux of CO_2 of about $-191 \pm 193\,Tg\,C\,yr^{-1}$ for the period of 2000–2009. Both these approaches show the range of uncertainty 100–150 %. One of the major sources of these large uncertainties is the lack of spatial and temporal observations of these gases (Law et al., 2002; Patra et al., 2013).

The first observations of CO_2, CO and other greenhouse gases started in February 1993 from Cape Rama (CRI) on the south-west coast of India using flask samples (Bhattacharya et al., 2009). After that, several other groups have initiated the measurements of surface level greenhouse gases (Mahesh et al., 2014; Sharma et al., 2014; Tiwari et al., 2014; Lin et al., 2015). Most of these measurements are made at weakly or fortnightly time intervals or at lower accuracy. These data are very useful for several studies like analyzing seasonal cycle, growth rate, and estimating the regional (subcontinental) carbon sources and sinks after combining their concentrations with inverse modelling and atmospheric tracer transport models. However, some important studies like their diurnal variations, temporal covariance ... etc. are not possible from these measurements due to their limitations. Analysis of temporal covariance of atmospheric mixing processes and variation of flux on shorter timescales, e.g., sub-daily, is essential for understanding local to urban scale CO_2 flux variations (Ahmadov et al., 2007; Pérez-Landa et al., 2007; Briber et al., 2013; Lopez et al., 2013; Ammoura et al., 2014; Ballav et al., 2015). Two aircraft based measurements programs namely, Civil Aircraft for the regular Investigation of the atmosphere Based on an Instrument Container (CARIBIC) (Brenninkmeijer et al., 2007) and Comprehensive Observation Network for TRace gases by AIrLiner (CONTRAIL) (Machida et al., 2008) have provided important first look on the South Asian CO_2 budget, but these data have their own limitations (Patra et al., 2011; Schuck et al., 2010, 2012). The focus of the Indigenous research is lacking in terms of making the continuous and simultaneous measurements of CO_2

and CO over the urban regions, where variety of emission sources influence the level of these gases.

Simultaneous continuous measurements of CO_2 and CO have been made since November 2013 from an urban site Ahmedabad located in the western India using very highly sensitive laser based technique. The preliminary results of these measurements for one month period have been reported in (Lal et al., 2015). These detailed measurements are utilized for studying the temporal variations (diurnal and seasonal) of both gases, their emissions characteristics on diurnal and seasonal scale using their mutual correlations, estimating the contribution of vehicular and biospheric emission components in the diurnal cycle of CO_2 using the ratios of CO to CO_2 and rough estimate of the annual CO emissions from study region. Finally, the measurements of CO_2 have been compared with simulations using an atmospheric chemistry-transport model to discuss roles of various processes contributing to CO_2 concentrations variations.

2 Site description, local emission sources and meteorology

The measurement facility is housed inside the campus of the Physical Research Laboratory (PRL), situated in the western part of Ahmedabad (23.03° N, 72.55° E, 55 m a.m.s.l.) in the Gujarat state of India (Fig. 1). It is a semi-arid, urban region in western India, having a variety of large and small scale industries (Textile mills and pharmaceutical production facilities) in east and north outskirts. The institute is situated about 15–20 km away from these industrial areas. The western part is dominated by the residential areas. The city has a population of about 5.6 million (Census India, 2011) and has large number of automobiles (about 3.2 million), which are increasing at the rate of about $10\,\%\,yr^{-1}$. Most of the city buses and auto-rickshaws (three-wheelers) use compressed natural gas (CNG) as a fuel. The transport-related activities are the major contributors of various pollutants (Mallik et al., 2015). The Indo-Gangetic Plain (IGP) is situated in the northeast of Ahmedabad, which is very densely populated region and has high levels of pollutants emitted from various industries and power plants

along with anthropogenic emissions from burning of fossil fuels and traditional biofuels (wood, cow-dung cake etc). The Thar Desert and the Arabian Sea are situated in the northwest and southwest of Ahmedabad respectively.

Figure 1 shows average monthly variability of temperature, relative humidity (RH), wind speed based on data taken from Wunderground (http://www.wunderground.com), rainfall from Tropical Rainfall Measuring Mission (TRMM) and planetary boundary layer (PBL) height from the Modern-Era Retrospective Analysis for Research and Applications (MEERA). The wind rose plot shows the surface level wind speed and direction during different seasons over Ahmedabad in 2014. This place is known for its semi-arid climate. Large seasonal variations are observed in the wind speed and direction over Ahmedabad. During monsoon (June–July–August), the inter-tropical convergence zone (ITCZ) moves northward across India. It results in the transport of moist and cleaner marine air from the Arabian Sea and the Indian Ocean to the study location by south westerly winds, or the so-called southwest monsoon (summer monsoon). The first shower due to the onset of the southwest monsoon occurs in July and it retreats in the mid of September over Ahmedabad. Due to heavy rain and winds mostly from oceanic region, RH shows higher values in July, August and September. Highest RH of about 83 % is observed in September. The long-range transport of air masses from the northeast part of the Asian continent starts to prevail over the Indian region when ITCZ moves back southward in September and October. These months are regarded as transition period for the monsoon. During autumn (September–October–November), the winds are calm and undergo a change in their direction from south west to north east. When the transition of winds takes placed from oceanic to continental region in October, the air gets dryer and RH decreases until December. The winds are north easterly during winter (December- January–February) and transport pollutants mostly from continental region (IGP region). During pre-monsoon season (March–April–May), winds are north westerly and little south westerly which transport mixed air masses from continent and oceanic regions. The average wind speed is observed higher in June and July while lower in October and March when transition of wind starts from

oceanic to continental and continental to oceanic respectively. The monthly averaged temperature starts increasing from January and attains maximum ($34.6 \pm 1.4\,^{\circ}C$) in June, followed by a decrease until September and temperature is slightly warmer in October compared to the adjacent months. The monthly variation in planetary boundary layer height (PBLH) closely resembles with the temperature pattern. Maximum PBLH of about 1130 m is found in June and it remains in the lower range at about 500 m during July to January. The ventilation coefficient (VC) is obtained by multiplying wind speed and PBL height which gradually increases from January to attain the maximum value in June and the lowest values of VC are observed in October and November.

3 Experiment and model details

3.1 Experimental method

The measurements of ambient CO_2 and CO are performed using a Picarro-G2401 instrument, which is based on the wavelength scanned cavity ring down spectroscopic (CRDS) technique. CRDS is now a well-established technique for making high-sensitivity and high precision measurements of trace gases in the ambient air, due to its three main characteristics (Bitter et al., 2005; Chen et al., 2010; Karion et al., 2013). First, it provides very long interaction path length (around 20 km) between the sample and the incident wavelength, by utilizing a 3-mirror configuration, which enhances its sensitivity over other conventional techniques like Non-dispersive Infrared Spectroscopy (NDIR) and Fourier Transform Infrared Spectroscopy (FTIR). The second is its ability to isolate a single spectral feature with a resolution of $0.0003\,cm^{-1}$, which ensures that the peak height or area is linearly proportional to the concentration. The third advantage is that the measurements of trace gases using this technique are achieved by measuring the decay time of light intensity inside the cavity while the conventional optical absorption spectroscopy technique is based on absorption of light intensity. Hence, it increases the accuracy of measurements because it is insensitive

to the fluctuations of incident light. The precision and accuracy of these measurements follow the WMO compatibility goals of ±0.1 ppm CO_2 and ±2 ppb CO.

Figure 2 shows the schematic diagram of the measurement system, which consists of the analyser, a glass bulb, a Nafion dryer, a heatless dryer, other associated pumps and a set of calibration mixtures. Atmospheric air is sampled continuously from the terrace of the building (20 m above the ground level) through an 1/4 inch PFA Teflon tube via a glass manifold. An external pump is attached on one side of the glass manifold to flush the sample line. Water vapor affects the measurements of CO_2 by diluting its mixing ratios in the air and by broadening the spectroscopic absorption lines of other gases. Although, the instrument has ability to correct for the water vapour interferes by using an experimentally derived water vapor correction algorithms (Crosson, 2008), but it has an absolute H_2O uncertainty of ∼ 1 % (Chen et al., 2010) and can introduces a source of error using a single water vapor correction algorithm (Welp et al., 2013). This error can be minimized by either generating the correction coefficients periodically in the laboratory or by removing the water vapour from the sample air. Conducting the water vapor correction experiment is bit tricky and need extra care as discussed by Welp et al. (2013). Hence, we prefer to remove water vapour from the sample air by introducing a 50-strand Nafion dryer (Perma Pure, p/n PD-50T-24MSS) in the upstream of the analyser. Nafion dryer contains a bunch of semi-permeable membrane tubing separating an internal sample gas stream from a counter sheath flow of dry gas in stainless steel outer shell. The partial pressure of water vapour in the sheath air should be lower than the sample air for effectively removing the water vapour from the sample air. A heatless dryer generates dry air using a 4 bar compressor (KNF, MODEL: NO35ATE) which is used as a sheath flow in Nafion dryer. After drying, sample air passes through the PTFE filter (polytetrafluoroethylene; 5 µm Sartorius AG, Germany) before entering the instrument cavity. This setup dries the ambient air near to 0.03 % (300 ppm) concentration of H_2O. The CO_2 concentrations are reported on the WMO scale, using the three calibration mixtures of CO_2 (350.67 ± 0.02, 399.68 ± 0.002 and 426.20 ± 0.006 ppm) from NOAA, Bolder USA, while the concentration of CO is re-

ported against a calibration mixture of CO (970 ppb) from Linde UK. An additional gas standard tank (CO_2: 338 ppm, CO: 700 ppm), known as the "target", is used to determine the precision of the instrument. The target tank values are calibrated against the CO_2 and CO calibration mixtures. The target gas is introduced in the instrument for a period of 24 h. For CO_2 and CO, the 5 min precisions were found to be 0.015 and 0.005 ppm respectively within 1σ. Maximum drift for 24 h has been calculated by subtracting the maximum and minimum value of 5 min average which were found to be 0.2 and 0.015 ppm respectively for CO_2 and CO. The linearity of the instrument for CO_2 measurements has been checked by using three calibration standards (350.67, 399.68 and 426.20 ppm) of CO_2. The linearity tests are conducted very frequently and the slope is found in the range of 0.99–1.007 ppm with correlation coefficient (r) of about 0.999.

3.2 Description of AGCM-based Chemistry Transport Model (ACTM)

This study uses the Center for Climate System Research/National Institute for Environmental Studies/Frontier Research Center for Global Change (CCSR/NIES/FRCGC) atmospheric general circulation model (AGCM)-based chemistry-transport model (ACTM). The model is nudged with reanalysis meteorology using Newtonian relaxation method. The U and V components of horizontal winds are used from the Japan Meteorological Agency Reanalysis (JRA-25) (Onogi et al., 2007). The model has $1.125^\circ \times 1.125^\circ$ horizontal resolution (T106 spectral truncation) and 32 vertical sigma-pressure layers up to about 50 km. Three components namely anthropogenic emissions, monthly varying ocean exchange with net uptake and terrestrial biospheric exchange of surface CO_2 fluxes are used in the model. The fossil fuel emissions for the model simulations are taken from EDGAR inventory for the year of 2010. Air-sea fluxes from Takahashi et al. (2009) have been used for the oceanic CO_2 tracer. The oceanic fluxes are monthly and are linearly interpolated between mid-months. The terrestrial biospheric CO_2 tracers are provided from the Carnegie-Ames-Stanford-Approach (CASA) process model (Randerson et al., 1997), after introducing a diurnal

variability using 2 m air temperature and surface short wave radiation from the JRA-25 as per Olsen and Randerson (2004). The ACTM simulations has been extensively used in TransCom CO_2 model inter-comparison studies (Law et al., 2008; Patra et al., 2008).

4 Results and discussion

4.1 Time series and general statistics

Figure 3a and c shows the time series of 30 min average CO_2 and CO concentrations for the period of November 2013–February 2014 and July 2014 to May 2015. The concentrations of both gases exhibit large synoptic variability because the site is close to anthropogenic sources. The concentrations and variability of both gases are observed lowest in the month of July and August. Maximum scatter in the concentrations and several plumes of very high levels both gases have been observed from October 2014 until mid-March 2015. Almost all plumes of CO_2 and CO are one to one correlated and are found during evening rush hours and late nights. Figure 3e and f shows the variations of CO_2 and CO concentrations with wind speed and direction for the study period except July, August and September due to non-availability of wind data. Most of the high and low concentrations of both these gases are found to be associated with low and high wind speeds. There is no specific direction for high levels of these gases. This probably indicates the transport sector is an important contributor to the local emissions since the measurement site is surrounded by city roads.

Figure 3b and d shows the probability distributions or frequency distributions of CO_2 and CO concentrations during the study period. The frequency distribution of CO_2 shows almost normal distribution while CO shows skewed towards right (lower concentrations). This is because, natural cycle of the biosphere (photosynthesis and respiration) along with some common controlling factors (local meteorology and anthropogenic sources), affects significantly the levels of CO_2. The control of the boundary

layer is common for the diurnal variations of these species because of their chemical lifetimes are longer (> months) than the timescale of PBL height variations (∼ h). However, biospheric fluxes of CO_2 can have strong hourly variations. During the study period the CO_2 concentrations varied between 382–609 ppm, with 16 % of data lying below 400 ppm, 50 % lying in the range 400–420 ppm, 25 % between 420–440 ppm and 9 % in the range of 440–570 ppm. Maximum frequency of CO_2 is observed at 402.5 ppm during the study period. The CO concentrations lies in the range of 0.071–8.8 ppm with almost 8 % data lies below the most probable frequency of CO at 0.2 ppm, while 70 % data lies between the concentrations of 0.21 and 0.55 ppm. Only 8 % data lies above the concentration of 1.6 ppm and rest of 14 % data lies between 0.55 and 1.6 ppm. The annual mean concentrations of CO_2 and CO are found to be 413.0 ± 13.7 ppm and 0.50 ± 0.37 ppm respectively, after removing outliers beyond 2σ values.

4.2 Seasonal variations of CO_2 and CO

The seasonal cycles of CO_2 and CO are mostly governed by the strength of emission sources, sinks and transport patterns. Although they follow almost identical seasonal patterns but the factors responsible for their seasonal behaviours are distinct as for the diurnal variations. We calculate the seasonal cycle of CO_2 and CO using two different approaches. In first approach, we use monthly mean of all data and in the second approach we use monthly mean for afternoon period (12:00–16:00 IST) only. All times are in Indian Standard Time (IST), which is 5.5 h ahead of GMT. The seasonal cycle from first approach depicts the combined influence of local emissions (mostly) as well as that of large scale circulation. The second approach removes the auto-covariance by excluding CO_2 and CO data mainly affected by local emission sources and represent seasonal cycles at the well mixed volume of the atmosphere. The CO_2 time series is detrended by subtracting a mean growth rate of CO_2 observed at Mauna Loa (MLO), Hawaii, i.e., 2.13 ppm yr^{-1} or 0.177 ppm $month^{-1}$ (www.esrl.noaa.gov/gmd/ccgg/trends/) for clearly depicting the seasonal cycle ampli-

tude. Figure 4a and b shows the variations of monthly average concentrations of CO_2 and CO using all daily (00:00–24:00 IST) data and afternoon (12:00–16:00 IST) data.

Both average concentrations (total and noon time) of CO_2 exhibit strong seasonal cycle, but show distinct patterns (occurrence of maxima and minima) to each other. This difference occurs because seasonal cycle of CO_2 from all data is mostly governed by the PBL ventilation and large scale circulation while the seasonal cycle from noon time mean concentration is mostly related to the seasonality of vegetation activity. The total and noon time mean concentrations of CO show almost similar pattern and evince that the seasonal cycle of CO_2 from the afternoon mean is mostly controlled by the biospheric productivity, since biospheric cycle does not influence CO concentration directly. In general, total mean values of CO_2 and CO are observed lower in July having concentration 398.78 ± 2.8 ppm and 0.15 ± 0.05 ppm respectively. A sudden increase in the total mean of both gases is observed from September to October and maximum concentrations of CO_2 and CO are observed to be 424.85 ± 17 ppm and 0.83 ± 0.53 ppm, respectively, during November. From January to May the total mean concentration of CO_2 decreases from 415.34 ± 13.6 to 406.14 ± 5.0 ppm and total mean concentration of CO decreases from 0.71 ± 0.22 to 0.22 ± 0.10 ppm. During monsoon months predominance of south-westerly winds which bring cleaner air from the Arabian Sea and the Indian Ocean over to Ahmedabad and high VC (Fig. 1) are responsible for the lower concentration of total mean of both the gases. CO_2 and CO concentrations are also at their seasonal low in the Northern Hemisphere due to net biospheric uptake and seasonally high chemical loss by reaction with OH, respectively. In addition, deep convections in the southwest monsoon season efficiently transport the Indian emission (for CO, hydrocarbons) or uptake (for CO_2) signals at the surface to the upper troposphere, resulting in concentrations at the surface in the summer compared to the winter months (Kar et al., 2004; Randel and Park, 2006; Park et al., 2009; Patra et al., 2011; Baker et al., 2012). During autumn and early winter (December), lower VC values cause trapping of anthropogenically emitted CO_2 and CO. This is the major cause for high CO_2 and CO concentrations during this period. The north-easterly winds bring

very high levels of pollutants from IGP region and could additionally enhance the levels of CO_2 and CO during these seasons (autumn and winter). Higher VC and predominance of comparatively less polluted mixed air masses from oceanic and continental region results in the lower total mean concentrations of both gases.

There are some clear differences which are observed in the afternoon mean concentrations of CO_2 as compared to daily mean. The first distinct feature is that significant difference of about 5 ppm is observed in the afternoon mean of CO_2 concentration from July to August as compared to difference in total mean concentration of about ~ 0.38 ppm for the same period. Significant difference in the afternoon concentrations of CO_2 from July to August is mainly due to the increasing sink by net biospheric productivity after the Indian summer monsoonal rainfall. Another distinct feature is that the daily mean concentration of CO_2 is found highest in November while the afternoon mean concentration of CO_2 attains maximum value (406 ± 0.4 ppm) in April. Prolonged dry season combined with high daytime temperature (about 41 °C) during April–May make the tendency of ecosystem to become moderate source of carbon exchange (Patra et al., 2011) and this could be responsible for the elevated mean noon time concentrations of CO_2.

The average amplitude (max–min) of the annual cycle of CO_2 is observed around 13.6 and 26.07 ppm from the afternoon mean and total mean respectively. Different annual cycles and amplitudes have been observed from other studies conducted over different Indian stations. Similar to our observations of the afternoon mean concentrations of CO_2, maximum values are also observed in April at Pondicherry (PON) and Port Blair with amplitude of mean seasonal cycles about 7.6 ± 1.4 and 11.1 ± 1.3 ppm respectively (Lin et al., 2015). Cape Rama (CRI), a costal site on the south-west coast of India show the seasonal maxima one month before than our observations in March with annual amplitude about 9 ppm (Bhattacharya et al., 2009). The Sinhagad (SNG) site located over the Western Ghats mountains, show very larger seasonal cycle with annual amplitude of about 20 ppm (Tiwari et al., 2014). The amplitude of mean annual cycle at the free tropospheric site Hanle at altitude of 4500 m is observed to be

8.2±0.4 ppm, with maxima in early May and minima in mid-September (Lin et al., 2015). Distinct seasonal amplitudes and patterns are due to differences in regional controlling factors for the seasonal cycle of CO_2 over these locations, e.g., the Hanle is remotely located from all continental sources, Port Blair site is sampling predominantly marine air, Cape Rama observes marine air in the summer and Indian flux signals in the winter, and Sinhagad represents a forested ecosystem. These comparisons show the need for CO_2 measurements over different ecosystems for constraining its budget.

The annual amplitude in afternoon and daily mean CO concentrations are observed to be about 0.27 and 0.68 ppm, respectively. The mean annual cycles of CO over PON and Port Blair show the maxima in the winter months and minima in monsoon months same as our observations with annual amplitudes of 0.078 ± 0.01 and 0.144 ± 0.016 ppm, respectively. Hence, the seasonal levels of CO are affected by large scale dynamics which changes air masses from marine to continental and vice versa and by photochemistry. The amplitudes of annual cycle at these locations differ due to their climatic conditions and sources/sinks strengths.

4.3 Diurnal variation

The diurnal patterns for all months and seasons are produced by first generating the time series from the 15 min averages and then averaging the individual hours for all days of the respective month and season after removing the values beyond 2σ standard deviations for each month as outliers.

4.3.1 Diurnal variation of CO_2

Figure 5a shows bi-modal feature in the diurnal cycle of CO_2 during the four seasons with morning and evening peaks. Both peaks are associated mostly with the vehicular emissions and PBL height during rush hours. There are many interesting features in the 00:00–08:00 IST period. Concentrations of CO_2 start decreasing from 00:00 to 03:00 IST and afterwards increases until 06:00 and 07:00 IST during monsoon and au-

tumn. It could be mostly due to the accumulation of CO_2 emitted from respiration by the biosphere in the nocturnal boundary layer. During winter and spring the concentrations during night hours are almost constant and increase is observed only from 06:00 to 08:00 IST during winter. Dormant of respiration during these two seasons due to lower temperature could be one of the possible factors for no increase in CO_2 concentrations during night. No peak during morning hours is observed in spring. Distinct timings for the occurrence of the morning peak during different seasons is generally related to the sunrise time and consequently the evolutions of PBL height. The sunrise occurs at 05:55–06:20, 06:20–07:00, 07:00–07:23 and 07:20–05:54 IST during monsoon, autumn, winter and spring, respectively. During spring and monsoon, rush hour starts after sunrise, so the vehicular emissions occur when the PBL is already high and photosynthetic activity has begun. But in winter and autumn rush hour starts parallely with the sunrise, so the emissions occur when the PBL is low and concentration build up is much strong in these seasons than in spring and monsoon seasons. CO_2 starts decreasing fast after these hours and attains minimum value around 16:00 IST. This quick drop of CO_2 after sunrise is linked to the dominance of photosynthesis over the respiration processes in addition to the higher atmospheric mixing height. CO_2 levels start increasing after 16:00 IST peak around 21:00 IST. Higher concentrations of CO_2 during these hours are mainly due to the rush hour vehicular emissions and less dilution due to the lower PBL height. Comparative levels of CO_2 during evening rush hours except monsoon confirm separately the major influence from the same type of sources (vehicular emission) in its levels which do not show large variability as in post-midnight hours.

The diurnal amplitude is defined as the difference between the maximum and minimum concentrations of CO_2 in the diurnal cycle. The amplitudes of monthly averaged diurnal cycle of CO_2 from July 2014 to May 2015 are shown in Fig. 5b. The diurnal amplitude shows large month to month variation with increasing trend from July to October and decreasing trend from October onwards. Lowest diurnal amplitude of about 6 ppm is observed in July while highest amplitude of about 51 ppm is observed in October.

The amplitude does not change much from December to March and is observed in the range of 25–30 ppm. Similarly from April to May, the amplitude also varies in a narrow range from 12 to 15 ppm. The jump in the amplitude of CO_2 diurnal cycle is observed highest (around 208 %) from July to August. This is mainly due to significant increase of biospheric productivity from July to August after the rains in Ahmedabad. It is observed that during July the noon time CO_2 levels are found in the range of 394–397 ppm while in August the noon time levels are observed in the range of 382–393 ppm. The lower levels could be due to the higher PBL height during afternoon and cleaner air, but in case of CO, average day time levels in August are observed higher than July. It rules out that the lower levels during August are due to the higher PBL height and presence of cleaner marine air, and confirms the higher biospheric productivity during August.

The monthly average diurnal cycles of the biospheric net primary productivity from CASA model for Ahmedabad and for the year of 2014 are shown Fig. 6. The details of CASA flux are given in the Sect. 3.2. It is observed that the model shows higher biospheric productivity in September and October while the observations are suggesting higher productivity in August. This indicates that the CASA model is not able to capture the signal of higher biospheric productivity for Ahmedabad and need to be improved. Similar discrepancy in the timing of maximum biospheric uptake is also discussed earlier by Patra et al. (2011) using inverse model CO_2 fluxes and CASA biospheric fluxes.

Near surface diurnal amplitude of CO_2 has been documented in humid subtropical Indian station Dehradun and a dry tropical Indian station Gadanki (Sharma et al., 2014). In comparison to Ahmedabad, both these stations show distinct seasonal change in the diurnal amplitude of CO_2. The maximum CO_2 diurnal amplitude of about 69 ppm is observed during the monsoon season at Dehradun (30.3° N, 78.0° E, 435 m), whereas maximum of about 50 ppm during autumn at Gadanki (13.5° N, 79.2° E, 360 m).

4.3.2 Diurnal variation of CO

Figure 7a shows seasonally averaged diurnal variation of CO. In general, the mean diurnal cycles of CO during all the seasons show lower concentration during noon

(12:00–17:00 IST) and two peaks, one in the morning (08:00–10:00 IST) and other in the evening (18:00–22:00 IST). This cycle exhibits the same pattern as the mean diurnal cycle of traffic flow, with maxima in the morning and at the end of the afternoon, which suggests the influence of traffic emissions on CO measurements. Along with the traffic flow, PBL dynamics also plays a critical role in governing the diurnal cycle of CO. The amplitudes of the evening peaks in diurnal cycles of CO are always greater than the morning peaks. It is because the PBL height evolves side by side with the morning rush hours traffic and hence increased dilution while during evening hours PBL height decrease along with evening time rush hours traffic and favours accumulation of pollutants until the late evening under the stable PBL conditions. The noon time minima is associated with the combined influence of boundary layer dilution and loss of CO due to OH radicals. The peaks during morning and evening rush hours, minima during afternoon hours in CO diurnal cycle during all seasons are similar as in CO_2. However, there are a few noticeable differences in the diurnal cycles of both the gases. The first noticeable difference is that the CO morning peak appears later than CO_2 peak. This is because as discussed earlier with sunrise time, PBL height starts to evolve and same time photosynthesis process also gets started and hence CO_2 morning peak depends on the sunshine time. But in case of CO, timing of the morning peak mostly depends on the rush hour traffic and is consistent at 08:00–10:00 IST in all seasons. The second noticeable difference is the afternoon concentrations of CO show little seasonal spread as compared to the afternoon concentrations of CO_2. Again, this is due to the biospheric control on the concentration of CO_2 during the afternoon hours of different seasons while CO levels are mainly controlled by the dilution during these afternoon hours. The third noticeable difference is that the levels of CO decrease very fast after evening rush hour in all seasons while this feature is not observed in case of CO_2 since respiration during night hours contributes to the levels of CO_2. The average morning (08:00–09:00 IST) peak values of CO are observed minimum (0.18 ± 0.1 ppm) in monsoon and maximum (0.72 ± 0.16 ppm) in winter while its evening peak shows minimum value (0.34 ± 0.14 ppm) in monsoon and maximum (1.6 ± 0.74 ppm) in autumn. The

changes in CO concentrations show large fluctuations from morning peak to afternoon minima and from afternoon minima to evening peak. From early morning maxima to noon minima, the changes in CO concentrations are found in the range of 20–200 % while from noon minima to late evening maxima the changes in CO concentrations are found in the range of 85 to 680 %. Similar diurnal variations with two peaks have also been observed in earlier measurements of CO as well as NO_x at this site (Lal et al., 2000).

The evening peak contributes significantly to the diurnal amplitude of CO. The largest amplitude in CO cycle is observed in autumn (1.36 ppm) while smallest amplitude is observed in monsoon (0.24 ppm). The diurnal amplitudes of CO are observed to be about 1.01 and 0.62 ppm respectively during winter and spring. The monthly diurnal cycle of CO (Fig. 7b) shows minimum (0.156 ppm) amplitude in July and maximum (1.85 ppm) in October. After October the diurnal amplitude keep on decreasing till monsoon.

4.4 Correlation between CO and CO_2

The relationships between CO to CO_2 can be useful for investigating the CO source types and their combustion characteristics in the city region of Ahmedabad. For correlations study, in principle the baseline levels need to be removed from the measured concentrations. Although, the most ideal case of determining the background levels are the continuous measurement of respective gases at a cleaner site. But due to unavailability of measurements at a near by cleaner site, we use the 5th percentile value of CO_2 and CO for each day as a background for corresponding day. The excess CO_2 (CO_{2exc}) and CO (CO_{exc}) above the background for Ahmedabad city, are determined for each day after subtracting the background concentrations from the hours of each day ($CO_{2exc} = CO_{2obs} - CO_{2bg}$, $CO_{exc} = CO_{obs} - CO_{bg}$).

We use robust regression method for the correlation study. It is an alternative to least squares regression method and more applicable for analysing time series data with outliers arising from extreme events (http://www.ats.ucla.edu/stat/stata/dae/rreg.htm). Figure 8a illustrates the correlations between CO_{exc} and CO_{2exc} for the four seasons.

The impact of the possible sources of CO and CO_2 varies from month to month and hence season to season. The lowest correlation ($r = 0.62, p = 0.0001$) is observed during monsoon, with a $\Delta CO_{exc}/\Delta CO_{2exc}$ ratio of 0.6 ± 0.1 ppb ppm^{-1}. Lowest correlation suggest that different mechanisms control the levels of CO and CO_2 during the monsoon season. As discussed previously, higher biospheric productivity during this season mostly controls the CO_2 concentrations while CO concentrations are mostly controlled by the long range transport and higher loss due to OH. Highest correlation ($r = 0.87, p < 0.0001$) with $\Delta CO_{exc}/\Delta CO_{2exc}$ ratio of 8.4 ± 0.17 ppb ppm^{-1} is observed during spring season. As illustrated by the diurnal cycle, the CO_2 is not significantly removed by the biosphere during spring with lower draw down in daily CO_2. Along with this, higher VC during this season will result in very fast mixing. Therefore, very fast mixing will mostly regulate their relative variation and will result in higher correlation in this season. Other factors like soil and plant respiration during this period may also control CO_2 concentrations due to which the correlation coefficient is not equal to 1. The ratio of $\Delta CO_{exc}/\Delta CO_{exc}$ is estimated to be 8.5 ± 0.15 ppb ppm^{-1} ($r = 0.72$) and 12.7 ± 0.17 ppb ppm^{-1} ($r = 0.74$) in autumn and winter respectively. Relatively higher ratios during winter than other three seasons indicate contribution of CO emission from additional biofuel burning sources. The winter time ratio is similar to the airmass influenced by both fossil fuel and biofuel emissions as discussed by Lin et al. (2015) over Pondicherry. Using CARIBIC observations, Lai et al. (2010) also reported the $\Delta CO/\Delta CO_2$ ratio in the range of 15.6–29.3 ppb ppm^{-1} from the airmass influenced by both biofuel and fossil fuel burning in the Indo-Chinese Peninsula. Further, $\Delta CO/\Delta CO_2$ ratio is also observed of about 13 ppb ppm^{-1} in South-east Asian outflow in February–April 2001 during the TRACE-P campaign and suggest the combined influence of fossil fuel and biofuel burning (Russo et al., 2003). The narrow range of the ratios from autumn to spring (8.4–12.7 ppb ppm^{-1}) suggest the dominance of local emission sources during these seasons, and this range corresponds to the range of anthropogenic combustion sources (10–15 ppb ppm^{-1}) in developed countries (Suntharalingam et al., 2004; Takegawa et al., 2004; Wada et al., 2011). This suggest that

the overall emissions of CO over Ahmedabad are mostly dominated by the anthropogenic combustion during these seasons.

The $\Delta CO_{exc}/\Delta CO_{2exc}$ slope and their correlation may depend on the time of the day due to the variation in different controlling factors on their levels. Hence, we computed the diurnal cycle of $\Delta CO_{exc}/\Delta CO_{2exc}$ slope for all the seasons by binning the data for both hour and month (3 month × 24 h) as shown in Fig. 8b. The colours indicate the correlation coefficients (r) for respective hour. These ratios do not reflect the diurnally varying PBL height, but rather the diurnally varying mix of fossil fuels and biogenic sources. The $\Delta CO_{exc}/\Delta CO_{2exc}$ slopes show very distinctive diurnal variation, being higher (30–50 ppb ppm^{-1}) in the evening rush hours with very good correlation ($r >$ 0.85) and lower (5–20 ppb ppm^{-1}) in the afternoon hours with lower correlation (r = 0.5–0.6) during all the four seasons. Negative and lower slopes in afternoon hours during monsoon season indicate higher biospheric productivity during this period. The slopes and their correlations are fairly comparable for all the four seasons in the evening rush hours which indicate stronger influence of common emission sources. Slopes during this time can be considered as fresh emissions since dilution and chemical loss of CO can be considered negligible for this time. These observed ratios are much lower than ratios related to domestic sources but are similar transport sector mostly dominated from gasoline combustion (Table 1). Except monsoon, the overall ratios in all four seasons were found in the range of 10–25 ppb ppm^{-1} during the daytime and 10–50 ppb ppm^{-1} during night-time.

4.5 Top-down CO emissions from observations

If the emissions of CO_2 are known for study locations, the emissions of CO can be estimated by multiplying the correlation slopes and molecular mass mixing ratios (Wunch et al., 2009; Wong et al., 2015). Final emissions of CO will depend on choosing the values of correlation slopes. The slopes should not be biased from particular local sources, chemical processing and PBL dynamics. We exclude monsoon data as the CO_2 variations mainly depend on the biospheric productivity during this season. As

discussed previously, the morning and evening rush hours data are appropriate for tracking vehicular emissions, while the afternoon data are affected by other environmental factors, e.g., the PBL dynamics, biospheric activity and chemical process. The stable, shallow night-time PBL accumulates emissions since the evening and hence the correlation slope for this period can be used as a signature of the city's emissions. Hence, we calculate the slopes from the data corresponding to the period of 23:00–05:00 IST. Additionally, slopes for morning hours (06:00–10:00 IST), afternoon hours (11:00–17:00 IST), and night hours (18:00–06:00 IST) are also used for estimating the CO emissions to study the difference in the estimation of CO emissions due to choosing different times for slopes. The CO emission (E_{CO}) for Ahmedabad is calculated using the following formula.

$$E_{CO} = \left(\alpha_{CO}\frac{M_{CO}}{M_{CO_2}}\right)E_{CO_2} \quad (1)$$

Where, α_{CO} is the correlation slope of CO_{exc} to CO_{2exc} ppb ppm^{-1}, M_{CO} is the molecular mass of CO in g mol^{-1}, M_{CO_2} is the molecular mass of CO_2 in g mol^{-1} and E_{CO_2} is the CO_2 emission in Gigagram (Gg) over Ahmedabad. The EDGARv4.2 emission inventory reported an annual emissions of CO_2 at 0.1° × 0.1° for the period of 2000–2008 (http://edgar.jrc.ec.europa.eu/overview.php?v=42). It reported an annual CO_2 emission of 6231.6 Gg CO_2 year^{-1} by EDGARv4.2 inventory over the box (72.3 < longitude < 72.7° E, 22.8 < latitude < 23.2° N) which contain Ahmedabad coordinates in center of the box. We assume that the emissions of CO_2 are linearly changing with time and using increasing rate of emission from 2005 to 2008, we extrapolate the emission of CO_2 for 2014 over same area. The bottom-up CO_2 emission for the Ahmedabad is thus estimated of about 8368.6 Gg for the year of 2014. Further, for comparing the estimated emission with inventory emissions we extrapolated the CO emissions also for the year of 2014 using same method applied as for CO_2. Further, we assumed same slopes for the year of 2008 and calculate CO emission for that year

also. The slope values for different time period, estimated and inventory emissions of CO using different values of slope are given in Table 2.

The correlation between CO_{exc} and CO_{2exc} for the period of 23:00–05:00 IST is very tight and slope for this period can be considered for estimating the fossil fuel CO emissions for Ahmedabad. Using this slope and based on CO_2 emissions from EDGAR inventory, the estimated fossil fuel emission for CO is observed to be 69.2 ± 0.7 Gg for the year of 2014. The EDGAR inventory underestimates the emission of CO as they give the estimate of about 45.3 Gg extrapolated for 2014. The slope corresponding to the night hours (18:00–06:00 IST) gives the highest estimate of CO. Using all combinations of slopes, the derived CO emissions are larger than the bottom-up EDGAR emission inventory.

4.6 Diurnal tracking of CO_2 emissions

CO has virtually no natural sources in an urban environment except oxidation of hydrocarbons. As we discussed earlier that incomplete combustion of fossil fuels is the main source of CO in urban environments and therefore can be used as a surrogate tracers to attribute CO_2 enhancements to fossil fuel combustion on shorter timescale. Several studies have demonstrated that the ratio of the excess concentrations of CO and CO_2 in background concentrations can be used to determine the fraction of CO_2 from fossil fuels and validated this method using carbon isotope ($\Delta^{14}CO_2$) measurements (Levin et al., 2003; Turnbull et al., 2006, 2011; Lopez et al., 2013; Newman et al., 2013). This quantification technique is more practical, less expensive and less time consuming in comparison to the $^{14}CO_2$ method (Vogel et al., 2010). For performing this analysis, the background concentrations of CO and CO_2 and the emission ratio of CO/CO_2 from anthropogenic emissions are required. The methods for calculating the background concentrations of CO_2 and CO are already discussed in Sect. 4.4. Figure 9a shows the excess diurnal variations of CO_2 above the background levels during different seasons. As discussed in the previous section, the vehicular emissions are major emission sources over the study locations. For calculating the emission ratio of CO/CO_2 from

the vehicular emissions, we used the evening time (19:00–21:00 IST) concentrations of CO_{2exc} and CO_{exc} for whole study period since correlation for this period is very high. The other reason for choosing this time is that there is insignificant contribution of biospheric CO_2 and no chemical loss of CO. We assume that negligible influence of other sources (open biomass burning, oxidation of hydrocarbons) during this period. The emission ratio for this time is calculated to be about 47 ± 0.27 ppb CO ppm^{-1} CO_2 with very high correlation ($r = 0.95$) (Fig. 9b) after excluding those data points, corresponding for which the mean wind speed is greater than 3 m s^{-1} for avoiding the effect of fast ventilation and transport from other sources. The tight correlation imply that there is no substantial difference in the emission ratio of these gases during the measurement period from November 2013 to May 2015. CO_{2exc} and CO_{exc} will be poorly correlated with each other if their emission ratio varies largely with time, assuming the correlation is mainly driven by emissions. Since this ratio is mostly dominated by the transport sector, this analysis will give mainly the fraction of CO_2 from the emissions of transport sector. We define it as $R_{CO/CO_{2veh}}$. The standard deviation shows the uncertainty associated with slope which is very small. The contribution of transport sector (CO_{2Veh}) in the diurnal cycle of CO_2 is calculated using the following formula.

$$CO_{2Veh} = \frac{CO_{obs} - CO_{bg}}{R_{CO/CO_{2veh}}} \quad (2)$$

where CO_{obs} is the observed CO concentration and CO_{bg} is a background CO value. Uncertainty in the CO_{2Veh} is dominated by the uncertainty in the $R_{CO/CO_{2veh}}$ and by the choice of CO_{bg}. The uncertainty in CO_{2Veh} due to the uncertainty in the $R_{CO/CO_{2veh}}$ is about 0.5 % or 0.27 ppm and can be considered negligible. As discussed in Sect. 3, the uncertainty in the measurements of CO_{bg} is very small and also can be considered negligible. Further, the contributions of CO_2 from other major sources are calculated by subtracting the CO_{2Veh} from the excess concentrations of CO_2. These sources are those sources which do not emit significant amount of CO and can be considered mostly as natural sources (respiration), denoted by CO_{2bio}.

The average diurnal cycles of CO_2 above its background for each seasons are shown in (Fig. 9a). The diurnal pattern of CO_{2Veh} (Fig. 9c) reflects the pattern like CO, because we are using constant $R_{CO/CO_{2veh}}$ for all seasons. Overall, this analysis suggests that the anthropogenic emissions of CO_2 from transport sectors during early morning from 06:00 to 10:00 IST varied from 15 to 60 % (4–15 ppm). During afternoon h (11:00–17:00 IST), the vehicular emitted CO_2 varied from 20 to 70 % (1–11 ppm) and during evening rush hours (18:00–22:00 IST), it varies from 50 to 95 % (2–44 ppm). During night/early morning hours (00:00–07:00 IST) respiration contributes from 8 to 41 ppm of CO_2 (Fig. 9d). The highest contributions from 18 to 41 ppm are observed in the autumn from the respiration sources during night hours, since there is more biomass during this season after the South Asian summer monsoon. During afternoon hours, lower biospheric component of CO_2 could be due to a combination of the effects of afternoon anthropogenic emissions, biospheric uptake of CO_2 and higher PBL height.

4.7 Model – observations comparison

4.7.1 Comparison of diurnal cycle of CO_2

We first evaluate the ACTM in simulating the mean diurnal cycle of CO_2 over Ahmedabad by comparing model simulated surface layer mean diurnal cycle of CO_2. The atmospheric concentrations of CO_2 are calculated by adding the anthropogenic component, oceanic component, biospheric component from CASA process model. Figure 10a and b shows the residuals (Hourly mean – daily mean) of diurnal cycles of CO_2 based on the observations and model simulations respectively. Model shows very little diurnal amplitude as compared to observational diurnal amplitude. Larger differences and discrepancies in night time and morning CO_2 concentrations between the model and observations might be contributed by diurnal cycle of the anthropogenic fluxes from local emissions and biospheric fluxes, and uncertainties in the estimation of PBLH by the model. Hence, there is a need for efforts in improving the regional anthropogenic emissions as well as module for estimating the PBL height. It may be pointed

out that the model's horizontal resolution (1.125° × 1.125°) is coarse for analysing local scale observations. However, model is able to capture the trend of the diurnal amplitude, highest in autumn and lowest in monsoon. Figure 10c shows better agreement (r = 0.75) between the monthly change in model and observational diurnal amplitude of CO_2 from monthly mean diurnal cycle however slope (m = 0.17) is very poor. We include the diurnal amplitudes of CO_2 for November and December 2013 also for improving the total number of data points. The model captured the spread in the day time concentration of CO_2 from monsoon to spring with a difference that model shows lower concentration of CO_2 during noon hours in autumn while observations show lowest in monsoon. Most of the atmospheric CO_2 uptake occur following the Southwest monsoon season during July–September (Patra et al., 2011) and as a consequence, we observe the lowest CO_2 concentration from the measurements during this season. But model is not able to capture this feature since CASA biospheric flux (Fig. 6) shows highest productivity in autumn and hence lowest concentrations of CO_2 in autumn during daytime. This also suggest that there is a need for improving the biospheric flux for this region. It should be mentioned here that CASA model used a land use map corresponding the late 1980s and early 1990s, which should be replaced by rapid growth in urbanised area in Ahmedabad (area and population increased by 91 and 42 %, respectively, between 1990 and 2011). The model resolution may be another factor for discrepancy. As Ballav et al. (2012) show that a regional model WRF-CO_2 is able to capture both diurnal and synoptic variations at two closely spaced stations within 25 km. Hence the regional models could be helpful for capturing these variabilities.

4.7.2 Comparison of seasonal cycle of CO_2

Figure 11a shows the performance of ACTM simulating mean seasonal cycle of CO_2 over Ahmedabad by comparing model simulated mean surface seasonal cycle of CO_2. Due to unavailability of data from March 2014 to June 2014 we plotted the monthly average of the year 2015 for same periods for visualizing the complete seasonal cycle of

CO_2. The seasonal cycles are calculated after subtracting the annual mean from each month, and corrected for growth rate using the observations at MLO. For comparison, we use the seasonal cycle calculated from afternoon time average monthly concentrations, since model is not able to capture the local fluctuations and produce better agreements when boundary layer is well mixed. In Table 3 we present the summary of the comparisons of model and observations. The model reproduces the observed seasonal cycle in CO_2 fairly well but with low seasonal amplitude about 4.15 ppm compared to 13.6 ppm observed. Positive bias during monsoon depicts the underestimation of biospheric productivity by CASA model. The root mean square error is observed highest to be 3.21 % in monsoon. For understanding the role of biosphere, we also compared the seasonal cycle of CO_2 from noon time mean data with the seasonal cycle of CO_2 fluxes over South Asia region which is taken from the Patra et al. (2011) where they calculated it using an inverse model by including CARIBIC data and shifted a sink of 1.5 Pg C yr^{-1} from July to August and termed it as "TDI64/CARIBIC-modified". Positive and negative values of flux show the net release and net sink by the land biosphere over the South Asia. This comparison shows almost one to one correlation in the monthly variation of CO_2 and suggest that the lower levels of CO_2 during July, August and higher level in April are mostly due to the moderate source and sink of South Asian ecosystem during these months respectively. Significant correlation (r = 0.88) between South Asian CO_2 fluxes and monthly mean CO_2 data for day time only suggest that the day time levels of CO_2 are mostly controlled by the seasonal cycle of biosphere (Fig. 11b).

Separate correlation between individual tracers of model and observed data has been studied to investigate the relative contribution of individual tracer component in the CO_2 variation (Fig. 11b). We did not include the oceanic tracer and observed CO_2 correlation result, since no correlation has been observed between them. The comparison is based on daily mean of entire time series. Correlation between biospheric tracers and observed CO_2 have been found negative. This is because during growing season biospheric sources act as a net sink for CO_2. Correlation of observed CO_2 with

fossil fuel tracer has been observed fairly well (r = 0.75). Hence, individual tracers correlation study also gives the evidence of the overall dominance of fossil flux in overall concentrations of CO_2 over Ahmedabad for entire study period, and by assuming fossil fuel CO_2 emission we can derive meaningful information on biospheric uptake cycle.

This study suggests that the model is able to capture seasonal cycle with lower amplitude for Ahmedabad. However, the model fails to capture the diurnal variability since local transport and hourly daily flux play important roles for governing the diurnal cycle and hence there is a need for improving these features of the model.

5 Conclusions

We report simultaneous in-situ measurements of CO_2 and CO concentrations in the ambient air at Ahmedabad, a semiarid urban region in western India using laser based CRDS technique during 2013–2015. The unique flow of air masses originating from both polluted continental regions as well as cleaner marine regions over the study location during different seasons make this study most important for studying the characteristics of both polluted and relatively cleaner air masses. Several key results are presented in this study. The observations show the range of CO_2 concentrations from 382 to 609 ppm and CO concentrations from 0.07 to 8.8 ppm, with the average of CO_2 and CO to be 416 ± 19 ppm and 0.61 ± 0.6 ppm respectively. The highest concentrations of both the gases are recorded for lower ventilation and for winds from north-east direction, representing CO_2 and CO transported from anthropogenic sources. The lowest concentrations of both the gases are observed for higher ventilation and for the southwest direction, where air travels from the Indian Ocean. Along with these factors, the biospheric seasonal cycle (photosynthesis outweighs respiration during growing season and reverse during fall season) also controls the seasonal cycle of CO_2. Lowest day time CO_2 concentrations ranging from 382 to 393 ppm in August, suggest for the stronger biospheric productivity during this month over the study region, in agreement with an earlier inverse modelling study. This is in contrast to the terrestrial flux simu-

lated by the CASA ecosystem model, showing highest productivity in September and October months. Hence, the seasonal cycles of both the gases reflect the seasonal variations of natural sources/sinks, anthropogenic emissions and seasonally varying atmospheric transport. The annual amplitudes of CO_2 variation after subtracting the growth rate based on the Mauna Loa, Hawaii data are observed to be about 26.07 ppm using monthly mean of all the data and 13.6 ppm using monthly mean of the afternoon period (12:00–16:00 IST) data only. Significant difference between these amplitudes suggests that the annual amplitude from afternoon monthly mean data only does not give true picture of the variability. It is to be noted that most of the CO_2 measurements in India are based on day time flask samplings only.

Significant differences in the diurnal patterns of CO_2 and CO are also observed, even though both the gases have major common emission sources and effects of PBL dynamics and advection. Differences in their diurnal variability is probably the effect of terrestrial biosphere on CO_2 and chemical loss of CO due to reaction with OH radicals. The morning and evening peaks of CO are affected by rush hours traffic and PBL height variability and occur almost same time throughout the year. However, the morning peaks in CO_2 changes its time slightly due to shift in photosynthesis activity according to change in sun rise time during different seasons. The amplitudes of annual average diurnal cycles of CO_2 and CO are observed about 25 and 0.48 ppm respectively (Table 4). Both gases show highest amplitude in autumn and lowest in monsoon. This shows that major influencing processes are common for both the gases, specific to this city and the monsoon India.

The availability of simultaneous and continuous measurements of CO_2 and CO have made it possible to study their correlations during different times of the day and during different seasons. The minimum value of slope and correlation coefficient of 0.8 ± 0.2 ppb ppm^{-1} and 0.62 respectively are observed in monsoon. During other three seasons, the slopes vary in narrow range (Table 4) and indicate about the common emission sources of CO during these seasons. These slopes lie in the range (10–15 ppb ppm^{-1}) of anthropogenic sources in developed countries, e.g., Japan. This

suggest that the overall emissions of CO over Ahmedabad are mostly dominated by the anthropogenic (fossil fuel) combustion. These slopes also show significant diurnal variability having lower values (about 5–20 ppb ppm^{-1}) during noon hours and higher values (about 30–50 ppb ppm^{-1}) during evening rush hours with highest correlation ($r > 0.9$). This diurnal pattern is similar to the traffic density and indicate the strong influence of vehicular emissions in the diurnal pattern of CO. Further, using the slope from the evening rush hours (18:00–22:00 IST) data as vehicular emission ratios, the contributions of vehicular emissions and biospheric emissions in the diurnal cycle of CO_2 have been segregated. At rush hours, this analysis suggests that 90–95 % of the total emissions of CO_2 are contributed by vehicular emissions. Using the relationship, the CO emission from Ahmedabad has been estimated. In this estimation, fossil fuel derived emission of CO_2 from EDGAR v4.2 inventory is extrapolated linearly from 2008 to 2014 and it is assumed that there are no year-to-year variations in the land biotic and oceanic CO_2 emissions. The estimated annual emission CO for Ahmedabad is estimated to be 69.2 ± 0.7 Gg for the year of 2014. The extrapolated CO emission from EDGAR inventory for 2014 shows a value smaller than this estimate by about 52 %.

The observed results of CO_2 are also compared with an atmospheric general circulation model based chemistry transport model simulated CO_2 concentrations. The model captures some basic features like the trend of diurnal amplitude, seasonal amplitude etc, qualitatively but not quantitatively. The model captures the seasonal cycle fairly good but the amplitude is very less as compared to the observations. Similarly, performance of the model capturing the change in monthly averaged diurnal amplitude is quiet good ($r = 0.72$), however the slope is very poor. We also examined the correlation between the hourly averaged observed CO_2 and tracer of fossil fuel from model simulation and found fairly good correlation between them. However, no significant correlation has been observed between observed CO_2 and biospheric tracer. It suggests that the levels of CO_2 over Ahmedabad are mostly controlled by the fossil fuel combustion throughout the year.

This work demonstrates the usefulness of simultaneous measurements of CO_2 and CO in an urban region. The anthropogenic and biospheric components of CO_2 have been studied from its temporally varying atmospheric concentrations, and validity of "bottom-up" inventory has been assessed. Use of $CO_{exc} : CO_{2exc}$ ratios avoid some of the problems with assumptions that have to be made with modelling. These results represent a major urban region of India and will be helpful in validating emission inventories, chemistry-transport and terrestrial ecosystem models. However, a bigger network of sites is needed to elucidate more accurate distribution of emissions and their source regions, and run continuously over multiple years for tracking the changes associated with anthropogenic activities and emission mitigation policies.

Acknowledgements. We thank PRL and ISROGBP-ATCTM for funding and support. We acknowledge the support of T. K. Sunil Kumar in making the measurements.

References

Ahmadov, R., Gerbig, C., Kretschmer, R., Koerner, S., Neininger, B., Dolman, A. J., and Sarrat, C.: Mesoscale covariance of transport and CO_2 fluxes: evidence from observations and simulations using the WRF-VPRM coupled atmosphere-biosphere model, J. Geophys. Res.-Atmos., 112, D22107, doi:10.1029/2007JD008552, 2007. 32189

Ammoura, L., Xueref-Remy, I., Gros, V., Baudic, A., Bonsang, B., Petit, J.-E., Perrussel, O., Bonnaire, N., Sciare, J., and Chevallier, F.: Atmospheric measurements of ratios between CO_2 and co-emitted species from traffic: a tunnel study in the Paris megacity, Atmos. Chem. Phys., 14, 12871–12882, doi:10.5194/acp-14-12871-2014, 2014. 32189

Andreae, M. O. and Merlet, P.: Emission of trace gases and aerosols from biomass burning, Global Biogeochem. Cy., 15, 955–966, doi:10.1029/2000GB001382, 2001. 32188, 32224

Baker, A. K., Schuck, T. J., Brenninkmeijer, C. A. M., Rauthe-Schöch, A., Slemr, F., van Velthoven, P. F. J., and Lelieveld, J.: Estimating the contribution of monsoon-related biogenic production to methane emissions from South Asia using CARIBIC observations, Geophys. Res. Lett., 39, L10813, doi:10.1029/2012GL051756, 2012. 32197

Ballav, S., Patra, P. K., Takigawa, M., Ghosh, S., De, U. K., Maksyutov, S., Murayama, S., Mukai, H., and Hashimoto, S.: Simulation of CO_2 Concentration over East Asia Us-

ing the Regional Transport Model WRF-CO2, J. Meteorol. Soc. Jpn., 90, 959–976, doi:10.2151/jmsj.2012-607, 2012. 32210

Ballav, S., Patra, P. K., Sawa, Y., Matsueda, H., Adachi, A., Onogi, S., Takigawa, M., and De, U.: Simulation of CO_2 concentrations at Tsukuba tall tower using WRF–CO_2 tracer transport model, J. Earth System Sci., in press, 2015. 32189

Bhattacharya, S. K., Borole, D. V., Francey, R. J., Allison, C. E., Steele, L. P., Krummel, P., Langenfelds, R., Masarie, K. A., Tiwari, Y. K., and Patra, P.: Trace gases and CO_2 isotope records from Cabo de Rama, India, Curr. Sci. India, 97, 1336–1344, 2009. 32189, 32198

Bitter, M., Ball, S. M., Povey, I. M., and Jones, R. L.: A broadband cavity ringdown spectrometer for in-situ measurements of atmospheric trace gases, Atmos. Chem. Phys., 5, 2547–2560, doi:10.5194/acp-5-2547-2005, 2005. 32192

Boden, T., Marland, G., and Andres, R.: Global, Regional, and National Fossil-Fuel CO_2 Emissions, Oak Ridge, Tenn., USA, doi:10.3334/CDIAC/00001_V2013, 2015. 32188

Brenninkmeijer, C. A. M., Crutzen, P., Boumard, F., Dauer, T., Dix, B., Ebinghaus, R., Filippi, D., Fischer, H., Franke, H., Frieß, U., Heintzenberg, J., Helleis, F., Hermann, M., Kock, H. H., Koeppel, C., Lelieveld, J., Leuenberger, M., Martinsson, B. G., Miemczyk, S., Moret, H. P., Nguyen, H. N., Nyfeler, P., Oram, D., O'Sullivan, D., Penkett, S., Platt, U., Pupek, M., Ramonet, M., Randa, B., Reichelt, M., Rhee, T. S., Rohwer, J., Rosenfeld, K., Scharffe, D., Schlager, H., Schumann, U., Slemr, F., Sprung, D., Stock, P., Thaler, R., Valentino, F., van Velthoven, P., Waibel, A., Wandel, A., Waschitschek, K., Wiedensohler, A., Xueref-Remy, I., Zahn, A., Zech, U., and Ziereis, H.: Civil Aircraft for the regular investigation of the atmosphere based on an instrumented container: The new CARIBIC system, Atmos. Chem. Phys., 7, 4953–4976, doi:10.5194/acp-7-4953-2007, 2007. 32189

Briber, B. M., Hutyra, L. R., Dunn, A. L., Raciti, S. M., and Munger, J. W.: Variations in Atmospheric CO_2 Mixing Ratios across a Boston, MA Urban to Rural Gradient, Land, 2, 304, doi:10.3390/land2030304, 2013. 32189

Cao, G., Zhang, X., Gong, S., and Zheng, F.: Investigation on emission factors of particulate matter and gaseous pollutants from crop residue burning, J. Environ. Sci., 20, 50–55, doi:10.1016/S1001-0742(08)60007-8, 2008. 32224

Chen, H., Winderlich, J., Gerbig, C., Hoefer, A., Rella, C. W., Crosson, E. R., Van Pelt, A. D., Steinbach, J., Kolle, O., Beck, V., Daube, B. C., Gottlieb, E. W., Chow, V. Y., Santoni, G. W., and Wofsy, S. C.: High-accuracy continuous airborne measurements of greenhouse gases

(CO_2 and CH_4) using the cavity ring-down spectroscopy (CRDS) technique, Atmos. Meas. Tech., 3, 375–386, doi:10.5194/amt-3-375-2010, 2010. 32192, 32193

Ciais, P., Sabine, C., Bala, G., Bopp, L., Brovkin, V., Canadell, J., Chhabra, A., DeFries, R., Galloway, J., Heimann, M., Jones, C., Quere, C., Myneni, R., Piao, S., and Thornton, P.: Carbon and Other Biogeochemical Cycles, Cambridge University Press, Cambridge, UK and New York, NY, USA, doi:10.1017/CBO9781107415324.015, book section 6, 465–570, 2013. 32187

Crosson, E.: A cavity ring-down analyzer for measuring atmospheric levels of methane, carbon dioxide, and water vapor, Appl. Phys. B, 92, 403–408, doi:10.1007/s00340-008-3135-y, 2008. 32193

Dhammapala, R., Claiborn, C., Simpson, C., and Jimenez, J.: Emission factors from wheat and Kentucky bluegrass stubble burning: comparison of field and simulated burn experiments, Atmos. Environ., 41, 1512–1520, doi:10.1016/j.atmosenv.2006.10.008, 2007. 32224

Gurney, K. R., Law, R. M., Denning, A. S., Rayner, P. J., Baker, D., Bousquet, P., Bruhwiler, L., Chen, Y. H., Ciais, P., Fan, S., Fung, I., Gloor, M., Heimann, M., Higuchi, K., John, J., Maki, T., Maksyutov, S., Masarie, K., Peylin, P., Prather, M., Pak, B. C., Randerson, J., Sarmiento, J., Taguchi, S., Takahashi, T., and Yuen, C.: Towards robust regional estimates of CO_2 sources and sinks using atmospheric transport models, Nature, 415, 626–630, doi:10.1038/415626a, 2002. 32187

Kar, J., Bremer, H., Drummond, J. R., Rochon, Y. J., Jones, D. B. A., Nichitiu, F., Zou, J., Liu, J., Gille, J. C., Edwards, D. P., Deeter, M. N., Francis, G., Ziskin, D., and Warner, J.: Evidence of vertical transport of carbon monoxide from Measurements of Pollution in the Troposphere (MOPITT), Geophys. Res. Lett., 31, L23105, doi:10.1029/2004GL021128, 2004. 32197

Karion, A., Sweeney, C., Wolter, S., Newberger, T., Chen, H., Andrews, A., Kofler, J., Neff, D., and Tans, P.: Long-term greenhouse gas measurements from aircraft, Atmos. Meas. Tech., 6, 511–526, doi:10.5194/amt-6-511-2013, 2013. 32192

Lai, S. C., Baker, A. K., Schuck, T. J., van Velthoven, P., Oram, D. E., Zahn, A., Hermann, M., Weigelt, A., Slemr, F., Brenninkmeijer, C. A. M., and Ziereis, H.: Pollution events observed during CARIBIC flights in the upper troposphere between South China and the Philippines, Atmos. Chem. Phys., 10, 1649–1660, doi:10.5194/acp-10-1649-2010, 2010. 32204

Lal, S., Naja, M., and Subbaraya, B.: Seasonal variations in surface ozone and its precursors over an urban site in India, Atmos. Environ., 34, 2713–2724, doi:10.1016/S1352-2310(99)00510-5, 2000. 32203

Lal, S., Chandra, N., and Venkataramani, S.: A study of CO_2 and related trace gases using a laser based technique at an urban site in western India, Curr. Sci. India, in press, 2015. 32190

Law, R. M., Rayner, P. J., Steele, L. P., and Enting, I. G.: Using high temporal frequency data for CO_2 inversions, Global Biogeochem. Cy., 16, 1.1–1.18, doi:10.1029/2001GB001593, 1053, 2002. 32189

Law, R. M., Peters, W., Rödenbeck, C., Aulagnier, C., Baker, I., Bergmann, D. J., Bousquet, P., Brandt, J., Bruhwiler, L., Cameron-Smith, P. J., Christensen, J. H., Delage, F., Denning, A. S., Fan, S., Geels, C., Houweling, S., Imasu, R., Karstens, U., Kawa, S. R., Kleist, J., Krol, M. C., Lin, S.-J., Lokupitiya, R., Maki, T., Maksyutov, S., Niwa, Y., Onishi, R., Parazoo, N., Patra, P. K., Pieterse, G., Rivier, L., Satoh, M., Serrar, S., Taguchi, S., Takigawa, M., Vautard, R., Vermeulen, A. T., and Zhu, Z.: TransCom model simulations of hourly atmospheric CO_2: experimental overview and diurnal cycle results for 2002, Global Biogeochem. Cy., 22, GB3009, doi:10.1029/2007GB003050, 2008. 32195

Le Quéré, C., Moriarty, R., Andrew, R. M., Peters, G. P., Ciais, P., Friedlingstein, P., Jones, S. D., Sitch, S., Tans, P., Arneth, A., Boden, T. A., Bopp, L., Bozec, Y., Canadell, J. G., Chevallier, F., Cosca, C. E., Harris, I., Hoppema, M., Houghton, R. A., House, J. I., Jain, A., Johannessen, T., Kato, E., Keeling, R. F., Kitidis, V., Klein Goldewijk, K., Koven, C., Landa, C. S., Landschützer, P., Lenton, A., Lima, I. D., Marland, G., Mathis, J. T., Metzl, N., Nojiri, Y., Olsen, A., Ono, T., Peters, W., Pfeil, B., Poulter, B., Raupach, M. R., Regnier, P., Rödenbeck, C., Saito, S., Salisbury, J. E., Schuster, U., Schwinger, J., Séférian, R., Segschneider, J., Steinhoff, T., Stocker, B. D., Sutton, A. J., Takahashi, T., Tilbrook, B., van der Werf, G. R., Viovy, N., Wang, Y.-P., Wanninkhof, R., Wiltshire, A., and Zeng, N.: Global carbon budget 2014, Earth Syst. Sci. Data Discuss., 7, 521–610, doi:10.5194/essdd-7-521-2014, 2014. 32187

Levin, I., Kromer, B., Schmidt, M., and Sartorius, H.: A novel approach for independent budgeting of fossil fuel CO_2 over Europe by $^{14}CO_2$ observations, Geophys. Res. Lett., 30, 2194, doi:10.1029/2003GL018477, 2003. 32207

Lin, X., Indira, N. K., Ramonet, M., Delmotte, M., Ciais, P., Bhatt, B. C., Reddy, M. V., Angchuk, D., Balakrishnan, S., Jorphail, S., Dorjai, T., Mahey, T. T., Patnaik, S., Begum, M., Brenninkmeijer, C., Durairaj, S., Kirubagaran, R., Schmidt, M., Swathi, P. S., Vinithkumar, N. V., Yver Kwok, C., and Gaur, V. K.: Long-lived atmospheric trace gases measure-

ments in flask samples from three stations in India, Atmos. Chem. Phys., 15, 9819–9849, doi:10.5194/acp-15-9819-2015, 2015. 32188, 32189, 32198, 32199, 32204

Lopez, M., Schmidt, M., Delmotte, M., Colomb, A., Gros, V., Janssen, C., Lehman, S. J., Mondelain, D., Perrussel, O., Ramonet, M., Xueref-Remy, I., and Bousquet, P.: CO, NO_x and $^{13}CO_2$ as tracers for fossil fuel CO_2: results from a pilot study in Paris during winter 2010, Atmos. Chem. Phys., 13, 7343–7358, doi:10.5194/acp-13-7343-2013, 2013. 32189, 32207

Machida, T., Matsueda, H., Sawa, Y., Nakagawa, Y., Hirotani, K., Kondo, N., Goto, K., Nakazawa, T., Ishikawa, K., and Ogawa, T.: Worldwide measurements of atmospheric CO_2 and other trace gas species using commercial airlines, J. Atmos. Ocean. Tech., 25, 1744–1754, doi:10.1175/2008JTECHA1082.1, 2008. 32189

Mahesh, P., Sharma, N., Dadhwal, V., Rao, P., Apparao, B., Ghosh, A., Mallikarjun, K., and Ali, M.: Impact of land-sea breeze and rainfall on CO_2 variations at a coastal station, Journal of Earth Science and Climatic Change, 5, 201, doi:10.4172/2157-7617.1000201, 2014. 32189

Mallik, C., Lal, S., and Venkataramani, S.: Trace gases at a semi-arid urban site in western India: variability and inter-correlations, J. Atmos. Chem., 72, 143–164, doi:10.1007/s10874-015-9311-7, 2015. 32190

Newman, S., Jeong, S., Fischer, M. L., Xu, X., Haman, C. L., Lefer, B., Alvarez, S., Rappenglueck, B., Kort, E. A., Andrews, A. E., Peischl, J., Gurney, K. R., Miller, C. E., and Yung, Y. L.: Diurnal tracking of anthropogenic CO_2 emissions in the Los Angeles basin megacity during spring 2010, Atmos. Chem. Phys., 13, 4359–4372, doi:10.5194/acp-13-4359-2013, 2013. 32188, 32207

Olsen, S. C. and Randerson, J. T.: Differences between surface and column atmospheric CO_2 and implications for carbon cycle research, J. Geophys. Res.-Atmos., 109, d02301, doi:10.1029/2003JD003968, 2004. 32195

Onogi, K., Tsutsui, J., Koide, H., Sakamoto, M., Kobayashi, S., Hatsushika, H., Matsumoto, T., Yamazaki, N., Kamahori, H., Takahashi, K., Kadokura, S., Wada, K., Kato, K., Oyama, R., Ose, T., Mannoji, N., and Taira, R.: The JRA-25 reanalysis, J. Meteorol. Soc. Jpn., 85, 369–432, doi:10.2151/jmsj.85.369, 2007. 32194

Park, M., Randel, W. J., Emmons, L. K., and Livesey, N. J.: Transport pathways of carbon monoxide in the Asian summer monsoon diagnosed from Model of Ozone and Related Tracers (MOZART), J. Geophys. Res.-Atmos., 114, D08303, doi:10.1029/2008JD010621, 2009. 32197

Patra, P. K., Law, R. M., Peters, W., Rödenbeck, C., Takigawa, M., Aulagnier, C., Baker, I., Bergmann, D. J., Bousquet, P., Brandt, J., Bruhwiler, L., Cameron-Smith, P. J., Christensen, J. H., Delage, F., Denning, A. S., Fan, S., Geels, C., Houweling, S., Imasu, R., Karstens, U., Kawa, S. R., Kleist, J., Krol, M. C., Lin, S.-J., Lokupitiya, R., Maki, T., Maksyutov, S., Niwa, Y., Onishi, R., Parazoo, N., Pieterse, G., Rivier, L., Satoh, M., Serrar, S., Taguchi, S., Vautard, R., Vermeulen, A. T., and Zhu, Z.: TransCom model simulations of hourly atmospheric CO_2: analysis of synoptic-scale variations for the period 2002–2003, Global Biogeochem. Cy., 22, GB4013, doi:10.1029/2007GB003081, 2008. 32195

Patra, P. K., Niwa, Y., Schuck, T. J., Brenninkmeijer, C. A. M., Machida, T., Matsueda, H., and Sawa, Y.: Carbon balance of South Asia constrained by passenger aircraft CO_2 measurements, Atmos. Chem. Phys., 11, 4163–4175, doi:10.5194/acp-11-4163-2011, 2011. 32189, 32197, 32198, 32201, 32210, 32211, 32238

Patra, P. K., Canadell, J. G., Houghton, R. A., Piao, S. L., Oh, N.-H., Ciais, P., Manjunath, K. R., Chhabra, A., Wang, T., Bhattacharya, T., Bousquet, P., Hartman, J., Ito, A., Mayorga, E., Niwa, Y., Raymond, P. A., Sarma, V. V. S. S., and Lasco, R.: The carbon budget of South Asia, Biogeosciences, 10, 513–527, doi:10.5194/bg-10-513-2013, 2013. 32187, 32189

Pérez-Landa, G., Ciais, P., Gangoiti, G., Palau, J. L., Carrara, A., Gioli, B., Miglietta, F., Schumacher, M., Millán, M. M., and Sanz, M. J.: Mesoscale circulations over complex terrain in the Valencia coastal region, Spain – Part 2: Modeling CO_2 transport using idealized surface fluxes, Atmos. Chem. Phys., 7, 1851–1868, doi:10.5194/acp-7-1851-2007, 2007. 32189

Peylin, P., Law, R. M., Gurney, K. R., Chevallier, F., Jacobson, A. R., Maki, T., Niwa, Y., Patra, P. K., Peters, W., Rayner, P. J., Rödenbeck, C., van der Laan-Luijkx, I. T., and Zhang, X.: Global atmospheric carbon budget: results from an ensemble of atmospheric CO_2 inversions, Biogeosciences, 10, 6699–6720, doi:10.5194/bg-10-6699-2013, 2013. 32187

Popa, M. E., Vollmer, M. K., Jordan, A., Brand, W. A., Pathirana, S. L., Rothe, M., and Röckmann, T.: Vehicle emissions of greenhouse gases and related tracers from a tunnel study: $CO : CO_2$, $N_2O : CO_2$, $CH_4 : CO_2$, $O_2 : CO_2$ ratios, and the stable isotopes ^{13}C and ^{18}O in CO_2 and CO, Atmos. Chem. Phys., 14, 2105–2123, doi:10.5194/acp-14-2105-2014, 2014. 32188

Randel, W. J. and Park, M.: Deep convective influence on the Asian summer monsoon anticyclone and associated tracer variability observed with Atmospheric Infrared Sounder (AIRS), J. Geophys. Res.-Atmos., 111, D12314, doi:10.1029/2005JD006490, 2006. 32197

Randerson, J. T., Thompson, M. V., Conway, T. J., Fung, I. Y., and Field, C. B.: The contribution of terrestrial sources and sinks to trends in the seasonal cycle of atmospheric carbon dioxide, Global Biogeochem. Cy., 11, 535–560, doi:10.1029/97GB02268, 1997. 32194

Russo, R. S., Talbot, R. W., Dibb, J. E., Scheuer, E., Seid, G., Jordan, C. E., Fuelberg, H. E., Sachse, G. W., Avery, M. A., Vay, S. A., Blake, D. R., Blake, N. J., Atlas, E., Fried, A., Sandholm, S. T., Tan, D., Singh, H. B., Snow, J., and Heikes, B. G.: Chemical composition of Asian continental outflow over the western Pacific: results from Transport and Chemical Evolution over the Pacific (TRACE-P), J. Geophys. Res.-Atmos., 108, 8804, doi:10.1029/2002JD003184, 2003. 32204

Sánchez-Ccoyllo, O., Ynoue, R., Martins, L., Astolfo, R., Miranda, R., Freitas, E., Borges, A., Fornaro, A., Freitas, H., Moreira, A., and Andrade, M.: Vehicular particulate matter emissions in road tunnels in Sao Paulo, Brazil, Environ. Monit. Assess., 149, 241–249, doi:10.1007/s10661-008-0198-5, 2009. 32224

Schuck, T. J., Brenninkmeijer, C. A. M., Baker, A. K., Slemr, F., von Velthoven, P. F. J., and Zahn, A.: Greenhouse gas relationships in the Indian summer monsoon plume measured by the CARIBIC passenger aircraft, Atmos. Chem. Phys., 10, 3965–3984, doi:10.5194/acp-10-3965-2010, 2010. 32189

Schuck, T. J., Ishijima, K., Patra, P. K., Baker, A. K., Machida, T., Matsueda, H., Sawa, Y., Umezawa, T., Brenninkmeijer, C. A. M., and Lelieveld, J.: Distribution of methane in the tropical upper troposphere measured by CARIBIC and CONTRAIL aircraft, J. Geophys. Res.-Atmos., 117, D19304, doi:10.1029/2012JD018199, 2012. 32189

Sharma, N., Dadhwal, V., Kant, Y., Mahesh, P., Mallikarjun, K., Gadavi, H., Sharma, A., and Ali, M.: Atmospheric CO_2 variations in two contrasting environmental sites over India, Air, Soil and Water Res., 7, 61–68, doi:10.4137/ASWR.S13987, 2014. 32189, 32201

Streets, D. G., Bond, T. C., Carmichael, G. R., Fernandes, S. D., Fu, Q., He, D., Klimont, Z., Nelson, S. M., Tsai, N. Y., Wang, M. Q., Woo, J.-H., and Yarber, K. F.: An inventory of gaseous and primary aerosol emissions in Asia in the year 2000, J. Geophys. Res.-Atmos., 108, 8809, doi:10.1029/2002JD003093, 2003. 32224

Suntharalingam, P., Jacob, D. J., Palmer, P. I., Logan, J. A., Yantosca, R. M., Xiao, Y., Evans, M. J., Streets, D. G., Vay, S. L., and Sachse, G. W.: Improved quantification of Chinese carbon fluxes using CO_2 / CO correlations in Asian outflow, J. Geophys. Res.-Atmos., 109, D18S18, doi:10.1029/2003JD004362, 2004. 32204

Takahashi, T., Sutherland, S. C., Wanninkhof, R., Sweeney, C., Feely, R. A., Chipman, D. W., Hales, B., Friederich, G., Chavez, F., Sabine, C., Watson, A., Bakker, D. C., Schuster, U., Metzl, N., Yoshikawa-Inoue, H., Ishii, M., Midorikawa, T., Nojiri, Y., Körtzinger, A., Steinhoff, T., Hoppema, M., Olafsson, J., Arnarson, T. S., Tilbrook, B., Johannessen, T., Olsen, A., Bellerby, R., Wong, C., Delille, B., Bates, N., and de Baar, H. J.: Climatological mean and decadal change in surface ocean pCO_2, and net sea–air CO_2 flux over the global oceans, Deep-Sea Res. Pt. II, 56, 554–577, doi:10.1016/j.dsr2.2008.12.009, 2009. 32194

Takegawa, N., Kondo, Y., Koike, M., Chen, G., Machida, T., Watai, T., Blake, D. R., Streets, D. G., Woo, J.-H., Carmichael, G. R., Kita, K., Miyazaki, Y., Shirai, T., Liley, J. B., and Ogawa, T.: Removal of NO_x and NO_y in Asian outflow plumes: aircraft measurements over the western Pacific in January 2002, J. Geophys. Res.-Atmos., 109, D23S04, doi:10.1029/2004JD004866, 2004. 32204

Tiwari, Y. K., Vellore, R. K., Kumar, K. R., van der Schoot, M., and Cho, C.-H.: Influence of monsoons on atmospheric CO_2 spatial variability and ground-based monitoring over India, Sci. Total Environ., 490, 570–578, doi:10.1016/j.scitotenv.2014.05.045, 2014. 32189, 32198

Turnbull, J. C., Miller, J. B., Lehman, S. J., Tans, P. P., Sparks, R. J., and Southon, J.: Comparison of $^{14}CO_2$, CO, and SF_6 as tracers for recently added fossil fuel CO_2 in the atmosphere and implications for biological CO_2 exchange, Geophys. Res. Lett., 33, L01817, doi:10.1029/2005GL024213, 2006. 32187, 32188, 32207

Turnbull, J. C., Karion, A., Fischer, M. L., Faloona, I., Guilderson, T., Lehman, S. J., Miller, B. R., Miller, J. B., Montzka, S., Sherwood, T., Saripalli, S., Sweeney, C., and Tans, P. P.: Assessment of fossil fuel carbon dioxide and other anthropogenic trace gas emissions from airborne measurements over Sacramento, California in spring 2009, Atmos. Chem. Phys., 11, 705–721, doi:10.5194/acp-11-705-2011, 2011. 32207

Vogel, F. R., Hammer, S., Steinhof, A., Kromer, B., and Levin, I.: Implication of weekly and diurnal ^{14}C calibration on hourly estimates of CO-based fossil fuel CO_2 at a moderately polluted site in southwestern Germany, Tellus B, 62, 512–520, doi:10.1111/j.1600-0889.2010.00477.x, 2010. 32207

Wada, A., Matsueda, H., Sawa, Y., Tsuboi, K., and Okubo, S.: Seasonal variation of enhancement ratios of trace gases observed over 10 years in the western North Pacific, Atmos. Environ., 45, 2129–2137, doi:10.1016/j.atmosenv.2011.01.043, 2011. 32204

Wang, Y., Munger, J. W., Xu, S., McElroy, M. B., Hao, J., Nielsen, C. P., and Ma, H.: CO_2 and its correlation with CO at a rural site near Beijing: implications for combustion efficiency in

China, Atmos. Chem. Phys., 10, 8881–8897, doi:10.5194/acp-10-8881-2010, 2010. 32187, 32188

Welp, L. R., Keeling, R. F., Weiss, R. F., Paplawsky, W., and Heckman, S.: Design and performance of a Nafion dryer for continuous operation at CO_2 and CH_4 air monitoring sites, Atmos. Meas. Tech., 6, 1217–1226, doi:10.5194/amt-6-1217-2013, 2013. 32193

Westerdahl, D., Wang, X., Pan, X., and Zhang, K. M.: Characterization of on-road vehicle emission factors and microenvironmental air quality in Beijing, China, Atmos. Environ., 43, 697–705, doi:10.1016/j.atmosenv.2008.09.042, 2009. 32224

Wong, K. W., Fu, D., Pongetti, T. J., Newman, S., Kort, E. A., Duren, R., Hsu, Y.-K., Miller, C. E., Yung, Y. L., and Sander, S. P.: Mapping $CH_4 : CO_2$ ratios in Los Angeles with CLARS-FTS from Mount Wilson, California, Atmos. Chem. Phys., 15, 241–252, doi:10.5194/acp-15-241-2015, 2015. 32205

Wunch, D., Wennberg, P. O., Toon, G. C., Keppel-Aleks, G., and Yavin, Y. G.: Emissions of greenhouse gases from a North American megacity, Geophys. Res. Lett., 36, L15810, doi:10.1029/2009GL039825, 2009. 32188, 32205

Table 1. Emission ratios of CO/CO_2 (ppb ppm^{-1}), derived from emission factors (gram of gases emitted per kilogram of fuel burned).

Biomass burning	Transport		Industry	Domestic	
Crop-residue[a,b,c]	Diesel[d,e,f]	Gasoline[d,f]	Coal	Coal[d,f]	Biofuel[c,d]
45.7–123.6	8.6–65.2	33.5	23.5–40.4	53.3–62.2	52.9–98.5

[a] Dhammapala et al. (2007). [b] Cao et al. (2008). [c] Andreae and Merlet (2001). [d] Streets et al. (2003). [e] Sánchez-Ccoyllo et al. (2009). [f] Westerdahl et al. (2009).

Table 2. Estimates of emissions of CO using the the CO_2 emission from EDGAR inventory over the box (72.3 < longitude < 72.7° E, 22.8 < latitude < 23.2° N) and observed $CO_{exc} : CO_{2exc}$ slopes for different time periods. The correlation coefficient for corresponding slopes are given inside the bracket in slope column. Monsoon data are not included for calculating slopes.

Time (IST)	Slope (ppb ppm^{-1}) Correlation coefficient (r)	EDGAR Emissions (Gg yr^{-1})		Estimated Emssions Gg (yr)
		CO_2	CO	
23:00–05:00 IST	13 ± 0.14 (0.84)			69.2 ± 0.7
06:00–10:00 IST	11.4 ± 0.19 (0.75)			60.7 ± 1.0
11:00–16:00 IST	14.9 ± 0.19 (0.78)	8368.6	45.3	79.3 ± 1.0
18:00–05:00 IST	34.6 ± 0.37 (0.76)			184.2 ± 1.9
Full day (24 h)	10.8 ± 0.09 (0.73)			57.5 ± 0.5

Table 3. Model performance matrices used to quantify the level of agreement between model simulations and observations. These statistics are based on hourly values in each day.

Parameter	Winter	Autumn	Monsoon	All months
MB (ppm)	−2.72	12.64	−2.45	2.27
FGE (%)	0.96	3.12	2.0	1.76
RMSE (ppm)	5.21	12.82	9.14	8.60
RMSE (%)	1.27	3.21	2.20	2.09

Table 4. Summary of results for the study period. The total refers to the average of all the 24 h data while noon time values refer to the average for 12:00–16:00 IST. The "exc" refer to the excess concentrations of CO_2 and CO after subtracting the background concentrations.

Period	Mean (ppm)		Diurnal amplitude (ppm)		Correlation $CO_{exc} : CO_{2exc}$	
	CO_2	CO	CO_2	CO	Slope (ppb ppm^{-1})	Correlation coefficient (r)
Monsoon	400.3 ± 6.8	0.19 ± 0.13	12.4	0.24	0.6 ± 0.1	0.62
Autumn	419.6 ± 22.8	0.72 ± 0.71	40.9	1.36	8.5 ± 0.2	0.72
Winter	417.2 ± 18.5	0.73 ± 0.68	31.7	1.01	12.7 ± 0.2	0.71
Spring	415.4 ± 14.8	0.41 ± 0.40	15.9	0.62	8.4 ± 0.1	0.87
Annual	413.0 ± 13.7	0.50 ± 0.37	25.0	0.48	8.3 ± 0.7	0.79

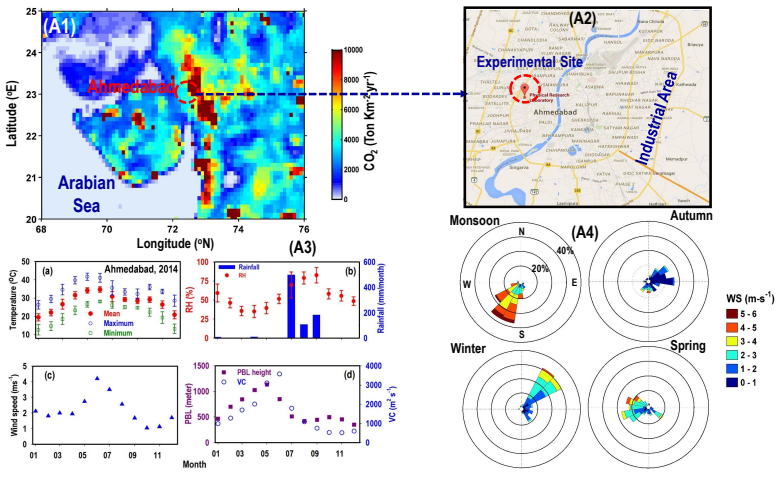

Figure 1. (A1) Spatial distribution of total anthropogenic CO_2 emissions from EDGARv4.2 inventory over Ahmedabad and surrounding regions. (A2) The Ahmedabad city map showing location of the experimental site (PRL). (A3: **a**–**d**) Monthly average temperature with monthly maximum and minimum value, relative humidity (RH), rainfall, wind speed, PBL height and ventilation coefficient (VC) over Ahmedabad during the year 2014. Temperature, RH and wind speed are taken from the Wunderground weather (www.wunderground.com) while rainfall and PBLH data are used from Tropical Rainfall Measuring Mission (TRMM) satellite and MEERA reanalysis data. (A4) Wind rose plots for Ahmedabad for the four seasons of 2014 using daily average data from the Wunderground.

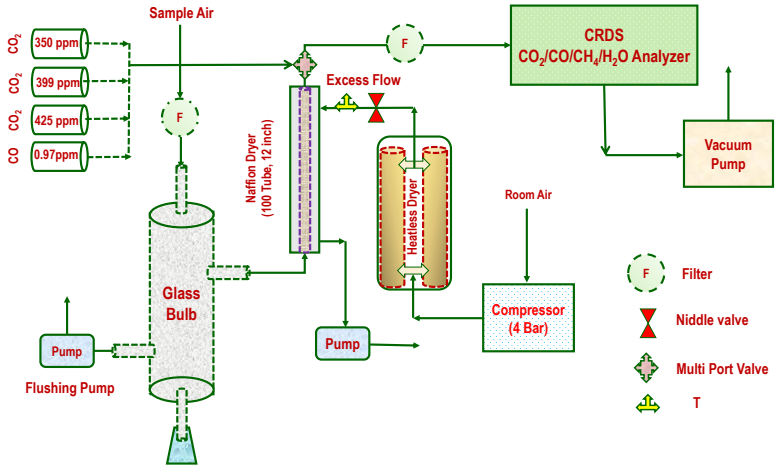

Figure 2. Schematic diagram of the analysis system. We introduced additionally a Nafion dryer in the inlet of instrument for removing the water vapour from the ambient air. The calibration mixtures (three) from NOAA, USA are used to calibrate CO_2 measurements and one calibration mixture from Linde, UK is used to calibrate CO measurements.

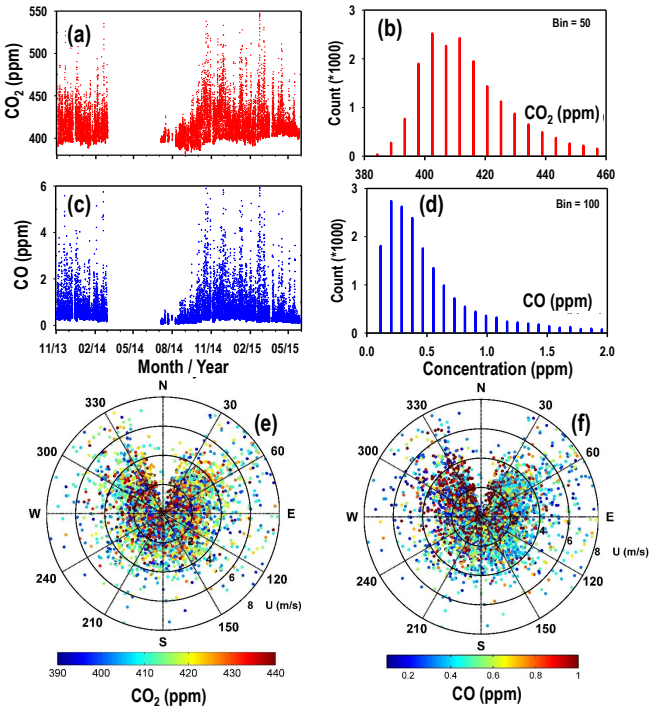

Figure 3. (a, c) Time series of 30 min average values CO_2 and CO measured at Ahmedabad for the study period. **(b, d)** The frequency distribution in CO_2 and CO concentrations for the study period using 30 min mean of both gases. **(e, f)** The polar plots show the variation of 30 min averaged CO_2 and CO at this site with wind direction and speed during the study period except July, August and September due to unavailability of meteorology data.

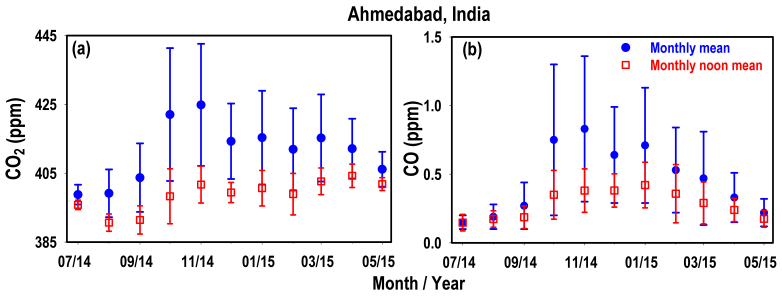

Figure 4. The seasonal variation of CO_2 and CO at Ahmedabad, India from July 2014 to May 2015 using their monthly mean concentrations. The blue dots and red rectangles show the monthly average concentrations of these gases for the total (00:00–24:00 IST) and noon time (12:00–16:00 IST) data respectively with 1σ spread. All times are in Indian Standard Time (IST), which is 5.5 h ahead of GMT.

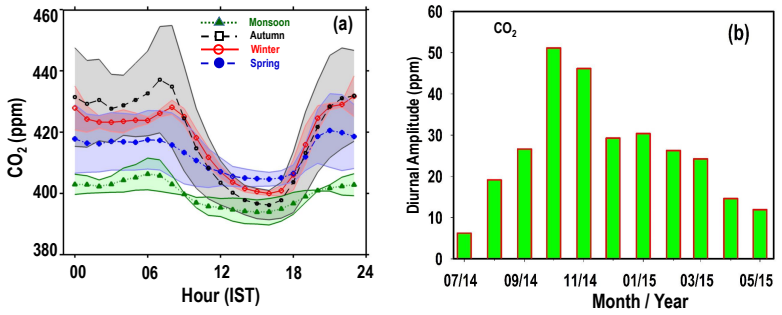

Figure 5. (a) Average diurnal variation of CO_2 over Ahmedabad during all the four seasons. **(b)** Monthly variation of average diurnal amplitude of CO_2 from July 2014 to May 2015.

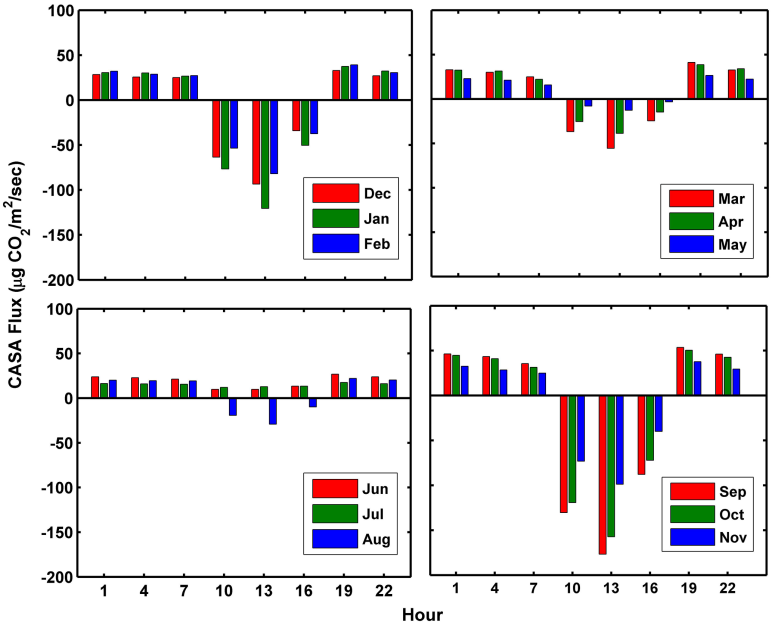

Figure 6. Diurnal variation of biospheric fluxes from the CASA ecosystem model.

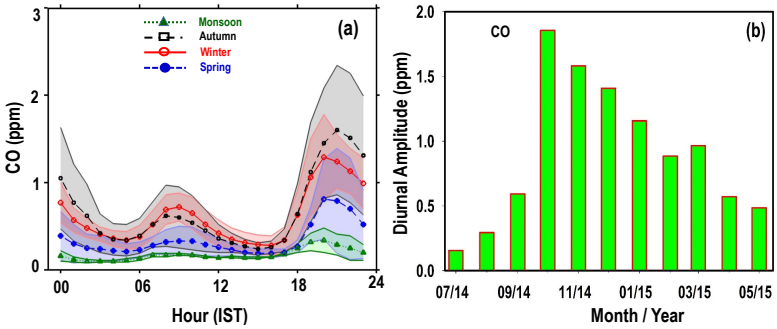

Figure 7. (a) Diurnal variation of CO over Ahmedabad during all the four seasons. **(b)** Monthly variation of the diurnal amplitude of CO.

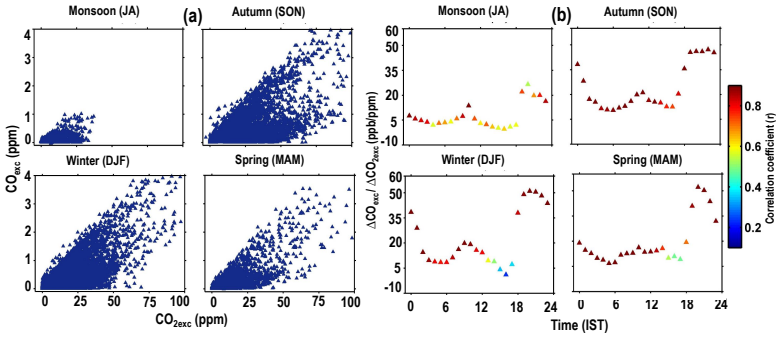

Figure 8. (a) Correlation of excess CO above background (CO_{exc}) with the excess CO_2 above background (CO_{2exc}) during all the four different seasons. Each data points are averaged for 30 min. **(b)** The diurnal variation of the $\Delta CO_{exc}/\Delta CO_{exc}$ slopes during all the four seasons. The colour bar in this plot shows the correlation coefficient (r) for corresponding time.

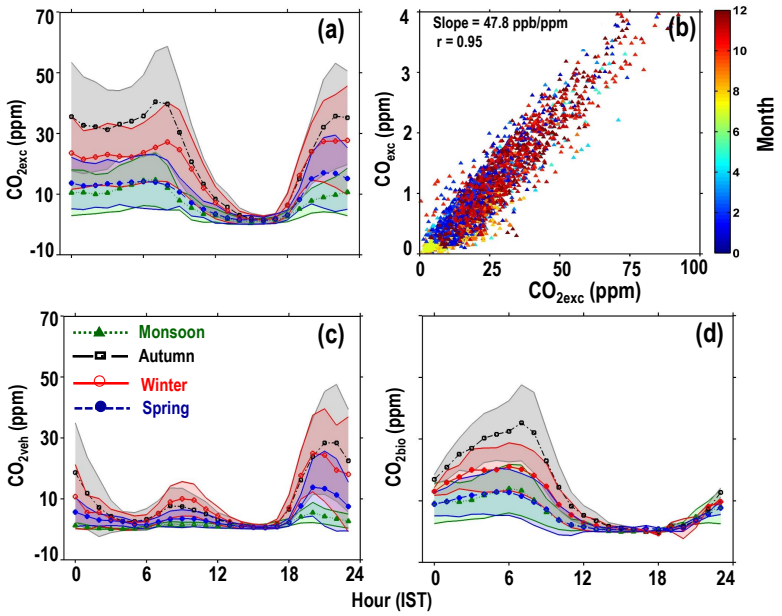

Figure 9. (a) Diurnal cycle of excess CO_2 over background levels during all the four seasons. **(b)** Correlation between excess CO and CO_2 for evening hours (18:00–21:00 IST) during the study period. Contributions of fossil fuel **(c)** and biosphere **(d)** in the diurnal variation of excess CO_2 in all the four seasons.

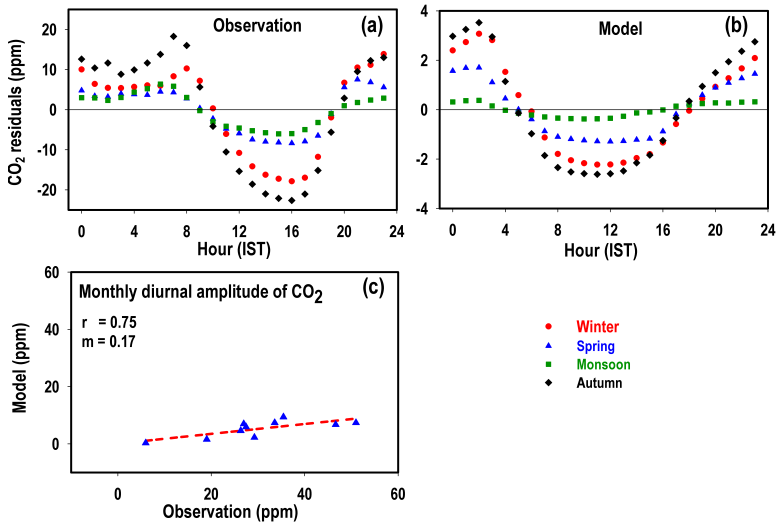

Figure 10. Residual of the diurnal cycle of CO_2 (in ppm) for **(a)** observations and **(b)** modal simulation over Ahmedabad in all the four seasons. Please note that the scales of model and observational diurnal cycles are different. **(c)** Correlation between observed and model simulated monthly mean diurnal cycle amplitudes.

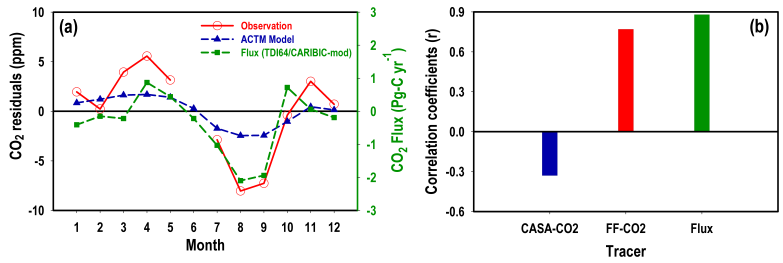

Figure 11. (a) The red circles and blue triangles show the mean seasonal cycles of CO_2 (in ppm) using afternoon values only, calculated from measurements and model over Ahmedabad. The green triangles show the seasonal cycles of CO_2 flux over South Asia, calculated from TDI64/CARIBIC-modified inverse model as given in Patra et al. (2011) (Fig. 3d). **(b)** Blue bar and red bar shows the correlation coefficient (r) of model CO_2 concentration of biospheric tracer and fossil fuel tracer component with observed concentrations of CO_2 taking the entire annual time series of daily mean data, respectively. The green bar shows the correlation coefficient between the monthly residuals of afternoon mean only and the CO_2 flux over South Asia.

A study of CO_2 and related trace gases using a laser-based technique at an urban site in western India

S. Lal[1,*], N. Chandra[1,2] and S. Venkataramani[1]

[1]Physical Research Laboratory, Ahmedabad 380 009, India
[2]Indian Institute of Technology, Gandhinagar 382 424, India

Continuous measurements of surface-level carbon dioxide (CO_2) along with its co-emitted carbon monoxide (CO) and methane (CH_4) are being made at Ahmedabad using a laser-based cavity ring down spectrometer, which offers much longer path length for accurate and fast measurements of these species simultaneously. The average data during November 2013 show large variability in all the three species. These measurements also show significant diurnal variations with maximum in CO being relatively the shortest-lived species in this set of gases. The correlations and slopes among them have been used to identify potential emission sources.

Keywords: Cavity ring down spectroscopy, fossil fuel, greenhouse gases, India, vehicular emissions.

CARBONDIOXIDE (CO_2) is the most important greenhouse gas (GHG) of anthropogenic origin. It is found to increase with time due to increasing use of fossil fuel combustion and biomass burning. The present level of background CO_2 has crossed 400 ppm and it is currently increasing at an average rate of 2.13 ppmv per year (in 2014) based on the Mauna Loa data (www.esrl.noaa.gov/gmd/ccgg/trends). Recent measurements show that the amplitude of seasonal variation of atmospheric CO_2 in the northern hemisphere has increased since 1950s (ref. 1). Effects of rising levels of this gas as well as other GHGs like CH_4 and N_2O are clearly evident in rising air temperature and associated effects all over the globe[2], as well as in the Indian region[3–5]. The Asian countries, including India and China are growing fast, which leads to increase in the emissions of these gases. Since the lifetimes of these species are high, the effects are going to be felt all over the globe irrespective of the emission locations.

Sources and sinks of these GHGs need to be identified and estimated accurately to understand their variability and future trends. The budgets of these gases can be estimated using top-down and bottom-up approaches. However, both approaches show larger uncertainties (100–150%) in the biospheric flux of CO_2 over South Asia than other continents, as shown by Patra *et al.*[6,7]. One of the major sources for these larger uncertainties is the lack of measurements with required temporal and spatial resolutions. There are several groups in the developed countries making such measurements, but these are lacking in India. Hence, there is a need for an observational network covering different ecosystems in India to make precise measurements of these gases in order to understand their variability, trends and improved understanding of their emission budgets in the Indian region. Since CO_2 is also related to the biosphere (photosynthesis and respiration), its measurements in different ecosystems are necessary. Several groups are now involved in the measurement of surface-level CO_2 in India[8–12]. Some of them are also making measurements of CO_2 flux using tower measurements[13–15]. However, there are limited measurements of CO_2 with other co-emitted gases like carbon monoxide (CO), methane (CH_4), etc. Simultaneous measurements of CO_2 with CO and CH_4 have their importance in terms of constraining emission sources and their nature. CO_2 measurements alone can give information on basic features in terms of diurnal variation, seasonal variation and their amplitudes, but cannot give information related to source types. Interrelations among these gases can yield important information on the type of emission sources. This communication presents some initial results from a recently initiated project as a part of the ISRO-GBP to study the levels, variability and trends in CO_2 and related trace gases at Ahmedabad.

There are many techniques to measure CO_2 in air. The collected air samples can be analysed using a gas chromatograph equipped with a flame ionization detector and a Ni-catalyst to convert CO_2 to methane, which is finally detected. Though the system is rugged, it has limitation related to portability, precision and accuracy. Infrared absorption-based (using non-dispersive infrared NDIR technique) analysers are highly portable with better sensitivity and accuracy. These systems have been extensively used for field studies, including aircraft-based measurements[16,17]. However, these have the problem of drift (zero and temperature drift) in the system and need frequent calibration. This problem is overcome in the systems based on cavity ring down spectroscopy (CRDS) technique. This technique is based on the measurement of the rate of absorption rather than the magnitude of absorption of a laser pulse confined in a closed optical cavity filled with the sample air. Since many atmospheric gases have absorption bands in the near-infrared region, it is possible to tune the laser wavelength for a specific gas molecule. Since the effective path length inside the cavity becomes very large (many kilometres), the sensitivity of this system becomes extremely good. It can measure gases in parts per billion level with high accuracy and with very fast response in seconds or less[18,19]. We have used an analyser based on this technique for the simultaneous measurements of CO_2, CO, CH_4 and water vapour (Picarro, G2401). The precisions for a 5 min average are ~50, ~2 and ~0.7 ppb for CO_2, CO and CH_4 respectively. It uses a pump to suck the inlet air through the analyser. Since we are not interested in measuring water vapour and to avoid

*For correspondence. (e-mail: shyam@prl.res.in)

its calibration and correction to calculate dry mole fractions, we remove water in the sample air before it enters into the system using a Nafion dryer (100 tubes, 24 inch length). It brings down the water level to about 0.03% from 2% to 3%. This analyser is frequently calibrated using three CO_2 mixtures from NOAA, USA at 350, 400 and 425 ppmv. The analyser is also calibrated for CO and CH_4 using gas mixtures from Linde, UK.

The measurements are being made from the sixth floor of the main building of the Physical Research Laboratory (PRL), Ahmedabad (23°N, 72.5°E, 49 m amsl). It is located in the western region of the city, dominated by various educational organizations and residential societies. A power house and some industries are located in the eastern parts of the city. The city has a population of about 50 lakhs and about 32 lakh registered vehicles, which are growing by about 10% per year. All these stationary and mobile fossil-fuel burning systems are a good source of gaseous and particulate pollutants. The city has a warm climate with high temperatures going up to 44°C in May and lowest temperature of about 8°C in January. The wind is mostly from the west except during the monsoon season, when it becomes southwest. Cool air during the winter comes from the northwest direction. The average annual rainfall is about 780 mm, which mostly occurs in July and August. Figure 1 shows air temperature, relative humidity, wind direction and wind speed, and solar radiation received at the ground in November 2013. These measurements are made using a weather station located in the PRL campus. There are some breaks in the data due to technical problems. The air temperature during this month was in the range 17–33°C. The relative humidity was in the range 25–75%. Wind speed varied from 1 to 4 m s^{-1} and the direction changed from northeast to southwest. The relative humidity as well as the solar radiation showed slight decreasing trend during this month.

Continuous *in situ* surface-level observations of CO_2, CO and CH_4 using this system started at PRL in November 2013. Figurer 2 shows the 30-min average mixing ratios of these species from 3 to 30 November. There is a large variability in the levels of these gases during this month. Relatively lower values of these gases were observed during 16–19 November, while higher levels were observed during 20–27 November. A plume of very high levels of these gases was observed on 21 November. However, CH_4 level was highest on 7 November when the other two gases did not show any abnormal increase. The minimum level of CO_2 observed during this month was about 390 ppmv and it went as high as 558.6 ppmv. The average level of CO_2 during this month was found to be 418.3 ± 17.6 ppmv. Similarly, minimum level of CO was found to be 0.2 ppmv and highest level (7.0 ppmv) was observed coinciding with the high level of CO_2. The average level of CO was found to be 0.73 ± 0.65 ppmv. Methane showed 1.95, 5.7 and 2.41 ± 0.42 ppmv respectively, for minimum, highest and mean levels. Maximum variability has been observed in the levels of CO as its lifetime (few weeks to two months) is the shortest among the three gases.

To illustrate the nature of average diurnal cycle of CO_2, CO and CH_4, we standardized it by averaging

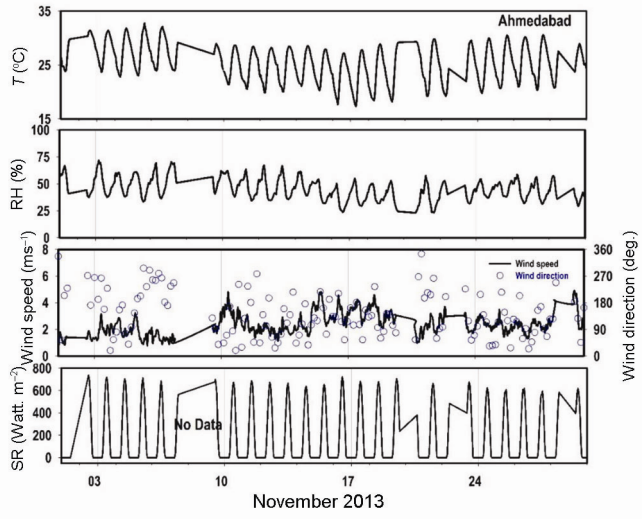

Figure 1. Variability of meteorological parameters measured using a weather station located at PRL, Ahmedabad.

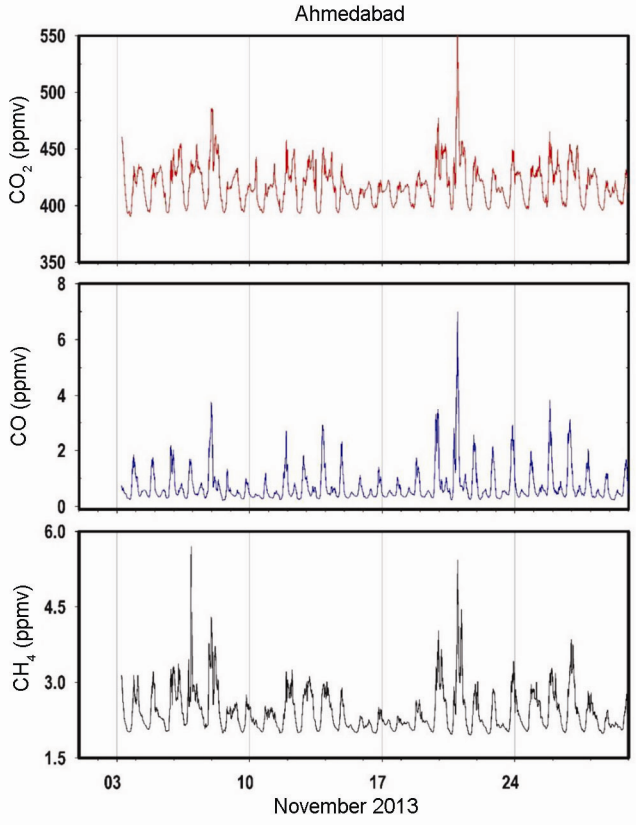

Figure 2. Variability in the 30-min average mixing ratios of CO_2, CO and CH_4 measured at PRL, Ahmedabad during November 2013.

of every second data for respective hour of all the days of observations after removing the outer values beyond two sigma as outliers. Figure 3 shows the average diurnal patterns based on hourly average values for these gases during November 2013. Highest values of hourly average CO_2 (431 ppmv) are observed during the morning around 0800 h and in the late evening around 2200 h. These are also the periods of maximum variability. There is a slow increase in the levels of CO_2 after the midnight (~0200 h) low. This is mainly due to respiration by the plants. After the peak around 0800 h, the level of CO_2 starts decreasing as the planetary boundary layer (PBL) height increases and as the photosynthesis in plants increases. The minimum CO_2 (396 ppmv) during the day is observed around 1600 h, when the diurnal value of air temperature is highest and the PBL height is also high. This gives higher volume for mixing of the pollutants in the atmosphere. CO_2 levels again increase after this minimum due to lowering of the PBL, increase in the vehicular traffic as well as decrease in the photosynthesis activity. The variability in CO_2 is high from late night to morning (2–3%) and minimum (0.6%) during afternoon hours. The

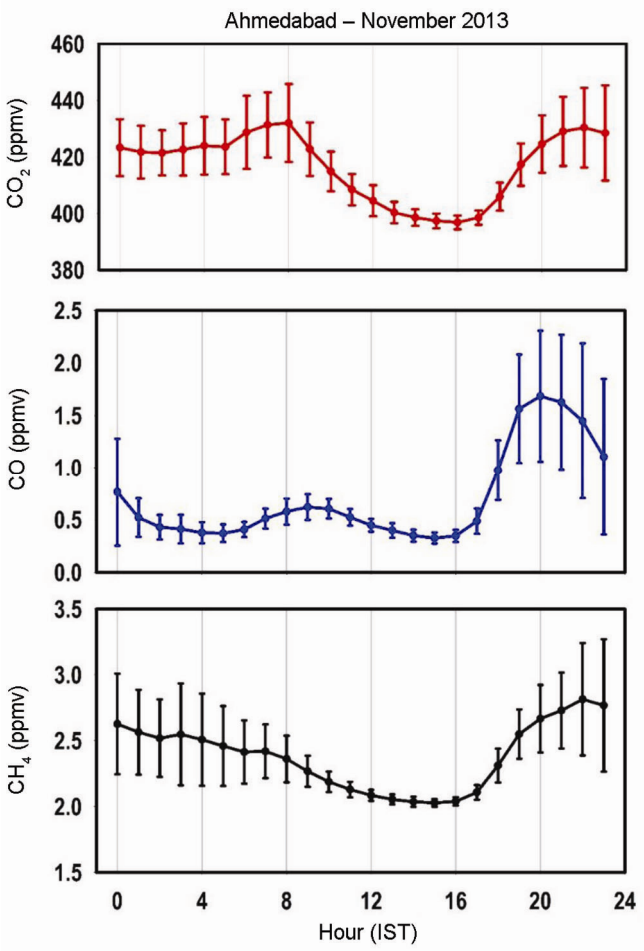

Figure 3. Average diurnal variations of CO_2, CO and CH_4 observed during November 2013 at Ahmedabad.

average diurnal amplitude during this month is about 35 ppmv. The only other measurements for diurnal variations in India are available for Dehradun and Gadanki[11], and for Sriharikota[10]. Dehradun and Gadanki show diurnal amplitudes of 30 and 40 ppmv respectively, whereas Sriharikota shows an amplitude of only 17 ppmv. Though the diurnal amplitude observed at Ahmedabad is in the range of Dehradun and Gadanki, but their average CO_2 levels during 2010–2011 are much lower (~355–360 ppmv), than the average CO_2 level of 418.3 ppmv observed at Ahmedabad during November 2013. CO also shows a similar diurnal variation but with some differences. Its levels keep on decreasing after the evening maximum around 2000 h to a low value of about 0.370 ppmv around 0500 h. After this, there is a slight increase till about 0900 h after which its values start decreasing again.

The minimum (0.325 ppmv) is reached around 1500 h. Like CO_2, CO values also start increasing after this minimum, but peak around 2000 h in the evening. Timings are slightly different for CO compared to CO_2, which also has the effects of biosphere in addition to fossil-fuel combustion and biomass burning. The variability in CO is also high (30–65%) from late night to early morning, and minimum (16%) during afternoon hours. CH_4, on the other hand, has different diurnal variation. After the peak (2.81 ppmv) in the evening around 2200 h, its values keep on decreasing till the afternoon minimum (2.02 ppmv) around 15 h. This species also has high variability (12–16%) in the late night and early morning, and minimum (2%) during afternoon hours.

These three gases have some common emission sources and some specific different sources. As mentioned earlier, CO_2 has both biospheric and combustion of fossil fuel and biomass burning. CO has emission sources from fossil-fuel combustion and biomass burning as well as oxidation from hydrocarbons. However, CH_4 has different sources such as wetlands, rice agriculture, landfills, coal mines, biomass burning as well as losses of compressed natural gas (CNG). There are many buses and autos being run on CNG in this city. Hence, the diurnal variations of these gases are different. The only common features are minimum in the afternoon and maximum in late evening/night. These features are dominated by the change in the height of the PBL from highest in the afternoon to lowest in the night/early morning. Also, both CO and CH_4 have losses by OH radicals. Since mixing ratios of OH are maximum during noon hours, so is the loss of both these gases. However, the reaction rate of OH with CH_4 is very slow (6.3×10^{-15} cm^3 mol^{-1} s^{-1}), which is only 1/24th that of reaction with CO (1.5×10^{-13} cm^3 mol^{-1} s^{-1}). The lifetime of CH_4 is about 8–10 years. CO_2 does not have any chemical loss. Hence its lifetime is highest (~40–50 years) among these gases.

Meteorological factors also play an important role in the distribution of trace gases. We have already discussed

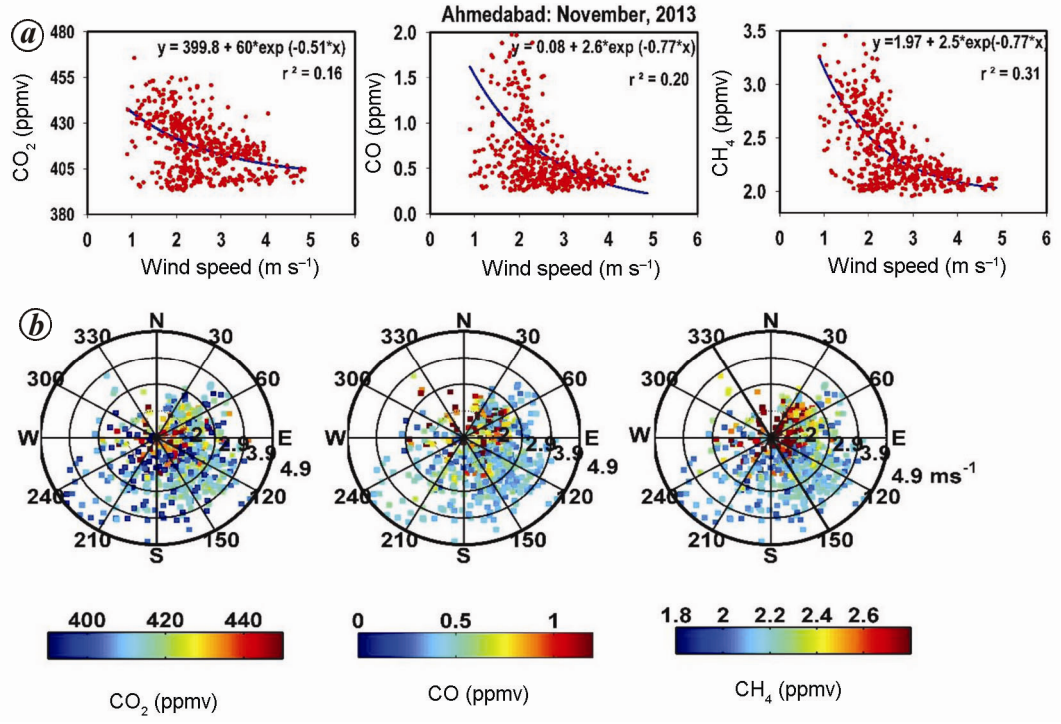

Figure 4. ***a***, Variations of measured CO_2, CO and CH_4 with wind speed observed at Ahmedabad during November 2013. ***b***, Polar diagrams showing variations of observed trace gases with wind speed and wind direction.

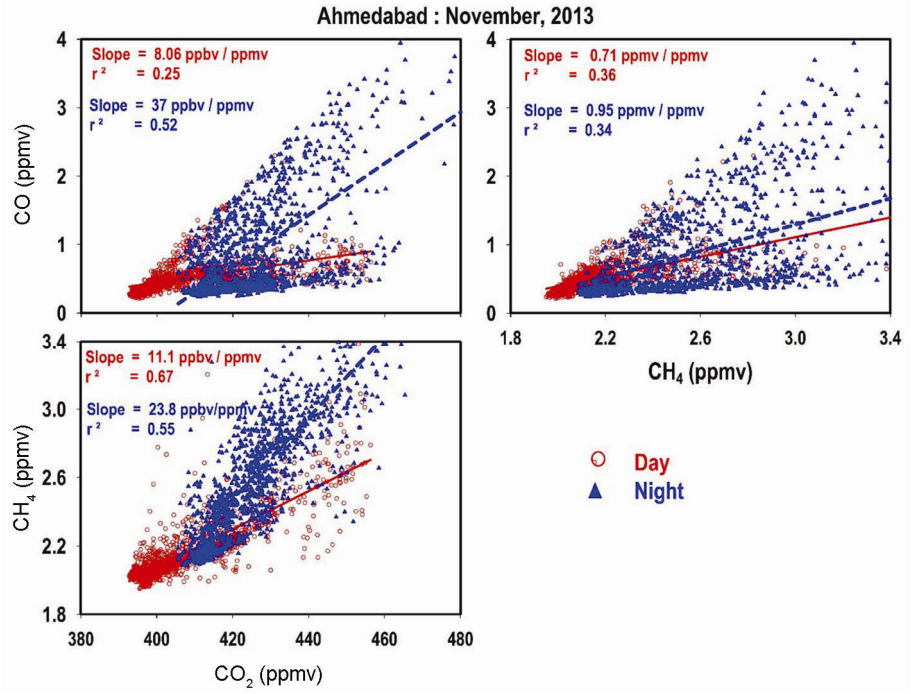

Figure 5. Correlations and slopes for CO–CO_2, CH_4–CO_2 and CO–CH_4 combinations during day and night. These are based on 15 min average data observed during November 2013 at Ahmedabad.

the role of PBL earlier. Air temperature and humidity also have an impact on some of the emission sources as well as chemistry. However, advection can change their concentrations significantly. Figure 4 *a* shows variation of mixing ratios of these species with wind speed. It is clearly evident that higher wind speed lowers the levels of these gases. However, the correlations are not good as wind direction and other factors also contribute to their changes.

Figure 4 *b* shows the wind polar diagrams, colour coded with the mixing ratios of CO_2, CO and CH_4, for November

2013. The episodes of higher mixing ratios of CO_2 (>425 ppmv), CO (>1 ppmv) and CH_4 (>2.5 ppmv) are mostly found when wind direction is in between 30° and 150°. The main city, a power house and several industries lie in this direction range. Also, higher levels of these gases are observed when the wind speed is low.

These three gases have some common emission sources and losses. Correlations and slopes can give some hint on the dominant emission sources or losses. For example, fossil fuel and biomass burning both emit CO_2 and CO, but CO emission is more during biomass/biofuel burning compared to that from fossil-fuel combustion. Hence the correlation slopes of CO with CO_2 will vary with the efficiency of combustion[20–22] and thus will provide a good proxy for evaluating the signature of source type and their combustion efficiencies. A good correlation between two gases will indicate if major emission sources or loss processes are common. In order to study the important common sources of CO_2, CO and CH_4, we calculated the correlations of CO–CO_2 and CH_4–CO_2 separately for day (07 : 00–18 : 45 h) and night (19 : 00–06 : 45 h). The ordinary least square regression method has been imposed to the 15-min average data of CO, CH_4 and CO_2 for estimating the correlation slopes and regression coefficients. Figure 5 shows correlations and slopes for different combinations.

Correlation of CO_2 with CO is not good, particularly during daytime as CO_2 has other biospheric sources and sinks and the lifetimes of the two gases are different. The slope ($\Delta CO/\Delta CO_2$) is found to be 8 and 37 ppbv/ppmv during day and night respectively, for this month at Ahmedabad. The average slope based on all the data is 16 ppbv/ppmv. The average ratio ($\Delta CO/\Delta CO_2$) is found around 13.4 ppbv/ppmv over Puducherry, India during April–May–June only based on weekly flask measurements during 2007–2011. Similar measurements for Hanle, India, a free tropospheric site, give this ratio in the range 35–55 ppbv/ppmv (ref. 12). Over China, the $\Delta CO/\Delta CO_2$ ratios are found in the range of 40–45 ppbv/ppmv (refs 23, 24), while southern California shows this ratio to be around 11 ppbv/ppmv (ref. 25). This shows the dominance of fossil fuel at Ahmedabad.

The correlation between CH_4 and CO_2 is found to be higher, 0.67 and 0.55 during day and night respectively, even though they are not emitted from common major sources. The atmospheric lifetimes of both gases are much longer than the timescale for mesoscale transport. Even if emitted from different sources, the dynamics in the boundary layer will cause mixing on very short timescales. The slope ($\Delta CH_4/\Delta CO_2$) is observed to be 11.1 and 23.8 ppbv/ppmv during day and night respectively, and the slope based on all the data is found to be 18 ppbv/ppmv in November at Ahmedabad. Puducherry, a southeast coastal station shows this ratio in the range of 6–9 ppbv/ppmv (ref. 12). Several studies have reported strong correlation between CH_4 and CO_2 over different urban regions and observed slopes in the range of 5–8 ppbv/ppmv (refs 25, 26). Higher ratio at Ahmedabad indicates relatively stronger source for methane.

Further, we have also derived the slope for CO–CH_4 ($\Delta CO/\Delta CH_4$), which is observed to be 0.71 and 0.95 ppmv/ppmv during day and night respectively. These are not very different from the average slope of 0.96 ppmv/ppmv based on all the data. However, correlations are poor (~0.35). Puducherry and Port-Blair show this ratio in the range of 0.4–1.4 ppbv/ppmv (ref. 12). The difference in the slopes is due to different types of emission sources.

Continuous measurements of CO_2 together with CO and CH_4 have been initiated at Ahmedabad. The average values of CO_2, CO and CH_4 for November 2013 are 418.3 ± 17.6, 0.73 ± 0.65 and 2.41 ± 0.42 ppmv respectively. Higher variabilities have been observed during the day and from day-to-day. Higher variability in CO is due to its relatively shorter lifetime. The observed $\Delta CO/\Delta CO_2$ slope indicates emissions in Ahmedabad are dominated by fossil fuel. The $\Delta CH_4/\Delta CO_2$ slope is higher than other sites, which suggests that there is significant source for CH_4 also in this city.

This analysis shows the importance of such simultaneous measurements to find the major emission sources.

1. Graven, H. D. *et al.*, Enhanced seasonal exchange of CO_2 by northern ecosystems since 1960. *Science*, 2013, **341**, 1085–1089.
2. Myhre, G. *et al.*, *Anthropogenic and Natural Radiative Forcing*, IPCC, Cambridge University Press, Cambridge, UK, 2013, pp. 659–740.
3. Kothawale, D. R. and Rupa Kumar, K., On the recent changes in surface temperature trends over India. *Geophys. Res. Lett.*, 2005, **32**, L18714; doi: 10.1029/2005GL023528.
4. Kulkarni, A. *et al.*, Glacial retreat in Himalaya using Indian Remote Sensing satellite data. *Curr. Sci.*, 2007, **92**, 69–74.
5. Mallik, C. and Lal, S., Changing long-term trends in tropospheric temperature over two megacities in the Indo-Gangetic Plain. *Curr. Sci.*, 2011, **101**, 637–644.
6. Patra, P. K. *et al.*, Carbon balance of South Asia constrained by passenger aircraft CO_2 measurements. *Atmos. Chem. Phys.*, 2011, **11**, 4163–4175.
7. Patra, P. K. *et al.*, The carbon budget of South Asia. *Biogeosciences*, 2013, **10**, 513–527.
8. Tiwari, Y. K. *et al.*, Carbon dioxide observations at Cape Rama, India for the period 1993–2002: implications for constraining Indian emissions. *Curr. Sci.*, 2011, **101**, 1562–1568.
9. Tiwari, Y. K. *et al.*, Influence of monsoons on atmospheric CO_2 spatial variability and ground-based monitoring over India. *Sci. Total Environ.*, 2014, **490**, 570–578.
10. Mahesh, P. *et al.*, Impact of land–sea breeze and rainfall on CO_2 variations at a coastal station. *J. Earth Sci. Climatic Change*, 2014, **5**; doi: 10.4172/2157-7617.1000201.
11. Sharma, N. *et al.*, Atmospheric CO_2 variations in two contrasting environmental sites over India. *Air, Soil Water Res.*, 2014, **7**, 61–68.
12. Lin, X. *et al.*, Five-year flask measurements of long-lived trace gases in India. *Atmos. Chem. Phys. Discuss.*, 2015, **15**, 7171–7238.
13. Patel, N., Dadhwal, V. and Saha, S., Measurement and scaling of carbon dioxide (CO_2) exchanges in wheat using flux-tower and remote sensing. *J. Indian Soc. Remote Sensing*, 2011, **39**, 383–391.

14. Patil, M. *et al.*, Measurements of carbon dioxide and heat fluxes during monsoon-2011 season over rural site of India by eddy covariance technique. *J. Earth Syst. Sci.*, 2014, **123**, 177–185.
15. Watham, T. *et al.*, Monitoring of carbon dioxide and water vapour exchange over a young mixed forest plantation using eddy covariance technique. *Curr. Sci.*, 2014, **107**, 858–867.
16. Anderson, B. E. *et al.*, Airborne observations of spatial and temporal variability of tropospheric carbon dioxide. *J. Geophys. Res.: Atmos.*, 1996, **101**, 1985–1997.
17. Machida, T. *et al.*, Worldwide measurements of atmospheric CO_2 and other trace gas species using commercial airlines. *J. Atmos. Ocean. Technol.*, 2013, **25**, 1744–1754.
18. Chen, H. *et al.*, High-accuracy continuous airborne measurements of greenhouse gases (CO_2 and CH_4) using the cavity ring-down spectroscopy (CRDS) technique. *Atmos. Meas. Tech.*, 2010, **3**, 375–386.
19. Karion, A. *et al.*, Long-term greenhouse gas measurements from aircraft. *Atmos. Meas. Techn.*, 2013, **6**, 511–526.
20. Suntharalingam, P. *et al.*, Improved quantification of Chinese carbon fluxes using CO_2/CO correlations in Asian outflow. *J. Geophys. Res.: Atmos.*, 2004, **109**; doi: 10.1029/2003JD004362.
21. Takegawa, N. *et al.*, Removal of NO_x and NO_y in Asian outflow plumes: aircraft measurements over the western Pacific in January 2002. *J. Geophys. Res.: Atmos.*, 2004, **109**, doi: 10.1029/2004 JD004866.
22. Turnbull, J. C. *et al.*, Comparison of $^{14}CO_2$, CO, and SF_6 as tracers for recently added fossil fuel CO_2 in the atmosphere and implications for biological CO_2 exchange. *Geophys. Res. Lett.*, 2006, **33**; doi: 10.1029/2005GL024213.
23. Han, S. *et al.*, Temporal variations of elemental carbon in Beijing. *J. Geophys. Res.: Atmos.*, 2009, **114**; doi: 10.1029/2009JD012027.
24. Wang, Y. *et al.*, CO_2 and its correlation with CO at a rural site near Beijing: implications for combustion efficiency in China. *Atmos. Chem. Phys.*, 2010, **10**, 8881–8897.
25. Wunch, D. *et al.*, Emissions of greenhouse gases from a North American megacity. *Geophys. Res. Lett.*, 2009, **36**; doi: 10.1029/2009GL039825.
26. Wong, K. W. *et al.*, Mapping $CH_4 : CO_2$ ratios in Los Angeles with CLARS-FTS from Mount Wilson, California. *Atmos. Chem. Phys.*, 2015, **15**, 241–252.

ACKNOWLEDGEMENTS. We thank PRL, Ahmedabad for encouragement and ISRO-GBP for financial support. We also thank P. K. Patra (JAMSTEC, Japan) for useful discussions; T. K. Sunilkumar (PRL) for help and S.L. thanks Tom Ryerson (NOAA, Boulder, USA) for useful suggestions about CO_2 measurements. We also thank the reviewer for useful comments and suggestions.

Received 2 June 2015; revised accepted 5 August 2015

doi: 10.18520/v109/i11/2111-2116

Observations of snow–meteorological parameters in Gangotri glacier region

H. S. Gusain*, Manish Kala, Ashwagosha Ganju, V. D. Mishra and Snehmani

Snow and Avalanche Study Establishment,
Research and Development Centre, Chandigarh 160 036, India

In this communication analysis of the snow–meteorological parameters recorded in the Gangotri glacier region has been presented. Maximum temperature, minimum temperature, snowfall, snow cover thickness, incoming shortwave radiation flux, reflected shortwave radiation flux and albedo have been recorded at 'Bhojbasa' observation station. Meteorological data of 13 years from 2000 to 2012 have been presented for annual and seasonal variations in temperature, snowfall and snow cover thickness. Winter, pre-monsoon, monsoon and post-monsoon data have been considered for analysis. Annual mean maximum and minimum temperature are 11.1 ± 0.7°C and –2.3 ± 0.4°C respectively. Mean values of these parameters obtained for winter season are 3.0 ± 1.0°C and –10.4 ± 1.3°C respectively. Mean annual snowfall amount is 257.5 ± 81.6 cm and maximum snow cover thickness varies from 42 to 205 cm for different years. Incoming shortwave radiation flux and reflected shortwave radiation flux have been recorded using pyranometer sensor mounted on automatic weather station, and data for 2012 and 2013 are presented. Incoming shortwave radiation flux and total atmospheric transmissivity have been estimated. Mean annual atmospheric transmissivity is 0.37 at the observation location. Mean seasonal albedo for winter season is observed to be quite high compared to other seasons. Maximum and minimum temperature reveal an increase of 0.9°C and 0.05°C respectively, during the decade. Annual snowfall amount reveals a decrease of 37 cm in the decade. The observed temperature and snowfall patterns during the past 13 years, at the present study location, indicate that trends in Central Himalaya may be in accordance with the observed trends in the Western Himalaya.

Keywords: Albedo, glacier, snowfall, snow cover, temperature.

THE Himalaya Mountains are the abode of the largest number of glaciers outside the polar regions. These glaciers are the major source of many perennial river systems, including the Ganga, Indus and Brahmaputra[1]. These rivers play a critical role in meeting the demands of water, irrigation and hydropower[1,2]. Gangotri glacier is one of the most well-studied glaciers in India and is the largest glacier in the Garhwal Himalaya[3]. Studies of the Gangotri glacier have been conducted for analyses of glacier

*For correspondence. (e-mail: gusain_hs@yahoo.co.in)